UNIVERSITY OF Southampton

University of Southampton Research Repository
ePrints Soton

Copyright © and Moral Rights for this thesis are retained by the author and/or other copyright owners. A copy can be downloaded for personal non-commercial research or study, without prior permission or charge. This thesis cannot be reproduced or quoted extensively from without first obtaining permission in writing from the copyright holder/s. The content must not be changed in any way or sold commercially in any format or medium without the formal permission of the copyright holders.

When referring to this work, full bibliographic details including the author, title, awarding institution and date of the thesis must be given e.g.

AUTHOR (year of submission) "Full thesis title", University of Southampton, name of the University School or Department, PhD Thesis, pagination

http://eprints.soton.ac.uk

UNIVERSITY OF SOUTHAMPTON

FACULTY OF PHYSICAL SCIENCES AND ENGINEERING

SCHOOL OF PHYSICS AND ASTRONOMY

A Novel Magneto Optical Trap for Integrated Atom Chips

by

Joseph Adam Rushton

Thesis for the degree of Doctor of Philosophy

July 2015

UNIVERSITY OF SOUTHAMPTON

ABSTRACT

FACULTY OF PHYSICAL SCIENCES AND ENGINEERING
SCHOOL OF PHYSICS AND ASTRONOMY

Doctor of Philosophy

A NOVEL MAGNETO OPTICAL TRAP FOR INTEGRATED ATOM CHIPS

by Joseph Adam Rushton

This thesis describes the design and construction of a new magneto optical trap that is suitable for use in integrated atom chips and other vacuum systems in which optical access is limited to a single window. The trap design relies on the switching of optical and magnetic fields and can operate at frequencies at least within the region of 1 kHz to 60 kHz. The design does not need patterned surfaces in order to generate the necessary beam geometry, requiring only the use of a single, standard mirror. Early temperature measurements have indicated that the trap may be capable of sub-Doppler cooling, and that it is able to capture on the order of 1.7×10^6 atoms in a capture volume of $0.18\,\mathrm{cm}^3$.

Contents

Declaration of Authorship

I, Joseph Adam Rushton , declare that the thesis entitled *A Novel Magneto Optical Trap for Integrated Atom Chips* and the work presented in the thesis are both my own, and have been generated by me as the result of my own original research. I confirm that:

- this work was done wholly or mainly while in candidature for a research degree at this University;
- where any part of this thesis has previously been submitted for a degree or any other qualification at this University or any other institution, this has been clearly stated;
- where I have consulted the published work of others, this is always clearly attributed;
- where I have quoted from the work of others, the source is always given. With the exception of such quotations, this thesis is entirely my own work;
- I have acknowledged all main sources of help;
- where the thesis is based on work done by myself jointly with others, I have made clear exactly what was done by others and what I have contributed myself;
- parts of this work have been published as: [1]

Signed:.....

Date:.....

Acknowledgements

Foremostly, I could never have completed this thesis without the lifelong help and support from my loving mum, Rebecca. I had severe doubts about whether I could finish this work, and it would be impossible for me to overemphasise the importance of her help in keeping me going.

I would like to thank Matt Himsworth for his great advice throughout my time on this project, making me grasp the nettle when I was concerned about breaking things. I also would have been unable to complete chapter two of this thesis without all of the work he put into the feasibility study into miniaturized magneto optical traps[1]. I would also like to thank James Bateman who conjured the phoenix of the SMOT out of the ashes of the failed Φ-MOT design. The time I spent working with Alex Dunning made this experience infinitely more pleasurable, and he was always able to offer helpful advice when the lab daemons struck. I'm going to miss all of the antics in the office, particularly those of Jeff and Steve, who were always the centre of attention. I also appreciate all of the help and advice given to me by Gareth Savage from the electronics workshop, who was very patient with all of my questions. Finally I would like to thank Mark Scully and Mark Bampton from the mechanical workshop, who also had to suffer my pestering.

My father, Matthew, of course has also been a great help ensuring that I've been well fed and watered, and has provided me with good company over these last few years.

So long, and thanks for all the beer.

.

Everybody does have a book in them, but in most cases that's where it should stay.

CHRISTOPHER HITCHENS

Chapter 1

Introduction

1.1 Ultracold Atoms and Atom Chips

Soon after A. Ashkin suggested in 1970 the possibility of using resonant light to trap neutral atoms in circular orbits[2], T.W. Hänsch and A.L. Schawlow proposed that near resonant red-detuned laser light could be used to cool neutral atoms through the process of Doppler cooling[3]. Several designs were later conceived to spatially confine these atoms using just the scattering force[4, 5], however Ashkin and J.P.Gordon later proved that this was impossible due to an optical analogy of Earnshaw's theorem[6]. Steven Chu *et al.* first achieved three dimensional Doppler cooling in 1985, lowering the temperature of their sodium atoms to approximately 240 µK, yet trapping had still not been achieved[7]. Other proposals were suggested to get around the Earnshaw theorem by using AC light fields, magnetic field gradients and optical pumping[8–10], and following an idea suggested by Jean Dalibard, the Magneto Optical Trap (MOT) was demonstrated by E.L. Raab *et al.* in 1987[11].

Further techniques, such as magnetic trapping and evaporative cooling[12], brought temperatures down to the nanokelvin regime, opening the door for Bose-Einstein condensation (BEC) in these atomic vapours[13]. The coherent nature of these systems means that they can be used in atom interferometers, much in the same way coherent light is used in optical interferometers. The superior sensitivity of cold atom interferometry allows the production of highly accurate clocks, gravimeters and rotation sensors and enables tests of fundamental physics and precise measurements of physical constants[14–18].

In recent years interest has grown in so called atom chips[19]. These microfabricated devices use lithographically defined wires and mirrors to cool, trap and manipulate atoms close to surfaces. Atom chips typically use 'mirror-MOTs' in conjunction with magnetic trapping and evaporative cooling to produce BECs microns above their substrates. Various atom chip based sensors[20, 21], atomic clocks[22] and even magnetic conveyor belts have been demonstrated[23] and proposals have been made to use them as the basis of quantum computers[24].

Whilst atom chips themselves are microfabricated devices on the order of the size of a matchbox, they cannot operate on their own and still require ancillary equipment such as vacuum chambers, pumps and lasers to provide any functionality. The footprint of this equipment, however, can take up a large proportion of a laboratory's space and thus serves to anchor what would otherwise be rather portable devices. The potential benefit of mobile atom chips is evident by their accuracy in timing and sensing applications, but many of these cannot be realized until the burden of this anchor is lifted by miniaturizing this associated technology.

1.2 The Chip Scale Vapour Cell and Atomic Clock

One of the great innovations towards the goal of miniaturising atomic physics packages was demonstrated in 2003 when Li-Anne Liew *et al.* from the National Institute of Standards and Technology (NIST) presented a microfabricated caesium vapour cell consisting of an etched silicon wafer sandwiched between a pair of quartz windows[25]. The sandwich was sealed using the well characterized anodic bonding technique and allowed for cells with internal volumes below $1\,\mathrm{mm}^3$, much smaller than the packages permitted by traditional glass-blowing technology. Liew *et al.* also described two separate methods with which to dispense the alkali metal within the package, either by a chemical reaction of barium azide with caesium chloride or direct injection of liquid caesium whilst in an oxygen free environment. The former technique allowed the sealing to be enacted in an ultra high vacuum, whilst the latter was a simpler technique for applications that could cope with higher background pressures. This miniature vapour cell demonstrated the viability of microfabricating atomic physics packages and foreshadowed future developments such as portable atomic spectroscopic and time standards.

Svenja Knappe *et al.* continued the development of these vapour cells at NIST, revealing the first caesium Chip Scale Atomic Clock (CSAC) in 2004[26]. Previous designs of miniature atomic clocks usually required the use of microwave cavities

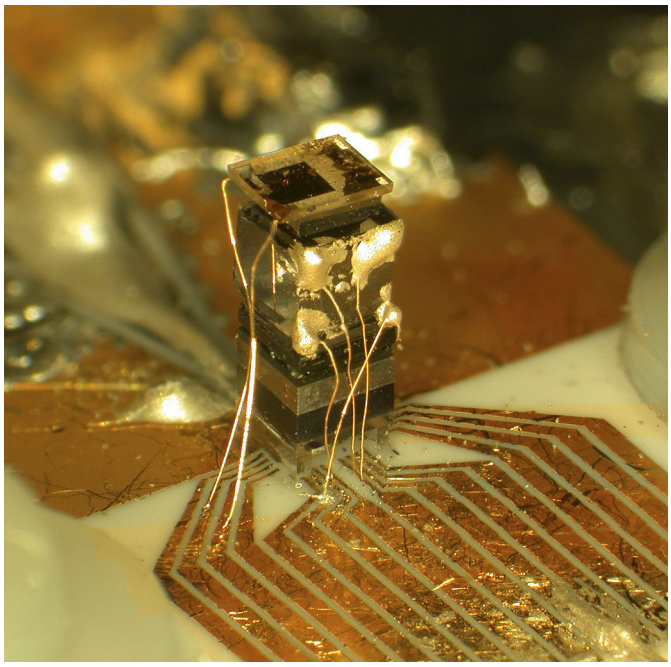

Figure 1.1: Chip Scale Atomic Clock (CSAC) by Svenja Knappe *et al.* at NIST. The total height of the stack is 4.2 mm. This image is in the public domain because it is a work of the United States Federal Government, under the terms of Title 17, Chapter 1, Section 105 of the US Code.

in order to induce their magnetic dipole transitions, which had necessarily limited their size to at least half the wavelength of the clock transition, corresponding to $\sim$ 1.6 cm for caesium. The CSAC, however, was able to be reduced to sizes much smaller than this because it probed the clock transition using the all optical phenomenon of Coherent Population Trapping, realizing a resonance width of 7.1 kHz[27, 28]. The CSAC consisted of a stack of microfabricated elements including the vapour cell of Liew *et al.* in combination with a Vertical Cavity Surface Emitting Laser VCSEL, collimating and polarizing optics, filters, heaters and a photodiode, all of which when combined was smaller than a grain of rice. The clock operated by modulating the VCSEL at half of the clock frequency of caesium in order to produce two first order optical sidebands separated by the hyperfine transition. The vapour becomes transparent if the modulation frequency is exactly half of the transition frequency, so a photodiode measures the transmission through the vapour cell while an external servo loop acts to maximize this value by tuning the modulation frequency, thus keeping it locked to the atomic reference.

The importance of the work at NIST is that it illustrated the great benefits of miniaturising physics packages through wafer level microfabrication, both resulting

in a vast improvement in power consumption and portability, but also showing how readily these processes could be scaled up and thus become more economical.

Chapter 2

Integrated Atom Chips

One approach to producing a portable atom chip is to miniaturize the existing technology, for example the miniature vacuum chamber and ion pump used by ColdQuanta[29]. We instead are interested in creating an Integrated Atom Chip (IAC), so rather than placing an atom chip in a miniaturized vacuum chamber, we invert the design so that the chip itself becomes the vacuum chamber. In designing these devices, we will need to replace external turbomolecular and ion vacuum pumps with non-evaporable getter films and planar microfabricated mini-ion pumps[30]. Lasers which would usually be located on an optical bench need to be redesigned such that they are fabricated on or in the chip and external coils used to produce the magnetic fields must be substituted with a combination of thin magnetic films and on-chip deposited wires and coils.

An integrated atom chip has the obvious advantage over existing atom chip designs of an increase in portability and because of this, allows practical mobile cold atom sensors for applications such as geodesy and the prospecting for both oil and minerals. Microfabrication not only allows for the reduction of device size, but also lends itself to mass production, enabling this technology to become more affordable and opening the way for possible new applications.

We aim to produce an IAC package that is completely self contained and that can be manufactured using techniques developed for MEMs and the semiconductor industry, rather than just shrinking the current designs of vacuum chambers and external optics. This should make the fabrication suitable for parallel processing, both to allow for mass production of these devices, but also to reduce their experimental cost to research institutions.

2.1 Technical Challenges

In order to produce integrated atom chips we have to tackle a number of engineering problems. Perhaps most obviously, we need to produce a chamber which can seal an ultra high vacuum and we must be able to maintain this pressure for the lifetime of the device. Suitable atom sources need to be sealed into the chips which are able to provide atoms on demand but stable enough to maintain a high vacuum and last for the lifetime of the chip. A trap geometry needs to be invented that is compatible with the design of the integrated atom chip, taking into consideration the possible constraints of the system such as reduced optical access and, if necessary, appropriate electrical and optical feedthroughs need to be developed to allow for manipulation of the cold atoms from the outside world. Also the external electronic and optical systems, such as the laser stabilization, beam modulators and electronic feedback systems need to be shrunk to a size on the order of the integrated atom chips themselves.

Our goal is to design an integrated atom chip with a device lifetime of 1000 days. This figure is fairly low for a commercial product but presents significant theoretical and technical challenges whilst acting as a benchmark for future designs. The typical lifetime of consumer applications using MEMS vacuum encapsulation is around 3 to 5 years and up to 20 years if used in avionics. Our 1000 day figure is thus approaching the lower end expected of a consumer device[31]. The prototype chip must maintain a vacuum of 10^{-10} mbar and be able to do so with passive pumping alone, as although integrated ion pumping has been demonstrated previously[32], the added complexity of this technology has led us to leave this to be implemented in a later model. Cold atom clouds can form in magneto optical traps even at pressures on the order of the room temperature vapour pressure of rubidium[33], however as the pressure increases the lifetime of atoms in the trap reduces as a result of collisions with those of the background. Although higher pressure traps have lower lifetimes than their counterparts, they offer high capture rates and so are frequently employed to pre-cool atoms before being loaded into a secondary, low pressure MOT. We chose a target pressure of 10^{-10} mbar for our integrated atom chips as it allows the freedom to implement dual chamber designs, but also is sufficiently low to form Bose-Einstein condensates without this secondary chamber if light induced atomic desorption is used to enhance the loading rate[34].

2.2 Ultra High Vacuum

Macroscopic vacuum chambers typically use stainless steel components, often with the standard ConFlat or Klien flanges being employed to connect them together. Construction of a vacuum chamber begins with a thorough degrease of these pieces, starting the process using a simple detergent followed by an acetone bath and, after perhaps a number of intermediate solvents, a final clean with methanol. The vacuum chamber is then assembled, and if Ultra High Vacuum (UHV) or even lower pressures are desired then baking is performed to remove gas in the walls of the steel which would otherwise drastically increase the base pressure. For unbaked systems, the outgassing is dominated by absorbed gas in the metal's surface oxide, however baked systems experience outgassing that is primarily determined by diffusion through the bulk of the material[35, 36]. This baking process is accompanied by a combination of turbo-molecular and rough pumping so that the desorbing material can be removed. Upon completion of the bake, the chamber is sealed off from these pumps and a number of ion pumps are activated to bring the pressure into the UHV region.

One way to miniaturise this system would be to microfabricate a series of MEMS pumps analogous to those used in standard vacuum chambers [37]. In a commercial product, however, there would often be no need to open the device up to atmospheric pressures, and so a simpler and more effective method of providing in-chip ultra high vacuum would be to seal the device whilst already in a UHV environment.

As the vacuum chamber is formed within our atom chips we first must etch or machine a cavity into the substrate and then hermetically bond a capping wafer to it after the appropriate pumps, wires and atom sources are placed within. Optical access is essential to be able to magneto optically trap atoms within an IAC, so there must be a transparent region through which lasers can be passed and through which the atoms can be imaged. This would be achieved most easily by using a glass wafer as the capping layer, and this is the approach we are taking in our initial designs. The substrate that forms half of the integrated vacuum chamber must have a negligible vapour pressure, a low outgassing and permeability rate, and it must be able to be etched or machined. There must be suitable bonding techniques that can hermetically seal the substrate to glass, and the materials must have closely matched coefficients of thermal expansion (CTE) so that they do not experience cracks due to stresses exerted during outgassing and other microfabrication processes.

First we consider using stainless steel as the substrate with which to form the micro-chambers of our integrated atom chips. Stainless steel is widely used in vacuum chambers, having been extensively studied for that purpose, and there are a few bonding techniques available to adhere it to glass. The mismatch in coefficients of thermal expansion preclude naïvely producing a stainless steel to glass bond at high temperature because the fragility of glass under tension makes it liable to crack upon cooling. Kovar is used in vacuum chamber viewports as it has a CTE that is well matched to glass, however we can immediately discount its use due to its undesirable magnetic properties. Compression seals instead rely on the compressive strength of glass, avoiding the application of tension, yet this technology does not lend itself to wafer level microfabrication. Housekeeper seals can be used for materials with poorly matched CTEs, however these rely on forming a tapered metal edge which again may pose difficult to microfabricate.

Having discounted stainless steel we can now see that silicon is a natural choice for the substrate of our devices. Being the most commonly used semiconductor in electronics, many microfabrication procedures have been designed to work with the material and it is commonly available in high purity. In addition, silicon has extremely low permeation and outgassing rates. There are a number of glasses that have closely matched CTEs to silicon and these can be bonded though a number of microfabrication techniques.

The vacuum requirements of MEMS devices differ hugely depending on their application, this varies from $10^{3}\,\mathrm{mbar}$ to $10^{-4}\,\mathrm{mbar}$ for absolute pressure sensors to lower than $10^{-4}\,\mathrm{mbar}$ for microbolometers[38]. The lowest measured pressure we have found reported in a MEMS device is $10^{-8}\,\mathrm{mbar}$ for a field emission display. This, admittedly, was maintained through the use of an external pump that acted upon a evacuation tube, and was also seemingly inferred from measurements using a vacuum gauge external to the MEMS package[39]. Pressures in other MEMS devices may be lower than this value, however without suitable in chip gauges they lack the means to measure the quality of their vacuum. It is a matter of serendipity that the cold atoms that we wish to trap within our devices have the capability of measuring their background pressure. This is possible because the loading rate of a magneto optical trap is a linear function of the background pressure. This relationship has been known since MOTs were first demonstrated, but with the ready availability of vacuum gauges it was not characterised until 2012 when Arpornthip *et al.* showed that the MOT loading time τ is related to the vacuum pressure by the proportionality constant of $(2 \times 10^{-8}\,\mathrm{mbar\,s})/\tau$[40].

2.2.1 Pumping

Our integrated atom chips will be sealed under ultra high vacuum, however without the use of in-chip pumps, the quality of the vacuum will soon decrease as the internal surfaces of the chip outgas, the seals leak and contaminants permeate through the chip's walls. As mentioned earlier in this chapter, the pumping scheme that will be employed in our first integrated atom chips is purely passive, leaving ion pumping elements to be incorporated in subsequent designs. In our prototype IACs, we will be using Non Evaporable Getter films, NEGs, to passively pump any reactive gases that may desorb from the chips' walls.

Getters are alloy depositions that act as pumps due to their ability to react with and adsorb chemically active gaseous species that are incident upon them. NEGs are getters which have the added property that during activation and reactivation any adsorbed material on the film's surface does not outgas, ruining the vacuum. Instead the reacted species diffuse into the bulk of the material, revealing a fresh surface ready for further pumping whilst maintaining the existing vacuum.

2.2.2 Permeation

Two of the greatest concerns that threaten the vacuum in integrated atom chips are hydrogen and the noble gases, of which helium is a particular worry. The Achilles heel of our passively pumped micro-chamber is that non-evaporable getters are unable to pump the nobles due to their very low chemical reactivity and, as as result, their permeation is one of the weakest links in maintaining ultra high vacuum. Helium is often used as a tracer due to its ability to pass through extremely small leaks and, as considered in this section, is able to permeate glass.

The permeation of gas through the walls of a vacuum chamber can be broken down to several steps[41]:

1. Gas molecules are incident upon the external walls of the chamber.
2. Adsorption of the gas onto the material's surface.
3. If energetically favourable the permeating gas disassociates upon adsorption.
4. The molecules are then dissolved into the surface of the material to a degree that depends on their solubility.

5. The gas diffuses through the bulk along a concentration gradient as per Fick's first law (equation 2.2), eventually reaching another surface.

6. The dissolved gas moves from the bulk of the material to this new surface.

7. Desorption of the gas occurs on the vacuum side of the chamber wall, if necessary recombining as it does so.

Surfaces complicate the permeation process as, for example, the oxide layer that is found upon stainless steel vacuum chambers can act as a barrier to throttle permeation (and degassing), and the recombination of disassociated molecules upon desorption acts as a further restriction[36, 42, 43]. The influence of a material's surface only acts to reduce the permeation rate of gases, as a result treating permeation as mere diffusion through the bulk can only overestimate the permeation rate, and so this conservative approach is taken in the following subsection.

2.2.2.1 Bulk Diffusion

To quantify the permeation through the walls of a vacuum chamber we begin with Boyle's law, which states that the product of the pressure and volume for a given mass of gas is constant at a constant temperature. This provides a measure of the quantity of a gas, from which the flow rate into a volume V can be defined as:

$$Q = \frac{d(PV)}{dt} \tag{2.1}$$

where P is the pressure of a gas within the volume. Fick's first law states that upon reaching a steady state F, the rate at which a substance diffuses through a barrier of unit area is proportional to the concentration gradient across the barrier:

$$F = \frac{Q}{A} = -D\frac{\partial C}{\partial x} \tag{2.2}$$

where C is the concentration of the diffusing substance, D is the diffusion coefficient and x is the space coordinate normal to the barrier's surface. The diffusion coefficient is exponentially dependent on temperature:

$$D = D_0 \exp\left(\frac{-E_D}{k_B T}\right) \tag{2.3}$$

where E_D is the activation energy for diffusion, k_B is the Boltzmann constant and T is the barrier temperature. The concentration of gas dissolved within the surface of a solid is determined by Henry's law, which states that it is related to

the partial pressure of the gas at the surface by:

$$C = SP^n \tag{2.4}$$

where the parameter S is the solubility of the gas in the solid and n is a constant that depends on the material and is equal to one for non-metals and is one half for diatomic molecules in metals. This latter case is known as Sieverts' law. As with the diffusion coefficient, the solubility also takes the form of an Arrhenius equation:

$$S = S_0 \exp\left(\frac{-E_S}{k_B T}\right) \tag{2.5}$$

where E_S is the energy of solution. Combining Henry's law with Fick's first law of diffusion we can find the diffusion rate of a quantity of gas through the walls of a vacuum chamber of thickness d and surface area A:

$$Q = \frac{KA(P_{ext}^n - P_{int}^n)}{d} \tag{2.6}$$

where P_{ext} and P_{int} are respectively the partial pressures of the diffusing substance within the atmosphere and inside the vacuum chamber, and $K = DS$ is the permeation rate. This diffusion rate relies on the assumption of Fick's first law that the concentration gradient has reached a steady state within the barrier. If this is not the case then Fick's second law must be employed, which states that the time dependence of the concentration along a diffusion barrier is determined by the differential equation:

$$D\frac{\partial^2 C}{\partial x^2} = \frac{\partial C}{\partial t} \tag{2.7}$$

which is analogous to Fourier's heat equation, and can be solved using the same techniques[44–46].

The materials that are used to make integrated atom chips must be thoroughly degassed prior to assembly in an effort to increase device lifetime. Degassing removes dissolved gas particles within the vacuum chamber's walls and grants a delay period before which permeation into the chamber can reach its maximum flow rate. A well degassed barrier should begin completely devoid of the contaminating gas, and thus would have a concentration of zero throughout its extent $C(x, t = 0) = 0$. If at time $t = 0$ one side of the barrier at $x = 0$ is exposed to a partial gas pressure of P_{ext} then from Henry's law (eq. 2.4) we can say the concentration of this gas at its surface must equal to $C(x = 0, t) = SP_{ext}^n$. This assumption is justified considering the time scales of diffusion throughout the bulk are significantly longer than those which govern the initial absorption of the gas

into the material's surface. The concentration at the vacuum side of the barrier is assumed to be zero throughout the diffusion process $C(x = d, t) = 0$, which is appropriate if the chamber's partial pressure is negligible compared to the atmospheric partial pressure, and thus does not have an appreciable influence on the permeation rate. In equilibrium, after a sufficient time has passed, equation 2.2 shows that the concentration is linear across the barrier and is determined by the two boundary conditions at the surfaces of the material. The equilibrium concentration is thus given by $C_{eq}(x) = SP^n_{ext}(1 - \frac{x}{d})$, from which we can define a new function $v(x, t)$ that relates the equilibrium concentration to that found at time t at position x:

$$C(x, t) = C_{eq}(x) + v(x, t) \tag{2.8}$$

Taking time and position derivatives of this function gives:

$$\frac{\partial v}{\partial t} = \frac{\partial C}{\partial t} - \frac{\partial C_{eq}(x)}{\partial t} = \frac{\partial C}{\partial t} \tag{2.9}$$

$$\frac{\partial^2 v}{\partial x^2} = \frac{\partial^2 C}{\partial x^2} - \frac{\partial^2 C_{eq}(x)}{\partial x^2} = \frac{\partial^2 C}{\partial x^2} \tag{2.10}$$

which shows that $v(x, t)$, like $C(x, t)$, must also satisfy equation 2.7, but with the easier to solve boundary conditions $v(x = 0, t) = v(x = d, t) = 0$. This differential equation can be solved using the separation of variables to yield a Fourier series with an exponential time dependence:

$$v(x, t) = \sum_{m=1}^{\infty} B_m \sin\left(\frac{m\pi x}{d}\right) \exp\left(-D\left(\frac{m\pi}{d}\right)^2 t\right) \tag{2.11}$$

We can now find the expansion coefficients by using the initial condition that the membrane begins completely degassed $v(x, t = 0) = C(x, t = 0) - C_{eq}(x) = -SP^n_{ext}(1 - \frac{x}{d})$:

$$\begin{aligned} B_m &= \frac{2}{d}\int_0^d v(x, t = 0) \sin\left(\frac{m\pi x}{d}\right) dx \\ &= -\frac{2}{d}\int_0^d SP^n_{ext}\left(1 - \frac{x}{d}\right) \sin\left(\frac{m\pi x}{d}\right) dx \\ &= -\frac{2SP^n_{ext}}{m\pi} \end{aligned} \tag{2.12}$$

which leads to the solution:

$$v(x, t) = -\sum_{m=1}^{\infty} \frac{2SP^n_{ext}}{m\pi} \sin\left(\frac{m\pi x}{d}\right) \exp\left(-D\left(\frac{m\pi}{d}\right)^2 t\right) \tag{2.13}$$

$$C(x,t) = SP_{ext}^{n}\left[(1-\frac{x}{d}) - \sum_{m=1}^{\infty}\frac{2}{m\pi}\sin\left(\frac{m\pi x}{d}\right)\exp\left(-D\left(\frac{m\pi}{d}\right)^{2}t\right)\right] \quad (2.14)$$

Although we know how $C(x,t)$ is related to the pressure in the cavity from Henry's law $P_{int}(t) = \sqrt[n]{C_(x=d,t)/S}$, we cannot use equation 2.14 to directly find it as we have set the concentration to equal zero on the vacuum side of the barrier in choosing our boundary conditions. We can however combine equations 2.1 and 2.2 to find how the rate of change of the chamber pressure is related to the concentration profile in the material:

$$\frac{\partial P}{\partial t} = -\frac{DA}{V}\frac{\partial C}{\partial x} \quad (2.15)$$

then using equation 2.14 we can determine the rate at which gas flows into the cavity:

$$\frac{\partial P(x=d,t)}{\partial t} = \frac{DSA}{Vd}P_{ext}^{n}\left[1+\sum_{m=1}^{\infty}2\cos(m\pi)\exp\left(-D\left(\frac{m\pi}{d}\right)^{2}t\right)\right] \quad (2.16)$$

which after a sufficiently long time reduces back to the rate shown in equation 2.6, again under the assumption that the cavity pressure makes a negligible reduction of the permeation rate. Equation 2.16 can now be integrated to find the pressure in the cavity at time t:

$$P_{int}(t) = \frac{DSA}{Vd}P_{ext}^{n}\left[t - \frac{d^2}{6D} - \sum_{m=1}^{\infty}\frac{2}{D}\left(\frac{d}{m\pi}\right)^{2}(-1)^{m}\exp\left(-D\left(\frac{m\pi}{d}\right)^{2}t\right)\right] \quad (2.17)$$

where we have used the fact that the infinite alternating series in the result is given by the Dirichlet eta function:

$$\eta(2) = \sum_{m=1}^{\infty}\frac{(-1)^{m-1}}{m^2} = \frac{\pi^2}{12} \quad (2.18)$$

The cavity pressure predicted by equation 2.17 is only overestimated by our earlier decision to set the boundary condition of the cavity pressure to zero, thus we are erring on the safe side of this calculation. After a sufficiently long time the exponential in this function becomes negligible and the cavity pressure can be approximated by the linear function:

$$P_{int}(t) \approx \frac{DSA}{Vd}P_{ext}^{n}(t-t_c) \quad (2.19)$$

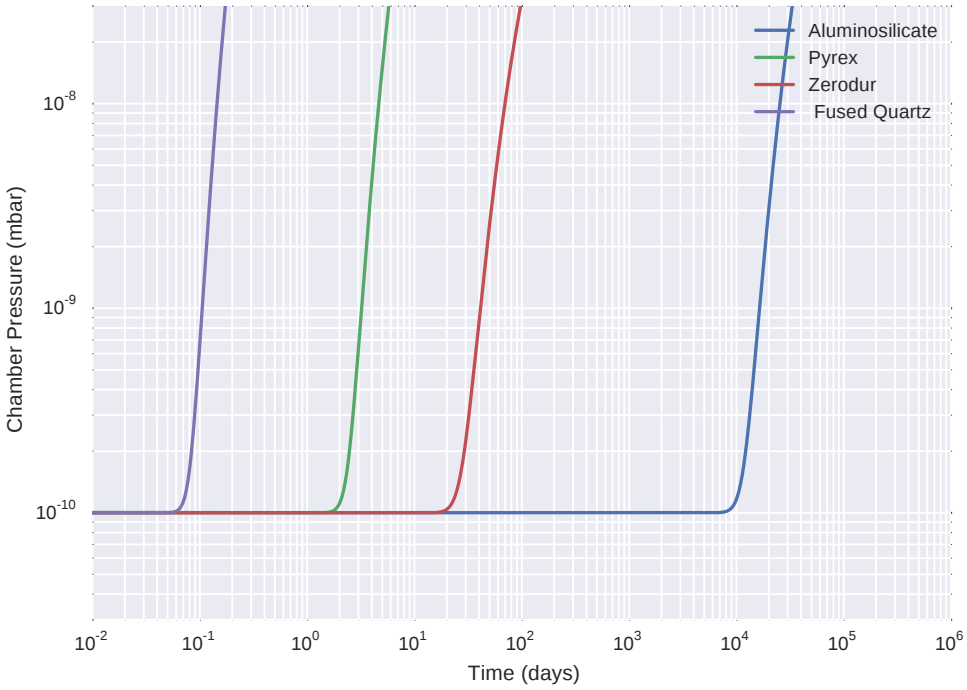

Figure 2.1: Theoretical pressure within several different integrated atom chips as a function of time due to helium permeation through their 1 mm thick glass capping wafers. The plots have been calculated using equation 2.17 and data has been sourced from[47, 48].

where $t_c = \frac{d^2}{6D}$ is the characteristic time, a measure of the time required to reach a constant flow of gas.

Our integrated atom chips will have a glass capping wafer to both seal our evacuated cavities, but also to allow for optical access into and out of the chips. As noble gases permeate through glasses, and also cannot be pumped by NEGs we have to choose an appropriate type of glass that has a sufficiently low permeation rate that the nobles do not significantly raise the base pressure of the cavities during the lifetime of the chips.

Figure 2.1 shows the time dependent partial pressure of helium within several atom chips with differing glass composition capping wafers as the gas permeates through them. All of the chips are modelled at a temperature of 20 °C and as having an internal volume of 0.5 cm^3 with a glass capping wafer 1.0 mm thick and single sided surface area 2.5 cm^2. The devices are modelled as being exposed to atmospheric air and thus are in the presence of a partial pressure of helium of 5.31×10^{-3} mbar[49–51]. The three glass wafers modelled are fused quartz, Pyrex (Corning 7740) and aluminosilicate (Corning 1720), and the permeation figures are

	Atomic/molecular diameter (Å)	Permeability constant K (fused silica) at 700 °C
Helium	1.95	2.1×10^{-8}
Hydrogen	2.5	2.1×10^{-9}
Deuterium	2.55	1.7×10^{-9}
Neon	2.4	4.2×10^{-10}
Argon	3.15	$<10^{-15}$
Oxygen	3.2	$<10^{-15}$
Nitrogen	3.4	$<10^{-15}$

Table 2.1: Atomic/molecular diameter and permeability of various gases through fused silica at 700 °C[41, 54].

taken from[47, 48]. The plot clearly shows that aluminosilicate glass has superior permeation properties, with a lifetime more than two orders of magnitude greater than the second best glass Zerodur.

Aluminosilicate also has a sufficiently well matched CTE to silicon for it to be anodically bonded, and so it is an ideal material for our devices, and is the main glass material we are investigating [52]. The permeation of other gases through glasses can be estimated by the relative size of the gaseous molecule, and table 2.1 shows this comparison for some of the smaller gases, the permeation rate dropping by five orders of magnitude for molecules larger than 0.25 nm[41]. These rates can be referenced to table 2.2 which shows the partial pressure of the gases more commonly found in the atmosphere. The other gas of concern with regard to permeation through glass is hydrogen, although it is not as much of a threat as it is pumped by non-evaporable getters, it has has very low amounts in the atmosphere and has a lower permeation than helium in glasses due it being transported as a diatomic form rather than dissociating upon adsorption[53]. As silicon is the other significant material in our integrated atom chips the permeation through it also has to be considered. Thankfully the permeation of these gases is very low through silicon due to its crystalline structure and so they do not provide a great threat to the vacuum. A collection of the wide variation in the diffusivity data of hydrogen and helium in silicon has been compiled from the literature and is presented in appendix C for reference.

2.2.3 Outgassing

In the previous section regarding permeation we considered the flow of gas through a barrier that is initially completely degassed. Outgassing could be defined to

	Partial pressure (mbar)[49]	Partial pressure (mbar)[50, 51]
N_2	791.86	791.1
O_2	212.25	212.3
CO_2	3.14×10^{-1}	3.58×10^{-1}
He	5.31×10^{-3}	5.31×10^{-3}
Ne	1.842×10^{-2}	1.842×10^{-2}
Ar	9.46	9.46
Kr	1.16×10^{-3}	1.16×10^{-3}
Xe	8.8×10^{-5}	8.8×10^{-5}
O_3	-	variable
N_2O	-	3.1×10^{-4}
CO	-	1.2×10^{-4}
H_2	-	5×10^{-4}
NH_3	-	1×10^{-4}
NO_2	-	1×10^{-6}
SO_2	-	2×10^{-7}
H_2S	-	2×10^{-7}
CCl_2F_2	-	4.9×10^{-7}
CCl_3F	-	2.8×10^{-7}

Table 2.2: Partial pressure of the constituents of dry atmospheric air assuming a total pressure of 1013.25 mbar[49–51].

encompass this, and any other inadvertent flux of atoms into a vacuum chamber however we instead regard outgassing as gas sources due to contaminants that have not been completely removed from the bulk of the chamber or remain adhered to its surfaces.

As mentioned previously, strict cleaning procedures must be followed to prepare a vacuum chamber for use, however the subsequent baking step is just as important, reducing the concentration of molecules available to outgas as the chamber is brought back to room temperature. The desorption rate of a material depends on the binding energies of the various contaminating gases to the surface, the surface temperature and surface coverage[55]. Two types of adsorption methods keep molecules and atoms adhered to the surface of a vacuum chamber. Van der Waals forces contribute contaminants with binding energies less than 0.4 eV, whilst chemisorption forms chemical bonds between the gas and the chamber's surface with energies that lie between 0.8 eV and 8 eV[55].

The surface desorption rate is given by[55, 56]:

$$\frac{dN}{dt} = -v_k \left(\theta N_0\right)^k \exp\left(\frac{-E_S}{k_B T}\right) \tag{2.20}$$

where N is the molecular surface density, N_0 is the molecular surface density at full coverage, θ is the fractional surface coverage, k is the desorption order, v_k is frequency of vibration of the molecules, which is typically on the order of 10^{13}Hz, and E_S is the desorption energy. The desorption is of first order when the rate depends linearly on the molecular surface density $N = N_0\theta$, which applies for physisorbed molecules and for non-dissociated chemisorbed molecules[57].

For small values of binding energy, E_S<0.7 eV, the desorption rate at room temperature is so high that the outgassing molecules can be rapidly removed from a chamber's surface, whilst in contrast large values of this parameter E_S>1.1 eV cause such glacial desorption rates that they do not pose a serious threat to the pressure of a chamber maintained at room temperature. It is the intermediate 'Outgassing Energy Range' (OER) which is problematic and prompts the use of a high temperature bake out to sufficiently degas these molecules[55]. Having a desorption energy of between 0.82 eV to 0.99 eV, water is in the OER and as a result is one of the most prominent gases during initial baking of vacuum chambers.

Using the same procedure as we employed in section 2.2.2 we can calculate the distribution of gas within the wall of a vacuum chamber, or any material to be used within the chamber, as it diffuses out while degassing. During degassing, the material is placed within another vacuum chamber which is held at a degassing pressure P_{dg}, the base partial pressure of the contaminant in the degassing chamber. Initially the material is assumed to have a uniform concentration of the contaminant throughout itself, and this concentration is determined from equation 2.4 to equal to $C(x, t = 0) = SP^n_{atm}$, where P_{atm} is the partial pressure of the contaminant in the atmosphere in which it was stored prior to degassing. During degassing the walls of the material are assumed to have a concentration of SP^n_{degas}, and this determines the boundary conditions of the problem to be $C(x = 0, t) = C(x = d, t) = SP^n_{degas}$. As before, we can transform the problem from solving $C(x, t)$ to $v(x, t)$ with equation 2.8. Once again, this function is zero at the walls of the material, giving rise to boundary conditions that make it easier to solve. The expansion coefficients for the solution are given by:

$$B_m = \frac{2}{d}\int_0^d -SP^n_{atm}\sin\left(\frac{m\pi x}{d}\right)dx \tag{2.21}$$

$$B_m = -\frac{2SP^n_{atm}}{m\pi}\left[1-(-1)^m\right] \tag{2.22}$$

$$v(x,t) = -\sum_{m=1}^{\infty}\frac{2SP^n_{atm}}{m\pi}\left[1-(-1)^m\right]\sin\left(\frac{m\pi x}{d}\right)\exp\left(-D\left(\frac{m\pi}{d}\right)^2 t\right) \tag{2.23}$$

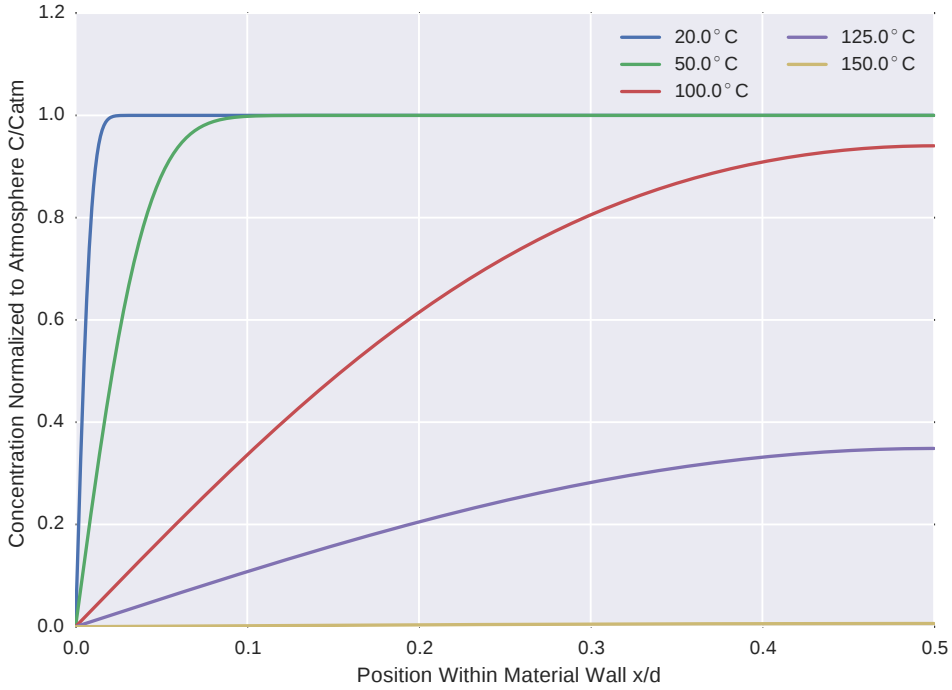

Figure 2.2: Concentration of helium within the walls of a 1.0 mm thick wafer of silicon after being degassed for one week at various temperatures. The base partial pressure of the degassing chamber is assumed to be 1.0×10^{-13} mbar and prior to degassing the wafer was assumed to have reached a concentration in equilibrium with the partial pressure of helium in the atmosphere (5.2×10^{-3} mbar). The plotted temperatures are 20°C, 50°C, 100°C, 125°C and 150°C.

The B_m term is equal to zero for even values of m, hence we can skip them in the summation and rewrite the function in terms of the concentration of the contaminant:

$$C(x,t) = SP^n_{degas} - \sum_{m=1}^{\infty} \frac{4SP^n_{atm}}{(2m-1)\,\pi} \sin\left(\frac{(2m-1)\,\pi x}{d}\right) \exp\left(-D\left(\frac{(2m-1)\,\pi}{d}\right)^2 t\right) \tag{2.24}$$

Figures 2.2 and 2.3 show the concentration profile of helium within a 1.0 mm thick wafer of silicon as it is degassed at a number of different temperatures for one week. The partial pressure of helium in the atmosphere was taken to be 5.2×10^{-3} mbar and the pressure of the degassing chamber was assumed to be 1.0×10^{-13} mbar.

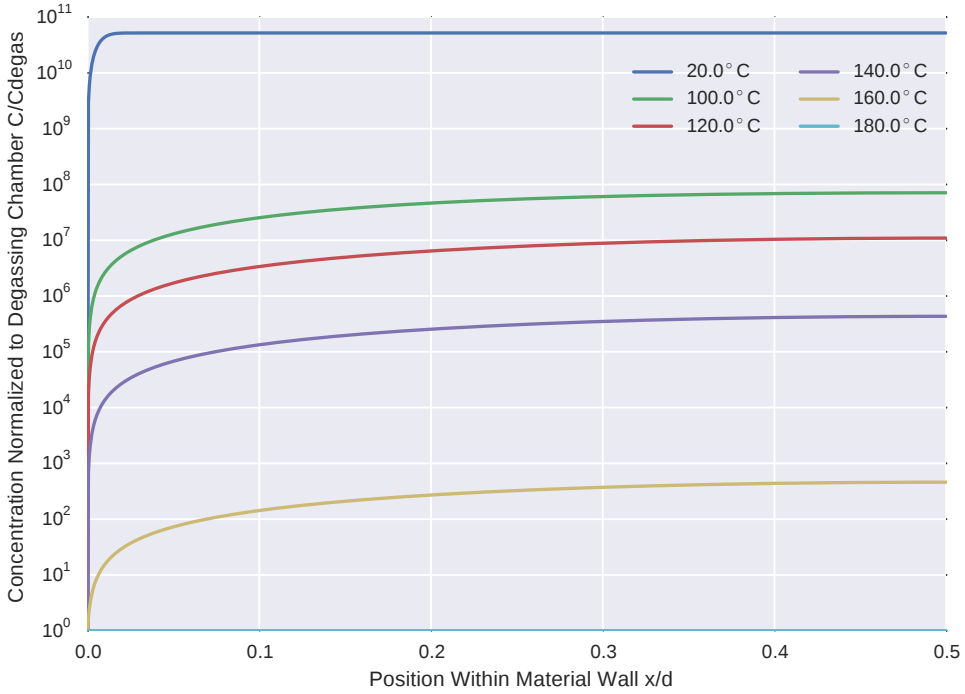

Figure 2.3: Concentration of helium within the walls of a 1.0 mm thick wafer of silicon after being degassed for one week at various temperatures. The base partial pressure of the degassing chamber is assumed to be 1.0×10^{-13} mbar and prior to degassing the wafer was assumed to have reached a concentration in equilibrium with the partial pressure of helium in the atmosphere (5.2×10^{-3} mbar). The plotted temperatures are 20°C, 100°C, 120°C, 140°C, 160°C and 180°C.

Using equation 2.15 and recognising that the same outgassing rate occurs both at $x = 0$ and $x = d$ we can calculate the total degassing rate of the material to be:

$$Q = V\frac{\partial P(t)}{\partial t} = \frac{8DSAP_{atm}^{n}}{d}\sum_{m=1}^{\infty}\exp\left(-D\left(\frac{(2m-1)\,\pi}{d}\right)^{2}t\right) \tag{2.25}$$

2.2.4 Leaks

The third type of atom source that we consider is the leaking of gas into the vacuum chamber through micro-channels and defects in seals. The rate at which the pressure rises within the cavity of an integrated atom chip is determined by the balancing of the leak rate and the pumping due to the NEG:

$$\frac{dP_c}{dt} = \frac{1}{V}\left(Q_L - L_P P_c\,(1-\theta)^{k}\right) \tag{2.26}$$

where Q_L is the leak rate into the chamber, P_c is the chamber pressure, θ is the fractional surface coverage of the NEG, L_P is its maximum pumping rate that occurs at zero coverage and k is the order of desorption. Upon sealing an integrated atom chip the pressure within its cavity drops until the leak rate matches the NEG pumping rate. It can be seen that for a sufficiently large capacity NEG this base pressure is approximated by:

$$P_{base} = \frac{Q_L}{L_P} \tag{2.27}$$

and is maintained until the surface coverage of the NEG becomes so great that the pumping rate drops dramatically and the chamber pressure rises. The calculation of the maximum leak rate can be simplified by modelling the NEG's pumping speed as constant at its maximum rate until it becomes completely saturated to its molar capacity C_G, at which point pumping ceases completely. Under these assumptions the ideal gas law can be combined with equations 2.1 and 2.26 to find an approximate value of the maximum leak rate:

$$Q_L = \frac{C_G RT}{\tau_L} \tag{2.28}$$

where R is the ideal gas constant, T is the absolute temperature and τ_L is the desired lifetime of the device. Figure 2.4 shows a simulation of the pressure in an integrated atom chip of volume $V = 0.5\,\mathrm{cm}^3$ containing an NEG with a capacity for 1.5×10^{14} molecules and an initial pumping speed of $L_P = 0.17\,\mathrm{l\,s}^{-1}$ over the course of its lifetime as it is exposed to a nitrogen leak of $Q_L = 7.0 \times 10^{-14}\,\mathrm{mbar\,l\,s}^{-1}$. The quoted NEG pumping speed and capacity corresponds to the nitrogen pumping parameters of the smooth Ti-Zr-V films measured by P. Chiggiato and P. Costa Pinto at CERN, assuming an NEG area of $1.0\,\mathrm{cm}^2$[58]. The simulated leak rate was chosen by using equation 2.28 to determine the maximum permissible value that would provide a chip lifetime of 1000 days. At the beginning of the simulation the atom chip is sealed and the pressure drops until the base pressure from equation 2.27 is reached. The atom chip maintains this pressure until the NEG becomes saturated at which point the pressure in the cavity rises sharply, coinciding with the prediction by equation 2.28 which is shown in the diagram as a dashed vertical line.

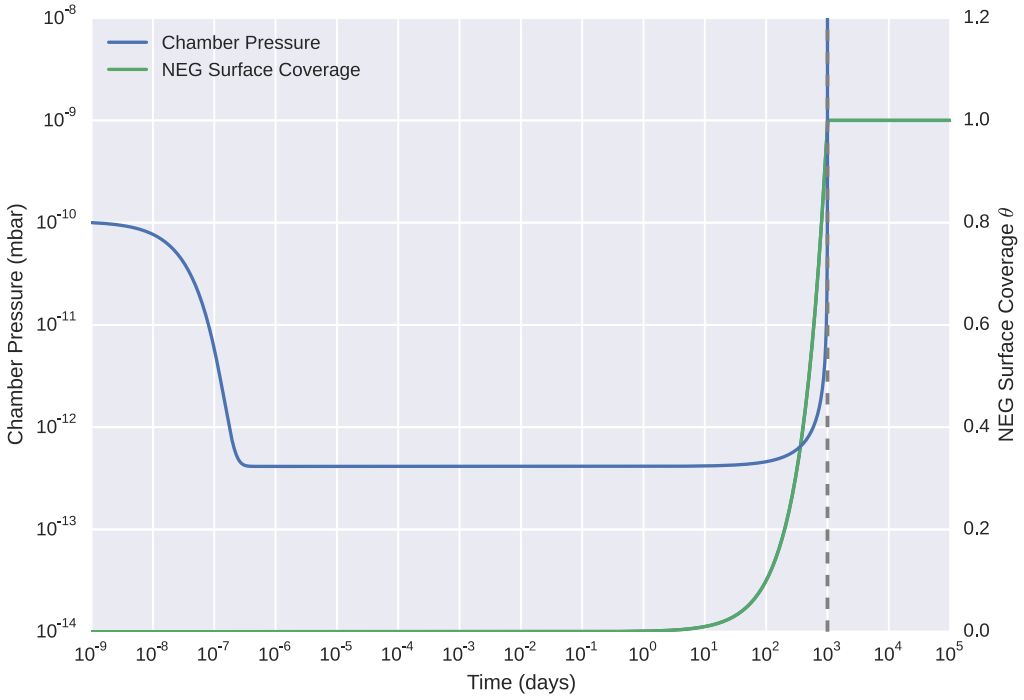

Figure 2.4: Simulated chamber pressure and NEG surface coverage of an integrated atom chip as nitrogen leaks in at a rate of 7.0×10^{-14} mbar l s^{-1}. The properties of the simulated NEG film are based upon the smooth Ti-Zr-V NEGs of P. Chiggiato and P. Costa Pinto at CERN[58].

2.2.5 Wafer bonding methods

2.2.5.1 Glass frit bonding

Glass frit bonding is a widespread wafer level technique for sealing MEMS devices through the use of a melted glass interface and has been used to seal silicon, silicon dioxide, silicon nitride, aluminium and glass in high yields without any special process modification[38]. The technique involves depositing glass paste onto a wafer via screen printing, which wets the surface as it melts. The melted glass is able to flow across surface defects and hence provides a hermetic seal for surfaces that are not completely uniform, even allowing for the inclusion of electrical feedthroughs. The glass paste consists of a powdered glass with an organic binding compound added to form a paste with sufficient viscosity to aid application. As with other bonding methods, the glass within the paste must have a coefficient of thermal expansion that is well matched with that of the wafers to be sealed to prevent thermal stresses from causing fractures and compromising

the bond. In addition to the selection of the glass to be used, inorganic additives are also included in these glass pastes to help improve matching.

After application of the glass paste on one of the bonding surfaces it is heated to burn out the organic binder that otherwise would provide a source of outgassing and reduce the strength of the bond. After this degassing has been completed, the glass is heated further to the wetting temperature as the materials to be bonded are pressed together whilst the glass reflows. To achieve a low wetting temperature compatible with other microelectronic processes lead glasses are usually used in glass frit bonds, restricting the choice of glass. More recently, however, lead free glass frit pastes have become available for example the 51115HT1 from Asahi Glass Company which was developed specifically for vacuum applications.

Leak rates of glass frit seals have been reported in the literature down to 7×10^{-9} mbar l s^{-1} with barriers only 200 µm thick, and it appears from the presented data that these rates could be further improved simply by using thicker walls[59]. D. Sparks *et al.*[60] produced a number of MEMS resonators that were sealed in vacuum with this technique and they were able to determine the background pressure from their quality factors. The lowest pressures inferred from these resonators is around 10^{-3} mbar, although the true pressures could be lower as the quality factor flattens out at lower pressures, reducing the accuracy of the measurement. Another variation on the method can be employed if the temperatures required during glass frit bonding causes an unacceptable level of outgassing. Lorenz *et al.* showed that a high powered laser could be used to selectively heat the glass paste, causing it to melt whilst keeping the remainder of the wafer relatively cool[61, 62]. They managed to keep the centre of a vacuum device below 200°C while its bonds were being formed at 440°C.

2.2.5.2 Eutectic bonding

A eutectic alloy is a composition of a number of metals that has the mixing ratio which gives the lowest possible melting point. Looking at the phase diagram of the alloys of gold and silicon it can been seen that pure gold melts at 1063°C and pure silicon melts at 1412°C, however many Au-Si mixtures have lower melting points than this and the eutectic alloy lies at 19% silicon, which has a melting point of 363°C[63].

Eutectic bonding is a type of solder seal that exploits the properties of eutectic alloys so that, for example, a wafer coated in gold that is pressed against a wafer

of silicon will experience silicon diffusion into the gold to form a eutectic alloy that melts at the interface at 363°C. Upon cooling the eutectic alloy solidifies, forming a hermetic eutectic bond.

Problems occur if the silicon wafer is not suitably cleaned before bonding as silicon dioxide exhibits poor wettability of gold resulting in poor adhesion, as even a native oxide is sufficient to compromise reliability. Another solution to this problem is to add an adhesion layer upon the oxide, such as titanium or chromium, before the gold is deposited. These intermediate layers act as diffusion barriers, but also cause further issues as silicides are able to form and as a result the temperature required to achieve a reliable bond raises to around 520°C[63]. Leak rates with eutectic bonding have been quoted below $1.1 \times 10^{-13}\,\mathrm{mbar\,l\,s^{-1}}$[64]

2.2.5.3 Anodic bonding

Anodic bonding is a technique which can be used to seal glasses to metals or semiconductors through heating the interface been the materials whilst applying a moderately high voltage across it. The electric field across the glass causes mobile alkali ions to move away from the material interface, leaving oxygen ions behind which are able to form bonds with the metal. Once again, matching CTEs is extremely important with this process. Leak rates with this bonding method have been reported down to $2.7 \times 10^{-14}\,\mathrm{mbar\,l\,s^{-1}}$[64]

2.2.5.4 Direct bonding

Direct bonding is the fusion of extremely flat surfaces through van der Waals forces, hydrogen bonds, capillary forces and/or electrostatic forces. Provided the surfaces are sufficiently flat, they will adhere at room temperature upon being brought into contact, a process which is often reversible. A much greater bond strength can be achieved by subsequent annealing of the interface, which forms chemical bonds between the surfaces[38]. There are two types of direct bonding for bonding silicon to silicon: hydrophilic and hydrophobic. Hydrophilic bonding concerns silicon wafers which have a surface layer of silicon dioxide, whilst hydrophobic bonding is used for wafers which have had this oxide removed.

Surface warping of up to 100 µm can produce acceptable direct bonds however this process is very sensitive to particles that get trapped between the surfaces causing unbonded regions. Cleanliness is particularly important for integrated

atom chips, as the thicker wafers that are required are less deformable and as a result less tolerant to particulates that they must seal around. Surface roughness is another important parameter, and it should remain below 0.3 nm to 0.5 nm for adequate bonding of hydrophilic silicon.

Hydrophilic wafer bonding can be used to bond a silicon wafer with a thermal oxide to another wafer with only a thin oxide layer. Pre treating of the silicon with RCA cleaning steps can leave a hydrophobic surface formed of Si-O-Si bonds and silanol groups (Si-OH). Initially water is present between the two wafers which produces van der Waals forces between the hydroxide in the silanol as a result of hydrogen bonds. This water partially diffuses out of the interface during annealing, but it also reacts with the surfaces to produce more Si-OH bonds. As the water is removed from the interface, the surfaces are brought closer together until eventually the hydroxide groups between opposing wafers are directly bonded together, which then react to form Si-O-Si bonds directly between the surfaces in addition to creating additional water. The remaining water can react with silicon to produce silicon dioxide and hydrogen, the latter of which can produce voids in the bond if the thermal oxide is not thick enough to absorb it all.

Hydrophobic wafer bonding can be used to bond bare silicon wafers together which have no oxide layers. In this process the wafers have their native oxide removed by dipping them in hydrofluoric acid. The acid leaves Si-F and Si-H bonds at the wafers' surface, which similarly to hydrophilic direct wafer bonding draws the surfaces together due to the van der Waals forces between H-F molecules. During annealing the number of H-F molecules joining the wafers decreases as they form additional bonds to the silicon surfaces. The wafers are brought closer together and eventually the Si-H bonds of opposing wafers bond to form a Si-Si interface, whilst producing hydrogen as a by-product. Unlike in hydrophilic direct bonding, this hydrogen does not have a layer of silicon dioxide in which to dissolve and so produces voids in the bond if it is unable to degas during annealing.

The problem of hydrogen voids can be avoided completely if hydrophobic direct bonding is performed under vacuum. In this variation of the technique the wafers are stripped of their oxide layer using a hydrofluoric acid dip as before, but then the wafers are immediately contacted to protect their surfaces before they reach the vacuum chamber. When ultra high vacuum is reached the wafers can be separated and then baked as to allow for the Si-H bonds to break, leaving dangling silicon bonds. The wafers are then allowed to cool so that the base pressure of the vacuum chamber is reduced. Finally the wafers are brought back together, allowing for

the dangling bonds to connect and giving a bond strength that is typical to that found in bulk silicon itself[65].

The lowest leak rate the author has found reported for direct bonding is 3.28×10^{-15} mbar l s^{-1}, for a MEMS nanoreactor device used to aid electron microscopy of chemical processes at the nanoscale[66].

Of all of these bonding techniques, anodic bonding and eutectic bonding seem the most promising for use in integrated atom chips, and as a result we are currently focusing our efforts in implementing these methods.

2.3 Atom sources

There are several methods that can be used to introduce atomic references into integrated atom chips, two of which were already mentioned in the previous chapter in the context of chip-scale atomic clocks: direct alkali metal injection and reaction of alkali salts with azides[25]. Whilst simple, direct injection is not a particularly attractive method as any subsequent high temperature process would result in a thorough coating of the chamber's internal walls and windows with the alkali metal. This would act to both reduce optical access, but also raise the base pressure of the device to the metal's vapour pressure. For the case of rubidium vapour, this would mean that the device would have to be cooled down to $-35\,^{\circ}$C to reach the desired pressure of 10^{-10} mbar. The problem of the coated windows, however, can be resolved instead by introducing a local cold-spot to the chip to act as a diversionary rubidium pump. Wax micro-packets have also been designed for use with CSACs, whereby pellets of alkali metal are stored in wax cells from which they can be released by laser ablation[67]. It seems unlikely though that the wax compound would be able to sustain ultra high vacuum nor be able to act as a barrier for gas permeation, and as with the direct injection and alkali salt-azide methods there is little that can be done to control the vapour pressure within the device in short time scales.

Both SAES and Alvatec are manufacturers of Alkali Metal Dispensers (AMDs), compounds which are stable under the moderately high temperatures required for device processing, but upon being heated further they can be used to controllably release alkali metals. These devices are usually activated in traditional vacuum chambers through the use of joule heating, but a focused laser can also be employed to remove the need for vacuum feedthroughs[68]. It is primarily as a result of this

high level of control that these devices will be employed in the first generation of our integrated atom chips, but they also have the benefit of being relatively inexpensive and easily available.

2.4 Trap geometry

One aspect which so far has been ignored in the discussion of our integrated atom chips is the need for a geometry of magneto optical trap that is compatible with our most simple integrated atom chip structures: a sealed vacuum cavity in silicon with a single window for optical access. This, of course, is the main subject of this thesis and so the currently available geometries will be investigated in more depth in section 3.6. Before this, we must first look at the principle of Doppler cooling and see how it can be combined with a positional dependent Zeeman splitting to yield magneto-optical trapping.

Chapter 3

Laser Cooling and Trapping

This chapter reviews the most basic of laser cooling and trapping techniques, that of Doppler cooling and magneto optical trapping. These methods allow for room temperature atoms moving at hundreds of metres per second to be cooled down to velocities on the order of tens of centimetres per second. These tools are commonly employed throughout atomic physics, in particular as an intermediate step in the process of producing the Bose-Einstein condensates that are central to many atom interferometers and atom chips. BECs require phase space densities far higher than those attainable through the techniques described here, and instead require approaches such as magnetic trapping and evaporative cooling, both of which are outside the scope of this thesis.

Here we begin with a brief explanation of Doppler cooling and its limitations before deriving the Zeeman splitting of rubidium's hyperfine structure and demonstrating how this can be exploited to produce a magneto optical trap. Cooling limits are then discussed before finally reviewing some of the alternative MOT geometries and evaluating their use in integrated atom chips.

3.1 Doppler Cooling

Doppler Cooling, which is also known as optical molasses, is a technique first suggested in 1975[3] and then implemented in 1985[7] which exploits the frequency dependent scattering rate of atoms in combination with the Doppler effect to create a velocity dependent force that acts to slow and thus cool atoms down. If a laser emitting photons of wavevector $\mathbf{k}$ is directed at an atom then these

photons are absorbed and emitted at the scattering rate Γ_s. Upon absorption the atom receives a quanta of momentum $\hbar\mathbf{k}$ from the photon, whilst when the atom spontaneously emits another photon the direction of the emission, and thus the recoil of momentum experienced by the atom, is completely random. Because the direction of spontaneous emission is random, the atom receives an average momentum transfer of $\hbar\mathbf{k}$ per scattering event. From this we can see that the average force on an atom is given by:

$$\mathbf{F} = \frac{d\mathbf{p}}{dt} = \hbar\mathbf{k}\Gamma_s = \frac{\hbar\mathbf{k}s_0\Gamma/2}{1 + s_0 + \left(2\delta/\Gamma\right)^2} \tag{3.1}$$

where the substituted term Γ_s comes from the steady state solution to the optical Bloch equations of a damped two level atom[69]. In this expression $\delta = \omega_L - \omega_0$ is the detuning of the laser frequency from resonance, Γ is the natural linewidth, and s_0 is the on resonance saturation parameter given by $s_0 = I/I_s$, where I is the intensity of the laser and I_s is the saturation intensity of the transition[1].

Given the above relationship, if we were to red-detune the laser's frequency from that of the transition then the average force exerted by the laser would be lower than if the laser was on resonance. If, however, the atom was moving towards the red detuned laser at velocity $\mathbf{v}$ then the light the atom sees would be Doppler shifted closer to resonance by $-\mathbf{k}\cdot\mathbf{v} = kv$, would be more likely to be absorbed and thus would experience a greater force from the laser. Conversely an atom that moves away from the laser sees photons Doppler shifted further from resonance by $-\mathbf{k}\cdot\mathbf{v} = -kv$, and so experiences a further diminished force.

This principle can be extended so that six red detuned laser beams are then directed towards the atom, two counter-propagating about it in each axis. A stationary atom in this configuration experiences an average force of zero, as the scattering rates from each laser are equal, however if the atom moves towards any of the lasers then it experiences an imbalance of the scattering rates due to the opposite Doppler shifts. From this we can see that we have engineered a velocity dependent force upon atoms which act to slow them down. In one dimension the total average force exerted by a pair of counter propagating lasers is given by:

[1] $\Gamma = 2\pi\cdot 6.07\,\mathrm{MHz}$ for the D_2 (λ =780 nm) line of rubidium, whilst I_s depends on the hyperfine transition being probed. For the case of circularly polarized light exciting $|F = 2, m_F = \pm 2\rangle \rightarrow |F' = 3, m'_F = \pm 3\rangle$ transitions I_s=1.67 mW cm^{-2}.

$$\mathbf{F}_{tot} = \mathbf{F}_+ + \mathbf{F}_- = \frac{\hbar \mathbf{k}_+ s_0 \Gamma/2}{1 + s_0 + \big(2(\delta - \mathbf{k}_+ \cdot \mathbf{v})/\Gamma\big)^2} + \frac{\hbar \mathbf{k}_- s_0 \Gamma/2}{1 + s_0 + \big(2(\delta - \mathbf{k}_- \cdot \mathbf{v})/\Gamma\big)^2} \tag{3.2}$$

where detuning of the laser, δ, in equation 3.1 has been replaced with the total detuning that includes the shift due the Doppler effect $\delta - \mathbf{k}_\pm \cdot \mathbf{v}$. The subscripts label the laser beams and signify their direction in our one dimensional space.

3.1.1 Simplification of the Velocity Dependent Force

If we consider the cooling force experienced by an atom in one dimensional optical molasses in the situation when the atomic velocities are small then we can expand the expression of the average force using the Taylor series:

$$\begin{aligned} \mathbf{F} &= \mathbf{F}_+(\delta - \mathbf{k}_+ \cdot \mathbf{v}) + \mathbf{F}_-(\delta - \mathbf{k}_- \cdot \mathbf{v}) \\ &= \mathbf{F}_+(\delta) + \frac{d\mathbf{F}_+(\delta)}{d\delta}(-\mathbf{k}_+ \cdot \mathbf{v}) + \mathbf{F}_-(\delta) + \frac{d\mathbf{F}_-(\delta)}{d\delta}(-\mathbf{k}_- \cdot \mathbf{v}) + \mathcal{O}((\mathbf{k} \cdot \mathbf{v})^2) \end{aligned} \tag{3.3}$$

Because the two cooling beams have wavevectors of equal magnitude and opposite signs, for a stationary atom the average scattering force due to both beams cancels out, i.e. $\mathbf{F}_+(\delta) = -\mathbf{F}_-(\delta)$.

$$\mathbf{F} \approx \frac{d\mathbf{F}_+(\delta)}{d\delta}(-\mathbf{k}_+ \cdot \mathbf{v}) + \frac{d\mathbf{F}_-(\delta)}{d\delta}(-\mathbf{k}_- \cdot \mathbf{v}) \tag{3.4}$$

The derivatives can be calculated by differentiating equation 3.1:

$$\frac{d\mathbf{F}_+(\delta)}{d\delta} = \frac{-2\hbar \mathbf{k}_+ \Gamma_s (2/\Gamma)^2 \delta}{1 + s_0 + (2\delta/\Gamma)^2} = \frac{-4\hbar \mathbf{k}_+ s_0 \delta/\Gamma}{(1 + s_0 + (2\delta/\Gamma)^2)^2} \tag{3.5}$$

and so finally, noting $\mathbf{k} = \mathbf{k}_+ = -\mathbf{k}_-$, the total force can be written as:

$$\mathbf{F} \approx \frac{4\hbar \mathbf{k} \Gamma_s (2/\Gamma)^2 \delta}{1 + s_0 + (2\delta/\Gamma)^2} \mathbf{k} \cdot \mathbf{v} = \frac{8\hbar \mathbf{k} s_0 \delta/\Gamma}{(1 + s_0 + (2\delta/\Gamma)^2)^2} \mathbf{k} \cdot \mathbf{v} \tag{3.6}$$

$$\mathbf{F} \approx -\alpha \mathbf{v} \tag{3.7}$$

where the proportionality constant is given by:

$$\alpha = -\frac{4\hbar k^2 \Gamma_s (2/\Gamma)^2 \delta}{1 + s_0 + (2\delta/\Gamma)^2} = -\frac{8\hbar k^2 s_0 \delta/\Gamma}{(1 + s_0 + (2\delta/\Gamma)^2)^2} \tag{3.8}$$

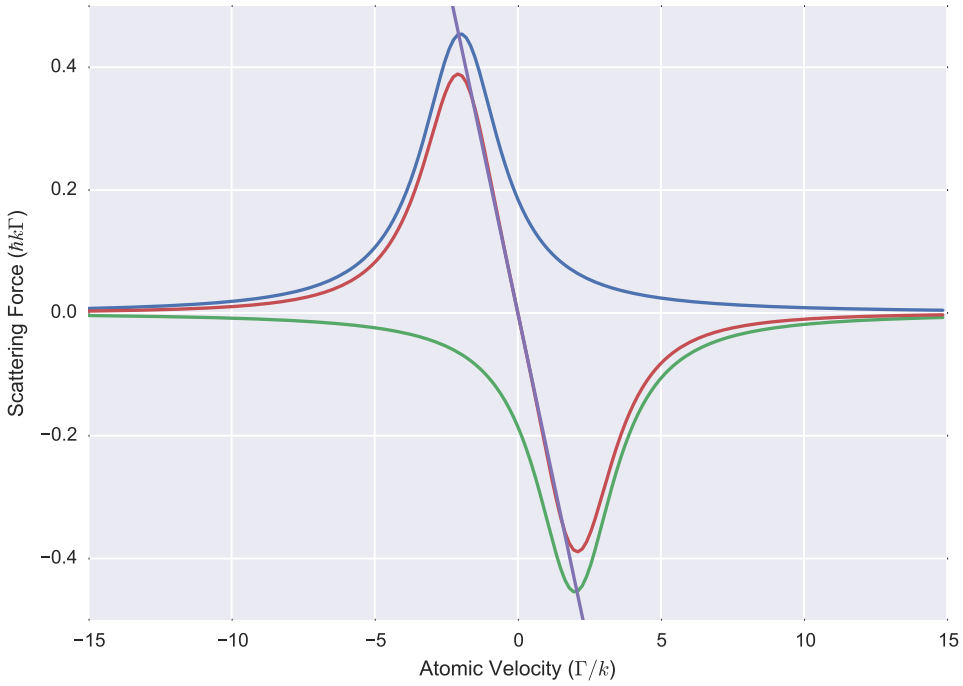

Figure 3.1: Scattering force exerted upon an atom of rubidium 85 by a pair of counter propagating laser beams with a red detuning of $\delta = -2\Gamma$ and saturation parameter $s_0 = 10.0$. The blue curve is the force due to the beam propagating in the positive direction, the green curve is the force due to the negatively propagating beam and the red curve is the total force. The purple line shows an approximation of the total scattering force given by equation 3.6.

This proportionality constant is positive for negative values of the laser detuning and so produces the damping force we expected. Figure 3.1 shows a plot of the full expression of the one dimensional Doppler cooling force given by equation 3.2 in addition to the linear approximation of equation 3.6. It can be seen that the approximation remains fairly accurate until the atomic velocities introduce a Doppler shift that approaches the detuning of the lasers $v \sim \delta/k$.

Although the average velocity of a Doppler cooled atom is zero, the root mean squared value of its velocity is non-zero, meaning that atoms will undergo a random walk in velocity and position space[70]. Not only does this diffusion give us the Doppler temperature limit for our cooled atoms, it also enforces a finite lifetime for them to remain in the cooling region. Suggestions have been made to construct laser geometries that could both cool and trap atoms with the scattering force alone, however the optical Earnshaw theorem showed that this is not possible.

3.1.2 Optical Earnshaw Theorem

The optical Earnshaw theorem derived by A.Ashkin and J.P.Gordon[6] shows that it is impossible to stably trap atoms using only the scattering force.

In equilibrium there cannot be a net flux of energy into or out of any proposed optical trap, thus the divergence of the Poynting vector must be zero $\nabla \cdot (E \times H) = 0$ everywhere within it. The theorem then assumes that the force exerted upon the atom is proportional to the intensity of the light throughout the trap, so in turn the force is proportional to the Poynting vector. It follows that the divergence of the force must be also equal to zero, and thus any lines of force that enter the trap must also exit it, making it inherently unstable.

The assumption that the force is proportional to the Poynting vector is invalid if we consider optical pumping effects, because the strength of the absorption depends on the energy level of the atom, saturation effects and on the application of external fields which can (de)tune transitions from the laser and in turn alter absorption strengths, bypassing the theorem[9]. The magneto optical trap described in section 3.3 does not rely merely on the confinement of magnetic moments in its operation, but instead uses the Zeeman effect to create a positional dependent scattering rate to bypass the optical Earnshaw theorem.

3.2 Hyperfine Structure and the Zeeman Effect

In order to understand the principle of magneto optical trapping we must first have a grasp of the origin of the hyperfine structure and how it is modified under the influence of magnetic fields through the Zeeman effect. Here an intuitive, classical, picture of the normal Zeeman effect is first given as an introduction, whilst the more realistic quantum model is provided in appendix B.

3.2.1 Classical Model of the Zeeman Effect

We can describe the Zeeman effect classically by considering the motion of an electron of an atom oscillating in the presence of an external applied magnetic field[71][72]. The Coulomb attraction between the electron and the atomic nucleus provides a restoring force $\mathbf{F}_a = -m_e\omega_0^2\mathbf{r}$, where ω_0 is the resonant frequency of the atom in the absence of a magnetic field, m_e is the electron rest mass and $\mathbf{r}$ is the

position vector from the nucleus to the electron. The presence of a magnetic field $\mathbf{B}$ exerts a force of $\mathbf{F}_m = -e\mathbf{v} \times \mathbf{B}$ on the electron, where $\mathbf{v}$ is its velocity and e is the elementary charge. As a result the motion of the electron is described by the differential equation:

$$m_e \frac{d\mathbf{v}}{dt} = -m_e \omega_0^2 \mathbf{r} - e\mathbf{v} \times \mathbf{B} \tag{3.9}$$

where for simplicity we define the magnetic field to be pointing in the $\hat{\mathbf{z}}$ direction, $\mathbf{B} = B\hat{\mathbf{z}}$. Solving this equation leads to the following three solutions that can be combined to find the general expression of the electron's motion $\mathbf{r} = r_x\hat{\mathbf{x}} + r_y\hat{\mathbf{y}} + r_z\hat{\mathbf{z}}$:

$$r_z = r_1 \cos(\omega_0 t + \phi_0) \tag{3.10a}$$

$$r_x = r_2 \cos(\omega_1 t + \phi_1), r_y = -r_2 \sin(\omega_1 t + \phi_1) \tag{3.10b}$$

$$r_x = r_3 \cos(\omega_2 t + \phi_2), r_y = r_3 \sin(\omega_2 t + \phi_2) \tag{3.10c}$$

The general solution thus contains six free parameters $(r_1, r_2, r_3, \phi_0, \phi_1, \phi_2)$, with the electron oscillating at frequency ω_0 in addition to the two new resonant frequencies:

$$\begin{aligned} \omega_1 &= -\Omega \pm \sqrt{\Omega^2 + \omega_0^2} \approx \omega_0 - \Omega \\ \omega_2 &= +\Omega \pm \sqrt{\Omega^2 + \omega_0^2} \approx \omega_0 + \Omega \end{aligned} \tag{3.11}$$

where the Larmor frequency, $\Omega = eB/2m_e$, is much smaller than ω_0 and so the applied approximations are justified.

As illustrated in figure 3.2, the unshifted frequency ω_0 corresponds to the electron oscillating along the z axis. In this case the electron only moves parallel to the magnetic field and so its motion, and thus energy, is unaffected by the field's presence. The two other frequencies correspond to solutions where the electron moves in circular orbits in the xy plane. The direction of this rotation determines the sign of the frequency shift and can be understood by considering the change in the strength of the effective central potential due to the magnetic force.

3.2.1.1 Radiation due to the Zeeman Effect

The atomic nucleus forms an electric dipole with the electron, the oscillations of which cause light to be radiated from the atom. The emitted light retains the frequency of the oscillating electron and so in a magnetic field the Zeeman effect

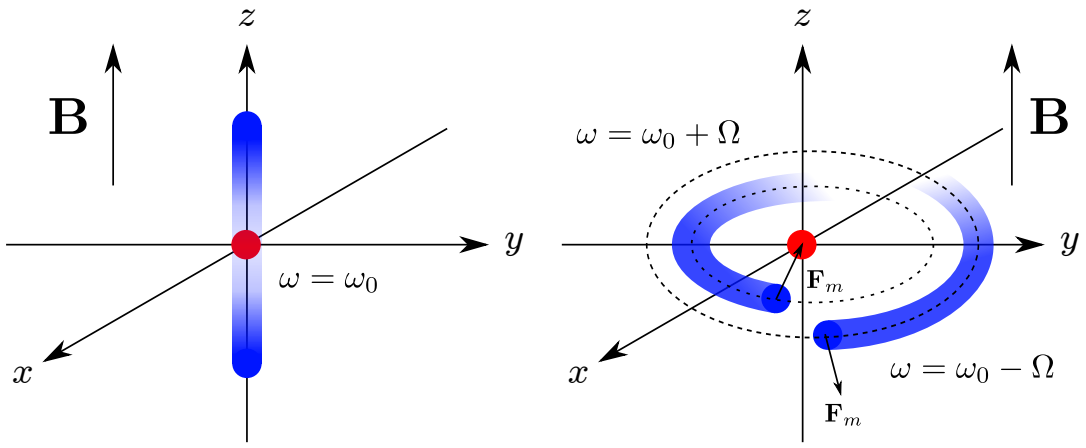

Figure 3.2: Classical picture of the motion of an electron of an atom subject to an external magnetic field. The oscillation frequency of the electron is ω_0 in every direction in zero magnetic field, however this splits into three frequencies, ω_0, $\omega_0 + \Omega$ and $\omega_0 - \Omega$, due to the Zeeman effect. The unshifted frequency corresponds to the electron oscillating along the z axis, while the shifted frequencies correspond to the electron moving in circular orbits in the xy plane.

causes the atom to fluoresce three frequency components of light, again separated by the Larmor frequency.

As light is a transverse wave, emission can only occur in a particular direction if there is a component to the electron's motion in the plane that is perpendicular to the light's wavevector. This shows, for example, that light cannot be emitted with frequency ω_0 with a wavevector of direction $\hat{\mathbf{k}} = \hat{\mathbf{z}}$ because the motion of this frequency component of the electron is purely along the z axis (see figure 3.3).

In general, the relative strength of the electron's fluorescence of polarization $\hat{\mathbf{e}}$ is proportional to $|\hat{\mathbf{e}} \cdot \mathbf{r}|^2$[73][74], and this fact is used in section 3.3.1.2 to determine the positional dependent absorption of atoms within the magneto optical trap.

The electron oscillations in the z axis can only produce linearly polarized light, and this is emitted everywhere except along the z axis. The electron's circular motion in the xy plane radiates linearly, elliptically and circularly polarized light and the degree of polarization is determined by the direction of the emission. The handedness of this polarization is dependent on the direction of rotation of the electron's orbital motion (an electron oscillating at frequency $\omega = \omega_0 + \Omega$ emits right handed polarizations[2] in directions with a positive z component, and left

[2]Here we use the convention that the handedness of polarization is defined from the point of view of the source.

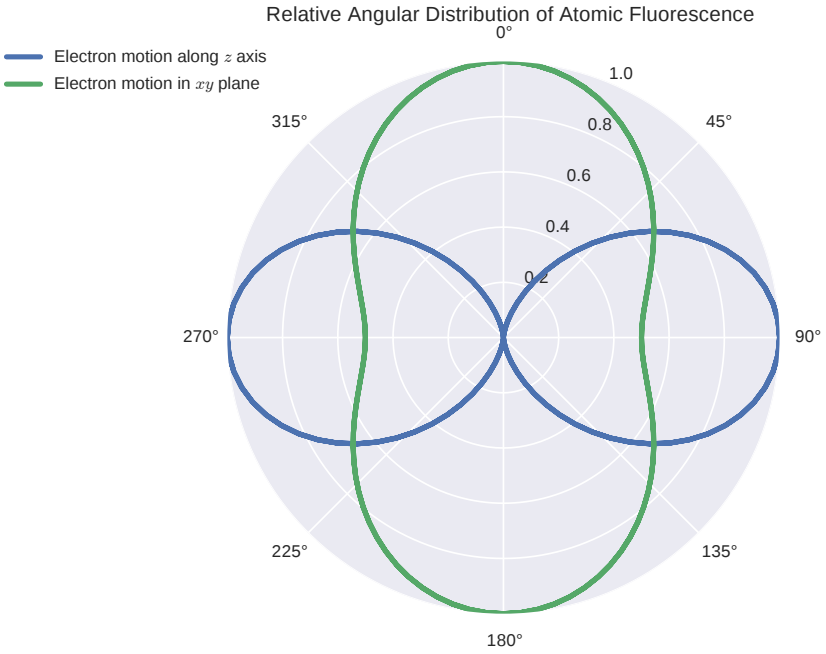

Figure 3.3: Relative strength of the atomic fluorescence of an atom due to the different possible electron motions shown in equation 3.10, as a function of the angle of the emitted light to the z axis. The blue plot corresponds to radiation due to an electron oscillating in the z axis, while the green plot corresponds to that of an electron exhibiting circular orbits in the xy plane. The polarization of the light corresponding to the blue trace is always linear, however that due to the green trace varies from circular to linearly polarized as a function of the angle. The fluorescence is rotationally symmetric about the z axis.

handed polarizations in directions with a $-z$ component. An electron oscillating at $\omega = \omega_0 - \Omega$ emits the polarizations of opposite helicity) but, unlike the linear oscillations, the circular orbits emit some degree of radiation in every direction from the atom.

3.2.1.2 The Classical Magnetic Moment of the Orbiting Electron

The magnetic moment of a conducting loop of wire is given by $\boldsymbol{\mu} = I\mathbf{A}$, where I is the current flowing through the wire and $\mathbf{A}$ is the vector area that the wire loop encloses. From this we can see that the magnetic moment of an orbiting classical

electron is given by:

$$\begin{aligned}\boldsymbol{\mu} &= I\mathbf{A} \\ &= -\frac{ev}{2\pi r}\mathbf{A} \\ &= -\frac{ep}{2m_e}\frac{\mathbf{r}\times\mathbf{v}}{v} \\ &= -\frac{\mu_B}{\hbar}\mathbf{L}\end{aligned} \tag{3.12}$$

where we have introduced the Bohr magneton, $\mu_B = e\hbar/2m_e$, and the electron's orbital angular momentum, $\mathbf{L}$. A magnetic moment in a magnetic field experiences a potential energy of $U = -\boldsymbol{\mu}\cdot\mathbf{B}$, so classically the Zeeman effect shifts the energy of the electron by:

$$\Delta E = \frac{\mu_B}{\hbar}\mathbf{L}\cdot\mathbf{B} \tag{3.13}$$

From which we can see that the energy of an atomic electron in a magnetic field is greater if the electron's angular momentum is aligned with the direction of the magnetic field.

The solutions to equation 3.9 pose no restrictions on the radii of the atomic oscillations (r_1, r_2, r_3), however we know from the Planck-Einstein relation that the frequency of the emitted radiation is related to its energy by $E = \hbar\omega$, and so the energy shift of the electron due to the Zeeman effect can be equated to the energy shift of its corresponding emitted photon:

$$\Delta E = \hbar\Delta\omega \tag{3.14}$$

If the orbital angular momentum of the electron is aligned to the magnetic field then the energy shift is positive, and so we find:

$$\frac{\mu_B}{\hbar}m_e r_3^2(\omega_0+\Omega)B = \frac{eB\hbar}{2m_e} \tag{3.15}$$

$$r_3 = \sqrt{\frac{\hbar}{m_e(\omega_0+\Omega)}} \tag{3.16}$$

Similarly if its orbital angular momentum points in the opposite direction:

$$r_2 = \sqrt{\frac{\hbar}{m_e(\omega_0-\Omega)}} \tag{3.17}$$

Which gives the modification of the atomic radius due to the presence of the magnetic field. Upon substitution of the Coulomb potential, $\omega_0^2 = (e^2/4\pi\epsilon_0 m_e r^3)$,

and setting the magnetic field to zero we find the Bohr radius:

$$r_1 = \frac{4\pi\epsilon_0\hbar^2}{m_e e^2} \tag{3.18}$$

The energy shift of each angular momentum state is only dependent on the strength of the magnetic field, the positive (negative) angular momentum z components always have greater (lower) energies in a magnetic field. The direction of the magnetic field only determines the angular dependence of the polarization of the atom's fluorescence and the angular dependence of the absorption of different polarized light.

It is clear that this description is insufficient to describe true atoms in that the electronic and nuclear spins have been neglected in addition to relativistic effects. A more realistic, quantum mechanical derivation of these energy shifts is given in appendix B.

3.3 The Magneto Optical Trap

The Magneto Optical Trap (MOT) is a device which combines the velocity dependent force of optical molasses with a magnetic field gradient to bypass the optical Earnshaw theorem and give a positional dependent force that acts to trap atoms. The most common form of MOT uses a pair of current carrying coils in an anti-Helmholtz configuration to produce a magnetic field zero at the centre of a vacuum chamber, in the cooling region of optical molasses where the beams overlap.

The addition of a pair of Helmholtz coils in the configuration shown in figure 3.4 produces a quadrupole magnetic field which acts to shift the resonant frequency of the atoms due to the Zeeman effect as described in section 3.2 and appendix B. The trap is designed such that as an atom moves away from the trap centre the Zeeman shift due to the increase in magnetic field strength moves the atoms closer to resonance with the surrounding lasers. Just as in Doppler cooling this change in detuning between pairs of lasers causes an imbalance in their scattering rates, however in a MOT the positional dependent imbalance of scattering rates is due to the orthogonal electric field rotations of opposing beams and their opposite coupling to the atoms in the presence of a positional dependent quantization axis. This gives rise to both a velocity and positional dependent force which not only cools the atoms but acts to push them back towards the trap centre.

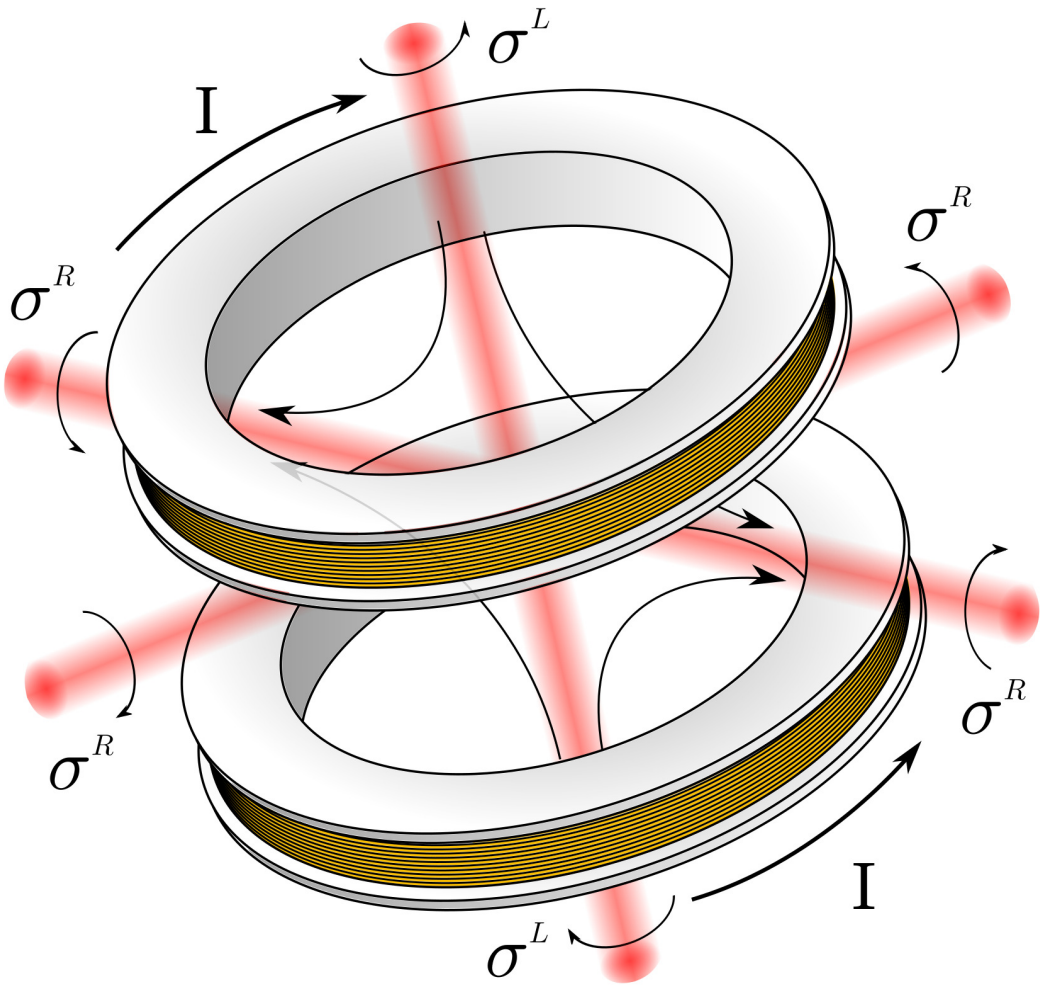

Figure 3.4: Geometry of a six beam magneto optical trap.

As shown in appendix B the interaction of an atom with a low strength magnetic field of magnitude B causes shifts in its energy levels by $\Delta E = g_F \mu_B m_F B$, where $\mu_B = e\hbar/2m_e$ is the Bohr magneton, m_F is the projection of the atom's angular momentum along B and g_F is the Landé g factor for the level in question. From this we can calculate how the Zeeman effect shifts the energy between two states of a toy atom with levels of total angular momentum $F = 0$ and $F' = 1$ and with g_F factors of unity:

$$\Delta E_{F'=1,m_{F'}=1,0,-1} - \Delta E_{F=0,m_F=0} = \begin{cases} \mu_B B & m_{F'} = 1 \\ 0 & m_{F'} = 0 \\ -\mu_B B & m_{F'} = -1 \end{cases} \tag{3.19}$$

Figure 3.5 shows the energy level splitting of this toy atom and the corresponding

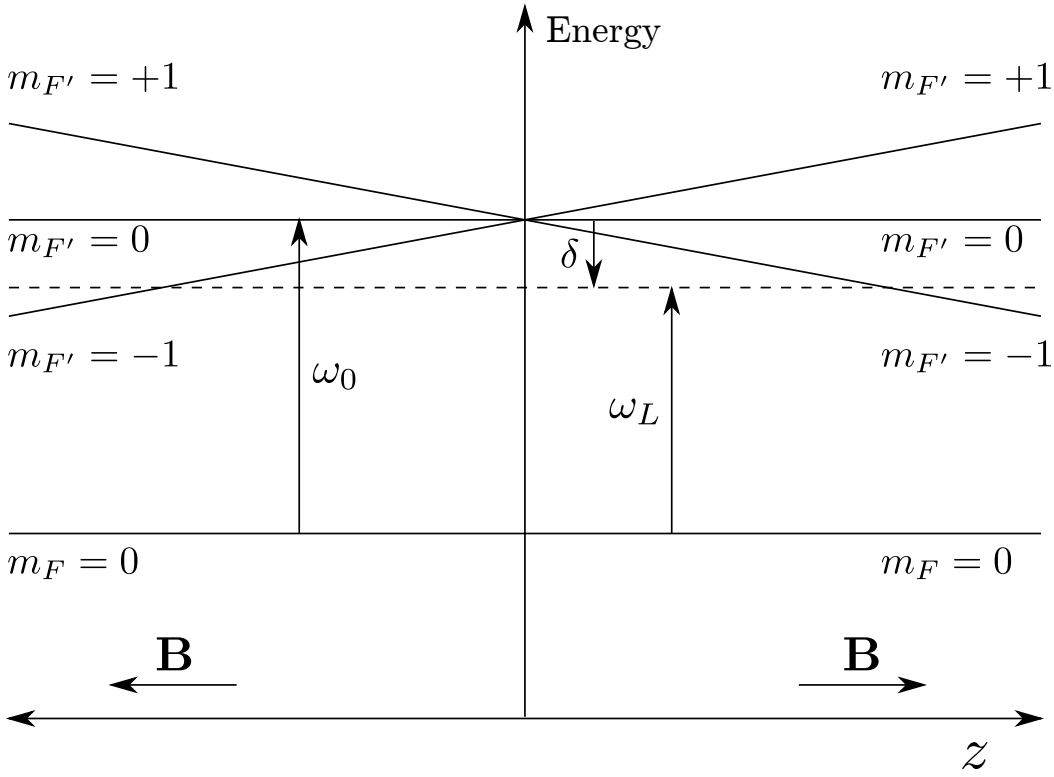

Figure 3.5: Positional dependent Zeeman splitting of toy atom across one dimension of a magneto optical trap.

coupling with incident light of detuning $\delta = \omega_L - \omega_0$ along an axis of a MOT. As the atom moves from the trap centre the $m_{F'} = -1$ level shifts to lower energies and thus is brought closer to resonance with the red detuned laser light. The scattering rate is imbalanced such that the atom experiences an average force back towards the centre of the trap. The cause of this imbalance is because the electric fields due to the circular polarization of each laser rotate around the quantization axis in opposite directions, and they have opposite coupling to the atom due to the opposite direction of the quantization field either side of the trap centre.

If we now consider the Zeeman energy level shifts for the realistic transitions of $5^2\mathrm{S}_{1/2}, F = 3 \rightarrow 5^2\mathrm{P}_{3/2}, F' = 4$ of rubidium 85, then we find:

$$\Delta E_{e-g} = g_{F_e}\mu_B m_{F_e} B - g_{F_g}\mu_B m_{F_g} B = \mu' B \tag{3.20}$$

where

$$\mu' = (g_{F_e} m_{F_e} - g_{F_g} m_{F_g})\mu_B \tag{3.21}$$

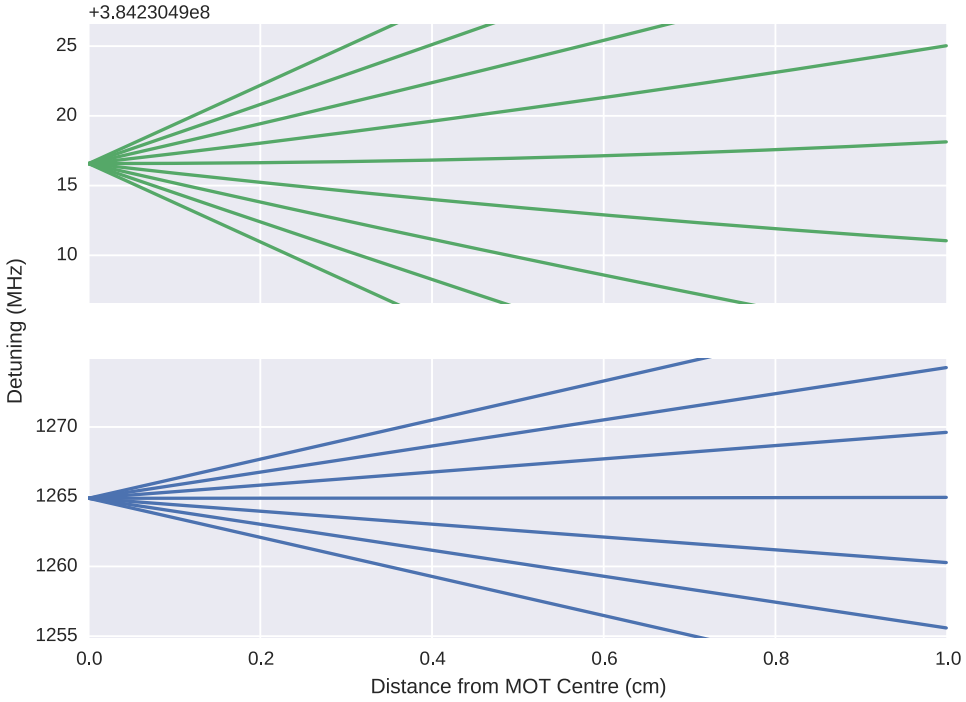

Figure 3.6: Positional dependent Zeeman splitting of ^{85}Rb across one dimension of a magneto optical trap. This plot was calculated using the method described in appendix B. Band bending is barely perceptible at these field levels, which justifies the approximation used in equation 3.20. The field gradient was set to typical value of $10\,\mathrm{G\,cm^{-1}}$. Note the large offset indicated in the upper sub plot.

and

$$g_F = g_J \frac{F(F+1) + J(J+1) - I(I+1)}{2F(F+1)} + g_I \frac{F(F+1) - J(J+1) + I(I+1)}{2F(F+1)} \tag{3.22}$$

Figure 3.6 shows the true splitting of the $5^2\mathrm{S}_{1/2}$ and $5^2\mathrm{P}_{3/2}$ energy levels of rubidium 85 in a magnetic field gradient typical of a MOT ($10\,\mathrm{G\,cm^{-1}}$). The plot was calculated using the techniques of appendix B, yet level bending due to state repulsion is barely visible at these field levels and so the linear approximation of equation B.5 (and hence equation 3.20) is valid. It should be noted that the energy levels of the negative (positive) m_F states shift to lower (higher) energies either side of $z = 0$, even though the magnetic field changes direction. The reason for this is that the definition of the energy level splitting is concerned with the projection of the atom's angular momentum onto the magnetic field, and the m_F levels themselves are labelled with respect to the magnetic field. Note that it is possible for states with positive (negative) m_F levels to shift to lower (higher)

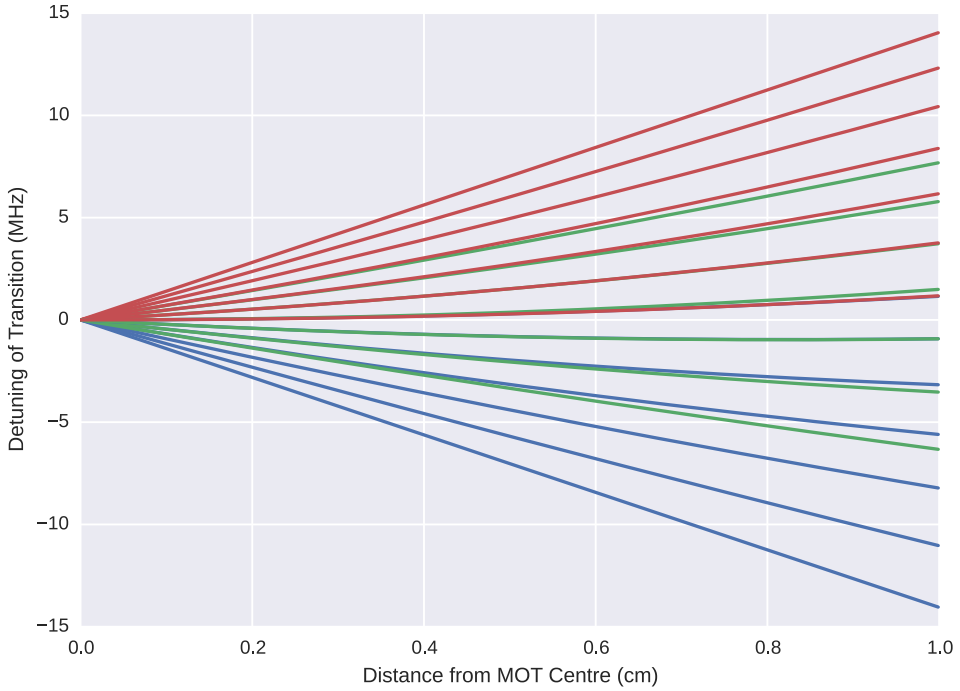

Figure 3.7: The positional dependent shift of the $5^2S_{1/2} \rightarrow 5^2P_{3/2}$ transition energies of a rubidium 85 atom in a magneto optical trap. The magnetic field gradient was set to typical value of $10\,\mathrm{G\,cm^{-1}}$.

energies in the presence of a magnetic field, but this only occurs for levels where the Landé g factor g_F is negative, for example the $F = 2$, $5^2S_{1/2}$ level of ^{85}Rb or the $F = 1$, $4^2S_{1/2}$ ground level of ^{39}K.

Figure 3.7 shows the positional dependent shift of the $5^2S_{1/2} \rightarrow 5^2P_{3/2}$ transition energies of a rubidium 85 atom in a magneto optical trap. The red lines correspond to σ^+ transitions, the blue lines correspond to σ^- transitions and the green lines are the possible π transitions. It is evident that σ^- transitions are required to get the greatest positional dependent force as they experience the greatest negative detuning.

3.3.1 Polarization Coupling within a MOT

The atoms within a MOT and the magnetic field centre of the trap are rarely coaxial with each pair of counter-propagating laser beams. Because of this, the magnetic field direction is seldom aligned with the wavevectors of any pair of beams, and in general both beams of each pair can couple with the atom to some degree to induce transitions. To see where the polarization and hence angular

dependence of the scattering rate comes from we must look at the on-resonance saturation parameter s_0 that was introduced in equation 3.1. The saturation parameter between a ground state $|g\rangle$ and excited state $|e\rangle$ can be written as:

$$s_0 = \frac{2|\Omega|^2}{\Gamma^2} = \frac{2E_0^2|\langle e|e\hat{\epsilon}\cdot\mathbf{r}|g\rangle|^2}{\hbar^2\Gamma^2} \tag{3.23}$$

where $\hat{\epsilon}$ is the polarization of the light, $\mathbf{r}$ is the electron's position vector and E_0 is the electric field due to the incident radiation. This can be written in terms of the light intensity I as $s_0 = I/I_s$, where the saturation intensity I_s is given by:

$$I_s = \frac{c\epsilon_0\Gamma^2\hbar^2}{4|\langle e|e\hat{\epsilon}\cdot\mathbf{r}|g\rangle|^2} \tag{3.24}$$

Circularly polarized light incident upon an atom at an angle θ to the $\hat{\mathbf{z}}$ axis has a wavevector of direction $\hat{\mathbf{k}} = \sin(\theta)\hat{\mathbf{x}} + \cos(\theta)\hat{\mathbf{z}}$ and polarization given by $\hat{\mathbf{e}}_\pm = A_x\hat{\mathbf{e}}_x + A_y\hat{\mathbf{e}}_y + A_z\hat{\mathbf{e}}_z = \frac{1}{\sqrt{2}}(\cos(\theta)\hat{\mathbf{e}}_x - \sin(\theta)\hat{\mathbf{e}}_z \pm i\hat{\mathbf{e}}_y)$, where the sign refers to the handedness of the light. This can be written in the spherical basis ($\hat{\mathbf{e}}_\pm = A_1\hat{\mathbf{e}}_1 + A_{-1}\hat{\mathbf{e}}_{-1} + A_0\hat{\mathbf{e}}_0$) by applying the transformation:

$$\begin{bmatrix} A_1 \\ A_{-1} \\ A_0 \end{bmatrix} = \begin{bmatrix} -\frac{1}{\sqrt{2}} & \frac{i}{\sqrt{2}} & 0 \\ \frac{1}{\sqrt{2}} & \frac{i}{\sqrt{2}} & 0 \\ 0 & 0 & 1 \end{bmatrix} \begin{bmatrix} A_x \\ A_y \\ A_z \end{bmatrix} \tag{3.25}$$

which yields:

$$\hat{\mathbf{e}}_\pm = \frac{1}{2}(-\cos\theta \mp 1)\hat{\mathbf{e}}_1 + \frac{1}{2}(\cos\theta \mp 1)\hat{\mathbf{e}}_{-1} - \frac{1}{\sqrt{2}}\sin\theta\hat{\mathbf{e}}_0 \tag{3.26}$$

The electron's position vector can also be written in the spherical basis in terms of the spherical harmonics $Y_{l,q}$:

$$\mathbf{r} = r_0\hat{\mathbf{e}}_0 + r_1\hat{\mathbf{e}}_1 + r_{-1}\hat{\mathbf{e}}_{-1} = r\sqrt{\frac{4\pi}{3}}(Y_{1,0}\hat{\mathbf{e}}_0 - Y_{1,-1}\hat{\mathbf{e}}_1 - Y_{1,1}\hat{\mathbf{e}}_{-1}) \tag{3.27}$$

Using the orthonormality condition ($\hat{\mathbf{e}}_q^*\cdot\hat{\mathbf{e}}_{q'} = \delta_{qq'}$) and the property of the spherical basis ($\hat{\mathbf{e}}_q^* = (-1)^q\hat{\mathbf{e}}_{-q}$)[75] we find:

$$\hat{\mathbf{e}}_\pm\cdot\mathbf{r} = \frac{1}{2}(-\cos\theta \mp 1)r\sqrt{\frac{4\pi}{3}}Y_{1,1} + \frac{1}{2}(\cos\theta \mp 1)r\sqrt{\frac{4\pi}{3}}Y_{1,-1} - \frac{1}{\sqrt{2}}\sin\theta r\sqrt{\frac{4\pi}{3}}Y_{1,0} \tag{3.28}$$

The matrix elements $\langle e|e\hat{\mathbf{e}}_\pm \cdot \mathbf{r}|g\rangle$ are only non zero if they are of the following form[69]:

$$\begin{aligned}
\langle F', m_F + 1|e\hat{\mathbf{e}}_\pm \cdot \mathbf{r}|F, m_F\rangle &= \frac{1}{2}(-\cos\theta \mp 1)\langle F', m_F + 1|er\sqrt{\frac{4\pi}{3}}Y_{1,1}|F, m_F\rangle \\
\langle F', m_F - 1|e\hat{\mathbf{e}}_\pm \cdot \mathbf{r}|F, m_F\rangle &= \frac{1}{2}(\cos\theta \mp 1)\langle F', m_F - 1|er\sqrt{\frac{4\pi}{3}}Y_{1,-1}|F, m_F\rangle \\
\langle F', m_F|e\hat{\mathbf{e}}_\pm \cdot \mathbf{r}|F, m_F\rangle &= -\frac{1}{\sqrt{2}}\sin\theta\langle F', m_F|er\sqrt{\frac{4\pi}{3}}Y_{1,0}|F, m_F\rangle
\end{aligned} \tag{3.29}$$

Or back in terms of the components of $\mathbf{r}$ in the spherical basis:

$$\begin{aligned}
\langle F', m_F + 1|e\hat{\mathbf{e}}_\pm \cdot \mathbf{r}|F, m_F\rangle &= \frac{1}{2}(-\cos\theta \mp 1)\langle F', m_F + 1|er_{-1}|F, m_F\rangle \\
\langle F', m_F - 1|e\hat{\mathbf{e}}_\pm \cdot \mathbf{r}|F, m_F\rangle &= \frac{1}{2}(\cos\theta \mp 1)\langle F', m_F - 1|er_1|F, m_F\rangle \\
\langle F', m_F|e\hat{\mathbf{e}}_\pm \cdot \mathbf{r}|F, m_F\rangle &= -\frac{1}{\sqrt{2}}\sin\theta\langle F', m_F|er_0|F, m_F\rangle
\end{aligned} \tag{3.30}$$

This shows that circularly polarized light can excite σ_+, σ_- and π transitions within a MOT, the strength of which is determined by the angle between its wavevector and the quantization axis.

3.3.1.1 Evaluation of the Dipole Matrix Elements

We can see from the Wigner-Eckart theorem that these dipole matrix elements can be written as a product of a Clebsch-Gordan coefficient and a reduced matrix element. Note that we use the convention here that the normalization term is contained within the reduced matrix element[74].

$$\langle F', m'_F|er_{-q}(-1)^q|F, m_F\rangle = \langle F'\|e\mathbf{r}\|F\rangle\langle F, m_F, 1, q|F', m'_F\rangle \tag{3.31}$$

This can also be expressed in terms of a Wigner 3j symbol:

$$\langle F', m'_F|er_q|F, m_F\rangle = (-1)^{F'-m'_F+q}\sqrt{2F+1}\langle F'\|e\mathbf{r}\|F\rangle \begin{pmatrix} F' & 1 & F \\ -m'_F & -q & m_F \end{pmatrix} \tag{3.32}$$

which is non zero only if $|F' - 1| \leq F \leq F' + 1$ and if $m_F - q = m'_F$, where q corresponds to the polarization of the radiation $q = -1, 0, 1$ that excites the transitions σ_+, π and σ_- respectively.

The reduced matrix elements $\langle F'\|e\mathbf{r}\|F\rangle$ and $\langle J'\|e\mathbf{r}\|J\rangle$ can also be related using a Wigner 6j symbol[74]:

$$\langle F'\|e\mathbf{r}\|F\rangle = (-1)^{J'+I+F+1}\sqrt{(2F'+1)(2J+1)}\langle J'\|e\mathbf{r}\|J\rangle \begin{Bmatrix} J' & F' & I \\ F & J & 1 \end{Bmatrix} \tag{3.33}$$

which is non zero only if the following relations hold: $|J'-F'| \leq I \leq J'+F'$,$|J'-J| \leq 1 \leq J'+J$,$|F-F'| \leq 1 \leq F+F'$ and $|F-J| \leq I \leq F+J$. Combining these equations leads to:

$$\begin{aligned}\langle F', m'_F|er_q|F, m_F\rangle = (-1)^{F'-m'_F+J'+I+F+1+q}\sqrt{(2F+1)(2F'+1)(2J+1)} \\ \langle J'\|e\mathbf{r}\|J\rangle \begin{pmatrix} F' & 1 & F \\ -m'_F & -q & m_F \end{pmatrix} \begin{Bmatrix} J' & F' & I \\ F & J & 1 \end{Bmatrix}\end{aligned} \tag{3.34}$$

which can be rewritten using $\langle J'\|e\mathbf{r}\|J\rangle = (-1)^{J'-J}\langle J\|e\mathbf{r}\|J'\rangle^*$, noting that the reduced dipole matrix elements are real when using the usual phase convention for the spherical harmonics[74]:

$$\begin{aligned}\langle F', m'_F|er_q|F, m_F\rangle = (-1)^{F'-m'_F+2J'-J+I+F+1+q}\sqrt{(2F+1)(2F'+1)(2J+1)} \\ \langle J\|e\mathbf{r}\|J'\rangle \begin{pmatrix} F' & 1 & F \\ -m'_F & -q & m_F \end{pmatrix} \begin{Bmatrix} J' & F' & I \\ F & J & 1 \end{Bmatrix}\end{aligned} \tag{3.35}$$

The values of the various dipole matrix elements of the D_2 line of ^{85}Rb have been calculated and tabulated relative to that of the reduced matrix element $\langle J=1/2\|e\mathbf{r}\|J'=3/2\rangle \approx 4.23ea_0$ in figure 3.8.

3.3.1.2 Balancing of the Scattering Forces

Now that we have evaluated the dipole matrix elements for a single circularly polarized beam we can find the saturation parameters associated with it by calculating the squared norm of the dipole matrix elements:

$$\begin{aligned}|\langle F', m_F+1|e\hat{\mathbf{e}}_\pm \cdot \mathbf{r}|F, m_F\rangle|^2 &= \frac{1}{4}[\cos^2\theta \pm 2\cos\theta + 1]|\langle F', m_F+1|er_{-1}|F, m_F\rangle|^2 \\ |\langle F', m_F-1|e\hat{\mathbf{e}}_\pm \cdot \mathbf{r}|F, m_F\rangle|^2 &= \frac{1}{4}[\cos^2\theta \mp 2\cos\theta + 1]|\langle F', m_F-1|er_1|F, m_F\rangle|^2 \\ |\langle F', m_F|e\hat{\mathbf{e}}_\pm \cdot \mathbf{r}|F, m_F\rangle|^2 &= \frac{1}{2}\sin^2\theta|\langle F', m_F|er_0|F, m_F\rangle|^2\end{aligned} \tag{3.36}$$

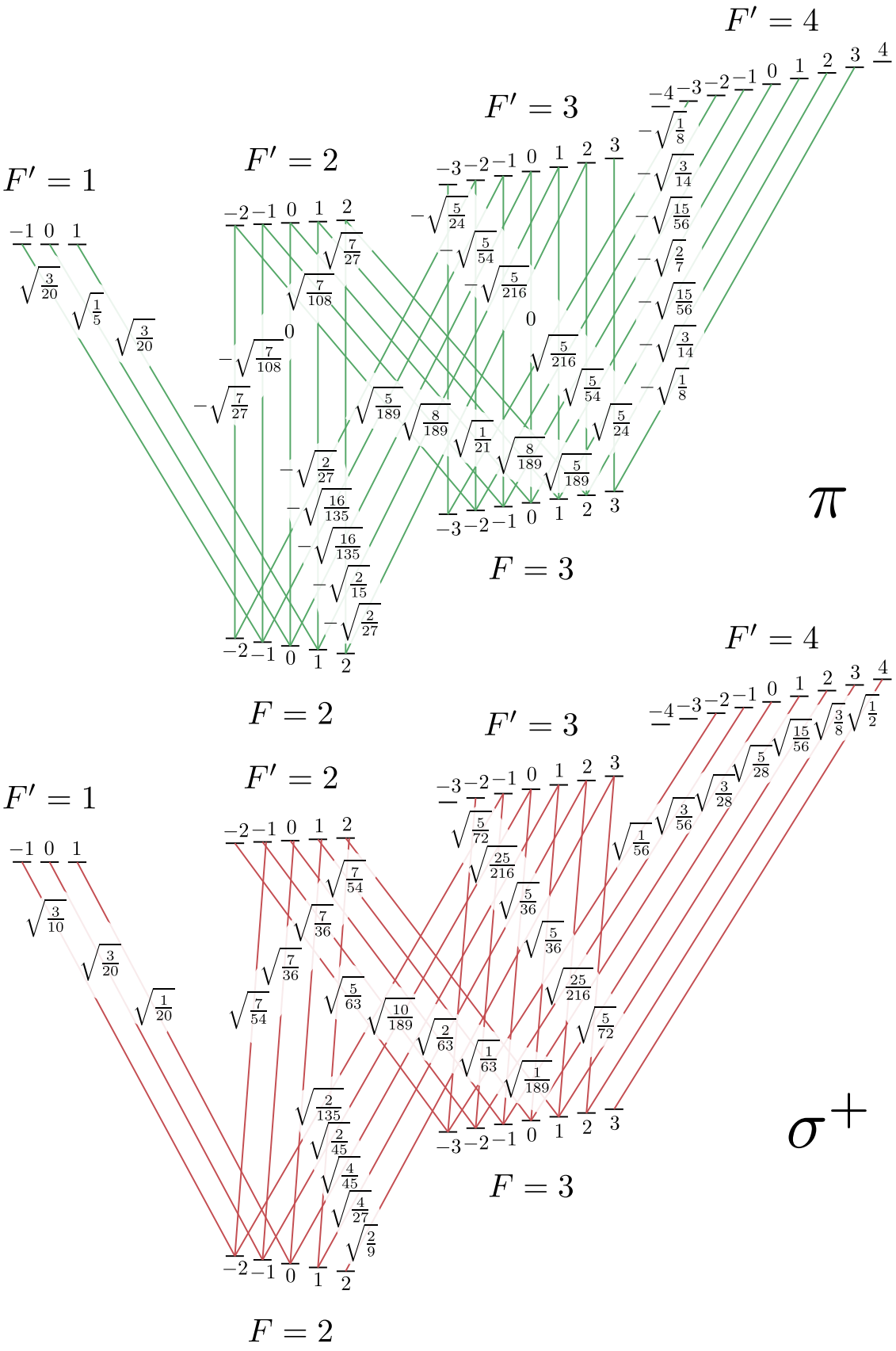

Figure 3.8: Relative Zeeman shifts and dipole moments for the transitions within the D_2 line of ^{85}Rb relative to the reduced matrix element $\langle J = 1/2 \| er \| J' = 3/2 \rangle \approx 4.23ea_0$. Only the π and σ^+ transitions are shown explicitly, however the σ^- dipole moments can be calculated by applying the transformation $m_F \to -m_F$ to the diagram showing the σ^+ dipole moments.

We can see from a Taylor series that at low intensities the scattering force exerted upon an atom due to a single beam is approximately proportional to the on resonance saturation parameter:

$$\begin{aligned}\mathbf{F} &= \frac{\hbar\mathbf{k}s_0\Gamma/2}{1+s_0+\left(2\delta'/\Gamma\right)^2} \\ &= \mathbf{F}(s_0=0) + \frac{d\mathbf{F}(s_0=0)}{ds_0}s_0 + \mathcal{O}(s_0^2) \\ &= \frac{\hbar\mathbf{k}s_0\Gamma/2}{1+\left(2\delta'/\Gamma\right)^2} + \mathcal{O}(s_0^2)\end{aligned} \tag{3.37}$$

where we have used the fact that the on resonance saturation parameter is proportional to the intensity of the beam. We must remember, however, that in a MOT the atoms scatter light from opposing pairs of beams and so the total average force for a pair of beams acting on one particular transition is given by:

$$\mathbf{F} = \frac{\hbar\Gamma}{2}\left[\frac{\mathbf{k}_+ s_{0+}}{1+\left(2\delta'_+/\Gamma\right)^2} + \frac{\mathbf{k}_- s_{0-}}{1+\left(2\delta'_-/\Gamma\right)^2}\right] \tag{3.38}$$

where the subscripts denote which beam each parameter relates to. For a correctly aligned MOT, atoms bathe in the light from counter propagating pairs of beams with circular polarizations of the same helicity but opposing direction (the second beam has a direction of $\theta' = \pi - \theta$). Inserting equations 3.23 and 3.24 we can find the average force due to each transition:

$$\begin{aligned}\mathbf{F}_{\sigma_+} = \frac{2I}{c\epsilon_0\Gamma\hbar}\Bigg[&\frac{\mathbf{k}_+|\langle F', m_F+1|e\hat{\mathbf{e}}_\pm(\theta)\cdot\mathbf{r}|F,m_F\rangle|^2}{1+\left(2\delta'_+/\Gamma\right)^2} \\ &+\frac{\mathbf{k}_-|\langle F', m_F+1|e\hat{\mathbf{e}}_\pm(\pi-\theta)\cdot\mathbf{r}|F,m_F\rangle|^2}{1+\left(2\delta'_-/\Gamma\right)^2}\Bigg]\end{aligned} \tag{3.39}$$

$$\begin{aligned}\mathbf{F}_{\sigma_-} = \frac{2I}{c\epsilon_0\Gamma\hbar}\Bigg[&\frac{\mathbf{k}_+|\langle F', m_F-1|e\hat{\mathbf{e}}_\pm(\theta)\cdot\mathbf{r}|F,m_F\rangle|^2}{1+\left(2\delta'_+/\Gamma\right)^2} \\ &+\frac{\mathbf{k}_-|\langle F', m_F-1|e\hat{\mathbf{e}}_\pm(\pi-\theta)\cdot\mathbf{r}|F,m_F\rangle|^2}{1+\left(2\delta'_-/\Gamma\right)^2}\Bigg]\end{aligned} \tag{3.40}$$

$$\mathbf{F}_\pi = \frac{2I}{c\epsilon_0\Gamma\hbar}\left[\frac{\mathbf{k}_+|\langle F', m_F|e\hat{\mathbf{e}}_\pm(\theta)\cdot\mathbf{r}|F, m_F\rangle|^2}{1+\left(2\delta'_+/\Gamma\right)^2} + \frac{\mathbf{k}_-|\langle F', m_F|e\hat{\mathbf{e}}_\pm(\pi-\theta)\cdot\mathbf{r}|F, m_F\rangle|^2}{1+\left(2\delta'_-/\Gamma\right)^2}\right] \tag{3.41}$$

The total detuning of each beam seen by an atom within the trap is given by $\delta'_\pm = \delta - \mathbf{k}_\pm\cdot\mathbf{v} - Gr$, where r is the distance of the atom from the trap centre and G is a factor given by:

$$G = \frac{\partial\omega}{\partial r} = \frac{\mu'}{\hbar}\frac{dB}{dr} \tag{3.42}$$

which from previous arguments is assumed to be constant at the field strengths within the trapping region, but is a different value for each transition (see figure 3.7). If we consider the case of a stationary atom, i.e. $\delta' = \delta'_+ = \delta'_-$, whilst noting that the beam's wavevectors are equal and opposite and then by inserting equation 3.36 we find:

$$\begin{aligned}\mathbf{F}_{\sigma_+} &= \pm\frac{1}{2}\cos\theta\frac{2I\mathbf{k}_+|\langle F', m_F+1|er_{-1}|F, m_F\rangle|^2}{c\epsilon_0\Gamma\hbar\left[1+\left(2\delta'/\Gamma\right)^2\right]} \\ &= \pm\frac{I\mathbf{k}_+|\langle F', m_F+1|er_{-1}|F, m_F\rangle|^2}{c\epsilon_0\Gamma\hbar\left[1+\left(2\delta'/\Gamma\right)^2\right]}\hat{\mathbf{k}}_+\cdot\hat{\mathbf{B}}\end{aligned} \tag{3.43}$$

$$\begin{aligned}\mathbf{F}_{\sigma_-} &= \mp\frac{1}{2}\cos\theta\frac{2I\mathbf{k}_+|\langle F', m_F-1|er_1|F, m_F\rangle|^2}{c\epsilon_0\Gamma\hbar\left[1+\left(2\delta'/\Gamma\right)^2\right]} \\ &= \mp\frac{I\mathbf{k}_+|\langle F', m_F-1|er_1|F, m_F\rangle|^2}{c\epsilon_0\Gamma\hbar\left[1+\left(2\delta'/\Gamma\right)^2\right]}\hat{\mathbf{k}}_+\cdot\hat{\mathbf{B}}\end{aligned} \tag{3.44}$$

$$\mathbf{F}_\pi = 0 \tag{3.45}$$

So we can see that the π transitions contribute zero average force, leaving only the σ transitions to be of interest, and giving the angular dependence shown in figure 3.9. It was mentioned earlier, and shown in figure 3.7, that the σ_- transitions experience the largest positional dependent detuning and as a result the magnitude of $\mathbf{F}_{\sigma_-}$ will dominate over $\mathbf{F}_{\sigma_+}$. We recall that the signs of these expressions are determined by the helicity of the laser beams and the choice of magnetic field direction, so we can ensure trapping will occur by choosing $\mathbf{F}_{\sigma_-}$ to be negative so that it acts to provide a restoring force.

The magneto optical trap will tend to optically pump the ^{85}Rb atoms into the $5^2S_{1/2}, F = 3, m_F = -3$ sub-level, and as a result in modelling the trap only the

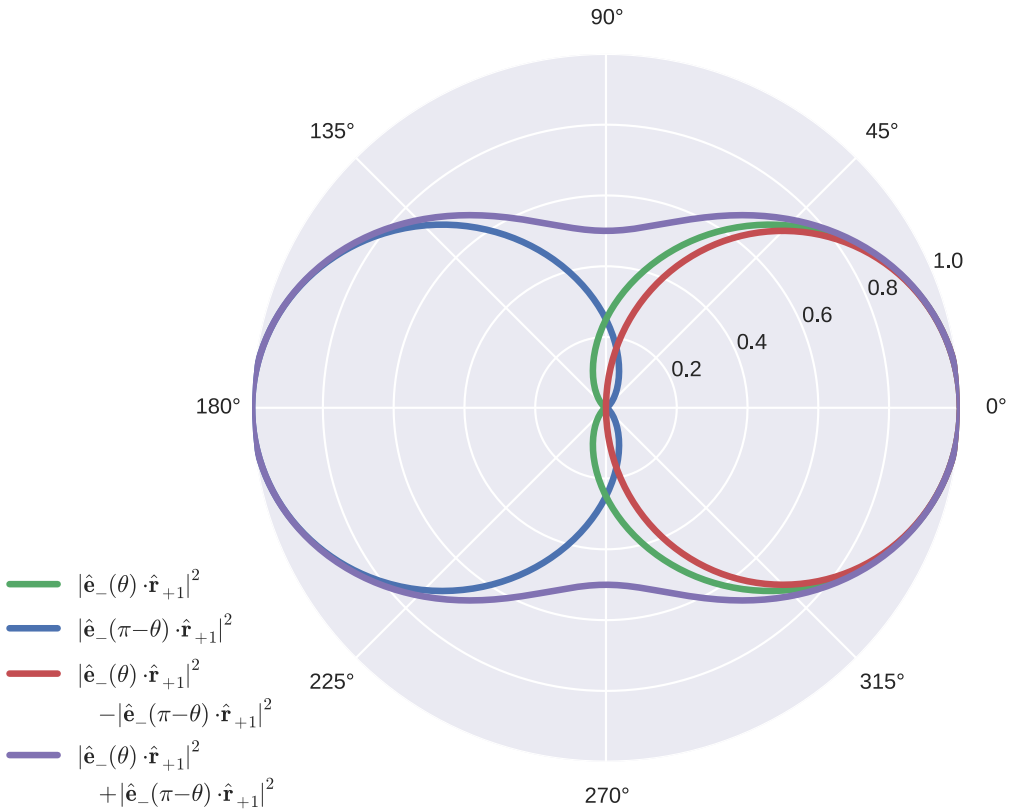

Figure 3.9: Relative probabilities of light with polarization $\hat{\mathbf{e}}_-$ and angle θ to the local direction of magnetic field (quantization axis) exciting σ_- transitions of an atom. The total absorption probability and absorption difference is also shown for an atom in the presence of two counter propagating beams with this same circular polarization (helicity). Each beam pair in a MOT provides an average force that is proportional to the difference in these absorption probabilities (see equations 3.43 to 3.45).

$m_F = -3 \rightarrow m_{F'} = -4$, $m_F = -3 \rightarrow m_{F'} = -3$ and $m_F = -3 \rightarrow m_{F'} = -2$ transitions are considered. In reality, atoms will be excited into other levels, in particular at the centre of the MOT where the levels become degenerate, but that type of simulation would require tracking the internal state of each atom, requiring a much slower simulation without much indication of any improvement. Figure 3.10 shows the force exerted upon a ^{85}Rb atom within a MOT at different speeds moving in the positive x direction.

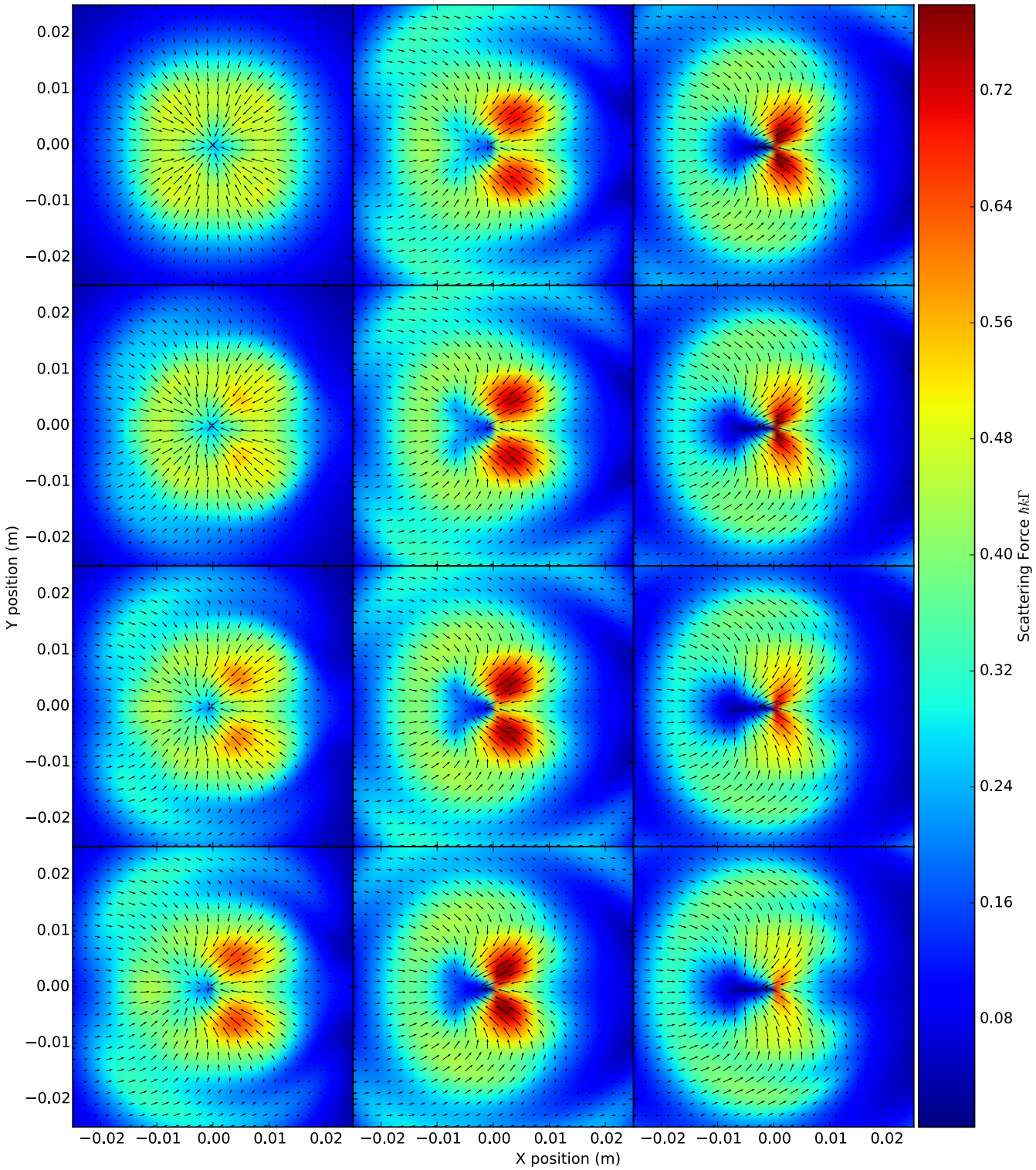

Figure 3.10: Average positional dependent force upon a ^{85}Rb atom in a MOT that has assumed to have been pumped into the $5^2S_{1/2}, F = 3, m_F = -3$ sub-level. Successive plots show the atom with an increasing speed in the positive x axis, $1.0\,\mathrm{m\,s^{-1}}$ per plot. The beam intensity is $I{\approx}6.68\,\mathrm{mW\,cm^{-2}}$, the detuning is $\delta = -2\Gamma$ and the magnetic field gradient is $10\,\mathrm{G\,cm^{-1}}$.

3.3.2 Repump laser

One factor which so far has been ignored in the discussion of the magneto optical trap is the need for a repumping laser, without which cold atom clouds cannot form. In our model of the MOT we have assumed that the atoms of rubidium 85 that begin in the $5^2S_{1/2}, F = 3$ level will always remain coupled to the laser light because the level to which the light is resonant, $5^2P_{3/2}, F' = 4$, only permits transitions back into the $F = 3$ level.

The laser light of the cooling beam, however, is red detuned from the cooling transition which brings it closer to resonance with the $5^2P_{3/2}, F' = 3$ level. This proximity, in combination with the additional tuning from the Doppler and Zeeman shifts and the finite linewidth of the cooling laser, results in a probability of the atoms becoming excited into the $F' = 3$ state. This excited level can collapse back into the cooling cycle, although another decay route is for the atom to relax into the $5^2S_{1/2}, F = 2$ ground state. This state does not interact with the cooling beams due to having a large frequency separation of approximately 3 GHz. Atoms which are pumped into this ground state no longer experience either cooling or trapping forces from the cooling lasers, so they are free to escape the trapping region.

To ensure that the atoms within the trap have a reasonable lifetime, another laser is added to the trapping scheme which is resonant to the $5^2S_{1/2}, F = 2 \rightarrow 5^2P_{3/2}, F' = 3$ transition. This 'repump' laser does not directly bring the atoms back into the cooling cycle, but instead pumps them into the $F' = 3$ level where upon relaxation they have a probability of collapsing back into the $F = 3$ ground state where they can again be cooled.

3.4 Cooling Limits

3.4.1 Doppler Temperature

Although the average force in a MOT acts to slow atoms down, the random nature of both absorption from beams of equal scattering rate and the subsequent remission of this radiation in random directions acts to cause the atoms to diffuse in momentum space and, in doing so, produces a heating effect. An atom receives $\hbar k$ of momentum in a random direction upon every relaxation event, and this

can be modelled as a random walk, where after N scattering events the atom has drifted in momentum space by a mean squared value of:

$$\langle p^2 \rangle = \langle (p_1 + p_2 + p_3 + ... + p_N)^2 \rangle \tag{3.46}$$

where the p_i terms correspond to each momentum exchange event of an atom due to the absorption and spontaneous emission of light from the two counter-propagating beams of equal power. If the situation is restricted to one dimension then these terms are equal to $p_i = \pm\hbar k$, the direction of each momentum exchange being random. This expression can be expanded using the multinomial theorem:

$$\begin{aligned} \langle p^2 \rangle &= \langle p_1^2 + 2p_1p_2 + 2p_1p_3 + ... + p_2^2 + 2p_2p_3 + 2p_2p_4 + ... + p_N^2 \rangle \\ &= \langle p_1^2 \rangle + \langle p_2^2 \rangle + \langle p_3^2 \rangle + ... + \langle p_N^2 \rangle \end{aligned} \tag{3.47}$$

where the last step is justified because each kick of momentum is uncorrelated with each other, and so the cross terms average to zero. From this we can see the mean squared distance diffused in momentum space is given by:

$$\langle p^2 \rangle = N\hbar^2k^2 \tag{3.48}$$

which increases at a rate given by:

$$\frac{d\langle p^2 \rangle}{dt} = \hbar^2k^2\frac{dN}{dt} = 4\hbar^2k^2\Gamma_s \tag{3.49}$$

where the number of scattering events is given by $N = 4\Gamma_s t$, and Γ_s is the scattering rate due to a single beam. The factor of four is because each scattering event is associated with an exchange of two photons of random direction, and the total scattering rate is doubled because of the presence of two beams. As shown in section 3.1.1, the cooling force exerted upon atoms within a MOT is proportional to their velocities:

$$F = \frac{dp}{dt} = -\alpha v \tag{3.50}$$

where the constant α is given by equation 3.8. This means that the rate at which the atoms' squared momentum reduces is given by:

$$\frac{d(p^2)}{dt} = 2p\frac{dp}{dt} = -2m\alpha v^2 \tag{3.51}$$

The Doppler temperature, T_D, of atoms within a MOT can be found by equating the heating rate caused by the momentum diffusion with the cooling rate due to

the velocity dependent force:

$$4\hbar^2 k^2 \Gamma_s = -2m\alpha v^2 \tag{3.52}$$

The temperature of atoms in one dimension is related to their root mean squared velocity by:

$$T = \frac{mv^2}{k_B} \tag{3.53}$$

so the Doppler temperature is:

$$\begin{aligned} T_D &= \frac{-2\hbar^2 k^2 \Gamma_s}{\alpha k_B} \\ &= \frac{\hbar}{2k_B} \frac{\delta^2 + \frac{\Gamma^2}{4}}{\delta} \end{aligned} \tag{3.54}$$

This function has a minimum at a detuning of $\delta = -\Gamma/2$, giving a minimum temperature of:

$$T_D = \frac{\hbar\Gamma}{2k_B} \tag{3.55}$$

which is approximately equal to $T_D = 145.57\,\mu\text{K}$ for ^{85}Rb. It was a great surprise when a paper published in 1988 reported temperatures of sodium atoms cooled via optical molasses down to 43 µK, significantly lower than the minimum value of 240 µK predicted by the Doppler limit[76]. Investigations into this anomalous behaviour led to the discovery of Sisyphus cooling by Claude Cohen-Tannoudji, which resulted in him receiving the Nobel prize in 1997.

3.4.2 Sisyphus Cooling

This sub-Doppler cooling process relies on the optical pumping of atoms as they move through polarization gradients of the red detuned cooling light of optical molasses. Sisyphus cooling occurs at the centre of a magneto optical trap where there is no magnetic field to act as the quantization axis. As a result the Zeeman sublevels seem to be degenerate, however upon being bathed in the red-detuned cooling beams the levels experience light shifts, the magnitude of which is proportional to the square of the Clebsch-Gordan coefficient for each transition and equally to the intensity of the light of each polarization that drives these transitions. The counter propagating beams interfere so that the polarization seen by the atoms varies spatially and in turn the light shift of the sublevels varies in strength spatially also. As shown in figure 3.11, atoms that move through this

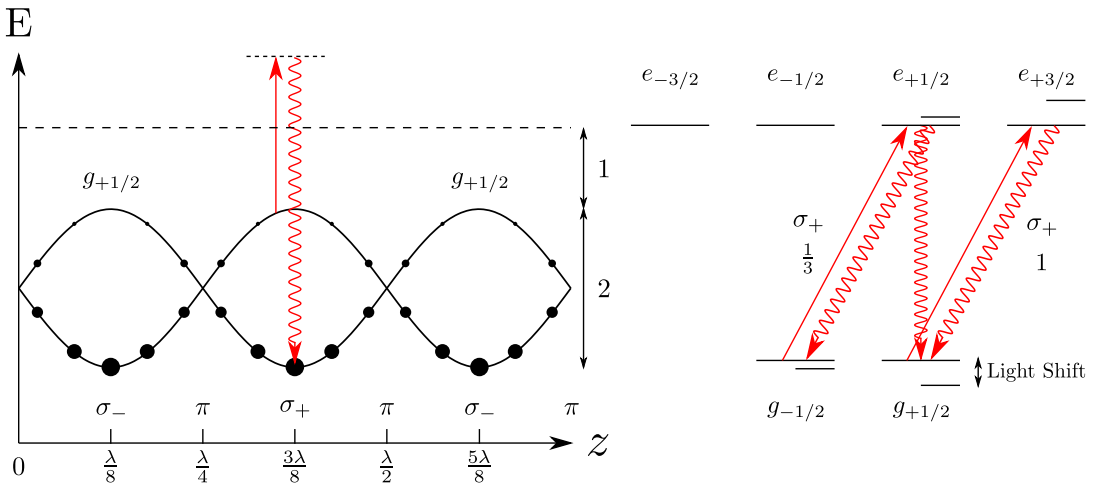

Figure 3.11: One dimensional Sisyphus cooling due to the interaction of red-detuned counter propagating linearly polarized beams upon an atom with transition $F_g = 1/2 \rightarrow F_e = 3/2$. The image on the left shows how the energy of the ground states varies due to the changing polarization of the total optical field. This energy change is due to the light shift, which is proportional to the square of the Clebsch-Gordan coefficient for each transition and hence causes an energy splitting of the ground states. The black circles represent the steady state occupation of the ground state due to optical pumping such as that shown for σ_+ transitions in the right image. Due to the absence of a magnetic field the polarization is defined with respect to the axis along which the laser beams propagate. Adapted from[77].

undulating potential are optically pumped into their lower energy state and in the process lose kinetic energy equal to the difference of their shifted energy levels, cooling them down. This process continues until the kinetic energy of the atoms is reduced enough so that they can no longer climb the potential hill and become trapped in the optical potential wells. At low laser intensities the temperature achieved through this process scales proportionally with the laser intensity and inversely proportional to the laser detuning. In spite of this fact, the temperature cannot be decreased indefinitely and is limited to the point where the energy extracted from Sisyphus cooling equates to the heating due to the photon recoils experienced by the atoms.

3.5 Scaling Laws of the Atom Number in a MOT

As the width of the laser beams of a MOT increases the steady state number of trapped atoms rises as a result of the increased distance over which the atoms experience a deceleration, allowing for faster atoms in the background vapour to be stopped. The scaling of atom number with beam width depends on the size of the trap, but it is always true that the steady state atom number N of a MOT can be calculated to be[78, 79]:

$$N \approx 0.1 \frac{L^2}{\sigma} \left(\frac{v_c}{\bar{v}_{vap}} \right)^4 \tag{3.56}$$

where L is the beam diameter, σ is the cross section of collisions which cause atoms to escape the trap, v_c is the capture velocity and $\bar{v}_{vap}$ is the average velocity of the atoms in the background vapour. The capture velocity can be determined through numerical simulations[79], and these have shown that sufficiently large MOTs exhibit an approximate scaling relationship of $N \propto L^{3.6}$, matching what has been determined experimentally[80, 81].

For small beam widths this scaling law is invalid, the reason can be understood by considering the approximation for low velocity atoms which, as shown in section 3.1.1, experience a force that is proportional to their velocity $F = -\alpha v$. Atoms in this regime undergo an exponential deceleration over a stopping distance $d = Mv_i/\alpha$, where M is the mass of the atom and v_i is its initial velocity as it enters the trap. An atom can only be captured if its stopping distance is smaller than the geometry of the trap $\sim L$, thus determining the capture velocity in this regime, $v_c = L\alpha/M$. Using this expression in combination with equation 3.56 the scaling relationship of small MOTs is found to be $N \propto L^6$.

As can be seen in figure 3.1 the linear approximation breaks down at a velocity of $v_t \sim \delta/k$, the point at which the Doppler shift equals to the laser's detuning. This corresponds to the maximum capture velocity which can be modelled by the rapid scaling law, and it follows that this transition region corresponds to a beam diameter of:

$$L \approx \frac{M\delta}{\alpha k} \tag{3.57}$$

which is $L \approx 2.2\,\text{mm}$ for ^{85}Rb assuming a detuning of $\delta = -\Gamma/2$ and on resonance saturation parameter of $s_0 = 2$.

3.6 Review of Alternate MOT Geometries

Since the first demonstration of the Magneto Optical Trap (MOT) by Raab *et al.*[11], there have been a number of variants of the original six beam geometry designed to be used in applications such as atom chips, atom sources and to study atom-surface interactions. These include the mirror, pyramidal and tetrahedral MOTs and more recently a trap utilizing optical gratings[82–86]. All of these designs have their advantages, but most of them require a high degree of optical access and so have limited use in integrated atom chips without employing the use of complex optical feedthroughs. The pyramidal geometry was one of the first which could be implemented by directing the optical fields through a single window, but the price of this design is the low atom number that results from its small capture volume, which is limited both by the difficultly of microfabricating large pyramidal cavities, but also due to an unfavourable relationship to beam size. The tetrahedral MOT addressed this problem by forming its atom clouds outside its reflective structure, but both of these designs have the significant disadvantage that if they are etched in silicon the fabrication is rather challenging. The tetrahedral mirror geometry was later reimplemented with a single optical grating allowing for a much higher atom number, but this design suffers in that it can only be used to trap a single species due to the fact the angles of the diffracted beams are wavelength dependent. We have demonstrated a new design of magneto optical trap which only requires optical access through a single viewport, is able to capture a large number of atoms, has inherently low scatter and can be used to trap multiple species simultaneously. This design has use in integrated atom chips where optical access is restricted, and this was the main motivation for its design.

3.6.1 Mirror MOT Geometry

The most basic type of mirror MOT simply consists of a pair of anti-Helmholtz coils aligned such that the axis though the coils lies at an angle of 45° to that of a mirror, with the magnetic field zero positioned slightly above its surface. One laser beam is directed towards the mirror along the coils' axis and, after reflection, this beam passes through a quarter wave plate before being retro-reflected to create a two dimensional trapping force in the plane defined by the retro-reflected beam.

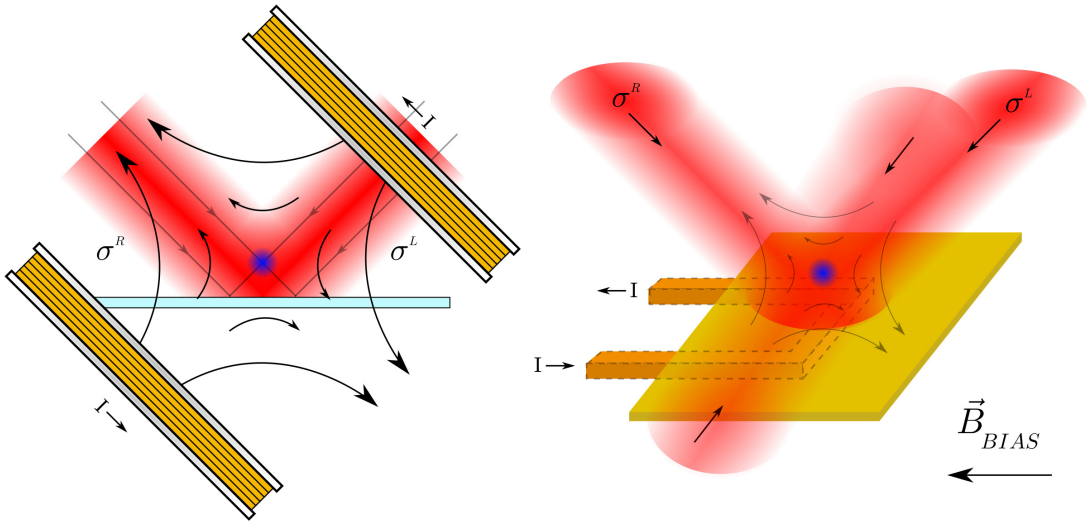

Figure 3.12: Illustration of a mirror MOT created with external anti-Helmholtz coils and another with the magnetic fields generated by a U shaped wire beneath the mirror in conjunction with a bias coil.

Trapping in the third dimension is produced by the addition of another retro-reflected beam directed at the magnetic field zero, in a direction perpendicular to the plane of the other beams.

Provided the trapping region is greater than about 2 mm from the mirror's surface the mirror MOT exhibits the same scaling law as that of the traditional six-beam MOT[87], albeit with half the capture volume for the same beam size. It is because of this fact that mirror MOTs are often used as the starting stage in atom chips, whereby the high loading rate away from the mirror is used to quickly collect a large number of atoms, before they are transferred into a magnetic trap closer to the mirror's surface for subsequent evaporation[82]. Often there is an intermediate stage where the atoms are brought into a compressed MOT close to the surface[19]. This secondary MOT does not use the anti-Helmholtz coils of the collection MOT, but instead replaces them with a U-shaped wire beneath the mirror in conjunction with a bias coil (see figure 3.12).

3.6.2 Pyramidal Traps

The pyramidal geometry, a cross-section of which is shown in figure 3.13, uses a reflective cavity to generate the required optical fields for magneto optical trapping through the use of a single laser. The pyramidal MOT employs the standard anti-Helmholtz pair of coils to form the required quadrupole magnetic field, and the correct polarization of the lasers are created by the multiple reflections in the

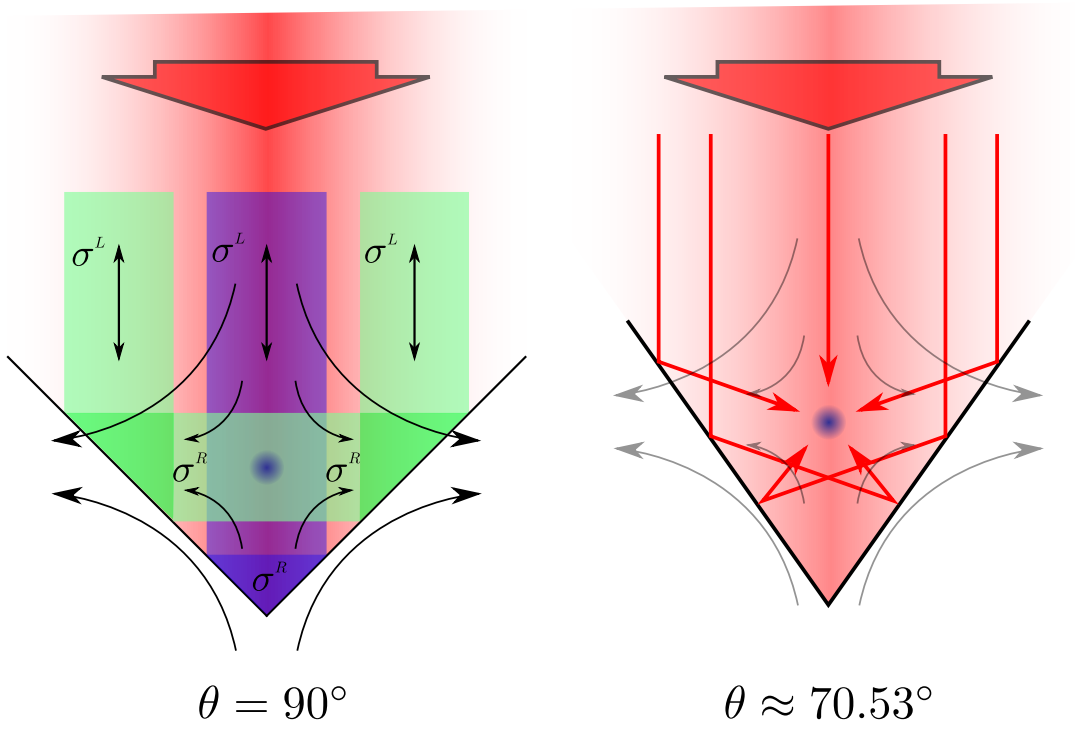

Figure 3.13: Geometry of a macroscopic pyramid MOT with an apex angle of 90° and the microfabricated equivalent etched into silicon with an apex angle of approximately 70.53°.

cavity, each of which reverse the handedness of the circular polarized light. Pyramidal MOTs have been created out of macroscopic mirrors[88], however they have also been microfabricated by anisotropically etching pits into particular planes of silicon[89–91]. Whilst these etched silicon traps were initially demonstrated with external coils they have since been implemented instead with a grid of planar wires arranged upon the silicon surface. It would appear that these cavities would be ideal for use in integrated atom chips, however the number of atoms within the resulting clouds do not scale particularly well with the volume of the cavities, and so fail to provide an adequate source of cold atoms for subsequent interferometry.

Microfabricated pyramidal MOTs exhibit the rapid scaling law ($N \propto L^6$) described in section 3.5, where N is the number of atoms within the trapped cloud and L is the size of the pyramid[91]. This relationship ensures that the number of trapped atoms rapidly decreases as the length scale of the trap is reduced. Based upon this scaling law, in a pyramid of depth equal to 1 mm it is expected that the number of captured atoms would only be on the order of 10. Clearly for this design to be of practical use the thickness of silicon required becomes prohibitively large, as even for cavities 2.5 mm deep only approximately 2000 atoms are able to be captured.

It is also worth noting that the capture volume of a pyramidal MOT is one sixth of the volume of a standard six-beam MOT with the same sized beams.

Atoms can also be lost from the trap due to collisions with the trap's walls, however this only contributes significantly when the chip wall to atom cloud distance is on the order of three Gaussian radii, and is described by the following relation[92, 93]:

$$\Gamma_{walls} = \frac{\bar{v}e^{-\frac{1}{2}(\frac{d}{\sigma})^2}}{\sqrt{8\pi}\sigma\left(1 + \mathrm{Erf}\left(\frac{d}{\sqrt{2}\sigma}\right)\right)} \tag{3.58}$$

where $\bar{v}$ is the average atomic velocity, d is distance to the trap surface and σ is the Gaussian radius of the atomic cloud.

Pyramid MOTs that are etched in silicon do not have the apex angle of 90° that is found in macroscopic pyramidal traps. The angle is instead determined by the structure of the silicon and is given by $\theta = \arccos(1/3) \approx 70.53°$. As a result of this acute angle, and as shown in figure 3.14, three different types of reflection are possible within the microfabricated pyramids. Type I reflections lead to trapping, as shown in figure 3.13, type II reflections do not intersect the trapping region and so do not need to be considered, however type III reflections cause anti-trapping. Each time light is reflected from the metallic surfaces the polarization of the light changes and in the case of type III reflections this causes the initially circular polarized light to transform into a polarization close to linear. Depending on the

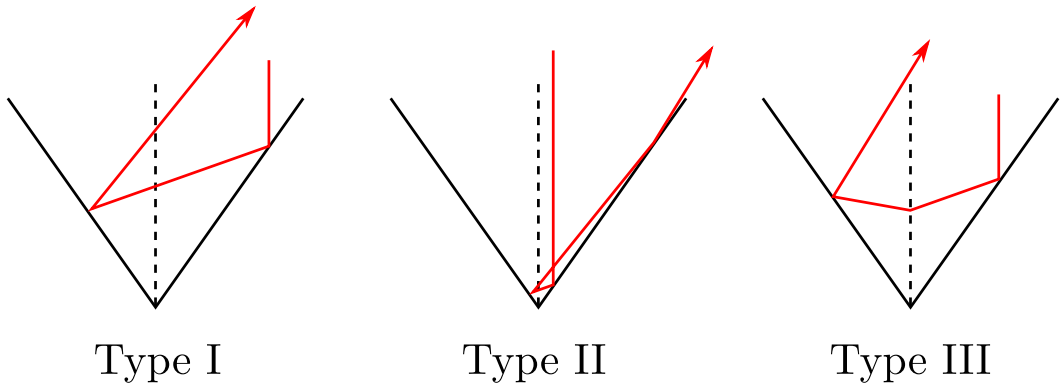

Figure 3.14: Possible reflections within a pyramid MOT. Type I reflections give the trapping and cooling forces, type II reflections do not intersect the trapping region and so can be ignored whilst type III reflections lead to anti-trapping. The type III reflections consist of three reflections, one of which is upon a face adjacent to the other surfaces and is not visible in the cross section. Adapted from [92].

intensity of these type III reflections, the reflectivity of the metallic mirrors and the imbalance of the vertical forces this can prevent atoms from being trapped[92]. In situations where this is the case the type III reflections can be removed by selectively etching the reflective surfaces into so called 'flower' patterns, however this does add additional steps and complexity to the fabrication procedure[90].

3.6.3 Tetrahedral Traps and the Grating MOT

The tetrahedral mirror MOT is a subclass of pyramidal trap that uses three reflective surfaces instead of the four that were typically found in earlier designs. This acts as an improvement in that its capture volume extends outside of the tetrahedral cavity, allowing for a greater flux of atoms into the trap[84]. The atom number in the tetrahedral MOT compares favourably to that of a six-beam MOT: M.Vangeleyn *et al.* measured an atom number of 1.3×10^6 for a tetrahedral trap of volume $400\,\mathrm{mm}^3$ compared to a traditional 6-beam design implemented in the same chamber which had a volume of $8000\,\mathrm{mm}^3$ and an atom number of 2×10^8. Using the $L^{3.6}$ scaling law it can be seen that we would only expect the 6-beam design to capture four times the atom number of the tetrahedral trap if it had been the same volume. It was argued that the tetrahedral trap's lower performance could be attributed to the experiment operating far from the optimal regime of the tetrad configuration, in addition to it having a reduction in the number of cooling beams compared to a six-beam trap[84]. Unfortunately, but as expected, for small tetrahedral traps the atom number scaling also reduces to the $N \propto L^6$ relationship[94]. The tetrahedral trap enters this rapid scaling regime when the length scale of the tetrahedron reaches 0.6 mm, however this is a significant improvement over that demonstrated with the square pyramidal traps, where the scaling regime starts to change at pyramid sizes around 7 mm[92].

The tetrahedral configuration is a rather forgiving geometry as it is able to operate at almost any mirror declination, θ. Reducing this angle increases the proportion of the trapping region that lies above the plane of the mirror, however the strength of the radial trapping decreases in doing so. The upwards reflecting beams also act to provide an increasing amount of axial anti-trapping as θ is reduced and as a result this gives a limit to their maximum permitted intensity, above which the trapping provided by the downwards beam is completely cancelled. Continuing to increase the declination above that of a pure tetra $\theta \approx 35.3^\circ$ makes it impossible to produce an optically balanced trap as the reflected intensity would need to be greater than the light incident upon the cavity. Angles greater than the pure

tetra are also undesirable because multiple reflections similar to those shown in figure 3.14 start to occur which provide anti-trapping and reduce the trap stability. Providing the declination remains lower than this critical angle there is no need for additional fabrication steps to etch the 'flower' patterns that are required in the pyramidal geometry.

A microfabricated tetrahedral trap has not yet been demonstrated however it has been proposed that they could be constructed through ion-beam milling. Another more exotic idea is to use the tip from an atomic force microscope to act as a 'stamp' with which to produce indents into a substrate that can subsequently be metallized[84]. Presumably the reason for the apparent loss in interest in tetrahedral traps is due to the emergence of microfabricated diffraction grating MOTs (GMOTs)[85, 86], a diagram of which is given in figure 3.15. This is a variant of the tetrahedral design that directs the cooling light in the tetrahedral beam geometry via the use of diffraction gratings instead of using mirrors. The fabrication procedure to manufacture these GMOTs is not trivial, however it is certainly a simpler, cheaper and more rapid method than that is required to create an etched pyramidal trap.

Like the tetrahedral MOT, the GMOT's capture region extends above the microfabricated surface, allowing for atoms to enter the trap from a greater solid angle, and also allowing for improved optical access to the atom cloud both for imaging and manipulation, particularly in the plane of the grating. One of the drawbacks of the GMOT geometry compared with that of the tetrahedral design, however, is that the sub-plane capture volume has been lost, resulting in a lower atom number for the same beam size.

Another way in which the GMOT differs from the tetrahedral mirror MOT is that its diffracted beams are of greater intensity than their mirror equivalent due to a geometric 'beam compression'. This compression compensates for the intensity attenuation that occurs when the diffracted beams are projected onto the axis of the incident beam, and as a result eliminates the dependence of the intensity balancing on the diffraction angle. The only condition for producing this balance in the GMOT is that the diffraction efficiency of the zeroth and first orders (R_0, R_1) must be related to the number of diffracted beams n by $R_1 = (1 - R_0)/n$, this relation can be reduced to $R_1 = 1/n$ if the zeroth order reflection is suppressed by either etching the grating to a depth of $\lambda/4$ or by removing its central region (if permitted by the geometry).

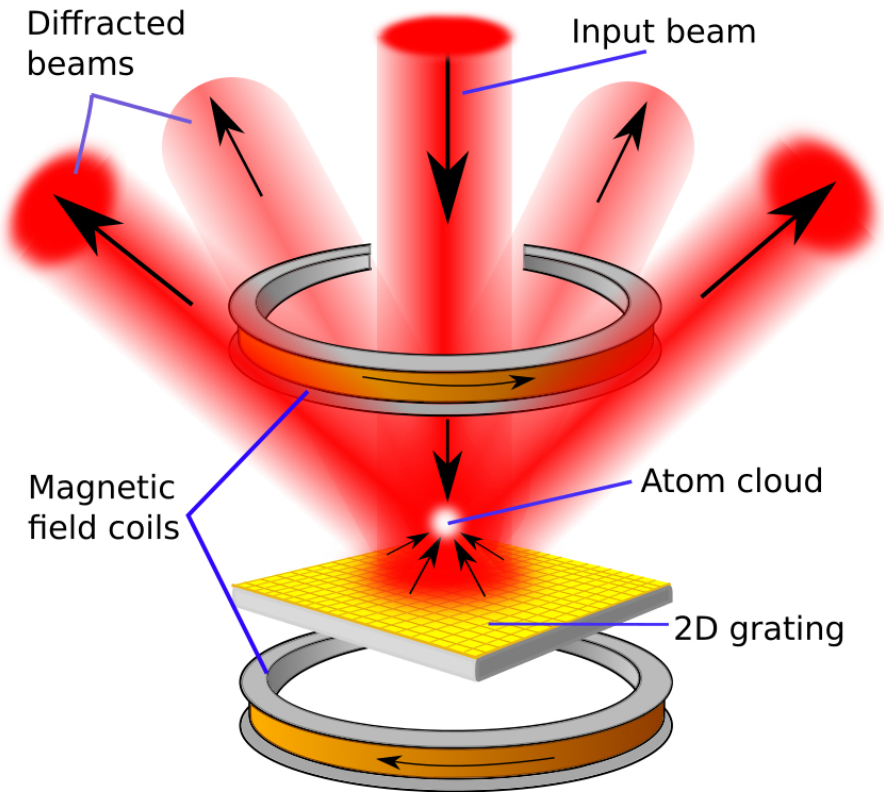

Figure 3.15: Illustration of the grating MOT[85, 86]. Image credit: Matthew Himsworth[1].

It is thought that the number of atoms captured by the GMOT would not enter the $N \propto L^6$ scaling regime until the beam diameter reduces below 2 mm[85], but the data that has been presented so far on this design only exhibits $N \propto L^{3.6}$ scaling. This is not surprising, however, as the grating traps that have been demonstrated have capture regions that have much greater volumes than those where the rapid scaling law comes into effect[86]. The scaling laws of small magneto optical traps have been analysed by G.W. Hoth *et al.*[81], who have found (as argued in section 3.5) that the $N \propto L^6$ law is exhibited by all small traps however the point at which this relationship comes into effect is dependent on how the dimensions of the trap are defined. They found that a more appropriate method to define trap dimensions would be the beam width at which point the intensity drops to that of the saturation intensity. This model fits their data rather more accurately than if the trap size is defined based on the beams' $1/e^2$ width and indicates that the scaling law enters the $N \propto L^6$ regime for beam sizes below $L = 2.3(1)$ mm and $L = 2.9(1)$ mm for detunings of $\delta = -2\Gamma$ and $\delta = -3\Gamma$ respectively.

	S	P	T	M	G
Scaling Regime Change	∼1-2 mm	∼7 mm	∼0.6 mm	-	∼2 mm
Ease of Imaging	Excellent	Poor	Good	Good	Poor
Bandwidth	None	None	None	None	100 nm
Optical Access	Poor	Excellent	Excellent	Good	Excellent
Phase Stability	Poor	Excellent	Excellent	Poor	Excellent
Fabrication Complexity	N/A	Very high	Very high	Low	High
Out of Plane Coils	No	No	No	Depends	No

Table 3.1: Comparison of the characteristics of various MOT geometries: the standard six beam MOT (S), microfabricated pyramidal MOT (P), tetrahedral MOT (T), mirror MOT (M) and the grating MOT (G). The row 'Scaling Regime Change' refers to the the size of MOT at which the atom number scaling regime changes between $N \propto L^{3.6}$ and $N \propto L^{6}$. The author is not aware of the scaling regime change being quoted in the literature for the mirror MOT, however it should be similar to that of a standard MOT.

3.6.4 Summary of MOT Geometries

In conclusion, ignoring the difficulty of fabrication, the tetrahedral MOT would be the geometry of choice for use in integrated atom chips due to its large capture volume compared to beam size, independence of the wavelength of the laser light used and relative ease of imaging due to its trapping point being located above the plane of its surface. The grating MOT is a good compromise as it has many of the benefits of the tetrahedral MOT whilst requiring a significantly less complex fabrication procedure. Microfabricated pyramidal MOTs both exhibit a poor scaling law and are difficult to manufacture so can be immediately discounted, whilst the standard mirror MOT is unsuitable due to the limited optical access provided by the prototype integrated atom chips. If this work were to be repeated the GMOT may have been chosen to be used with the initial integrated atom chips, however the author was not aware of this design early on in the project, and its cost may have been prohibitively high given the budget available at the time. Being unsatisfied with the choice of trap geometries, work began on producing a new design which did not require any complex microfabricated surfaces, but which would also be suitable in cases where optical access is restricted to a single window. This new trap is known as the SMOT.

Chapter 4

Theory of the SMOT

The idea for the Switching MOT (SMOT) was borne out of compatibility problems of existing MOT designs with the integrated atom chips we wished to prototype. The initial chip was designed for simplicity, and as a result only has a single window covering the miniature MOT chamber. This highly restricted optical access not only implied that all the trapping beams must pass through this single window, but also that none of the beams could be parallel to the plane of the mirror's surface within the chip, which itself is in a parallel plane to the capping window.

At the time of the SMOT's conception the most widely known MOT geometry compatible with our integrated atom chips was the pyramidal mirror MOT. This design has a complex fabrication procedure and also suffers from poor performance as it is scaled down to small volumes and so its adoption was discounted here. The Grating MOT (GMOT) had been unveiled in 2010, around the point when development had started on the SMOT, but the author was not aware of it at the time and so this geometry was not considered. Aside from the GMOT having a few drawbacks not seen with the SMOT, such as its wavelength dependence, grating MOTs are certainly a viable alternative for use in our integrated atom chips and as a result they are now being used here at Southampton by other group members.

The SMOT arose from an attempt to modify the standard mirror MOT (figure 3.12) so that the retro-reflected beam required in the plane of the mirror could be eliminated, hence allowing for the remaining beams to pass through a single window. It was observed that a cross-section taken through the plane occupied by these remaining beams resulted in a magnetic field that could be emulated by a pair of wires carrying currents in the same direction (figure 4.1). If the pair of wires were then to be replaced by a square loop of wire, with current passing from

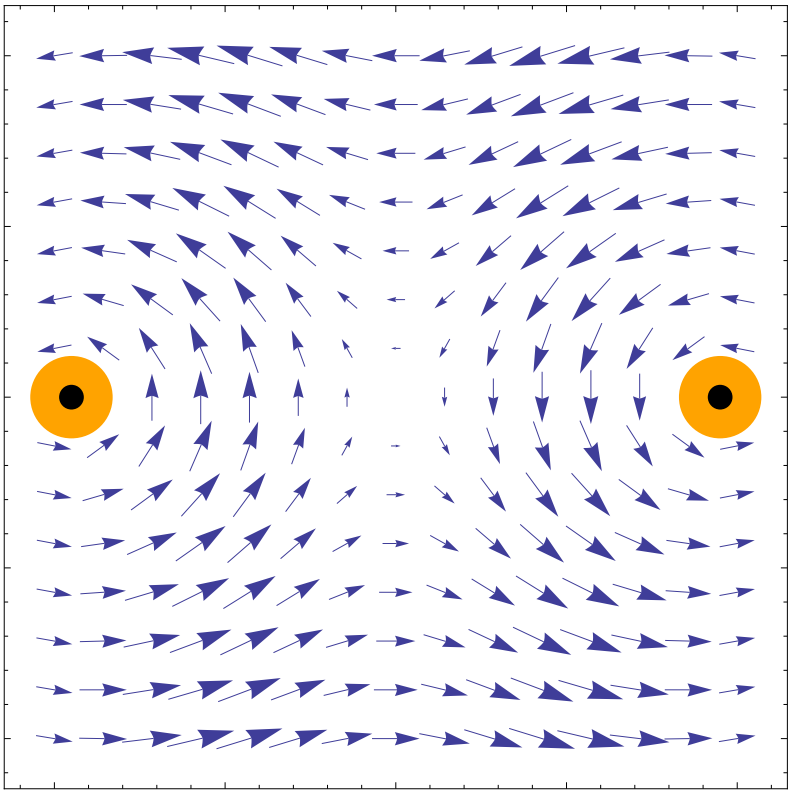

Figure 4.1: Diagram of the cross-section of a pair of current carrying wires showing the quadrupole magnetic field that they generate. Insertion of a mirror next to the magnetic field zero allows for a trapping scheme analogous to that of the mirror-MOT illustrated in figure 3.12. The dots on the wires indicate that the direction of current is out of the page.

one corner to the opposite diagonal, then there would be two orthogonal cross sections through the square which would yield the magnetic field distribution of figure 4.1. It was then argued that placing this current carrying square upon a mirror would allow trapping in three dimensions if in each plane a retro-reflected beam were to be directed to the magnetic field zero at an angle of 45° to the mirror. This 'Φ-MOT' as we called it was essentially an attempt to rotate the design of a standard mirror MOT to eliminate the troublesome beam in the mirror's plane whilst also producing a design amenable to microfabrication due to the absence of out of plane wires or coils.

After simulations of the Φ-MOT repeatedly failed to demonstrate trapping it was realized that although the magnetic fields looked as expected in the cross sections taken at the centre of the trap, those at the edge resulted in a shift in the position of the magnetic field zero. Looking at a three dimensional plot it became clear that a line of minimum magnetic field strength lay between two of the diagonals of the square, leaving the trap doomed to failure. In order to salvage this trap geometry,

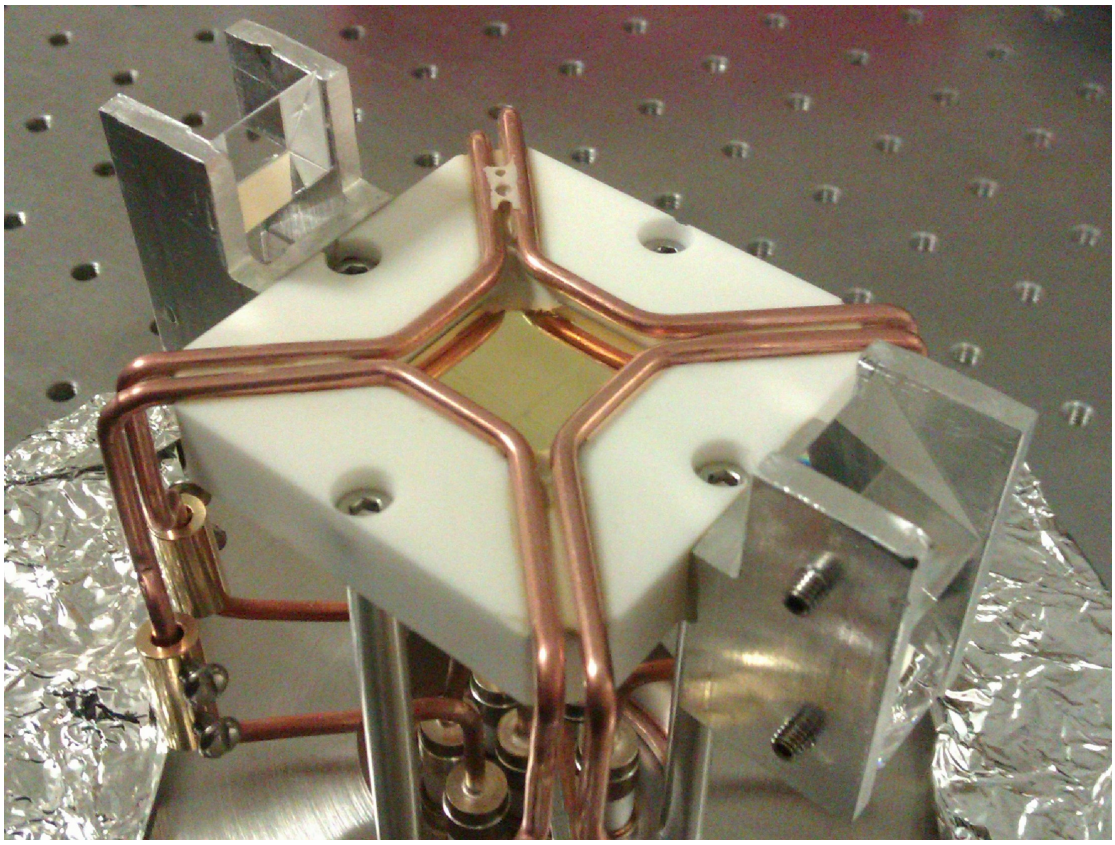

Figure 4.2: Photograph of the prototype SMOT before insertion into the vacuum chamber. Two prismatic periscopes surround the SMOT's ceramic base for use in 'Time of Flight' light sheet temperature measurements discussed in section 6.4.1. These prisms were designed to characterize the behaviour of the prototype SMOT and would not be used within an integrated atom chip.

James Bateman came up with the idea of converting the Φ-MOT into a time varying trap in a similar vein to the AC-MOT of M.Harvey and A.J.Murray[95]. This modification of the Φ-MOT later came to be named the Switching-MOT (SMOT).

The SMOT alternates between two states, each of which provides a trapping force in a two dimensional plane perpendicular to that of the mirror. These two trapping planes are orthogonal to each other meaning that, provided the states are switched quickly enough, the trapping force can be projected into three dimensions in an analogous scheme to the quadrupole ion trap.

As shown in figure 4.2, the conducting square of the Φ-MOT was replaced with two parallel pairs of wires which could be independently controlled. At any moment in time current only passes through one wire pair, whilst in the same instance only one retro-reflected beam is directed at the mirror (see figures 4.3 and 4.4). These

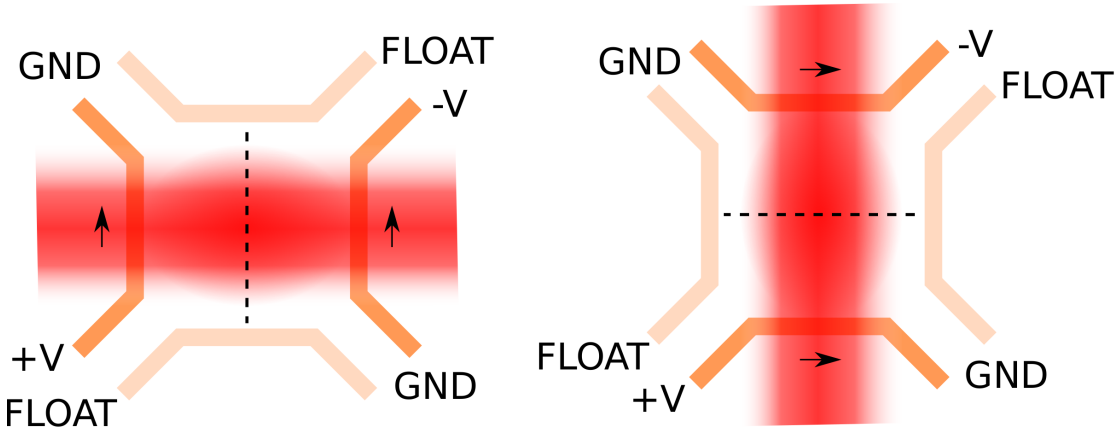

Figure 4.3: The two states of the SMOT, each of which produces a 2D trapping region indicated by the dotted lines. In each time step current only passes through one pair of wires, indicated by the arrows. At the same instant only one pair of cooling laser beams is directed at the mirror, in a direction perpendicular to that of the current. The trap rapidly oscillates between these states such that atoms cannot escape the trap and they instead form a 3D MOT at the trap's centre where the two 2D trapping regions intersect.

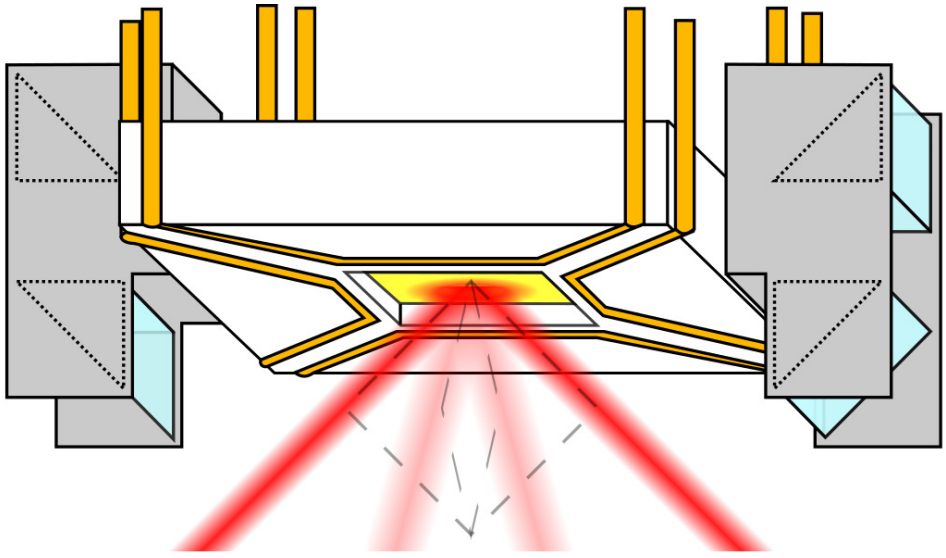

Figure 4.4: Diagram of the prototype SMOT showing the set of two retro-reflected beams, each of which are directed to the mirror at a 45° angle of incidence. All of the beams are circularly polarized, the retro-reflected beams having their handedness flipped via quarter-wave plates placed in front of their retro-reflecting mirrors. One of the beam pairs is opaque to illustrate that they are alternatively shuttered. The beams are not to scale, having been reduced in size for clarity.

act together to form a two dimensional trapping region equidistant between the wires. A short time later the optical and magnetic fields switch to the other state shown in figure 4.3 to produce a two dimensional trap equidistant between the other wire pair. If the state of the trap is switched rapidly enough then atoms will alternate between the orthogonal 2D traps to form a 3D MOT above the centre of the mirror.

4.1 The Magnetic Field Gradient of the SMOT

To calculate the currents required in the wires of the SMOT we first use Ampère's law to find the magnetic field strength at a distance r from the centre of an infinitely long wire:

$$B = \frac{\mu_0 I}{2\pi r} \tag{4.1}$$

where μ_0 is the permeability of free space and I is the current passing through the wire. If we model each wire pair of the SMOT as infinitely long wires carrying the same current and separated by a distance D on the x axis and centred around the origin then the resultant magnetic field at x is given by:

$$B(x) = \frac{\mu_0 I}{2\pi}\left[\frac{1}{\frac{D}{2}+x} - \frac{1}{\frac{D}{2}-x}\right] \tag{4.2}$$

Finally this expression can be differentiated and rearranged to obtain the relationship between the magnetic field gradient along the x axis and the current passing through the SMOT's wires.

$$I = \frac{2\pi}{\mu_0}\left[\frac{1}{\left(\frac{D}{2}+x\right)^2} + \frac{1}{\left(\frac{D}{2}-x\right)^2}\right]^{-1}\frac{\mathrm{d}B}{\mathrm{d}x} \tag{4.3}$$

from which we can determine that with our SMOT wire pairs separated by 20 mm we require 25 A to produce the typical 10 G cm^{-1} magnetic field gradient found at the centre of a standard MOT. The author instead aimed for a more achievable current of 20 A, which corresponds to a magnetic field gradient of 8 G cm^{-1}. This calculation of course has ignored end effects due to the finite length wires, so to

account for these we use the Biot-Savart law:

$$B(\mathbf{r}) = \frac{\mu_0 I}{4\pi} \int \frac{d\mathbf{l} \times \hat{\mathbf{r}}'}{|\mathbf{r}'|^2} \tag{4.4}$$

where $d\mathbf{l}$ is an infinitesimal length of wire pointing in the direction of conventional current, $\mathbf{r}$ is the vector to the point where the magnetic field is being calculated and $\mathbf{r}' = \mathbf{r} - \mathbf{l}$ is vector from the wire element to the point $\mathbf{r}$. Integrating over the finite length SMOT wires leads to the expression of the magnetic field gradient along the x axis:

$$\begin{aligned}\frac{\mathrm{d}B}{\mathrm{d}x} = \frac{\mu_0 I}{2\pi} \Bigg(& \frac{L/2}{\left(\frac{D}{2} - x\right)^2 \sqrt{\left(\frac{L}{2}\right)^2 + \left(\frac{D}{2} - x\right)^2}} + \frac{L/2}{\left[\left(\frac{L}{2}\right)^2 + \left(\frac{D}{2} - x\right)^2\right]^{3/2}} \\ & + \frac{L/2}{\left(\frac{D}{2} + x\right)^2 \sqrt{\left(\frac{L}{2}\right)^2 + \left(\frac{D}{2} + x\right)^2}} + \frac{L/2}{\left[\left(\frac{L}{2}\right)^2 + \left(\frac{D}{2} + x\right)^2\right]^{3/2}} \Bigg)\end{aligned} \tag{4.5}$$

where L corresponds to the length of the wires. Surprisingly the magnetic field gradient peaks for wires of finite length: For a wire pair with a 20 mm separation carrying 20 A, the maximum magnetic field gradient of 8.7 G cm^{-1} occurs when the wires are ∼28 mm long. The SMOT has a wire length of 20 mm and so with a driving current of 20 A the gradient is ∼8.5 G cm^{-1}.

The contribution to the magnetic field from the diagonal wire segments shown in figure 4.2 have not been explicitly included in the preceding calculations. This was because their directions were designed such that each current element $d\mathbf{l}$ would make a small enough angle to the displacement vector $\mathbf{r}'$ that the cross product terms in equation 4.4 would be small. In reality the influence of these wires is not truly negligible and so the Biot-Savart law was used to calculate the magnetic field (see figure 4.5) due to the more accurate representation of the wire geometry illustrated in figure 4.6. The corresponding field gradients were calculated to be ∼6.8 G cm^{-1}, ∼6.1 G cm^{-1} and ∼6.5 G cm^{-1} along x, z and the $z = x$ line, respectively. The validity of the different models of the SMOT's wires are compared in figure 4.7, where the corresponding gradients are plotted for a number of different directions passing through the trap centre. From now on in calculations of the SMOT's magnetic fields we only use the most accurate representation of the wires that is shown in figure 4.6.

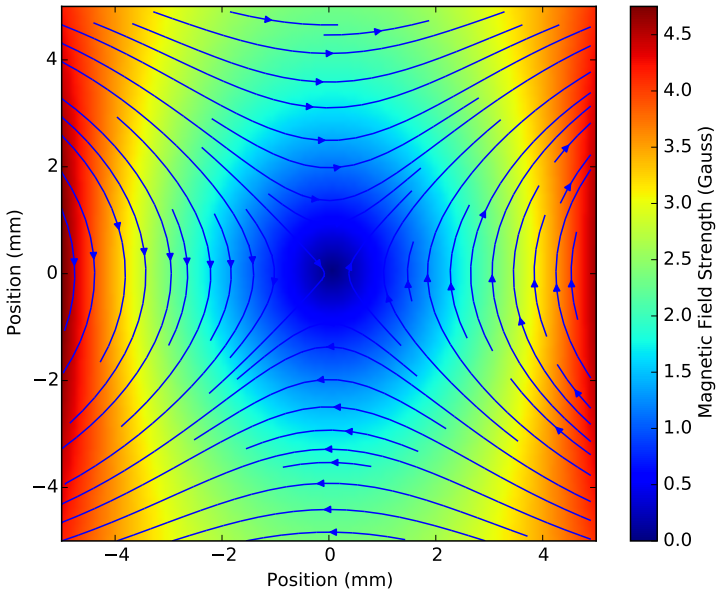

Figure 4.5: Accurate representation of the magnetic field strength in the xz-plane of the SMOT at $y = 0$, through the centre of the trap. The field was calculated via integration of the Biot-Savart law, simulating 20 A passing through the wires illustrated in figure 4.6.

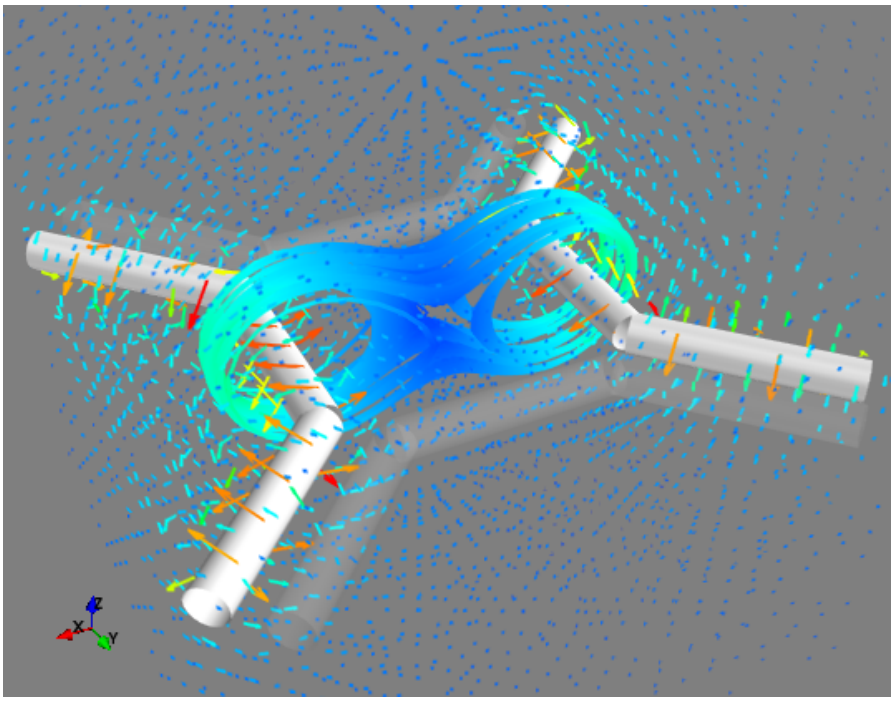

Figure 4.6: 3D plot showing the wires which were considered in order to calculate the magnetic field, and hence the forces acting upon atoms within the SMOT. A vector and streamline plot are also shown to illustrate the generated magnetic field. The opaque wires are off in this image, so do not contribute to the calculation and are only shown to indicate their location.

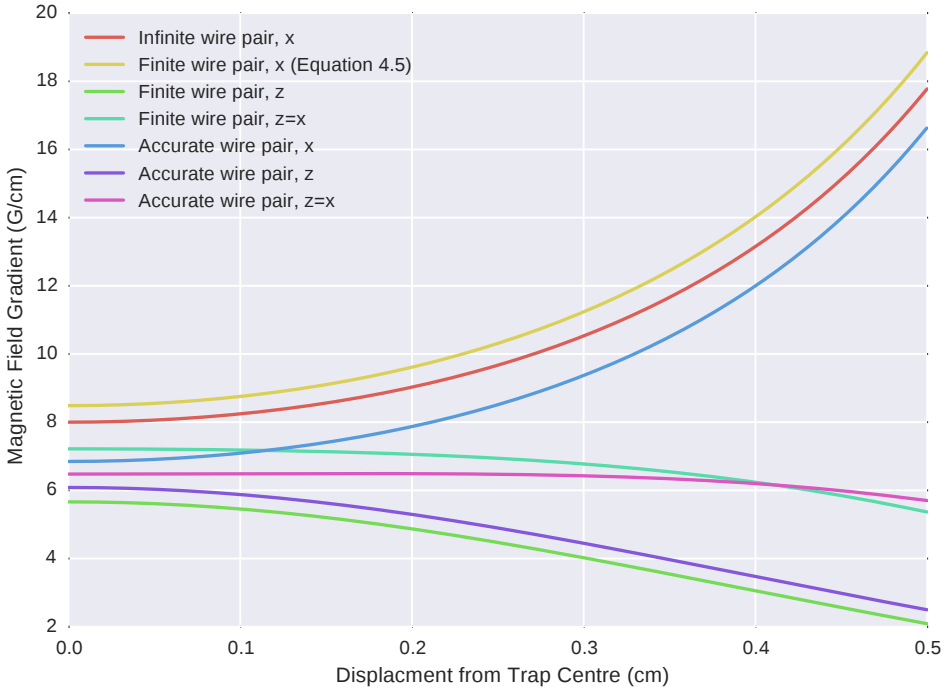

Figure 4.7: Gradient through the SMOT in the x, z and $z = x$ directions showing the accuracy of various approximations. The three models treat the SMOT wire pair as infinitely long, as 20 mm long segments or as a more accurate representation that includes the influence of the diagonal wires (illustrated in figure 4.6). In these calculations the wire pair is defined to be in the xy-plane with the currents nominally in the y direction. The simulated current through each wire is 20 A and the results were calculated via integration of the Biot-Savart law (equation 4.4).

4.2 The Need for Optical Switching

It should be apparent from the earlier discussion in this chapter why the magnetic fields need to be switched in order to produce trapping in the SMOT. The need for the optical switching is not so obvious, however, and indeed when the SMOT was conceived it was not considered necessary to achieve trapping.

To understand where this requirement originates we must first recall from equation 3.44 that in the regime of low intensity light, atoms that are stationary in a MOT experience a force from a counter-propagating pair of beams with wavevectors $\pm\mathbf{k}$ that is proportional to $\pm(\mathbf{k} \cdot \mathbf{B})\hat{\mathbf{k}}$, where $\mathbf{B}$ is the magnetic field at the atom's location and the sign is determined by the choice of beam polarization. From this we can see that in order to trap atoms within a MOT we must ensure that $\pm(\mathbf{k} \cdot \mathbf{B})\hat{\mathbf{k}}$ always points towards the trap centre, or in the case of the SMOT, that

for the beams active in each time-step this expression always points towards the corresponding centre line of zero magnetic field.

In order to make the SMOT's behaviour easier to interpret, in the following discussion the laser beams are treated as being infinitely large and of uniform intensity. Here we consider the magnetic field due to the SMOT wires modelled in the previous section, namely a pair of wires that lie in the xy-plane with the current nominally in the $+y$ direction, and the trapping region at the origin. We only need to analyse the trapping force in a single time step, as when the wires are switched the problem is identical and is merely rotated 90° around the z axis. In this scheme the cooling beams are directed to the line of magnetic field zero at a 45° angle of incidence, corresponding to the wavevectors $\mathbf{k}_{xz1} = |\mathbf{k}|(\hat{\mathbf{x}} - \hat{\mathbf{z}})/\sqrt{2}$ and $\mathbf{k}_{xz2} = |\mathbf{k}|(\hat{\mathbf{x}} + \hat{\mathbf{z}})/\sqrt{2}$ (the two retro-reflected beams are not written explicitly here). The magnetic field generated by the SMOT's wires can be roughly approximated[1] by:

$$\mathbf{B}(x, z) = G(z\hat{\mathbf{x}} + x\hat{\mathbf{z}}) \tag{4.6}$$

where G is the gradient of the field. As explained in section 3.3.1.2 the dominant force in a MOT is due to the scattering of light that excites σ_- transitions, and so the force exerted by a counterpropagating pair of beams with wavevectors $\pm\mathbf{k}_{xz1}$ is thus proportional to:

$$\begin{aligned}\mathbf{F}_{xz1} \propto \pm(\mathbf{k}_{xz1} \cdot \mathbf{B})\hat{\mathbf{k}}_{xz1} &= \pm \frac{|\mathbf{k}|}{\sqrt{2}}(\hat{\mathbf{x}} - \hat{\mathbf{z}}) \cdot G(z\hat{\mathbf{x}} + x\hat{\mathbf{z}})\hat{\mathbf{k}}_{xz1} \\ &= \pm \frac{G}{\sqrt{2}}(z - x)\mathbf{k}_{xz1}\end{aligned} \tag{4.7}$$

and similarly the dominant force due to the counter-propagating beams with wavevectors $\pm\mathbf{k}_{xz2}$ is proportional to:

$$\begin{aligned}\mathbf{F}_{xz2} \propto \mp(\mathbf{k}_{xz2} \cdot \mathbf{B})\hat{\mathbf{k}}_{xz2} &= \mp \frac{|\mathbf{k}|}{\sqrt{2}}(\hat{\mathbf{x}} + \hat{\mathbf{z}}) \cdot G(z\hat{\mathbf{x}} + x\hat{\mathbf{z}})\hat{\mathbf{k}}_{xz2} \\ &= \mp \frac{G}{\sqrt{2}}(z + x)\mathbf{k}_{xz2}\end{aligned} \tag{4.8}$$

where the signs are opposite to those of $\mathbf{F}_{xz1}$ due to the beams having opposite helicities as a result of the reflection on the SMOT's mirror. The total force due

[1] The force plots and simulations shown later in this chapter do not make this approximation, and instead use the accurate model discussed in the previous section. The simplification is used here merely to illustrate the origin of the anti-trapping that occurs in the absence of optical switching.

to all of the beams in the xz-plane is thus proportional to:

$$\begin{aligned}\mathbf{F}_{xz} = \mathbf{F}_{xz1} + \mathbf{F}_{xz2} &\propto \pm \frac{G}{\sqrt{2}}(z-x)\mathbf{k}_{xz1} \mp \frac{G}{\sqrt{2}}(z+x)\mathbf{k}_{xz2} \\ &\propto \pm \frac{G|\mathbf{k}|}{2}(z-x)(\hat{\mathbf{x}}-\hat{\mathbf{z}}) \mp \frac{G|\mathbf{k}|}{2}(z+x)(\hat{\mathbf{x}}+\hat{\mathbf{z}}) \\ &\propto \mp G|\mathbf{k}|(\mathbf{x}+\mathbf{z}) \end{aligned} \tag{4.9}$$

which with the correct choice of helicity is a restoring force in the xz-plane, and has no influence in the y axis. If we now consider the presence of a set of beams in the yz-plane corresponding to the wavevectors $\mathbf{k}_{yz1} = \frac{|\mathbf{k}|}{\sqrt{2}}(\hat{\mathbf{y}}-\hat{\mathbf{z}})$ and $\mathbf{k}_{yz2} = \frac{|\mathbf{k}|}{\sqrt{2}}(\hat{\mathbf{y}}+\hat{\mathbf{z}})$ (yet again the counter-propagating beams are not written explicitly.), then the dominant force due to σ_- transitions being excited by a pair of counter-propagating beams with wavevectors $\pm\mathbf{k}_{yz1}$ is proportional to:

$$\begin{aligned}\mathbf{F}_{yz1} \propto \pm(\mathbf{k}_{yz1}\cdot\mathbf{B})\hat{\mathbf{k}}_{yz1} &= \pm \frac{|\mathbf{k}|}{\sqrt{2}}(\hat{\mathbf{y}}-\hat{\mathbf{z}})\cdot G(z\hat{\mathbf{x}}+x\hat{\mathbf{z}})\hat{\mathbf{k}}_{yz1} \\ &= \mp \frac{G}{\sqrt{2}}x\mathbf{k}_{yz1} \end{aligned} \tag{4.10}$$

and similarly the dominant force due to the counter-propagating beams with wavevectors $\pm\mathbf{k}_{yz2}$ is proportional to:

$$\begin{aligned}\mathbf{F}_{yz2} \propto \pm(\mathbf{k}_{yz2}\cdot\mathbf{B})\hat{\mathbf{k}}_{yz2} &= \mp \frac{|\mathbf{k}|}{\sqrt{2}}(\hat{\mathbf{y}}+\hat{\mathbf{z}})\cdot G(z\hat{\mathbf{x}}+x\hat{\mathbf{z}})\hat{\mathbf{k}}_{yz2} \\ &= \mp \frac{G}{\sqrt{2}}x\mathbf{k}_{yz2} \end{aligned} \tag{4.11}$$

where once again the sign has flipped as a result of the change in helicity of the light upon reflection. The total force due to all of the beams in the yz-axis is thus proportional to:

$$\begin{aligned}\mathbf{F}_{yz} = \mathbf{F}_{yz1} + \mathbf{F}_{yz2} &\propto \mp \frac{G}{\sqrt{2}}x\mathbf{k}_{yz1} \mp \frac{G}{\sqrt{2}}x\mathbf{k}_{yz2} \\ &\propto \mp \frac{G|\mathbf{k}|}{2}x(\hat{\mathbf{y}}-\hat{\mathbf{z}}) \mp \frac{G|\mathbf{k}|}{2}x(\hat{\mathbf{y}}+\hat{\mathbf{z}}) \\ &\propto \mp G|\mathbf{k}|x\hat{\mathbf{y}} \end{aligned} \tag{4.12}$$

which provides a degree of anti-trapping regardless of the choice of helicity of the beams, and justifies the need for them to be shuttered in synchronization with

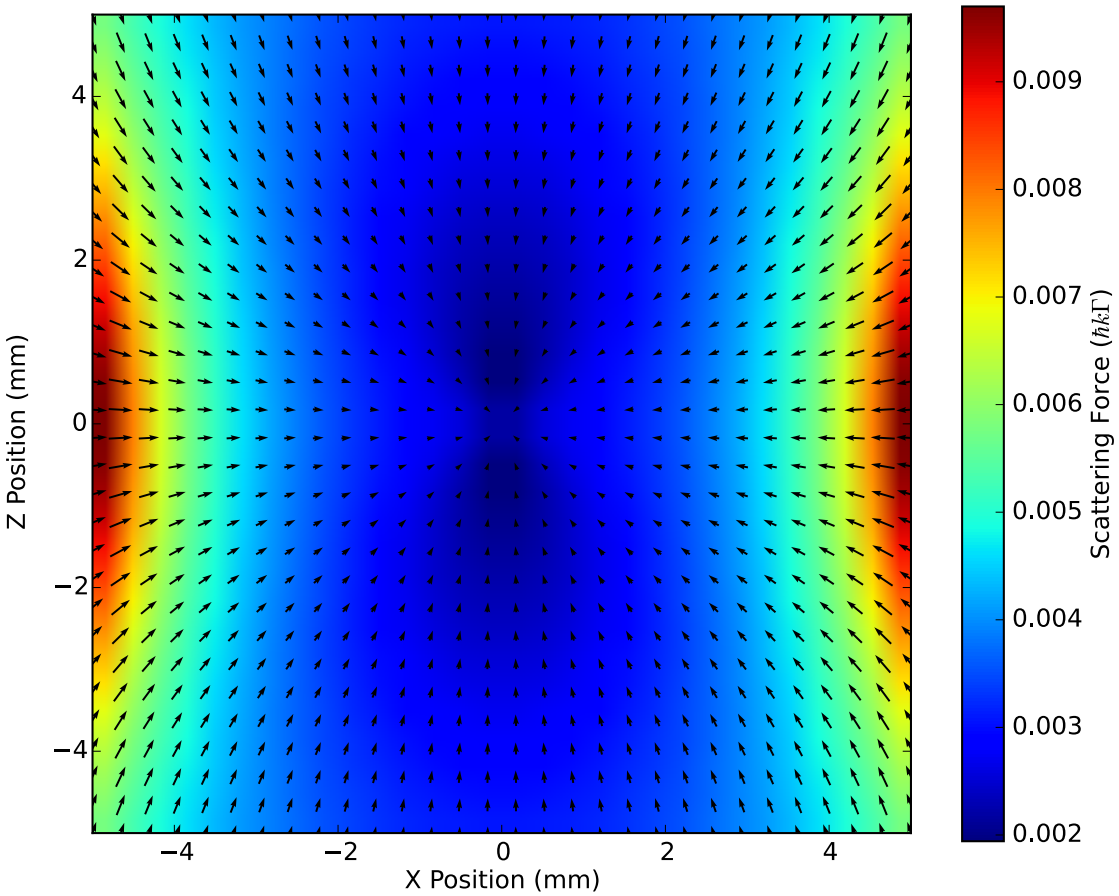

Figure 4.8: The scattering force for stationary rubidium atoms in the xz-plane of the SMOT at $y = 0.0\,\text{mm}$. The optical switching is turned off for this image, but anti-trapping is not visible because this only occurs in the y-axis (see figure 4.9). The intensity of the light is $0.2\,\text{mW}\,\text{cm}^{-2}$, the detuning is $\delta = -2\Gamma$ and the atom has assumed to have been pumped into the $5^2\text{S}_{1/2}, F = 3, m_F = -3$ sub-level.

the magnetic field switching[2]. Figure 4.9 shows a plot of the magnetic fields and corresponding scattering forces in various yz-planes at different positions along the x axis when the optical switching is turned off, with all of the beams constantly on. The plots clearly show the anti-trapping in the y-axis, which changes direction either side of the trap centre. Figure 4.8 shows the scattering force in the $y = 0$, xz-plane through the SMOT without optical switching (corresponding to the magnetic field shown in figure 4.5). No anti-trapping can be seen here though because, as shown by equation 4.12, this only occurs in the y-axis.

[2]There is some evidence to suggest that with suitable misalignment of the beams a degree of trapping can still occur in the absence of optical switching, however this has not been investigated further in this work.

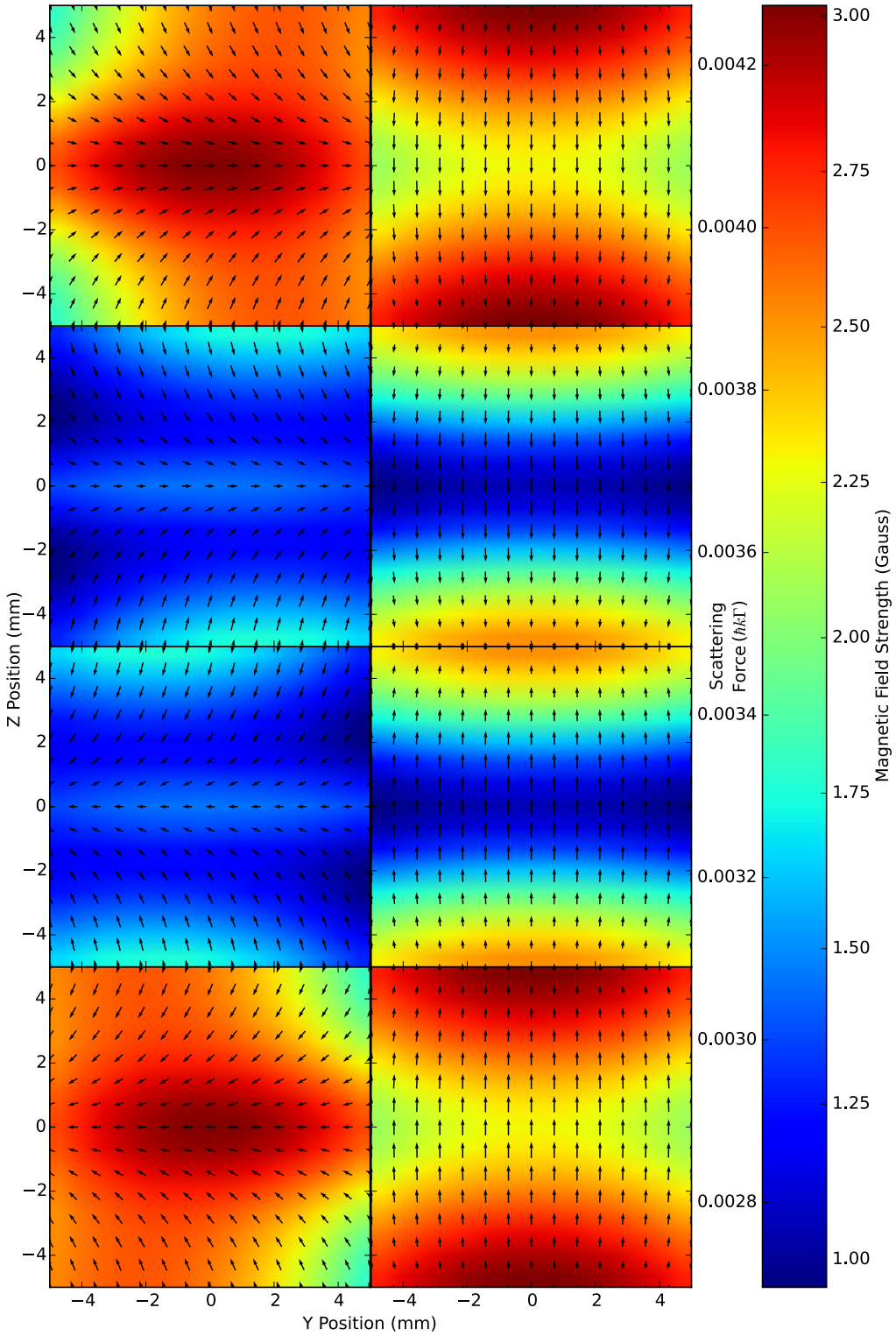

Figure 4.9: The scattering force (left images) and magnetic field (right images) for stationary rubidium atoms in yz-planes of the SMOT at $x = -3.0\,\mathrm{mm}$, $-1.5\,\mathrm{mm}$, $1.5\,\mathrm{mm}$ and $3.0\,\mathrm{mm}$ (top to bottom). The optical switching is turned off for these images, with all of the beams constantly on, hence the anti-trapping of atoms in the y axis described by equation 4.12 is clearly visible. The intensity of the light is $0.2\,\mathrm{mW\,cm^{-2}}$, the detuning is $\delta = -2\Gamma$ and the atom has assumed to have been pumped into the $5^2\mathrm{S}_{1/2}, F = 3, m_F = -3$ sub-level.

4.3 Trapping Simulations

In order to simulate the behaviour of the SMOT we use a similar procedure to that described elsewhere[79, 96] whereby the equations of motion are solved for an atom under the influence of the scattering force due to each beam. The forces exerted upon stationary atoms are clear from equations 3.43 to 3.45, but in the following simulations the atoms are moving and so this approximation cannot be made. Instead we go back to equation 3.1 to calculate the scattering rate due to each beam separately, with the detuning parameter being replaced for each beam $\delta \rightarrow \delta - \mathbf{k}_i \cdot \mathbf{v} - \mu'_j|\mathbf{B}(\mathbf{r})|/\hbar$, where the i subscripts denote the beam being considered, $|\mathbf{B}(\mathbf{r})|$ is the strength of the magnetic field at the position, $\mathbf{r}$, of the atom, and the μ'_j term determines the Zeeman energy shift of the jth transition being excited (equation 3.21). The on resonance saturation parameter, $s_{0,j}(\mathbf{k}_i, \mathbf{B}(\mathbf{r}), I_i(\mathbf{r}))$, was shown in section 3.3.1 to be dependent on the transition being excited, the projection of the polarization of the ith beam onto the direction of the atom's local magnetic field, and the intensity of this beam at that point. This means that the equations of 3.36 and equation 3.35 (or alternatively by using the values in figure 3.8) must be used to calculate this parameter at each location, and for each beam exciting each transition as an atom moves through the trap. The total force exerted upon the atom is given by:

$$\mathbf{F}_{tot} = \sum_{i,j} \mathbf{F}_{i,j} = \sum_{i,j} \frac{\hbar \mathbf{k}_i s_{0,j}(\mathbf{k}_i, \mathbf{B}(\mathbf{r}), I_i(\mathbf{r}))\Gamma/2}{1 + s_{0,j}(\mathbf{k}_i, \mathbf{B}(\mathbf{r}), I_i(\mathbf{r})) + \frac{4}{\Gamma^2}\left(\delta - \mathbf{k}_i \cdot \mathbf{v} - \frac{\mu'_j|\mathbf{B}(\mathbf{r})|}{\hbar}\right)^2} \tag{4.13}$$

where we have assumed that the scattering forces are small enough that the influence of each beam can be treated separately. The beams are also assumed to be perfectly collimated so that there is no spatial dependence of the direction of each beam's wavevectors, although this can be included in the model if need be. As before, in the following calculations we have assumed that the atom has been pumped into the $5^2S_{1/2}, F = 3, m_F = -3$ sub-level, but this model can be applied equally well without this assumption, and this is the approach others have taken[79, 96],where the levels are assumed to be equally populated and so the total scattering force is calculated by summing over all possible transitions.

In order to simulate the SMOT the `odeint` function from the SciPy Python library was used to numerically solve the equations of motion for a rubidium 85 atom experiencing the force of equation 4.13. The beams are simulated as being perfectly

collimated, as being Gaussian with radii of 4 mm, and as having the wavevectors:

$$\mathbf{k}_1 = \frac{|k|}{\sqrt{2}}(\hat{\mathbf{x}} - \hat{\mathbf{z}}), \mathbf{k}_2 = -\frac{|k|}{\sqrt{2}}(\hat{\mathbf{x}} - \hat{\mathbf{z}}), \mathbf{k}_3 = \frac{|k|}{\sqrt{2}}(\hat{\mathbf{x}} + \hat{\mathbf{z}}), \mathbf{k}_4 = -\frac{|k|}{\sqrt{2}}(\hat{\mathbf{x}} + \hat{\mathbf{z}})$$
$$\mathbf{k}_5 = \frac{|k|}{\sqrt{2}}(\hat{\mathbf{y}} - \hat{\mathbf{z}}), \mathbf{k}_6 = -\frac{|k|}{\sqrt{2}}(\hat{\mathbf{y}} - \hat{\mathbf{z}}), \mathbf{k}_7 = \frac{|k|}{\sqrt{2}}(\hat{\mathbf{y}} + \hat{\mathbf{z}}), \mathbf{k}_8 = -\frac{|k|}{\sqrt{2}}(\hat{\mathbf{y}} + \hat{\mathbf{z}}) \tag{4.14}$$

where the magnitude of each wavevector is equal. When optical switching is enabled only four of these beams are on (i.e. considered in the summation of equation 4.13) at any time step. The first four beams are on when current passes through the SMOT wires in the y axis, whilst the remaining four are only active when the current passes through the wires in the x axis.

As discussed in section 3.4.1, an atom within a MOT undergoes a random walk in momentum space due to the stochastic nature of the scattering events that it experiences. This effect could be approximated in the simulations by adding a vector to the atom's momentum with a random direction and of magnitude $\sqrt{R\Delta t\hbar/k}$, where R is the total scattering rate due to all of the beams and Δt is the simulation's time step. This would not, however, account for the diffusion in position space that also occurs during these steps. In these simulations the random walk in momentum and position space has not been included because the random nature of the walks may prevent a solution from converging, but also because the `odeint` function uses a variable step size and does not expose this value to the user.

Figure 4.10 shows the simulated path of two atoms moving in the SMOT starting with the same position and velocity, however the blue trace is the path taken when optical switching is enabled, and the green one is when all of the beams are left on. The plot shows that optical switching reduces the strength of the velocity dependent force, however it greatly enhances the trapping, without which the atoms are attracted to the line[3] $y = -x$. The atom still experiences a central force, however it is so weak that the atom moves towards the trap centre at a rate far below the RMS velocity expected of an atom at the Doppler temperature, and so the SMOT is not a reliable trap with the optical switching deactivated.

[3]This line becomes $y = x$ upon flipping the polarization of the beams in one plane along with the current direction of the corresponding wire pair.

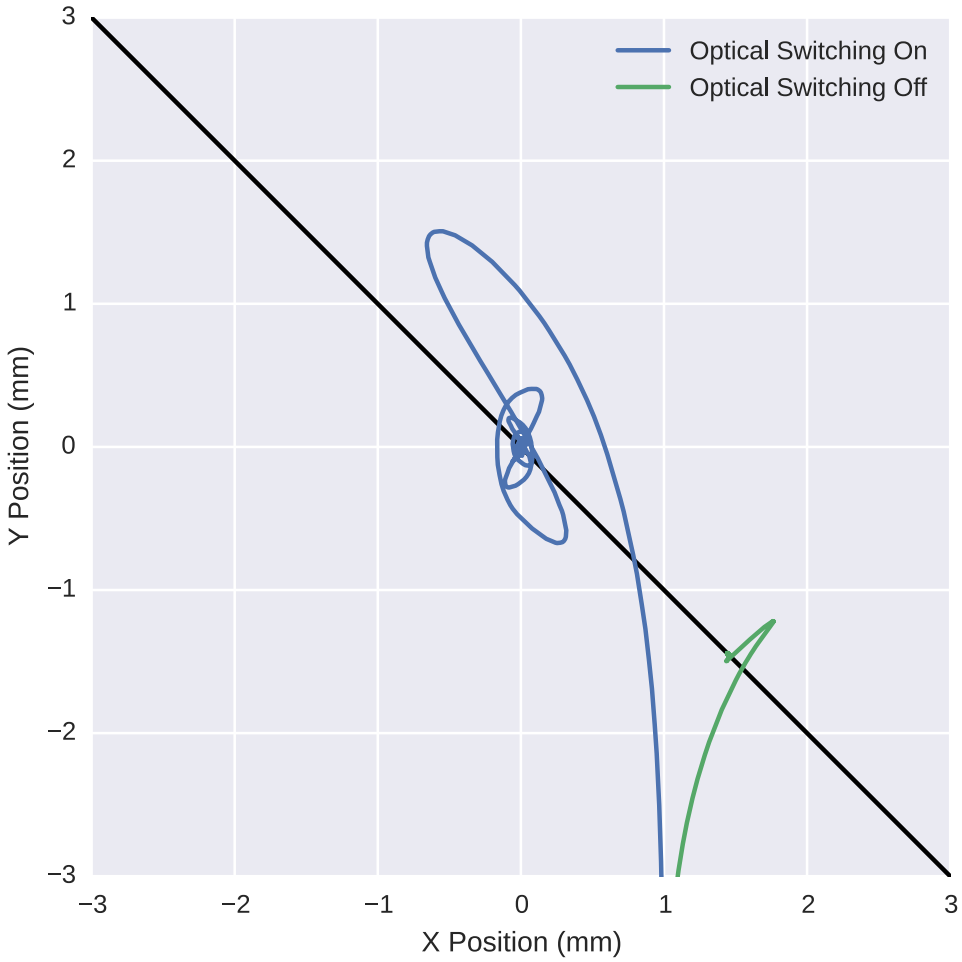

Figure 4.10: Two rubidium 85 atoms moving in the SMOT with the same initial conditions, however one trace shows the optical switching enabled whilst the other is with all of the beams constantly on. The atom experiences a greater velocity dependent force with the optical switching turned on, however instead of rapidly approaching the trap centre (the origin), it settles around the black line of $y = -x$. This atom still approaches the trap centre, however it does so at a velocity of $1.7\,\mathrm{mm\,s^{-1}}$, significantly lower than the RMS velocity at the Doppler temperature ($v = 207\,\mathrm{mm\,s^{-1}}$). The switching frequency in this simulation was 10 kHz, the SMOT wires carried a current of 20 A, the beams had Gaussian radii of 4 mm, a peak intensity of $2.0\,\mathrm{mW\,cm^{-2}}$ and a detuning of $\delta = -2\Gamma$. The simulation time was 30 ms, the atoms were initially placed at $\mathbf{x} = (1\hat{\mathbf{x}}\text{-}9\hat{\mathbf{y}}\text{-}9\hat{\mathbf{z}})\mathrm{mm}$ and had an initial velocity of $\mathbf{v} = (0.8\hat{\mathbf{y}}{+}0.8\hat{\mathbf{z}})\mathrm{m\,s^{-1}}$.

Chapter 5

Laser Stabilization

In chapter 3 it was explained that both laser cooling and magneto optical trapping require red detuned laser light however there was no mention of how this light is produced nor the frequency stability that it must have. The light of continuous wave lasers may naïvely be thought of as being monochromatic but in reality even the light from a laser operating with a single longitudinal mode has a finite linewidth. The temperatures and radii of atomic clouds produced by magneto optical traps have been shown to be dependent on the magnitude of this linewidth[97], but for our purposes we merely require that our lasers have a well defined detuning and as a result a linewidth that is smaller than the natural linewidth of the cooling transition.

With the advent of the compact disc writer relatively high power 785 nm laser diodes have become widespread and inexpensive. These emit light with a centre frequency that is conveniently only 5 nm away from that resonant with rubidium. This is within their region of tunability, and so these laser diodes provide a source of coherent light for atomic physics experiments that previously would require the use of expensive tunable dye lasers[98]. Laser diodes, however, have linewidths which are relatively broad, on the order of tens to hundreds of megahertz, compared to the natural linewidth of rubidium ($\Gamma \sim 2\pi \cdot 6.07\,\mathrm{MHz}$ for the cooling transition of ^{85}Rb) and so are often placed inside an external cavity with frequency selective feedback to both narrow their linewidths and to provide additional frequency tunability and stabilization.

The External Cavity Diode Lasers (ECDL) used in this project were designed by Tim Freegarde here at the University of Southampton based upon earlier work by A.Arnold *et al.*[99]. These ECDLs have evolved through several iterations,

but at their core they are essentially the same device providing coarse frequency adjustment through current and temperature control, the latter afforded through the use of a thermoelectric element placed close to the laser diode package, and fine tunability and linewidth reduction by feeding back the first order reflection from a holographic diffraction grating mounted upon a piezoelectric actuator in the Littrow configuration.

Matthew Himsworth has provided greater construction details in addition to extensive characterization of these devices in his doctoral thesis, but for the purposes of this work the Southampton ECDLs provide laser light whose frequency can be controlled on long time scales by adjusting the voltage applied to the piezo that is attached to the grating and on short time scales by the modulation of the current passing through the laser diode.

Laser stabilization is then performed by placing the ECDL in a feedback loop, where an error signal, typically derived from the laser passing through a spectroscopic reference, provides a voltage which is proportional to the error of its output frequency. This signal is then fed to a Proportional Integral Derivative (PID) controller which adjusts the laser diode current and piezo voltage such that the laser frequency changes in an effort to minimize the value of the error signal. For the majority of this project, the PID servo was an analog circuit designed and built by M.Himsworth, but prior to its arrival a Proportional-Integral (PI) controller circuit was designed around an 'Arduino'-like microcontroller based prototyping platform. This circuit, detailed further in appendix E, succeeded in locking to an error signal that was provided by Zeeman Modulation Spectroscopy (see section 5.2) achieving an approximate linewidth of 1.3 MHz.

The remainder of this chapter is mainly directed towards the various approaches the author used to generate the error signals, but first one of the more common methods is outlined, that of Frequency Modulation Spectroscopy.

5.1 Frequency Modulation Spectroscopy

One of the simplest techniques to generate an error signal for laser frequency stabilization is frequency modulation. In this method the laser frequency is modulated, typically by adding an AC component to the laser diode current or through the use of an electro-optic modulator and, as seen by the Jacobi-Anger expansion, generates a pair of sidebands separated from the carrier by the modulation frequency.

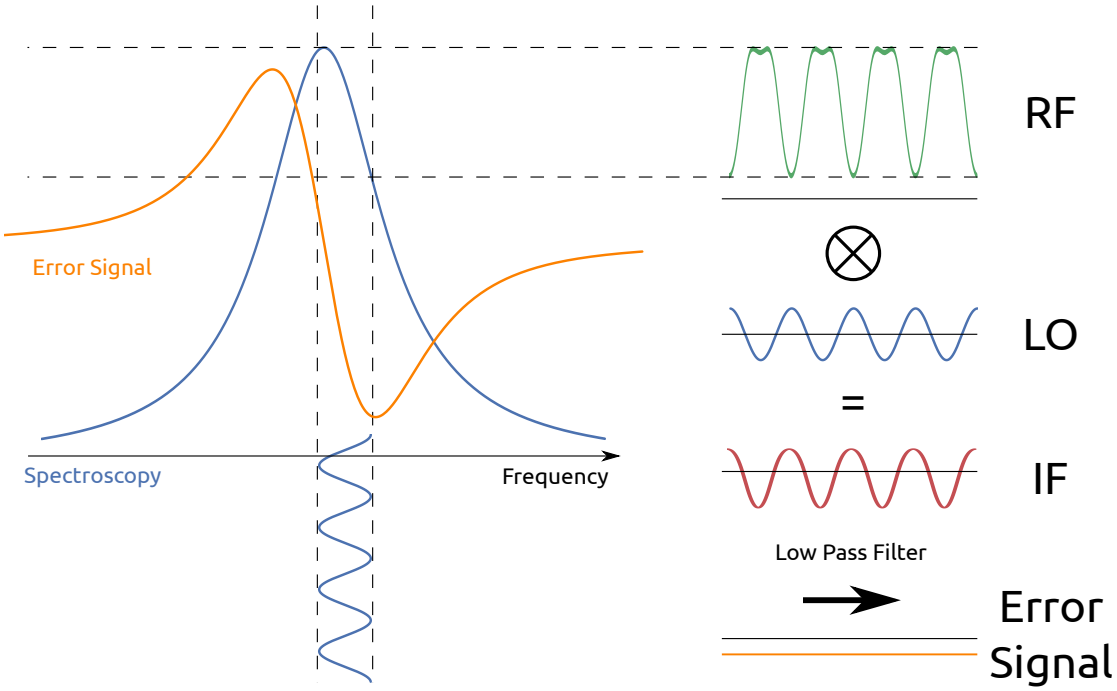

Figure 5.1: The demodulation process in frequency modulation spectroscopy. A laser is swept across a spectroscopic feature while its frequency is dithered at a much greater modulation frequency. The change in absorption of the laser as it is dithered is measured by a photodiode, and this Radio Frequency (RF) signal is multiplied by a Local Oscillator (LO) at the modulation frequency with a 'mixer' to generate an Intermediate Frequency (IF). This IF signal is then fed through a low pass filter to extract the DC level which represents the error signal. The laser can also be viewed in the frequency domain as a carrier with sidebands that are separated from it by the modulation frequency and the imbalance of the absorption of the sidebands causes the generation of the RF signal as they beat with the carrier.

The modulated beam passes through a spectroscopic reference vapour cell and due to an imbalance in the absorption of the sidebands a beat signal is generated between them and the carrier. This beat signal is measured with a photodiode and mixed with a local oscillator at the modulation frequency to produce a signal which is the derivative of the spectroscopic reference. As the resulting voltage is the derivative of the atomic spectrum, locking a laser to a zero crossing of the signal results in it being stabilized to a stationary point of an atomic feature, such as the peak of a transition.

In the regime of low modulation frequency this technique is known as wavelength modulation spectroscopy and, as shown in figure 5.1, can be viewed as the laser frequency being dithered across the spectroscopic feature to create a periodic change in the absorption at the modulation frequency. The phase of the absorption signal

is determined by which side of the spectroscopic feature the centre frequency of the laser sits, and this phase relationship determines the sign of the error signal after it is demodulated.

5.2 Zeeman Modulation

The first method that was employed here to generate an error signal for laser locking was Zeeman modulation (see figure 5.2). The principle of this technique is similar to that of frequency modulation however instead of modulating the laser frequency, a modulating magnetic field is applied to the reference vapour cell so that, due to the Zeeman effect, the spectroscopic sample is swept across resonance with the laser. This technique is particularly favourable over frequency modulation because it avoids the increase in laser frequency noise that results from the dithering of the laser diode current[100, 101].

In order to achieve this modulation a 'secondary' coil was wrapped around a rubidium vapour cell and placed in series with a capacitor forming a closed loop. This forms the tank of a resonant LC circuit into which energy can be coupled

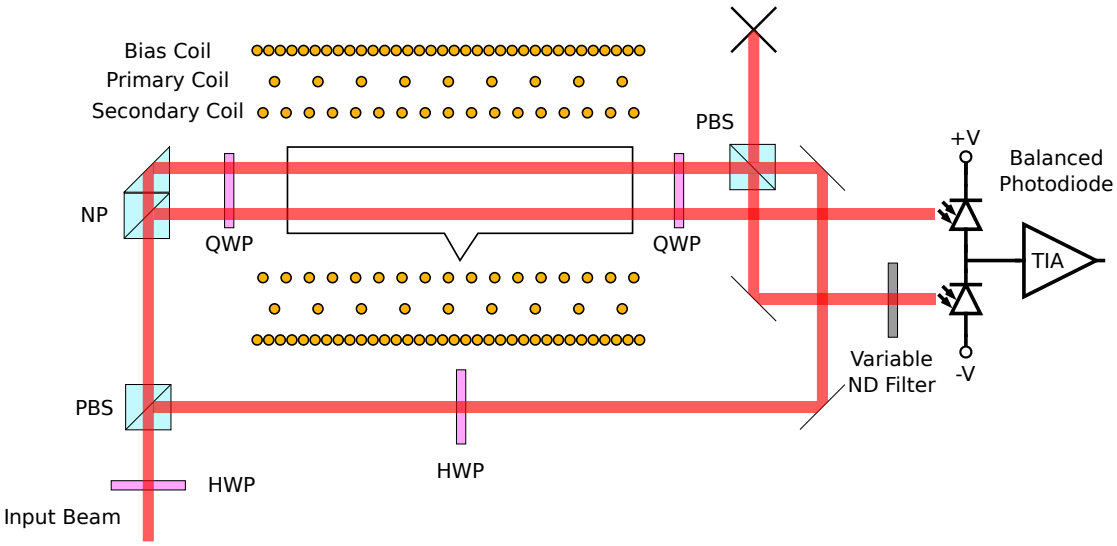

Figure 5.2: Schematic of the Zeeman modulation setup. Two probe beams pass through a vapour cell that has its resonant frequencies both detuned and modulated via a series of Zeeman shifting coils. The first probe beam detects the hyperfine structure of the vapour by counter-propagating with a saturating pump beam. The second probe merely measures the Doppler broadened background so that it can be subtracted from the first probe with a balanced photodiode. All of the beams are circularly polarized so that they only probe the transitions that experience negative energy shifts.

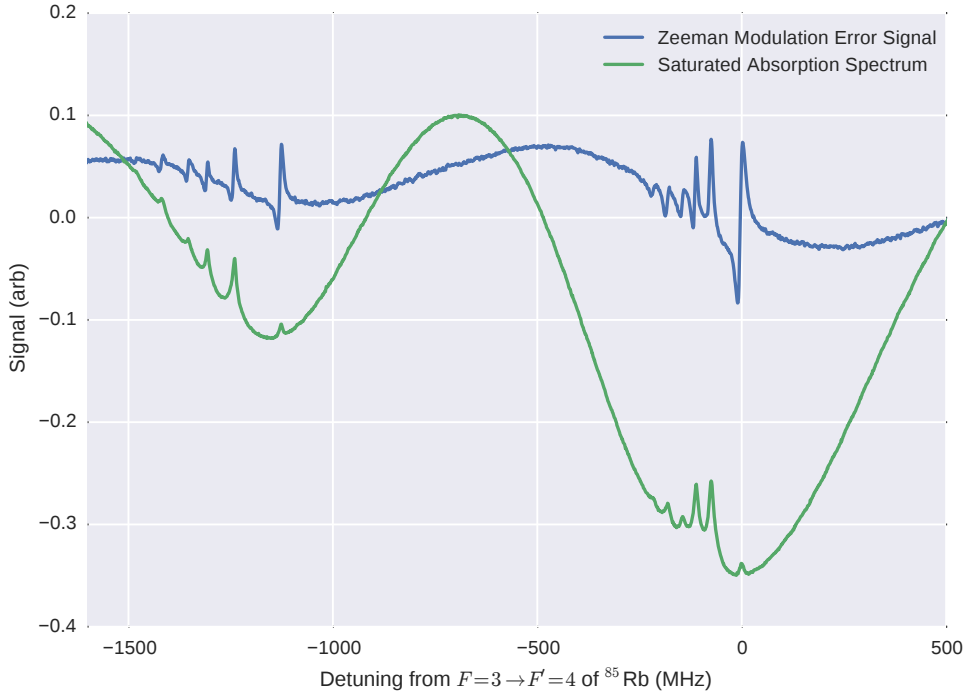

Figure 5.3: The error signal of rubidium generated using Zeeman modulation with a saturated absorption signal shown for reference. The frequency is listed relative to the $F = 3 \rightarrow F' = 4$ transition of ^{85}Rb. The modulation frequency was approximately 520 kHz.

from the oscillating magnetic field of a 'primary' coil. The primary coil is wrapped around the secondary on the cell, but the number of turns differs between the coils so that together they act as a transformer to step-up from the current that is applied to the primary.

A signal generator was then attached to the primary in series with an impedance matching resistor. The signal generator was not capable of supplying a large enough current to Zeeman modulate the vapour cell directly, hence the need for the transformer and resonant circuit in the design.

The laser was split into three beams: a pump and probe beam which counter-propagated through the vapour cell in the typical Doppler-free spectroscopy configuration. The third beam was used as a background reference which was subtracted from the probe beam by a balanced photodetector (Thorlabs PDB210A/M). In practice the background removal seemed to reduce the signal to noise ratio of the error signal so as shown in figure 5.3 it was rarely used.

A third, 'offset', coil was also wrapped around the vapour cell to provide a DC

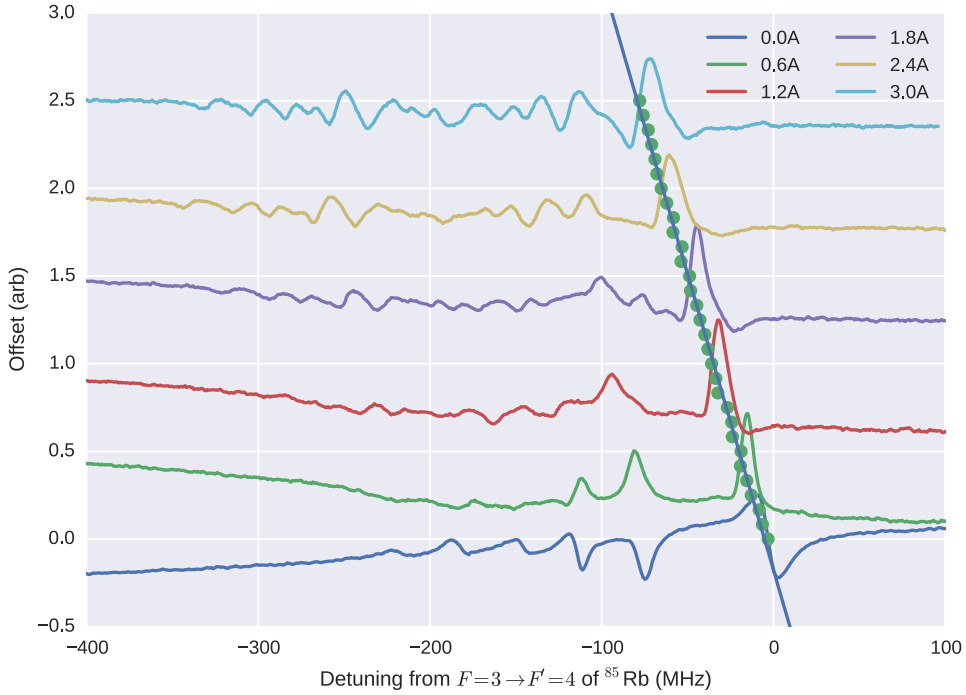

Figure 5.4: Detuning of Zeeman modulation error signal with respect to the $F = 3 \rightarrow F' = 4$ transition of ^{85}Rb due to the application of a current in the offset coil. The data was taken with a modulation frequency of $\approx 520\,\text{kHz}$ and the traces plotted are offset from each other by a value of 0.5 to aid readability. The blue line is a fit to the zero crossings, and corresponds to a detuning of $-24.7\,\text{MHz}\,\text{A}^{-1}$. The green circles represent all the zero-crossing data that was used to create the line of best fit.

magnetic field in addition to the RF fields oscillating in the transformer coils. This DC coil enabled the red detuning of the cooling laser required for optical cooling. Figure 5.4 shows how the error signal for the cooling transition of rubidium 85 shifts as the current in the bias coil is varied. Changing the bias coil current alters the DC level of the error signal, so in plotting figure 5.4 the individual traces have been offset so there is a zero crossing at the centre of each slope corresponding to the cooling transition.

The offset coil had approximately 140 turns of 0.71 mm diameter enamelled wire which was measured with a hall probe to have a field of about $15.5\,\text{G}\,\text{A}^{-1}$, yielding an expected shift of the $|F = 3, m_F = -3\rangle \rightarrow |F' = 4, m_F = -4\rangle$ transition of ^{85}Rb of $(m_{F_e} g_{F_e} - m_{F_g} g_{F_g})\mu_B B = -21.7\,\text{MHz}\,\text{A}^{-1}$. A fit of the zero crossings in figure 5.4 gives a figure of $-24.7\,\text{MHz}\,\text{A}^{-1}$, which is fairly close to the expected value.

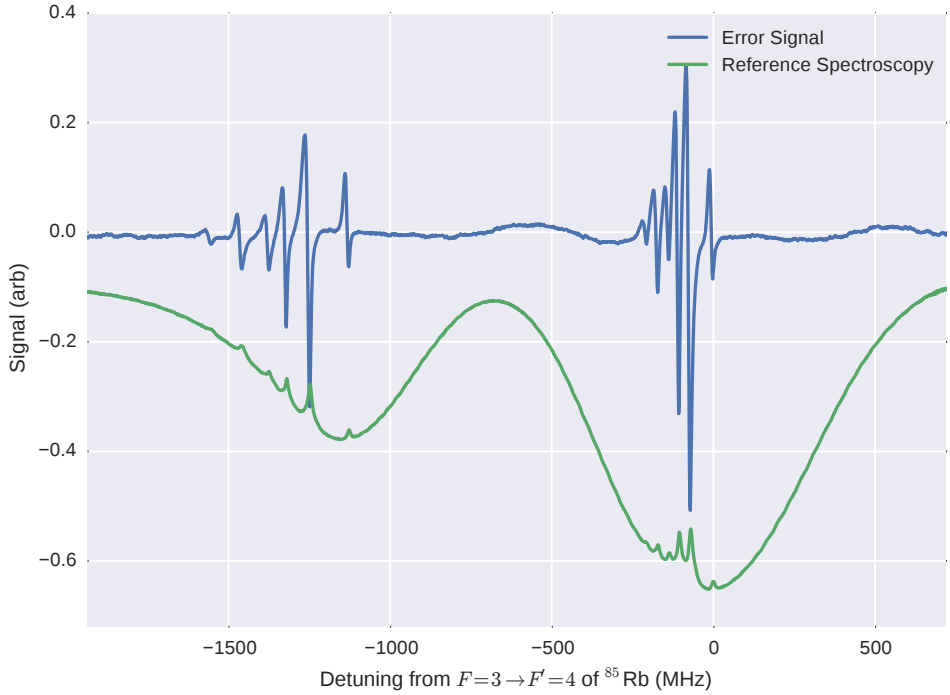

Figure 5.5: Illustration of the background noise within the laboratory. This figure shows a rather good example of an error signal and reference spectroscopy of ^{85}Rb, however it was measured with the signal generator turned off, the coil removed from the vapour cell and even with the local oscillator disconnected from the frequency mixer. Although this signal appears to be of a high quality with low background noise, it was caused by noise being picked up in the piezo sweep circuit and acted to distort the 'true' error signal generated by Zeeman modulation. The strength of this false error signal was proportional to the sweep amplitude and so was impossible to lock to. As a result, the signal was removed by the insertion of a 0.07 MHz high pass filter on the RF input of the frequency mixer.

A surprising issue emerged whilst using the Zeeman modulation technique whereby electrical noise that was picked up by the piezo sweep circuit impressed a modulation to the laser frequency. This noise was also picked up by the frequency mixer, even with its local oscillator port disconnected, and so produced the error signal shown in figure 5.5. Initially it was thought that the noise was being coupled to the Zeeman modulation coils, however the issue still persisted even when they were removed. Ironically this unintentional signal was stronger than that created by the Zeeman modulation technique, however it was impossible to lock to because its strength was found to be proportional to the piezo sweep amplitude. This superfluous signal thus only served to distort the true error signal from the Zeeman modulation, and so was eliminated by the insertion of a 0.07 MHz high

pass filter on the RF input of the frequency mixer.

Ultimately there were a number of problems with the Zeeman modulation technique which led to it being abandoned. The modulating coil served to act as an antenna which radiated noise into other equipment in the laboratory. Similarly, radiating magnetic fields from other devices in the laboratory were picked up by the modulation coils and added noise to the error signal. The shifting DC level of the error signal made it very difficult to accurately adjust the detuning of the laser whilst maintaining an atom cloud within the MOT, and finally the switching schemes of the SMOT explained in section 6.1 were much more suitably combined with Modulation Transfer Spectroscopy.

5.3 Modulation Transfer Spectroscopy

Modulation Transfer Spectroscopy (MTS) is a pump-probe spectroscopic technique that utilizes a modulated pump beam and unmodulated probe beam to produce an error signal with which to lock a laser. The main advantage of MTS over other techniques is that in the absence of Residual Amplitude Modulation (RAM), there are no spectroscopic features except around closed transitions. This means that locking to the cooling transitions[1] of either ^{85}Rb or ^{87}Rb is made extremely easy, as their zero crossings are the only two features that appear and, in addition, balanced photodetection is not needed to subtract the background signal, as it is absent in this technique by its very nature.

The usual approach to produce the modulated pump beam of modulation transfer spectroscopy is to employ the use of an Electro-Optic Modulator (EOM). An EOM is a device that drives a low frequency electric field across a crystal that exhibits the Pockels effect, a linear shift of refractive index in response to an applied electric field, in order to induce a time varying refractive index that manifests itself upon a beam passing through the crystal in the form of a phase modulation. This phase modulation in turn can be viewed in the frequency domain as a carrier beam of frequency equal to the unmodulated light with successive side bands either side of the carrier separated by the modulation frequency ω_{mod}. Due to budgetary constraints an EOM was not available for use in the spectroscopic experiment, however as a result of a change in the optical shuttering scheme detailed in section

[1] Of course, we actually require light that is red detuned from a cooling transition, but this is imposed by the difference in the centre frequencies of the MTS AOM discussed in this section and the switching AOMs in section 6.1.1.

6.1 an Acousto Optic Modulator (AOM) had become available to be used in its place.

An AOM is a device that uses a piezoelectric transducer to generate sound waves in a transparent crystal that results in a periodic variation in its refractive index. These sound waves hence act as a grating for light that passes through the crystal and as a result produce a number of diffracted beams, the order of each depending on the number of phonon-photon interactions that occur. There are two types of AOMs available: those whose crystals have parallel faces in order to create standing sound waves and those whose crystal faces are angled allowing light to only interact with travelling sound waves. Both types of AOM produce deflected beams however standing wave AOMs are more complex in that each spatially separated beam that it produces (including the undiffracted order) contains multiple frequency components. Here we only use travelling wave AOMs which output light of a single frequency $\omega = \omega_0 + m\omega_{AOM}$ for each diffracted order m, where ω_{AOM} is the operating frequency of the AOM and ω_0 is the frequency of the light going into the AOM. The deflection angle also depends on these parameters in addition to the speed of sound in the crystal, but the precise angle is not important for this discussion. In order to use an AOM to modulate the pump beam for modulation transfer spectroscopy we can dither the frequency applied to it so that the diffracted beams it produces obtain sidebands analogous to those that an EOM generates due to phase modulation.

If we apply a frequency modulated signal to the AOM of $\omega_{AOM} = \omega_{AOM_0} + \Delta\omega \cos(\omega_{mod} t)$, where ω_{mod} is the modulation frequency, ω_{AOM_0} is the centre frequency of the AOM and $\Delta\omega$ is the maximum frequency deviation from the centre frequency, then this modulation will be imposed upon the various diffracted beams to give light of instantaneous frequency of $\omega(t) = \omega_0 + m\left(\omega_{AOM_0} + \Delta\omega \cos(\omega_{mod} t)\right)$, which we can see gives rise to side-bands on the beam:

The instantaneous frequency is related to the phase by the relationship:

$$\frac{d\phi}{dt} = \omega(t) \tag{5.1}$$

which can be integrated to find:

$$\begin{aligned}\phi &= \int_0^t \omega(t')dt' = \int_0^t \left[\omega_0 + m\left(\omega_{AOM_0} + \Delta\omega\cos\left(\omega_{mod}t'\right)\right)\right]dt' \\ &= \left[\omega_0 + m\omega_{AOM_0}\right]t + \int_0^t m\Delta\omega\cos\left(\omega_{mod}t'\right)dt' \\ &= \left[\omega_0 + m\omega_{AOM_0}\right]t + \frac{m\Delta\omega}{\omega_{mod}}\sin\left(\omega_{mod}t\right) \end{aligned} \tag{5.2}$$

Thus the input beam of form $E(t) = E_0 e^{i\omega_0 t}$ is modulated to become:

$$\begin{aligned}E_{mod}(t) &= E_0 e^{i\left(\omega_0 t + m\left(\omega_{AOM_0}t + \frac{\Delta\omega}{\omega_{mod}}\sin(\omega_{mod}t)\right)\right)} \\ E_{mod}(t) &= E_0 e^{i\left(\omega_0 + m\omega_{AOM_0}\right)t} e^{i\frac{m\Delta\omega}{\omega_{mod}}\sin(\omega_{mod}t)}\end{aligned} \tag{5.3}$$

Using the Jacobi-Anger identity:

$$e^{iz\sin\theta} = \sum_{n=-\infty}^{\infty} J_n(z)\, e^{in\theta} \tag{5.4}$$

where $J_n(z)$ corresponds to Bessel functions of the first kind. We can see that:

$$\begin{aligned}E_{mod}(t) &= E_0 e^{i\left(\omega_0 + m\omega_{AOM_0}\right)t} \sum_{n=-\infty}^{\infty} J_n\left(\frac{m\Delta\omega}{\omega_{mod}}\right) e^{in\omega_{mod}t} \\ E_{mod}(t) &= \sum_{n=-\infty}^{\infty} E_0 J_n\left(\frac{m\Delta\omega}{\omega_{mod}}\right) e^{i\left(\omega_0 + m\omega_{AOM_0} + n\omega_{mod}\right)t}\end{aligned} \tag{5.5}$$

In this experiment only the first diffracted order is used, so we can set $m = 1$, thus we find that our probe beam is composed of a carrier of frequency $\omega_0 + \omega_{AOM_0}$, plus successive side-bands either side of the carrier separated by frequency ω_{mod}. This is now similar to the modulation achieved via an EOM, except the side-bands are spatially separated from the carrier due to the frequency dependent scattering angle of the AOM, and the centre frequency is shifted by an amount equal to the average frequency applied to the AOM. To generate an error signal with MTS we require that our side bands are co-propagating with the carrier so that upon reaching the vapour cell the pump carrier, probe carrier and pump sideband interact together through the non-linearity of the vapour[2] in a process which has been attributed to four wave mixing[102, 103]. To recombine the spatially separated orders they are retro-reflected back through the AOM in the double pass configuration, again taking the first order diffraction that it scatters. Because the

[2]This process is modelled in appendix D

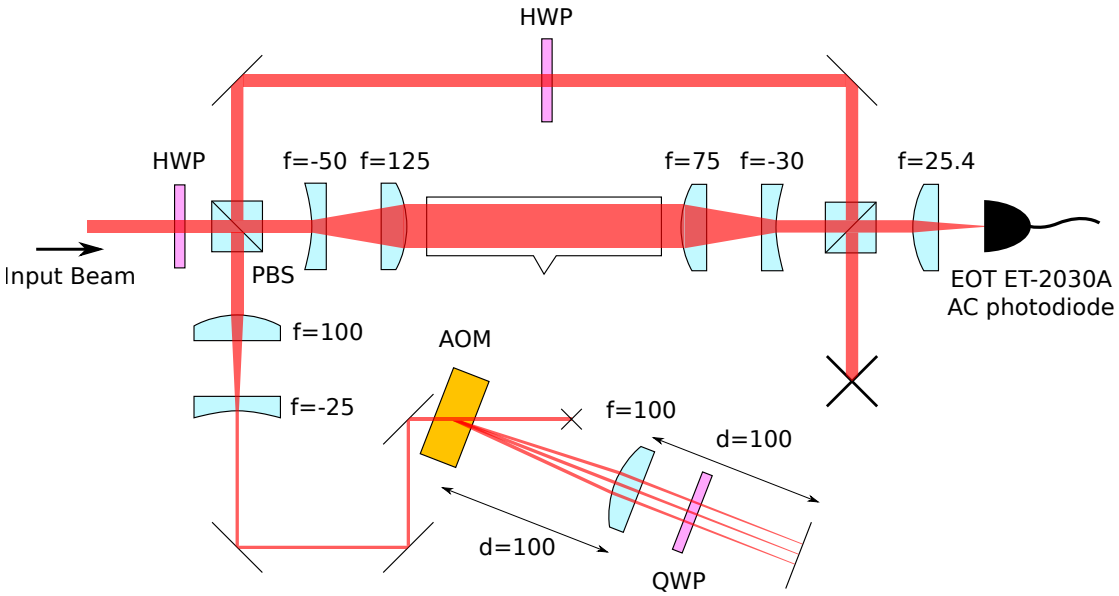

Figure 5.6: Schematic of Modulation Transfer Spectroscopy setup. All dimensions are in millimetres and both beam splitters shown are the polarizing type.

pump beam passes twice through the AOM it is further modulated, so we can apply the same procedure as before to find the final form of the pump:

$$E_{mod}(t) = \sum_{n=-\infty}^{\infty} \sum_{n'=-\infty}^{\infty} E_0 J_n\left(\frac{\Delta\omega}{\omega_{mod}}\right) J_{n'}\left(\frac{\Delta\omega}{\omega_{mod}}\right) e^{i\left(\omega_0+2\omega_{AOM_0}+(n+n')\omega_{mod}\right)t} \quad (5.6)$$

which we can now see as a carrier of frequency of $\omega_0 + 2\omega_{AOM_0}$ with side-bands again separated by frequency ω_{mod} and weighted by Bessel functions.

To produce the signal to the AOM the DC+RF output from a Minicircuits ZFBT-4R2GW bias tee is connected to the tuning pin of a Minicircuits ZX95-100-S+ Voltage Controlled Oscillator (VCO). A DC voltage is applied to the DC input of the bias tee to set the AOM's centre frequency and a sine wave at the modulation frequency is applied to the RF input. The output of the VCO is passed through a Minicircuits ZHL-3010+ low noise amplifier and this signal is connected to the AOM so that it sees an input frequency of $\omega_{AOM} = \omega_{AOM_0} + \Delta\omega\cos(\omega_{mod}t)$.

For the optical beam path (see figure 5.6), a portion of the cooling laser is extracted and reduced to a quarter of its size with a telescope before being passed through an 80 MHz Gooch and Housego AOM (Model R23080-1-LTD) arranged in the double pass configuration (described in detail in[104]). The zeroth order beam from the AOM is blocked, and the first order passes through a convex lens of focal length $f = 100\,\text{mm}$ at a distance $L_1 = f$ from the scattering point inside the

AOM. This lens acts to focus the diffracted light from the AOM, such that each beam remains parallel to each other as the AOM frequency is modulated. These parallel beams are then retro-reflected by a mirror at distance $L_2 = f$ from the lens, such that they are focused on the mirror's surface. These beams pass back through the AOM and then recombine in the first order diffraction. The final beam that results from the double pass configuration has a centre frequency that is 160 MHz detuned from that of the input beam and a modulation frequency of approximately $\omega_{mod} \approx 2\pi \cdot 3\,\mathrm{MHz}$.

The speed of the sound waves propagating through TeO_2, the crystal material in the AOM used here, is $\sim 4.2\,\mathrm{km\,s^{-1}}$. This means that for a modulation frequency of $\omega_{mod} \approx 2\pi \cdot 3\,\mathrm{MHz}$ the sound wave can only propagate 1.4 mm in the time that one period of modulation oscillation occurs[102, 105]. This shows that to achieve a bandwidth of this frequency the input beam should be small compared to this distance. In this case the beam was reduced with a telescope because the limited space on the optical bench meant that a long focal length lens couldn't be used, and strongly focusing the beam would result in a low diffraction efficiency due to poor Bragg matching in the AOM[104].

As the pump and probe beams have centre frequencies separated by $2\omega_{AOM_0}$, atoms moving at a velocity $\mathbf{v}$ in the vapour cell see the probe light as having a frequency of $\omega_{pr} = \omega_0 - \mathbf{k} \cdot \mathbf{v}$ and the pump as a frequency of $\omega_{pu} = \omega_0 + 2\omega_{AOM_0} + \mathbf{k} \cdot \mathbf{v}$, where $\mathbf{k}$ and $-\mathbf{k}$ are the wavevectors of the probe and pump beams respectively. Atoms can only interact with both beams when these apparent frequencies are the same, and so it follows that the only atoms that are probed are those which are moving towards the probe light at a speed of $v = \omega_{AOM_0}/k \approx 62\,\mathrm{m\,s^{-1}}$ relative to the lab frame. Since MTS produces its spectral features only for atoms that are moving towards the probe beam at this velocity, then upon locking the laser to a zero-crossing the laser emits light which is detuned from the same feature in the lab frame by the AOM's centre frequency. In many applications this would not be useful, however it is particularly well suited for use with the SMOT because the shift in the centre frequency can be used to compensate for that of the 'switching' AOMs described later in section 6.1.1. This setup has the additional benefit that the red-detuning required for cooling and trapping can be implemented easily and accurately by setting the difference between the centre frequencies of the AOMs.

As mentioned above, Residual Amplitude Modulation can cause an additional spectroscopic signal to interfere with that produced by MTS. This signal occurs regardless of whether the probed transition is closed or not, and so RAM introduces

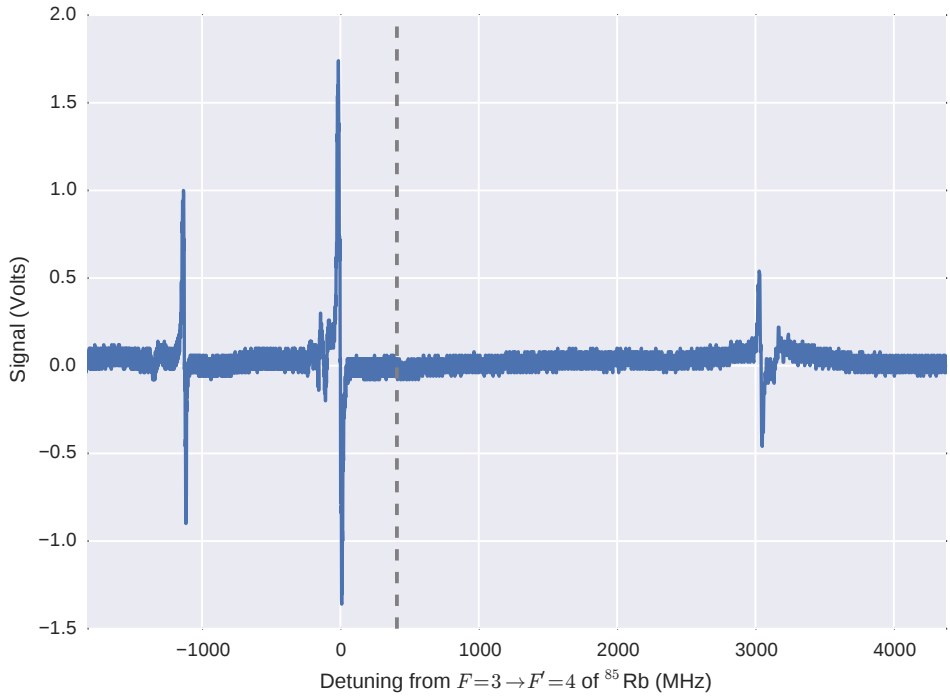

Figure 5.7: Error signal from Modulation Transfer Spectroscopy relative to the $F = 3 \rightarrow F' = 4$ cooling transition of ^{85}Rb. The dashed line shows where two data sets were stitched together due to the piezo driver's limited output sweep. The background level is almost completely due to background noise in the laboratory and is present even with the laser beams blocked.

superfluous features to the error signal and should be eliminated. RAM is caused if the pump beam's power varies as it is modulated and this can occur if alignment of the cat's eye retro-reflector is not perfect, or if the modulation frequency exceeds the bandwidth of the AOM. This can be corrected by using direct digital synthesis to generate the individual side-bands electronically so that their relative power can be adjusted to account for the AOM's frequency dependent efficiency[106]. An alternate, easier approach was taken here whereby RAM caused by the finite bandwidth and misalignment of the AOM can be compensated via (mis)alignment of the overlapping pump and probe beams in the vapour cell (and vice versa)[107].

Figure 5.7 shows the error signal produced by MTS with three sharp zero-crossings corresponding (from left to right) to the $F = 2 \rightarrow F' = 3$ transition of ^{87}Rb and the $F = 3 \rightarrow F' = 4$ and $F = 2 \rightarrow F' = 1$ transitions of ^{85}Rb. There are a few other hyperfine transitions visible due to incompletely compensated RAM, but these are insignificant compared to those caused by MTS. These results were so

successful that all of the data characterizing the SMOT presented in this thesis was taken whilst using this technique.

5.4 Direct Current Modulation

In order to generate the repump light for trapping without employing an additional diode laser the author adopted a direct modulation technique, whereby the current of the cooling laser is modulated at a frequency of $f_m \approx 2.92\,\text{GHz}$, approximately equal to the ground state splitting of ^{85}Rb, so that one of the sidebands that arises as a result of this modulation is resonant with the repumping transition[108]. To facilitate this modulation, a new laser PCB was designed for the ECDL in an attempt to maximize power transfer to the laser diode. The board contained an impedance matching circuit and a bias-tee, so that the constant current signal from the laser diode controller could be combined with that of the modulating input as close to the laser as possible. In an attempt to enhance the modulation the cavity length of the ECDL was then extended to $L = c/2f_m \approx 5\,\text{cm}$, where c is the speed of light, in order to match its free spectral range to the modulation frequency[109]. Figure 5.8 shows the spectrum of the modulated cooling laser taken with a Thorlabs SA210-5B 10 GHz FSR scanning Fabry-Perot interferometer. In this image the cavity length has been tuned to give significant enhancement to the strength of the sidebands, allowing even the second order peaks to be visible. Here the sidebands were not tuned exactly to the repump transition, and in general when this tuning was achieved the modulation strength was far weaker.

It may seem from figure 5.8 that the linewidth of the laser is very large ($\sim 120\,\text{MHz}$) however this is likely a gross overestimate considering the specifications of the etalon. The cavity has a factory measured finesse of 150, and given that it has free spectral range of $\Delta f = 10\,\text{GHz}$ this corresponds to a maximum resolution of $\delta f \sim 67\,\text{MHz}$. Due to this fairly poor resolution it was not expected that even with perfect alignment an accurate measurement of the linewidth would be possible, and given the purpose of the measurement was to measure the modulation depth, no particular attention was paid to optimize the interferometer's resolution.

The factory measured value of the etalon's finesse can be assumed to be equal to the reflectivity finesse, F_R, because the manufacturers of the device state that the contribution due to the mirror surface quality is negligible[110]. The effective

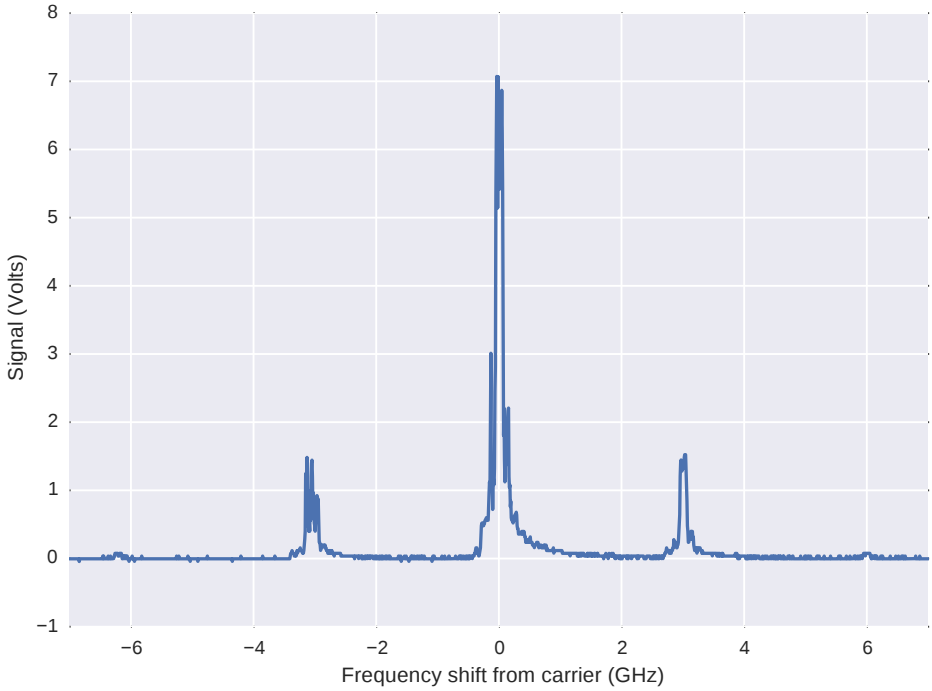

Figure 5.8: Trace from a Thorlabs SA210-5B 10 GHz FSR scanning Fabry-Perot interferometer observing the frequency spectrum of the modulated cooling laser. Sidebands are resolvable at multiples of the modulation frequency, which has been assumed to equal to 3 GHz in plotting this figure as the source data did not include a scan across the free spectral range of the etalon. The cooling laser was operating with an extended cavity to achieve modulation enhancement[109], however the sidebands were not correctly tuned to the repump transition in this image, and in general the modulation strength was far lower.

finesse of the etalon, F_T, however will not be equal to the reflectivity finesse unless the illumination finesse, F_I, is suitably large, which is only the case for a well aligned input beam of sufficiently small width[3]. The effective finesse of the cavity is given by:

$$F_T = \left(\frac{1}{F_R^2} + \frac{1}{F_I^2} \right)^{-1/2} \tag{5.7}$$

where the illumination finesse is given by:

$$F_I = \frac{\lambda r^3}{H^4} \tag{5.8}$$

where λ is the wavelength of the input light, r is the radius of curvature of the mirrors (which is approximately equal to the length $d = 7.5\,\text{mm}$ of the confocal

[3]Thorlabs recommends a beam diameter of 150 µm for the SA210 series of interferometers.

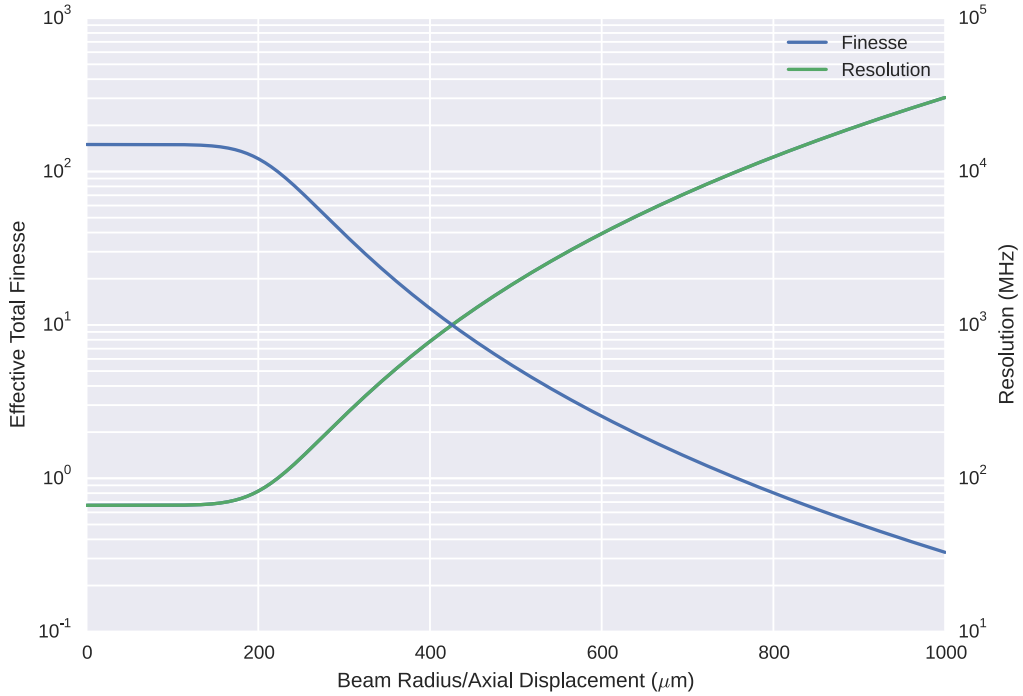

Figure 5.9: Effective finesse and resolution of a Thorlabs SA210-5B 10 GHz FSR scanning Fabry-Perot interferometer as a function of an input ray's axial displacement.

cavity) and H corresponds to the off-axis displacement of the incoming beam. The illumination finesse quantifies the reduction in the interferometer's resolution that results from poor choice of beam parameters, and arises due to the varying round trip distance as the beam moves off the cavity's axis. Asymmetric line shapes are symptomatic of a poor illumination finesse, and so looking at figure 5.8 it can be seen that the cavity resolution is indeed suboptimal.

Figure 5.9 shows a plot of the effective finesse and resolution, $\delta f = \Delta f / F_t$, for the Fabry-Perot interferometer as a function of the input beam's axial displacement. The axial displacement can also be interpreted as the radius of a beam coaxial with the etalon, and this shows that even a perfectly aligned beam requires a radius of only 239 µm to limit the resolution of the interferometer to the 120 MHz linewidth of figure 5.8.

The large linewidth shown in figure 5.8 can mostly be accounted for by a high illumination finesse, but it is possible that the linewidth of the cooling laser was larger than usual both because the laser's cavity was detuned from the transitions of rubidium, and hence was free-running, but also due to the presence of current noise that was coupled to the laser from the modulation circuitry. Regardless, it

is known from previous work by M.Himsworth that the Southampton ECDLs can achieve a fairly respectable linewidth of 570 ± 140 kHz, and there is no reason to suspect they behaved any differently here[111].

Although attractive due to its simplicity, a number of problems were found with direct current modulation: A powerful +27dBm Minicircuits TVA-11-422 RF instrument amplifier was required to amplify the modulation signal to a level that produced sufficiently large sidebands to trap atoms within the SMOT. The poor performance of the modulation was likely a result of the geometry of both the laser PCB and possibly the bond wires in the laser diode package causing reflected or radiated signals. A microstrip was etched onto the laser diode PCB in an attempt to maintain the characteristic impedance of the preceding coaxial cable, however better results may have been obtained if the cable were to be terminated at a capacitor positioned directly on the laser diode's pins. This is the approach that has been taken by other groups, and has resulted in satisfactory results without any other attempt at impedance matching[108, 112, 113]. The large RF signals also interfered with the temperature controlling electronics of the laser diode, resulting in instantaneous jumps in the measured laser diode temperature upon toggling the modulation power. These temperatures were almost certainly fictitious, however the fluctuating measurements would lead to the controller of the laser diode's thermoelectric cooler to start oscillations of the true temperature. The laser diode was also not anti-reflection coated and this will have resulted in a significant reduction of the effectiveness of the modulation enhancement[109]. Finally, one of the most frustrating aspects of this technique was that the relatively low frequency free spectral range of the ECDL's extended cavity made the laser much more likely to mode-hop. These frequent mode hops were particularly troublesome when coupled with the temperature oscillations of the thermoelectric controller, and caused rapidly moving mode edges that would regularly bring the laser out of lock.

5.5 Offset Phase Lock Stabilization

Although the ~ 3 GHz direct current modulation technique was successful in producing the required repump light for trapping, the numerous problems associated with it prompted its replacement. A new system was thus adopted with a separate repumping laser that could provide greater stability and tunability than the direct modulation technique, whilst still maintaining the same phase coherence with the cooling laser that the prior method offered.

This system that was introduced is known as an offset phase lock loop and stabilizes a new, separate, repumping laser to a frequency that is offset from the reference cooling laser. A servo monitors the frequency difference between the lasers and provides current and piezo feedback to the repump so that this frequency difference remains locked to that of a reference signal. The optical set-up of this technique is not particularly involved, however is shown in figure 6.3 for reference. A portion of both the cooling and repump beams of the same polarization were aligned to combine at a non polarizing beam cube. Both of the beams then emerge from one of the cube's output ports and then co-propagate through a $f = 35\,\text{mm}$ plano-convex lens to be focused onto the 60 µm diameter active area of an EOT ET-4000 12.5 GHz photodiode. A $\sim 2.92\,\text{GHz}$ beat signal is generated by the interference of the two beams, and this signal is measured by the photodiode and amplified by two Mini-Circuits ZX60-6013E-S+ 20-6000 MHz amplifiers before being fed into a custom phase locking circuit based upon prior work by J.Appel *et al.*[114]. The circuit uses an ADF4007 from Analog Devices to divide the frequency of the beat signal by 64, and this divided signal is available at the MUXOUT pin of the chip, so it can be monitored with an oscilloscope to both tune the frequency of the repump laser and to ensure that it is correctly locked. The circuit also receives a signal from a ZX95-100-S+ Mini-Circuits Voltage Controlled Oscillator (VCO) which has its frequency divided by 2 before being compared to that of the divided beat signal. The circuit then generates an error signal indicating the difference in frequency between the divided signals and this is fed to the piezo and current modulation inputs of the repump laser to produce a feedback loop that aims to minimize the difference in the divided signals. The result of the set-up is that the circuit acts to stabilize the frequency of the repump light such that is is separated from the cooling laser by a frequency given by $\Delta f = 32 f_{VCO}$. This is particularly convenient because the $f_{VCO} \approx 91\,\text{MHz}$ reference signal can be measured easily with a moderately fast oscilloscope, whilst with the direct modulation technique the input modulation frequency was $\sim 2.92\,\text{GHz}$, too fast to be detected and its frequency verified with the oscilloscopes available here.

Chapter 6

Implementation of the SMOT

In addition to the precise laser stabilization discussed in the previous chapter numerous other technical dependencies exist that need to be resolved in order to both demonstrate the principle of the SMOT and to characterize its behaviour. This new MOT geometry requires an optical system that is capable of rapidly switching the direction of the cooling and repump laser beams, and this must be synchronized with the pulsing of the magnetic field generating currents that alternate between the two pairs of SMOT wires. A suitable current source must be designed that is capable of driving the high currents through these wires and it must be capable of doing so at frequencies on the order of tens of kilohertz. After demonstrating the principle of the trap its behaviour must be characterized by measuring the temperature and atom number of the ultra cold clouds that it collects, and these properties must be evaluated at a variety of trap frequencies in order to determine an optimal configuration. Finally this data collection must be facilitated through the use of a computer control system to interface with an oscilloscope, signal generator and high speed camera allowing for automated time of flight measurements and analysis.

6.1 Laser System

6.1.1 Optical switching schemes

Following the numerical simulations of the SMOT in section 4.3 it was established that the cooling and repump beams would need to be switched between two paths in order to prevent a degree of anti-trapping. The simulations showed that the

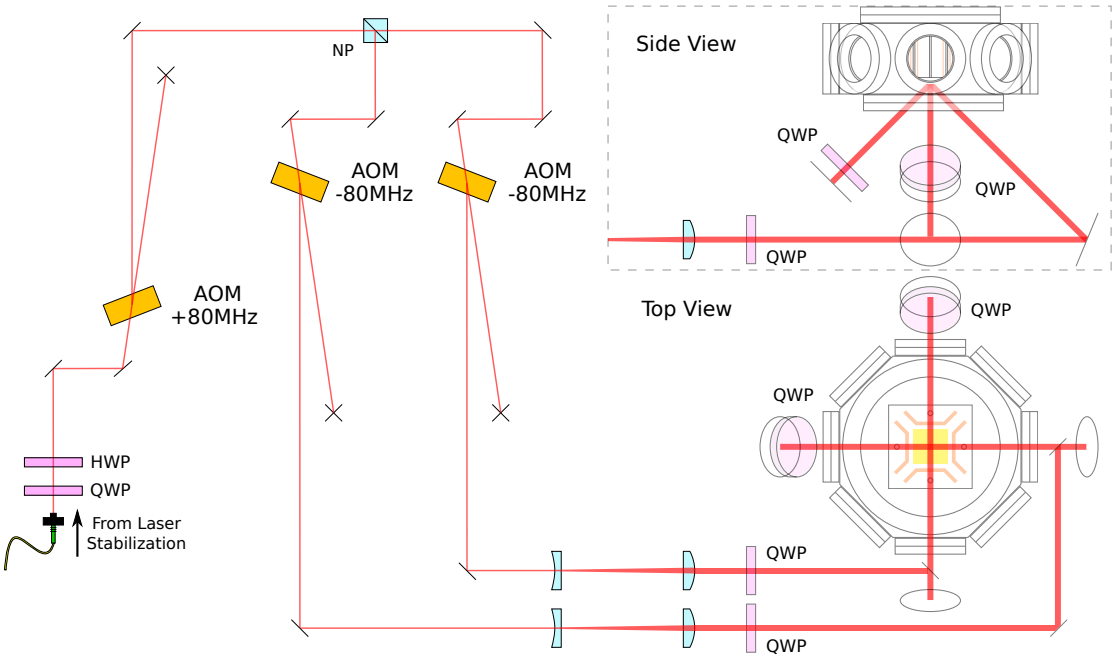

Figure 6.1: The initial scheme used to perform optical shuttering. Light that contains components stabilized to the cooling and repump transitions passes from the spectroscopy setup through an optical fibre to a series of AOMs. The first AOM operates continuously, shifting the frequency of the light by 80 MHz. This detuned light is then split into two paths each of which passes through another AOM. These subsequent AOMs act as optical shutters, being controlled by two signals sent from a data acquisition card. The secondary AOMs also shift the light by −80 MHz so that the light directed into the chamber is brought back into resonance with the cooling and repump transitions. A close-up showing how the beams are directed onto the SMOT's mirror is shown in figure 4.4.

trap should operate at frequencies in the kilohertz region, and as a result the use of mechanical shutters was immediately discounted as a viable option due to their low switching speeds. The use of AOMs (whose operation is described in section 5.3) on the other hand was a far more logical option due to their extremely rapid rise-times on the order of tens to hundreds of nanoseconds, mainly limited by the propagation speed of sound waves as they travel though their crystal, across the waist of the shuttered beam[115].

The first optical switching scheme that was used is shown in figure 6.1. The design consists of three AOMs, two of which provide the shuttering by scattering light into their first diffracted orders upon receiving signals output from a data acquisition card. The first diffracted orders were used because they have the greatest extinction ratio, however due to the nature of the AOMs they also receive a frequency shift equal to the AOM operating frequency. The diode lasers in this

setup were locked to the cooling and repump transitions of rubidium 85 through the use of Zeeman modulation in conjunction with ∼2.92 GHz current modulation and so this frequency shift imparted by the shuttering AOMs would act to detune the output beams far from resonance. This detuning prompted the inclusion of a third 'shifting' AOM in the switching scheme whose only purpose was to shift the frequency of the stabilized light in the opposite direction to that caused by the shuttering AOMs, such that after passing through them the light would be brought back onto resonance. Later it was realized that the inclusion of a third AOM was not necessary to remove the frequency shifts of the shuttering AOMs, and instead the use of a novel double pass configuration could provide the same functionality with an even greater extinction ratio. This approach, however, was not tested because a Pockels cell had become available with which to implement a more efficient switching scheme, but the principle of this double pass configuration was successfully demonstrated shortly afterwards by another group[116].

The second optical switching scheme, as shown in figure 6.2, used a Pockels cell as an electronically controlled waveplate to alternate the cooling and repump light between horizontal and vertical polarization so that it could be directed to two different output paths through the use of a polarizing beam splitter. This approach was superior to the first due to a much higher efficiency than that exhibited by the series of AOMs, each of which loses a significant quantity of power in the unused diffraction orders in addition to an inherent maximum efficiency of 50% due to each beam being dumped for half of the switching period. The electro-optical scheme also offers greater simplicity, requiring fewer components than the previous approach and furthermore does not introduce a frequency shift onto the beams which would otherwise have to be removed again later.

This switching scheme, whilst effective, was not used for very long in the experiment because the author became alerted to a variation of the Modulation Transfer Spectroscopic technique which, as a result of being implemented through the use of a double-passed AOM rather than an EOM, produces an error signal shifted in frequency from the spectroscopic reference by the AOM driving frequency (see section 5.3). This technique, in combination with the greater available laser power afforded by a recently built Tapered Amplifier (TA) prompted the return to a switching scheme reminiscent of that of the first one, but with the modification of the removal of the shifting AOM from the output path of the cooling and repump beams. This final design hence served to save power that would otherwise be lost in the shifting AOM and, whilst not as efficient as the second approach, allowed

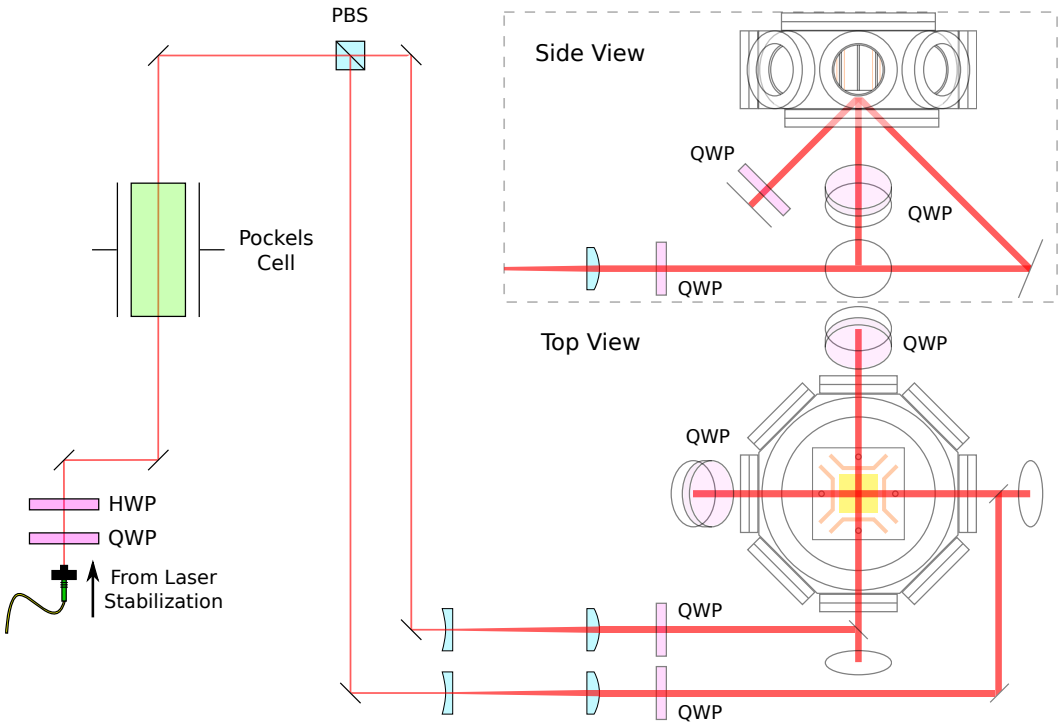

Figure 6.2: The second scheme used to perform optical shuttering. Light that contains components stabilized to the cooling and repump transitions passes from the spectroscopy setup through an optical fibre to a Pockels cell which acts as a voltage controlled wave plate. The Pockels cell rotates the polarization of the light depending on a signal from a data acquisition card so that the light can be directed between two optical paths by a polarizing beam splitter . This technique is superior to that shown in figure 6.1 due to its much higher efficiency, but ultimately was abandoned because of the adoption of the technique of Modulation Transfer Spectroscopy, which was more suited to the scheme shown in figure 6.3. A close-up showing how the beams are directed onto the SMOT's mirror is shown in figure 4.4.

for the use of a spectroscopic technique that offered a stronger error signal which was easier to lock to than what was previously available.

6.1.2 Final Optical Design

The final optical setup is shown in figures 6.3 and 6.4. A $\sim 15\,\mathrm{mW}$ beam emitted from the cooling ECDL passes through a tapered amplifier to give $\sim 200\,\mathrm{mW}$ of frequency locked cooling light. A portion of this light passes through an 80 MHz AOM arranged in the double pass configuration to provide the modulated light required for the laser stabilization (see section 5.3). This AOM receives a centre

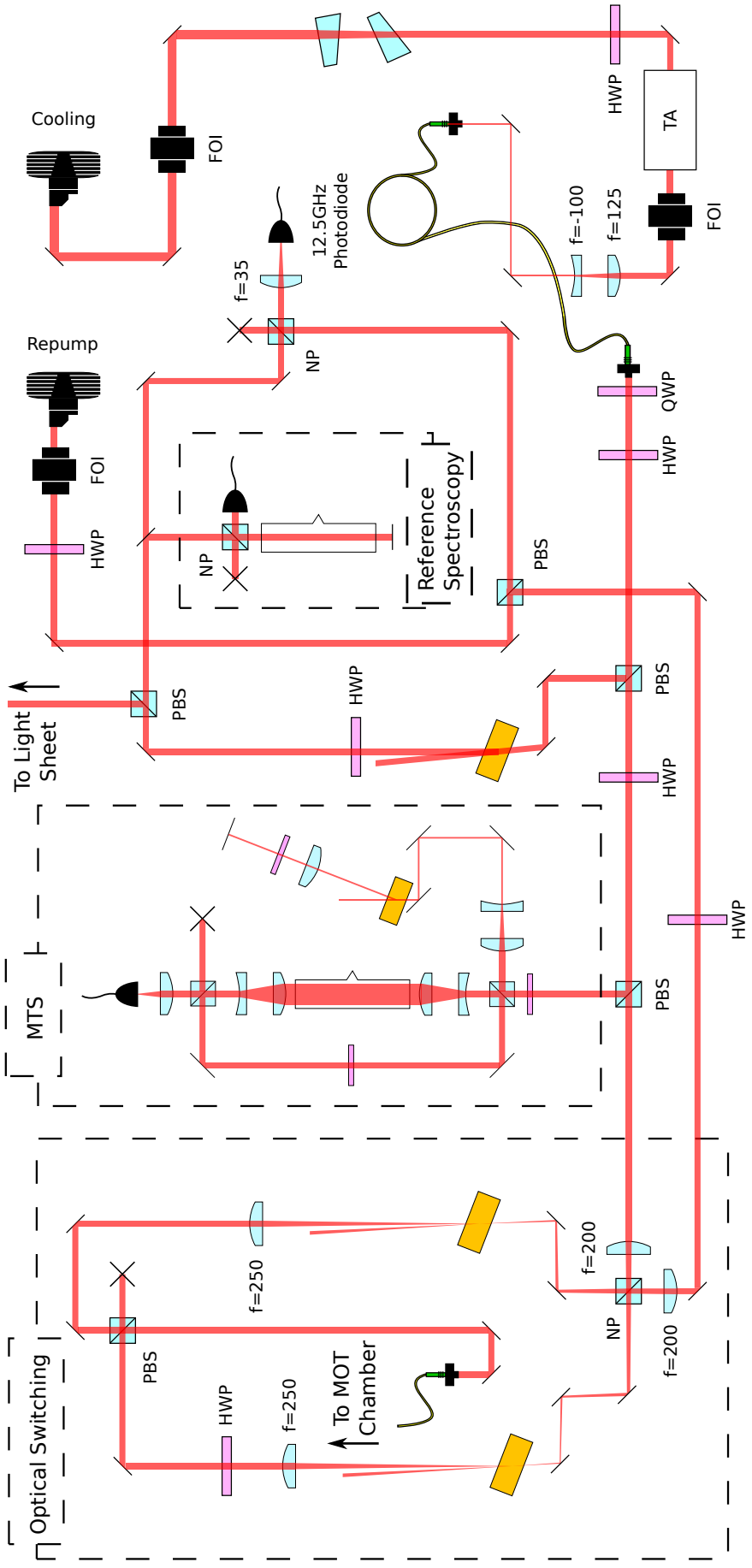

Figure 6.3: Laser set-up used to generate the cooling and repump light for the SMOT. The Modulation Transfer Spectroscopic set-up is shown in more detail in figure 5.6. All dimensions are in millimetres.

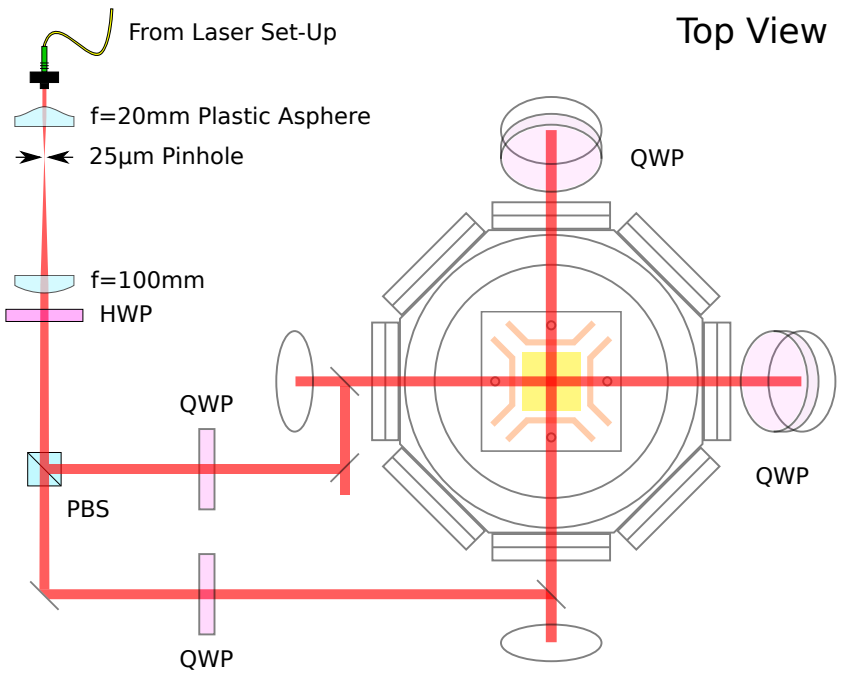

Figure 6.4: Spatial filtering and beam separation before entering the vacuum chamber holding the prototype SMOT. A close-up showing how the beams are directed onto the SMOT's mirror is shown in figure 4.4.

driving frequency of (80+δ)MHz, where δ is the detuning of the cooling beam from resonance and, on top of this, the AOM receives a frequency modulation of 3 MHz (further described in section 5.3). Because the AOM is arranged in a double pass configuration the modulated pump light in the vapour cell has a centre frequency detuned from the probe light by 2(80+δ)MHz, meaning upon locking to the zero crossing corresponding to the $5^2S_{1/2}, F = 3 \rightarrow 5^2P_{3/2}, F' = 4$ transition of ^{85}Rb, the light emitted from the cooling laser is -(80+δ)MHz detuned from the transition observed for atoms stationary in the laboratory frame.

To produce the optical switching required for the SMOT we again opted to use a pair of 80 MHz AOMs as shutters. The -(80+δ)MHz detuned cooling beam is divided into a vertical and horizontal polarized component which separately pass through the two shuttering AOMs. These AOMs not only serve to 'blank' the beams, but also act to shift them back to δMHz from resonance. Now the beams are again resonant with their respective transitions they are recombined so that they can be coupled into an optical fibre leading to the MOT chamber. At the other end of the fibre the beams are cleaned by using a 20 mm plastic aspheric lens to focus through a 25 µm spatial filter before they are expanded with a telescope to a $1/e^2$ radius of 4.0 mm and then finally separated with a polarizing beam splitter so they can be directed into the vacuum chamber. These beams

may seem unnecessarily small given the amount of power afforded by the tapered amplifier, however the maximum size is limited by the SMOT's wires which cause shadowing for beams of diameter greater than $\sim 7.5\,\text{mm}$. The signals to the AOM shutters are governed by a Minicircuits ZX80-DR230-S+ RF switch connected to a computer controlled Data AcQuisition (DAQ) card. The RF switch receives an 80 MHz sine wave from a Minicircuits ZX95-100-S+ voltage controlled oscillator and this signal is output to one of two ZHL-3010+ amplifiers, each of which drive one of the switching AOMs depending on the state of a 2-bit signal emitted from the DAQ.

A second ECDL provides the repumping light required to prevent atoms becoming lost from the MOT. This laser is offset phase locked to the cooling beam by a custom circuit which attempts to stabilize the $\sim 2.92\,\text{GHz}$ beat note that they produce on a fast photodiode (see section 5.5). The repump light is then recombined with the cooling light at a beam splitter directly before it reaches the AOM shutters.

6.2 Generation of the Magnetic Fields

6.2.1 FET Based Current Switching

In order to generate the required current through the SMOT's wires, and thus the magnetic fields for trapping, a circuit was devised by a previous member of the group to drive the gates of four Field Effect Transistors (FETs), each of which controls the flow of current through one of the SMOT's four wires. One quarter of the circuit is shown in figure 6.5, which was repeated for each of the four FETs. For each wire, a signal output from a data acquisition card was passed to a Fairchild 6N137 optocoupler which, along with an isolated 12 V DC/DC converter and external floating power supply, ensured that each output was also isolated. The output of each optocoupler was connected both to a pull up resistor and the input pin of a Microchip TC1411 FET driver, and each of these was connected to the gate of a F3711Z FET from International Rectifier. The FETs were then wired to the SMOT in series with a number of ballast resistors as shown in figure 6.6 such that the current drawn from each power supply would remain approximately constant throughout the switching cycle and hence reduce the stress put upon them.

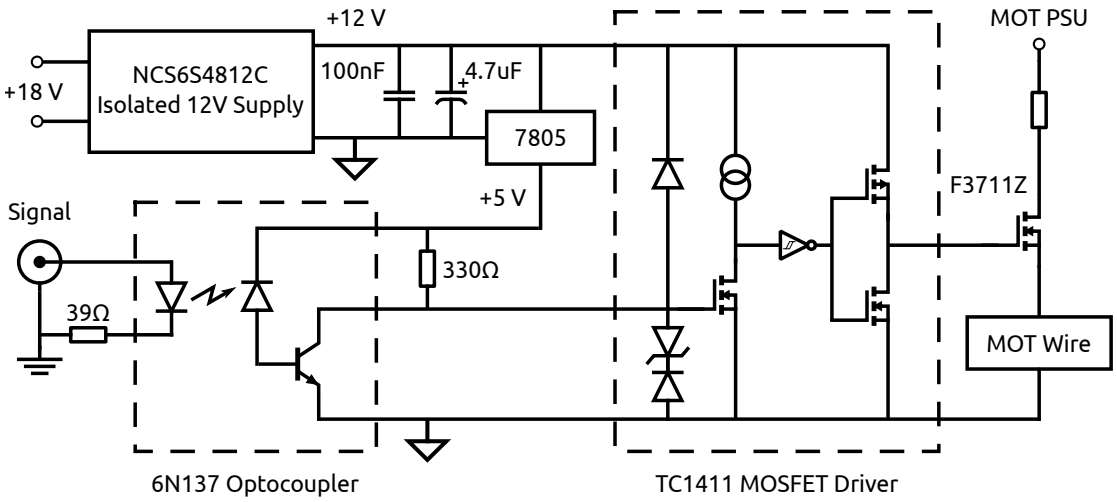

Figure 6.5: FET driving circuit that was initially used to generate the SMOT wire currents. This circuit was repeated for each of the four SMOT wires, however two high current power supplies were used as shown in figure 6.6. The circuit should not be replicated as shown here as it contains several design flaws that are discussed in the main text.

Whilst this circuit produced currents sufficient to enable the first successful demonstration of the SMOT it also was the cause of a significant amount of electrical noise. This noise made it extremely difficult to maintain stable atom clouds within the MOT and hence to determine the dependence of their properties on the switching frequency. Amongst other devices, this ElectroMagnetic Interference (EMI) was picked up by the laser stabilization circuit and vastly increased the frequency at which it would be brought out of lock. It was suspected that the cause of the EMI was radiation emitted due to the high frequency harmonics of the sharp switching edges of the current waveform. Such issues are commonly found with switched mode power supplies and the clock signals of high frequency digital electronics.

In hindsight there were several other problems that existed with this circuit, some of which may have needlessly exacerbated the EMI issues. The input resistor to the optocoupler was so small that a 5 V logic level derived from a signal generator with a 50 Ω output impedance would result in an input current that would exceed the optocoupler's absolute maximum rating. The optocoupler also has slightly asymmetric on/off switching times and so the current draw from the high current power supplies is not truly constant as expected. Bypass capacitors were also omitted from many of the devices in the circuit including those for the FET driver and optocoupler, which are listed in their respective datasheets as being mandatory. Perhaps the biggest design flaw is the lack of bypass capacitor for

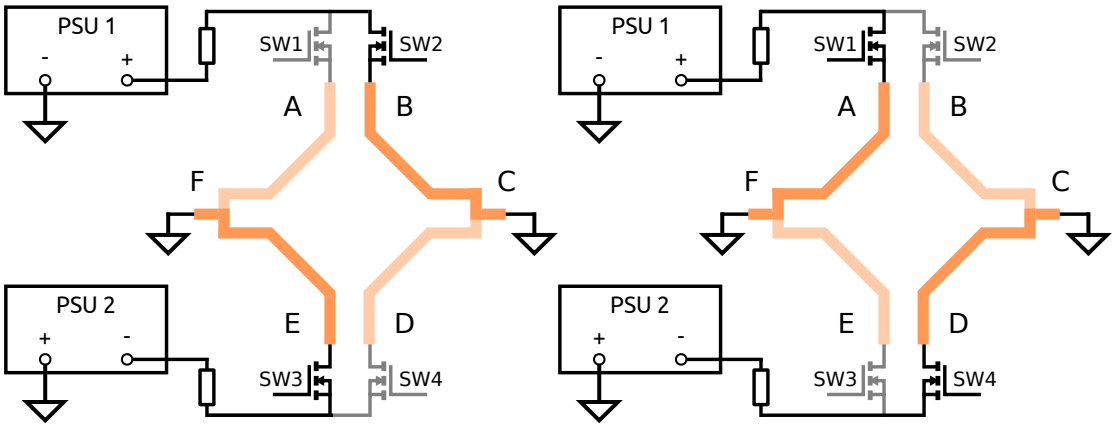

Figure 6.6: The two states of the SMOT wires as they are switched by the FET driving circuit of figure 6.5. The FETs are connected so that the current drawn from each of the power supplies remains approximately constant.

the FETs themselves, the result of which means that any high frequency currents drawn from the MOT wires must be sourced by the higher impedance path of the power supplies. This creates a larger loop area for the high frequency currents that could have otherwise been shorted by appropriate bypass capacitors, and so unnecessarily increases the amount of radiated EMI.

To reduce the amount of electromagnetic interference caused by these switching transients the author decided to replace the FET based magnetic field switching scheme with one which would drive sinusoidal currents and thus would not experience the troublesome high frequency harmonics.

6.2.2 Audio Amplifier Based Current Switching

In order to produce the SMOT magnetic field switching based upon a sinusoidal current waveform a rack mount Behringer Europower EPX4000 audio power amplifier was employed. This device is designed to drive the large speakers found in concerts and public address systems and as a result it expects the load to which it is connected to have a nominal impedance of 2 Ω, 4 Ω or 8 Ω depending on the mode in which it operates. The square wave signals previously sent from the DAQ to the FET driving circuits were replaced with a sine wave sent from the DAQ's analogue output to the audio amplifier. The output of the audio amplifier was then connected to an Ohmite TA1K0PH2R50KE 2.5 Ω high power resistor, and this was water cooled with an Ohmite CP4-114C cold plate. Four Schottky diodes were then inserted in series with the power resistor and the MOT wires as shown

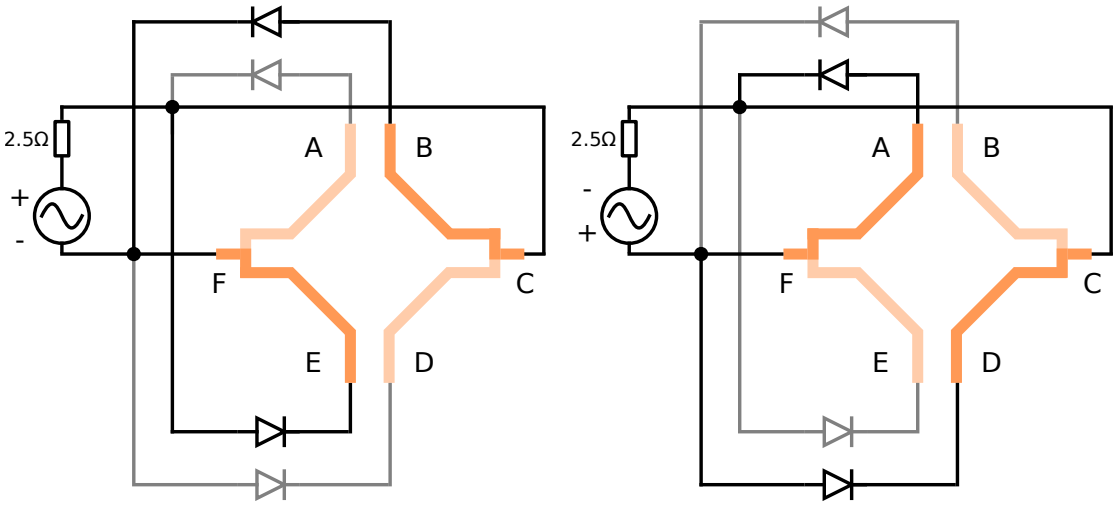

Figure 6.7: First wiring method used with sine wave based magnetic field switching. The current limiting resistor was subsequently replaced with a 5 Ω value to allow use of the audio amplifier in its bridge mode. A more suitable wiring method was adopted (figure 6.8) to allow for greater currents with this restriction.

in figure 6.7 so that the resulting half wave rectification in each wire pair produced the required magnetic field switching for trapping. As shown in figure 6.9 the bandwidth of the audio amplifier was non-negligible, so for every frequency setting the phase and amplitude of the signal output from the DAQ was adjusted so that, after amplification, the peak to peak voltage across the high power resistor remained constant and in synchronization with the optical switching.

Once again this produced sufficiently high currents to demonstrate magneto-optical trapping and furthermore it succeeded in reducing the amount of electrical noise compared to that which had plagued the FET based approach. The amplifier, however, was very susceptible to overheating, and this would result in the amplifier temporarily attenuating its output every few seconds, even if the gain of the amplifier was turned down far from its maximum. To try and increase the current output the high power resistor was replaced with a 5 Ω Ohmite TA1K0PH5R00KE[1], allowing for the amplifier to be placed in its higher power 'bridge mode', and the half wave rectifying circuits were rewired as shown in figure 6.8 to a more sensible configuration that doubled the available current at the same power dissipation. This failed to solve the amplifier's overheating problems, and so it was suspected that either the non-linearity of the diodes or the inductance of the wires were presenting a load to the amplifier that it couldn't drive. To

[1]This resistor later failed due to exceeding the manufacturer's maximum ratings and so was replaced with two TE Connectivity TE1000B10RJ 10 Ω high power resistors that were wired in parallel.

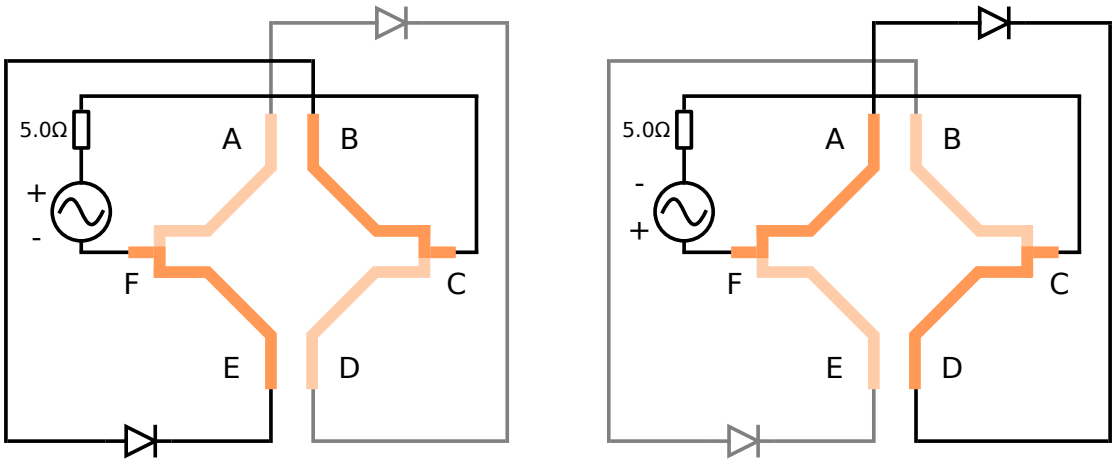

Figure 6.8: Second wiring method used with sine wave based magnetic field switching.

test this the SMOT wires and the diodes were removed from the amplifier output, ensuring that it would see an almost purely resistive dummy load. Surprisingly the amplifier still continued to overheat, indicating the problem was with the amplifier itself.

The Behringer EPX4000 was selected to drive the SMOT currents due to its high power specification and stability with inductive loads. It perhaps is not surprising that an audio amplifier should claim to drive inductive loads when speakers themselves are inherently inductive[2]. This, however, highlights the rather odd convention of specifying the load presented by speakers as a particular resistance considering the fact that their impedance is frequency dependent. The EPX4000 is sold as a 4 kW amplifier, however this refers only to the peak power that it can deliver into a 4 Ω load whilst in its bridge mode. A more useful figure is the 'RMS power' quoted in the specifications, however the term itself is a misnomer that is fairly commonly used in the context of audio amplifiers. RMS power is usually stated to indicate the average power delivered to a load, calculated from a measurement of the RMS voltage and the RMS current. Taking the root mean square of the instantaneous power delivered to the load does not yield the average power, and is instead correctly calculated by integrating this waveform over unit time[118]. The highest specified RMS power of the EPX4000 is listed as 3 kW into a 4 Ω load whilst in bridge mode. Assuming the same power could be delivered to the 5 Ω load that was used here, that would correspond to a peak current in the half rectified SMOT wires of ~ 34.6 A, well in excess of the ~ 29.2 A required to achieve the desired magnetic field gradient of $10\,\mathrm{G\,cm^{-1}}$.

[2]This stability is often granted through the use of a Zobel network on the output of the amplifier, acting as a short at high frequencies[117].

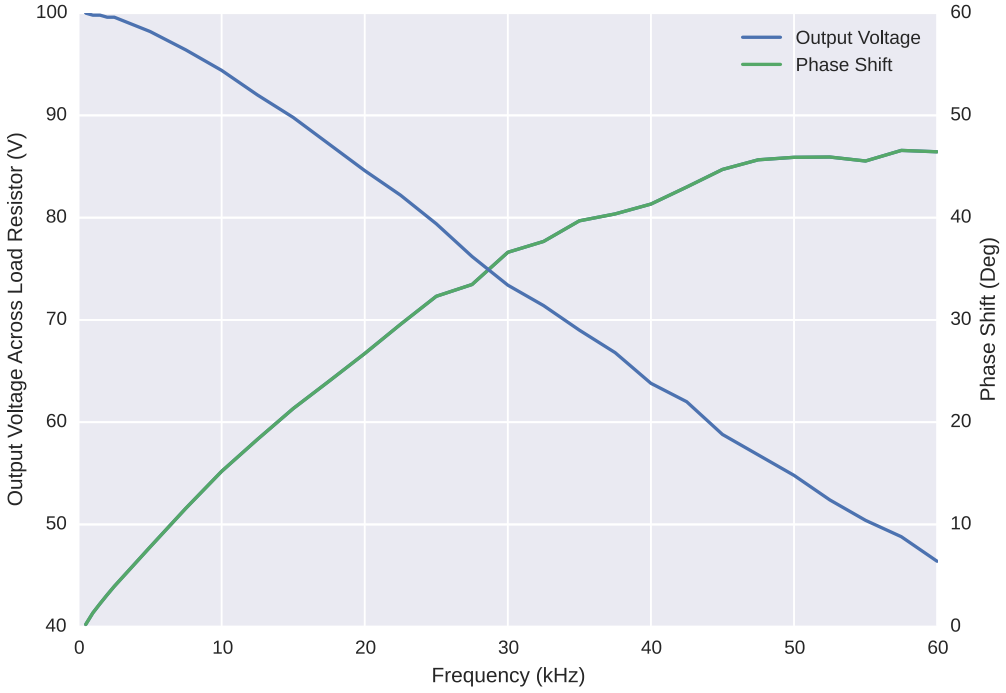

Figure 6.9: Bode plot of Behringer Europower EPX4000 amplifier used to calibrate DAQ phase and amplitude output.

In practice the amplifier could not attain this output current, instead overheating when only 475 W was output into a 5 Ω load at a switching frequency of 10 kHz. Basic power calculations lead to further doubts about the validity of the claimed specifications of the amplifier. Considering the device has an C14 IEC power inlet (sometimes mistakenly referred to as a 'kettle' plug) which is only rated up to 10 A and generously assuming that the mains voltage is 240 V (rather than the nominal value of 230 V) this implies the amplifier has a maximum input power of 2.4 kW. Even if the IEC input socket is allowed to draw the maximum current of 13 A allowed by a BS 1363 plug then the maximum input power to the amplifier is still only 3.1 kW, meaning that the device would have to have efficiency of 96 % to meet its specification of delivering 3 kW into a 4 Ω load, a claim that seems unlikely to be possible. Whilst preliminary data was collected with using the EPX4000, the overheating eventually resulted in the amplifier's destruction. Whilst the author considered purchasing a replacement audio amplifier to complete the experiment, the poor performance of the previous device left a feeling of great scepticism that another commercial audio amplifier could meet its specifications and so work was instead directed towards constructing a bespoke current driver.

6.2.3 Design of Bespoke Current Driver

After the dissatisfaction of the previous methods of generating the magnetic fields for trapping the author briefly considered building a 1.5 kW amplifier based on a project designed by Elliott Sound Products[119]. This project does not seem to be tested, however, and once again is designed for 4 Ω loads whilst the load used for the SMOT wires can be almost arbitrarily small, allowing for a lower output voltage. In light of this, the design effort instead was centred around a power op-amp from Apex Microtechnology, the PA50, which is specified as a 40 A output device capable of dissipating 400 W. Other op amps from the Apex line of products were considered, however the PA50 was chosen due to a lower voltage drop across its output transistors, and hence reduced power dissipation, at the expense of a reduced power bandwidth, protection and other features. The design goal of this bespoke current driver was to be able to continuously drive a 40 A peak to peak sine wave through the half wave rectifiers of figure 6.8 at frequencies varying from 1 kHz to 60 kHz.

The wires of the SMOT were measured with an Agilent U1733 LCR meter to give the model of the load shown in figure 6.10, where the previous 5 Ω load resistor has been replaced by the 1 Ω of figure 6.11. As a first estimate of the behaviour of the amplifier we can approximate the load by a resistor of value R =1.0283 Ω in series with an inductor with inductance L =1.815 µH. These values are calculated for this model by finding the inductance and resistance of each individual arm of the two half-wave rectifiers and then taking the average of these values over both arms. This assumes that at any point the load is only conducting through one pair of diodes, and that these diodes' properties do not otherwise affect the load.

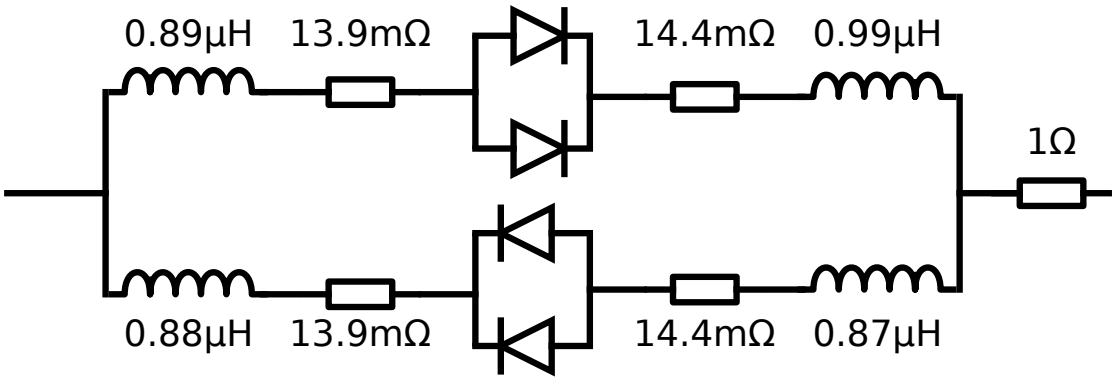

Figure 6.10: Electrical model representing the SMOT wires and load resistor, the values of which were measured with an Agilent U1733 LCR meter.

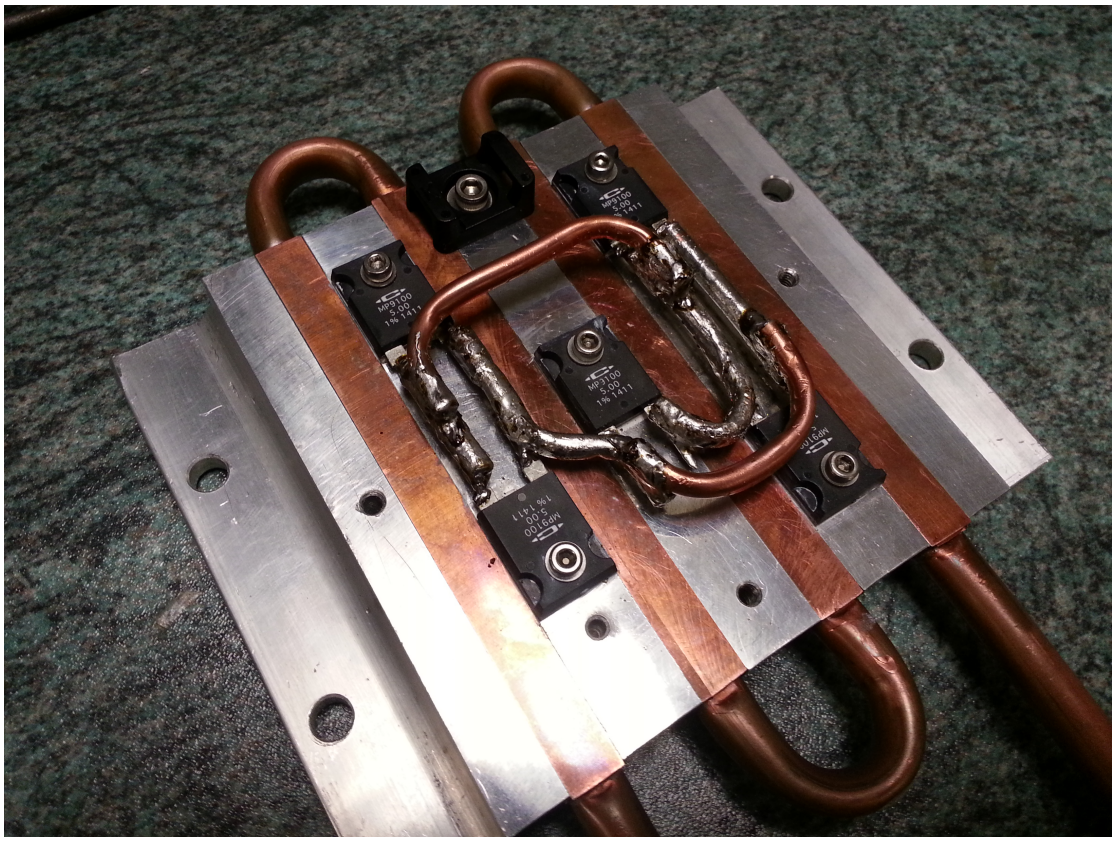

Figure 6.11: Five watercooled 5 Ω, 100 W resistors (MP9100 series from Caddock Electronics, Inc.) wired in parallel to produce the 1 Ω load/sense resistor of the voltage controlled current amplifier. Copper tubing is used here instead of litz wire (see section 6.2.3.1) due to the short lengths of cable required.

Upon application of a voltage across a resistor and inductor placed in series the drawn current exponentially rises with a time constant of $\tau = L/R$. This is the time required for the current to increase to $1 - 1/e \approx 63.2\%$ of its maximum value, and for the model used here this corresponds to $\tau = 1.77\,\mu s$. Whilst this limits the speed at which a square wave voltage source can drive current through the SMOT wires, the current driven by a sine wave voltage source instead merely experiences an attenuation to $1/\sqrt{2}$ of its maximum value. This also corresponds to the point where the power delivered to the resistor drops to half, and with this model of the SMOT's wires this occurs at an angular frequency of $\omega = 1/\tau = R/L = 2\pi{\cdot}90\,\text{kHz}$.

One of the greatest problems in the design of this driver is the power dissipation within the amplifier and how this determines its excursions within the Safe Operating Area (SOA). Although the PA50 is listed as a 400 W amplifier this is merely the power that can be dissipated within it, in conjunction with a perfect heat sink, to maintain the maximum recommended junction temperature of 150 °C

whilst the case is held at a temperature of 25 °C[3]. This power specification does not imply that 400 W can be delivered to the amplifier's load and, perhaps counter intuitively, these powers are not directly comparable.

The instantaneous power dissipation in an op amp's output transistors is given by the product of their output currents with the voltage drop across them. The voltage drop is given by $V_{CE} = V_s - V_o$, the difference between the output voltage V_o and that of the corresponding supply V_s, and demonstrates the importance of providing the lowest possible supply voltage to the op amp to reduce this dissipation. The output transistors require their gate voltages to be approximately 10 V higher than their source voltages in order to maximally turn on. This means that if the gate and source voltages are derived from the same supply voltage then the transistors can never fully turn on, significantly increasing the minimum voltage drop across them[4] and hence reducing the output voltage swing. Some amplifiers, including the PA50, have additional pins for optional 'boost' voltage rails which exceed those of the supply voltage. The boost voltages provide the extra 10 V to the gates that allow for the transistors to fully turn on, and this results in a greater output voltage swing but without the associated increase in power dissipation had the source voltage been increased instead.

To calculate the average power dissipated in the amplifier we consider that the output stage consists of two transistors in a push-pull configuration: one of which sources current to the load and the other which sinks current from it. The circuit is assumed to be operating in a linear regime, applying an output voltage V_o across the load and generating an output current I_o with some phase shift ϕ depending on its impedance Z_L:

$$V_o = V_p \sin(\omega t + \phi), I_o = I_p \sin(\omega t) \tag{6.1}$$

The instantaneous power dissipated by the current sourcing output transistor is given by:

$$\begin{aligned} P_{inst} &= (V_s - V_o) I_o \\ &= (V_s - V_p \sin(\omega t + \phi)) I_p \sin(\omega t) \\ &= V_s I_p \sin(\omega t) - V_p I_p \sin(\omega t + \phi) \sin(\omega t) \quad \text{for } 0 \leq t \leq T/2 \end{aligned} \tag{6.2}$$

[3]This, of course, implies the maximum thermal resistance of the junction to the case, which is equal to R_{jc} =0.31 °C W^{-1} in the situation of DC Output waveforms. AC output waveforms have a lower thermal resistance and hence permit greater power dissipation in the amplifier.

[4]This corresponds to a voltage drop of 6.5 V across the PA50 when outputting a current of 20 A.

where the domain of the function indicates that this is only valid when the current output is positive. The output waveforms and the supply rails of the amplifier are symmetric about zero volts so on average each transistor dissipates an equal amount of power. The total power dissipated in the amplifier is hence given by:

$$P_{avg} = \frac{2V_sI_p}{T}\int_0^{T/2}\sin(\omega t)\,\mathrm{d}t - \frac{2V_pI_p}{T}\int_0^{T/2}\sin(\omega t+\phi)\sin(\omega t)\,\mathrm{d}t \tag{6.3}$$

where the left hand term corresponds to the average input power of the amplifier:

$$\begin{aligned} P_{in} &= \frac{2V_sI_p}{T}\int_0^{T/2}\sin(\omega t)\,\mathrm{d}t \\ &= -\frac{2V_sI_p}{\omega T}\left[\cos(\omega t)\right]_0^{T/2} \\ &= \frac{2V_sI_p}{\pi} \end{aligned} \tag{6.4}$$

whilst the right hand term corresponds to the average power delivered to the load:

$$\begin{aligned} P_{load} &= \frac{2V_pI_p}{T}\int_0^{T/2}\sin(\omega t+\phi)\sin(\omega t)\,\mathrm{d}t \\ &= \frac{2V_pI_p}{T}\int_0^{T/2}\left[\cos(\omega t)\sin(\phi)+\sin(\omega t)\cos(\phi)\right]\sin(\omega t)\,\mathrm{d}t \\ &= \frac{2V_pI_p}{T}\left[\frac{1}{2\omega}\sin^2(\omega t)\sin(\phi)\right]_0^{T/2} + \frac{2V_pI_p}{T}\int_0^{T/2}\sin^2(\omega t)\cos(\phi)\,\mathrm{d}t \\ &= \frac{-V_pI_p}{2T}\cos(\phi)\int_0^{T/2}\left[e^{i2\omega t}-2+e^{-i2\omega t}\right]\,\mathrm{d}t \\ &= \frac{V_pI_p}{2}\cos(\phi) \\ &= V_{rms}I_{rms}\cos(\phi) \end{aligned} \tag{6.5}$$

where V_{rms} and I_{rms} are the root mean square voltage and current delivered to the load while the $\cos(\phi)$ term is known as the power factor. The total power dissipated into the amplifier is thus given by:

$$P_{avg} = \frac{2V_sI_p}{\pi} - V_{rms}I_{rms}\cos(\phi) \tag{6.6}$$

This expression can be differentiated to find the RMS voltage at which the average power dissipation in the amplifier is the greatest:

$$\left.\frac{V_{rms}}{V_s}\right|_{P_{max}} = \frac{\sqrt{2}}{\pi\cos(\phi)} \tag{6.7}$$

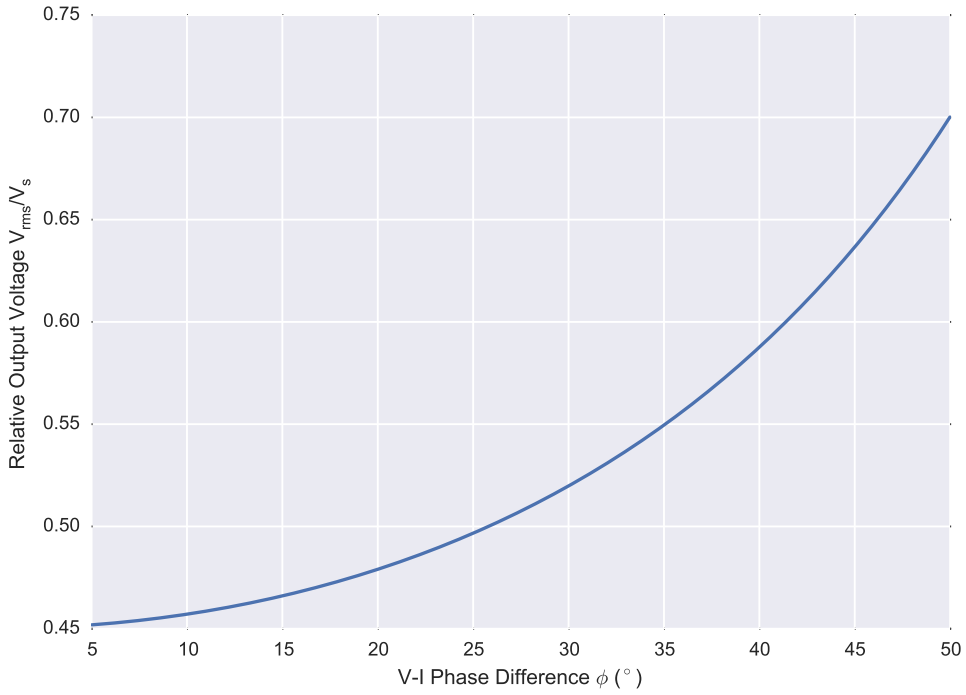

Figure 6.12: Relative output voltage corresponding to maximum power dissipation in current driver as a function of phase angle.

which is plotted in figure 6.12. Equation 6.7 can be substituted into equation 6.6 to find this maximum average power:

$$P_{max} = \frac{2V_s^2}{\pi^2 R} \tag{6.8}$$

which is independent of the frequency of the signal and of the reactance of the load, depending only on the resistive part of the impedance R. Whilst the average power dissipation is independent of the frequency and reactance of the load, the maximum instantaneous power clearly is not. We can demonstrate this from equation 6.2 by noting that for a purely reactive load the maximum instantaneous power dissipated by the amplifier equals the instantaneous input power, i.e. at that instant no power is delivered to the load. This stress is due to the phase lag between the output voltage and the output current, and is more easily analysed by looking at an SOA graph.

The SOA graph shows the operating parameters of instantaneous output current and voltage drop across the amplifier's output transistors $V_{CE} = V_s - V_o$ that should result in safe operation. There are several limiting factors: the maximum output current of the device operating with a low voltage drop is determined by

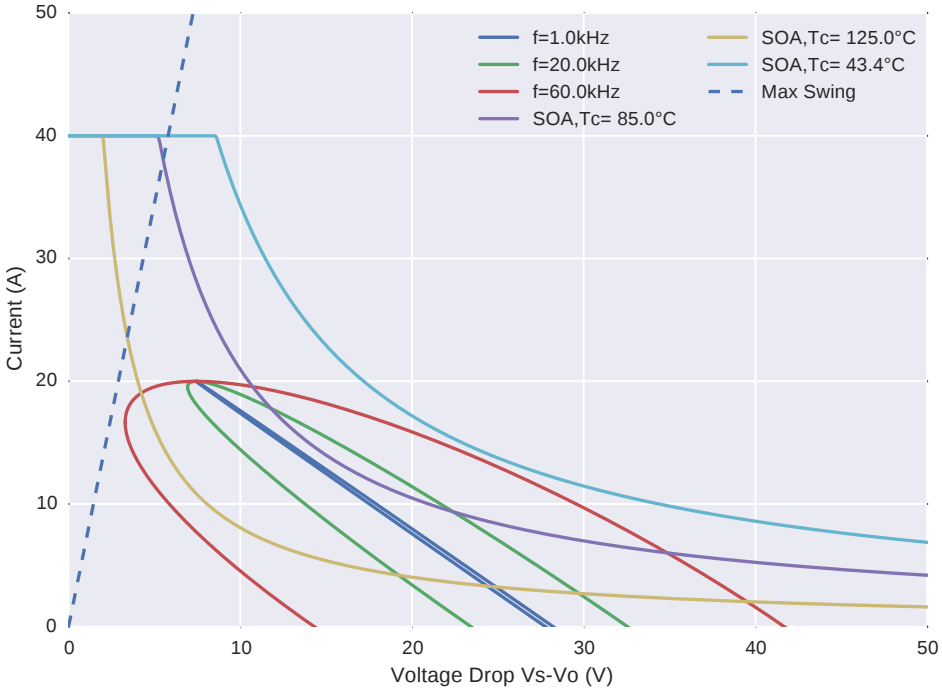

Figure 6.13: Linear plot of the safe operating area of the Apex PA50, and the excursions of the bespoke current driver at various switching frequencies assuming the average load of figure 6.10.

the fusing current of the bond wires; the instantaneous power dissipation provides the limit on the SOA graph in the intermediate region of voltage drop. Finally, the effect of secondary breakdown limits the safe current for high collector-emitter voltages, but this does not occur in MOSFET based devices and so does not need to be considered in this application. Purely resistive loads are the most simple and are represented on a linear plot of the SOA as a line, however as shown in figure 6.13 reactive loads split this line and instead trace out an ellipse. The safe operating area is dependent on the case temperature (T_c) of the amplifier, and this can be seen by observing that to maintain the junction temperature below the maximum value of 150 °C the average power dissipated in it has to be:

$$P_{avg} \leq \frac{150 - T_c}{R_{\theta jc}} \tag{6.9}$$

where $R_{\theta jc}$ is the thermal resistance of the amplifier's junction to case, and can be one of two values depending on whether the output waveform is AC or DC.

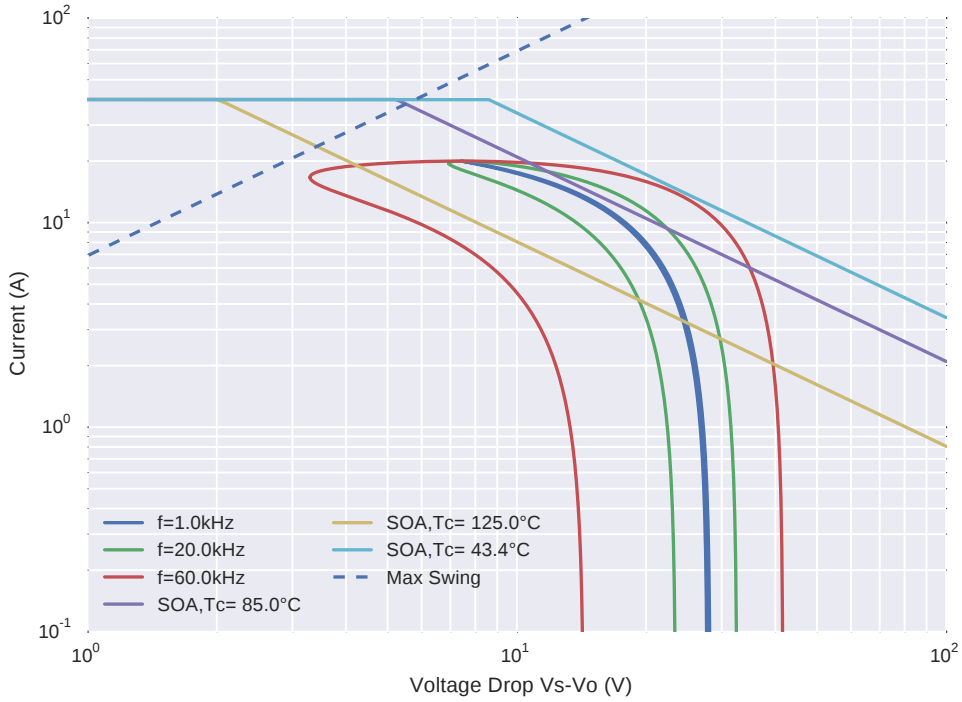

Figure 6.14: Safe Operating Area of the Apex PA50, and the excursions of the bespoke current driver assuming the average load of figure 6.10 at frequencies from 1 kHz to 60 kHz.

It follows that the maximum instantaneous output current to guarantee this temperature is maintained, is given by:

$$I_{SOA} \leq \frac{150 - T_c}{(V_s - V_o)\, R_{\theta jc}} \tag{6.10}$$

assuming that this value does not exceed the fusing current of the bond wires (40 A for the PA50). This equation is linear on a log-log plot and is usually presented in this way (see figure 6.14).

To calculate the steady state case temperature of the amplifier we use a thermoelectric model where the total power dissipated in the amplifier, P_{tot}, is given by the sum of the quiescent power of the amplifier P_q and the average power dissipation due to the driving of the load from equation 6.6:

$$\begin{aligned} P_{tot} &= P_q + P_{avg} \\ &= 2I_q V_s + P_{avg} \end{aligned} \tag{6.11}$$

where the quiescent power of each output transistor is given by the product of the

quiescent current ($I_q = 32\,\text{mA}$ maximum for the PA50) and the supply voltage. If the maximum RMS output voltage of the amplifier is below that given by equation 6.7 then the average power dissipation of the amplifier should never exceed P_{avg}. To ensure safety with any output voltage, however, we assume the maximum power dissipation possible from equation 6.8:

$$\begin{aligned} P_{tot}|_{max} &= 2I_qV_s + P_{max} \\ &= 2I_qV_s + \frac{2V_s^2}{\pi^2 R} \end{aligned} \tag{6.12}$$

The equilibrium case temperature can then be found as the amplifier is cooled by a heatsink:

$$\begin{aligned} T_c &= T_a + P_{tot}|_{max}\,(R_{\theta cs} + R_{\theta sa}) \\ &= T_a + \left[2I_qV_s + \frac{2V_s^2}{\pi^2 R}\right](R_{\theta cs} + R_{\theta sa}) \end{aligned} \tag{6.13}$$

where T_a is the temperature of the cooling reservoir for the heatsink, $R_{\theta cs}$ is the thermal resistance between the amplifier's case and the heatsink ($R_{\theta cs} = 0.05\,^\circ\text{C}\,\text{W}^{-1}$ for the PA50's TO-247 package with correctly applied thermal paste) and $R_{\theta sa}$ is the thermal resistance of the heatsink to the cooling reservoir. The heatsink chosen (Apex HS11) had the lowest thermal capacity that was available $R_{\theta sa} = 0.1\,^\circ\text{C}\,\text{W}^{-1}$ when used with a water cooling system with a sufficiently high flow rate, and this cooling water was assumed to have a conservative temperature of $T_a = 20\,^\circ\text{C}$.

The only things that remain to be decided are the voltages for the supply and the boost rails. To maintain the greatest voltage swing we know from earlier that the boost rails must be 10 V greater than those of the supply. Under these conditions the maximum swing, i.e. the minimum voltage drop across the amplifier is given by:

$$(V_s - V_o)\big|_{min} = I_o R_{drop} \tag{6.14}$$

where the worst case value for the PA50 is assumed ($R_{drop} = 0.145\,\Omega$) to give the dashed lines of figures 6.13 and 6.14. Now a supply voltage must be chosen that is high enough such that the path of the instantaneous power dissipation of the amplifier does not encroach on this dashed line, but low enough that the resulting case temperature of the amplifier produces a SOA curve that stays above the amplifier's excursions. The SOA graphs show that the restrictions provided

by all of these curves are satisfied by a supply voltage of $V_s = 28\,\mathrm{V}$ at frequencies from 1 kHz to 60 kHz, and these result in a maximum amplifier case temperature of $T_c = 43.4\,^{\circ}\mathrm{C}$.

The model used up until this point has ignored the influence of the Schottky diodes other than the switching action that they perform. Simulations and measurements both show however that the non-linear action of the diodes conspires with the series inductance of the half-wave rectifiers to produce strange current waveforms. In a newly designed system it would be more sensible to drive each SMOT wire pair with a separate amplifier, with the rectification occurring to the signal and not within the MOT wires themselves. The author was prevented from doing so in this experiment due to the wire pairs being connected within the vacuum chamber, a configuration that arose as a result of the limited number of connections on the vacuum feedthrough and because it did not impede the FET based switching that is was originally designed for.

To confirm the results of the calculations a SPICE simulation was undertaken to ensure the amplifier remained stable, that it did not overheat either the load resistors or itself and that it produced the correct output waveforms. The simulations were performed in LTSpice with a model of the PA50 provided by Apex Microtechnology and a model of the SCS230AE2 Schottky diodes by ROHM Semiconductor.

The final schematic of the amplifier is shown in figure 6.15. This diagram shows the PA50 used as a voltage controlled current amplifier with the wires of the SMOT placed in the feedback loop. The output current is determined by five 100 W 5 Ω resistors (MP9100 series from Caddock Electronics, Inc.) which are wired in parallel to act as a 1 Ω sense resistor (shown in figure 6.11). The amplifier provides a transconductance gain of approximately $10\,\mathrm{A\,V^{-1}}$ by driving the necessary voltage across the sense resistor that ensures the current passing through the feedback resistor equals to that flowing through the input resistor. A soft-mute circuit described by J.Firestone[120] is included in the design to prevent damage to the amplifier if power is initialized during the peak of waveform.

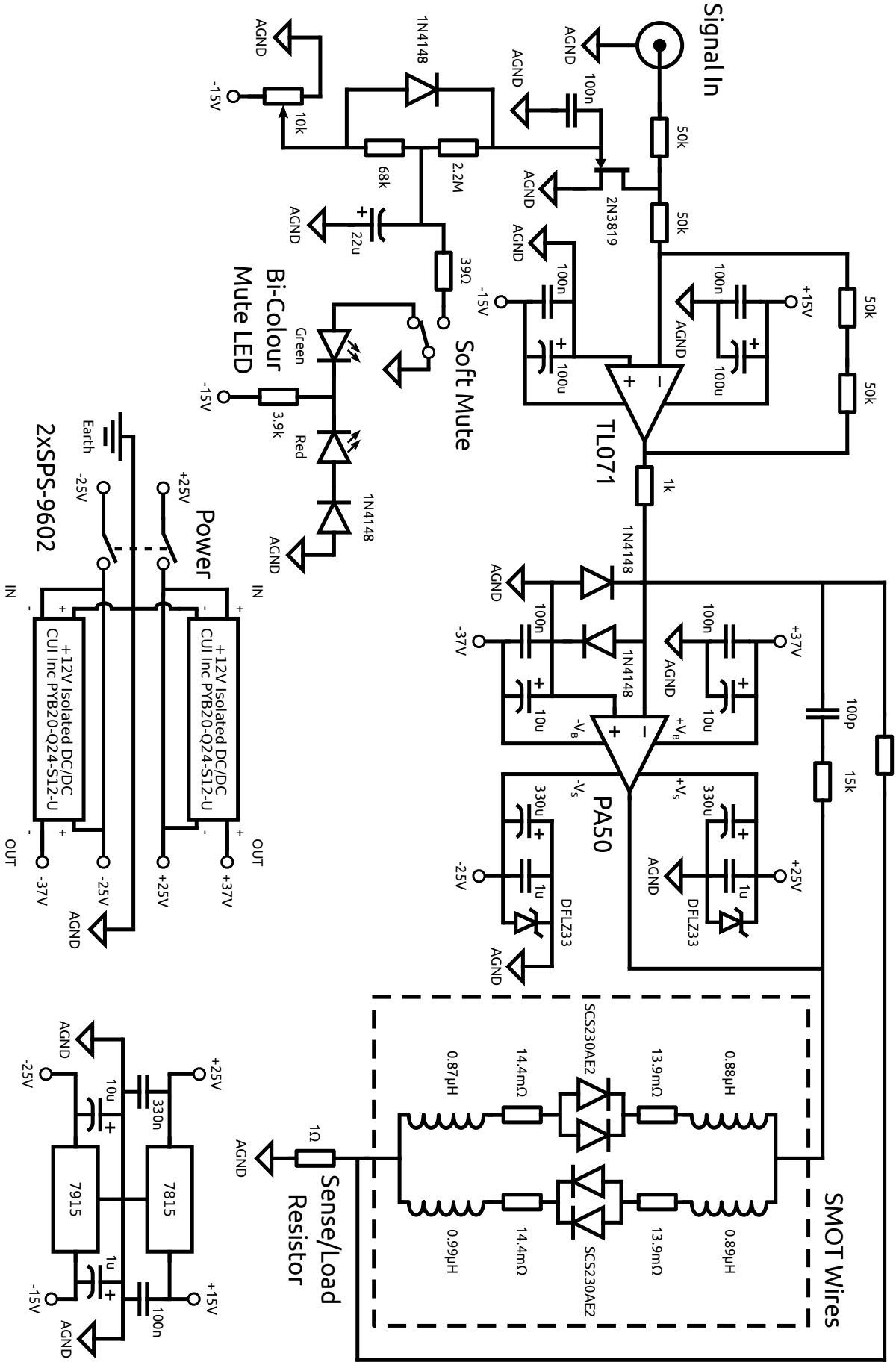

Figure 6.15: Schematic of bespoke current driver based around the Apex Microtechnology PA50 power operational amplifier.

6.2.3.1 The Skin Effect

As an alternating current passes through a conducting wire, time varying magnetic fields are created which circulate around the wire's axis. These changing magnetic fields self induce eddy currents within the wire which act to increase the current density at its surface, and conversely decrease the current density toward its centre. This is known as the skin effect, and can be calculated by solving Maxwell's equations within a conductor[121]. At higher frequencies the skin effect becomes more pronounced, acting to confine the conduction within a thin surface layer, reducing the effective cross sectional area of the wire and hence increasing its resistance. The skin effect can be characterized by the 'skin depth', the distance from the wire's surface at which the current density drops to $1/e$ of its maximum:

$$\delta = \sqrt{\frac{2}{\mu_r \mu_0 \epsilon_r \epsilon_0 \omega^2}} \left[\sqrt{1 + \left(\frac{\sigma}{\epsilon_r \epsilon_0 \omega} \right)^2} - 1 \right]^{-\frac{1}{2}} \tag{6.15}$$

this relationship can be simplified by assuming that the material is a good conductor ($\sigma/(\epsilon_r \epsilon_0 \omega) >> 1$):

$$\delta \approx \sqrt{\frac{2\rho}{\omega \mu_r \mu_0}} \tag{6.16}$$

where relative permeability of the material is approximately equal to one for copper. It was a concern that the high currents output from the current driver would be so great that they would both cause an unacceptably high level of resistance at the greatest desired frequency of 60 kHz, but also exceed the ampacity of the output wires due to the small cross sectional area in which the alternating current flows. The current driver was designed to output a maximum peak to peak current of 40 A, corresponding to an RMS current of $\sim$ 14.1 A. Ignoring the influence of the skin effect, a 16AWG ($\sim$ 1.3 mm^2) copper wire with 90 °C rated insulation is judged by the United States National Electric Code to have an ampacity of $\sim$ 18 A, sufficiently high to carry the required currents. Assuming that the current has an oscillation frequency of 60 kHz and the copper at room temperature has a resistivity of $\rho = 17.2\,\mathrm{n\Omega\,m}$, then the corresponding skin depth is $\delta \approx 269\,\mu\mathrm{m}$. The region that lies within the skin depth represents $\sim$ 66 % of the cross sectional area of the wire and as a result the actual conducting area is equivalent to $\sim$ 17.8AWG.

One method of reducing the influence of the skin effect is simply to use larger gauge wires so that there is a greater surface area under which the majority of the current

can flow. Welding cables were considered for this purpose, however their thickness makes them unwieldy, particularly when they need to be soldered to the relatively small contacts of the vacuum feedthrough and the current driver. An alternative method is to use litz wire, bundles of enamelled copper wires that are woven in a particular arrangement to break up the eddy currents in the core of the wires and to increase the surface area of copper. Litz wire is often encountered in induction heaters, high frequency transformers and radio systems and the laminations in transformer cores rely on a similar principle.

In order to choose the number of wires and the winding procedure, the method described by C.Sullivan and R.Y.Zhang was followed[122]. First a spool of enamelled wire was chosen with a diameter smaller than the skin depth of the highest frequency component, $d_s = 0.1\,\text{mm}$ was selected as it was the smallest wire available. The wire has a current rating of 30 mA, so it may seem logical to just twist a bundle of ~ 475 of these together to allow the maximum RMS current of 14.1 A. This would not prevent a 'bundle-level' skin effect, whereby wires at the centre of the bundle are underutilized due to the differing average magnetic field strength from those on the outside. Litz wire weaving is designed so each wire spends approximately the same amount of time at every radial position within the bundle, meaning that the currents must be shared equally between the strands[122, 123].

If only a simple twist is employed then a maximum of five wires can be bundled before they tend to arrange themselves such that they accumulate around a central wire. Multiple bundles can then be twisted together in subsequent steps, again in maximum groups of five, to always ensure equal currents for an arbitrary number of strands. For example, a litz wire consisting of 125 strands can be constructed by twisting these equal lengths into 25 groups of 5 wires, these 25 bundles of wires are then twisted into 5 groups of 5x5 litz which are finally twisted together to give a 5x5x5 litz wire. This method is rather laborious due to the large number of steps involved however it can be safely accelerated by increasing the number of wires in the lowest level bundle until the bundle diameter equals to two skin depths, the point where bundle-level skin effect starts to become significant[122]. In order to calculate the maximum number of wires in the first bundle an effective skin depth is used to take account of the voids that result from the imperfect wire packing:

$$\delta_{eff} = \frac{\delta}{\sqrt{F_p}} \tag{6.17}$$

where F_p is the litz packing factor, the ratio of the total cross sectional area of the n strands ($n\pi d_s^2/4$) to the cross sectional of the whole bundle ($\pi d_b^2/4$). This

Figure 6.16: The 'Leonardo' style rope winding machine used to produce the home-made litz wire. The bracket on the right of the image holds five hooks which turn simultaneously through the use of a crank. The left block holds a large hook which can be fixed in place or allowed to rotate. The separator is visible at the bottom of the image. Based upon[122].

equation can be found from 6.16 by assuming an average resistivity of the bundle $\rho_{eff} = \rho/F_p$.

$$d_b = 2\delta_{eff} = \frac{2\delta}{\sqrt{F_p}} = \frac{2\delta d_b}{\sqrt{n} d_s} \tag{6.18}$$

$$n = \frac{4\delta^2}{d_s^2} \tag{6.19}$$

For the skin depth calculated at the greatest SMOT switching frequency this results in a maximum lowest level bundle size of $n \sim 29$ strands, however in construction of the wire it was deemed easier to have an even number, so 28 strands were used to err on the side of safety. The final litz construction was thus decided to be 28x5x5, consisting of 700 individual strands with a total current rating of 21 A. The current rating exceeded the requirement of ~ 14.1 A both to account for any strands that may break and to simplify construction. In order to weave this wire, a 'Leonardo rope winding machine' was built (see figure 6.16)

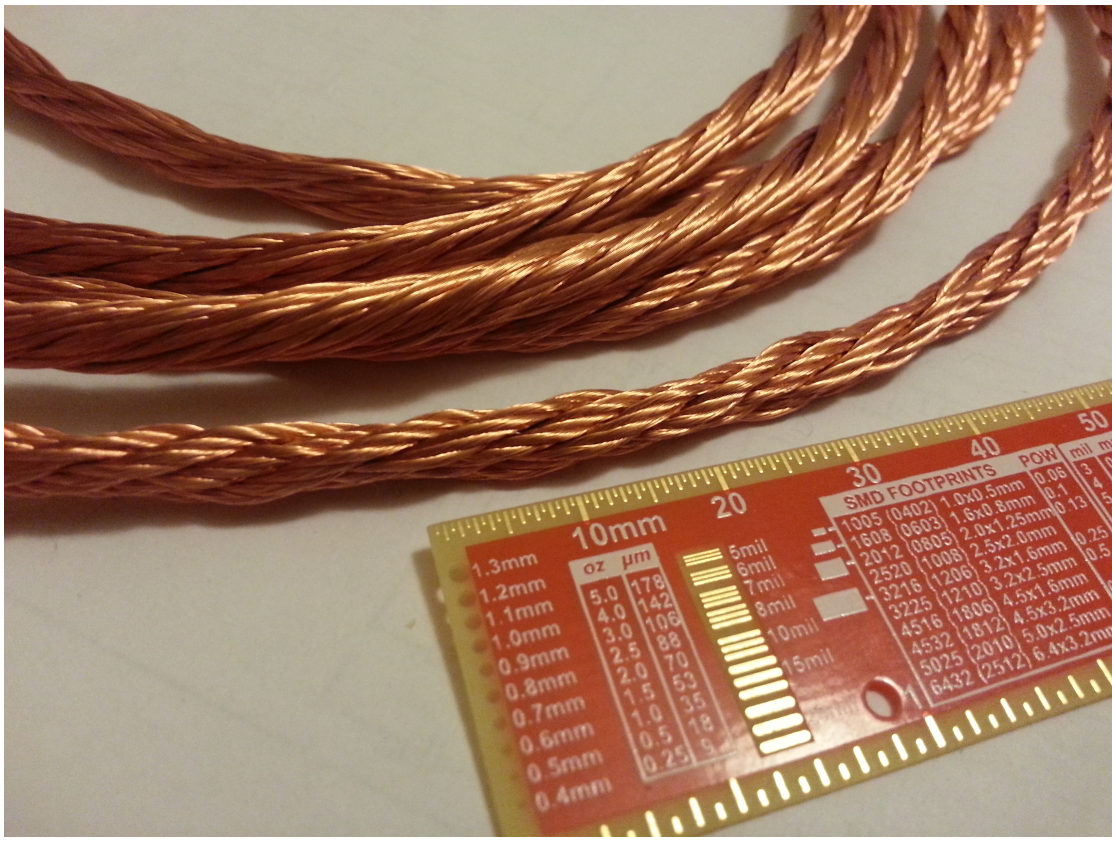

Figure 6.17: 28x5x5 litz wire wound from 0.1 mm diameter enamelled copper wire that was constructed using a Leonardo rope winding machine.

consisting of a large hook which could be either fixed or allowed to rotate and a separate series of five smaller hooks that turn in synchronization through the use of a crank. Each winding operation was preceded by threading the enamelled wire back and forth between the two sets of hooks so that each of the five smaller hooks connected 28 strands to the larger one. A separating disc with five notches was then inserted between the wires at the location of the large hook to ensure that the individual bundles of 28 did not prematurely twist together. The crank was then turned to achieve a pitch of approximately one twist per centimetre in each of the five bundles and then the large hook was allowed to rotate as the separator was brought forward to allow the five bundles to 'zip' together. Five of these 28x5 litz wires were constructed before being reattached to the winding machine to complete the final 28x5x5 weave that is shown in figure 6.17.

The efficacy of the home-made litz wire was compared to that of a commercial design purchased from RMCybernetics consisting of a 6x4 construction of 0.25 mm diameter enamelled wire. Each wire was tested by being soldered in series with a 51 Ω resistor to create a voltage divider, then after being connected to a signal generator the input and output voltages were measured as a function of frequency.

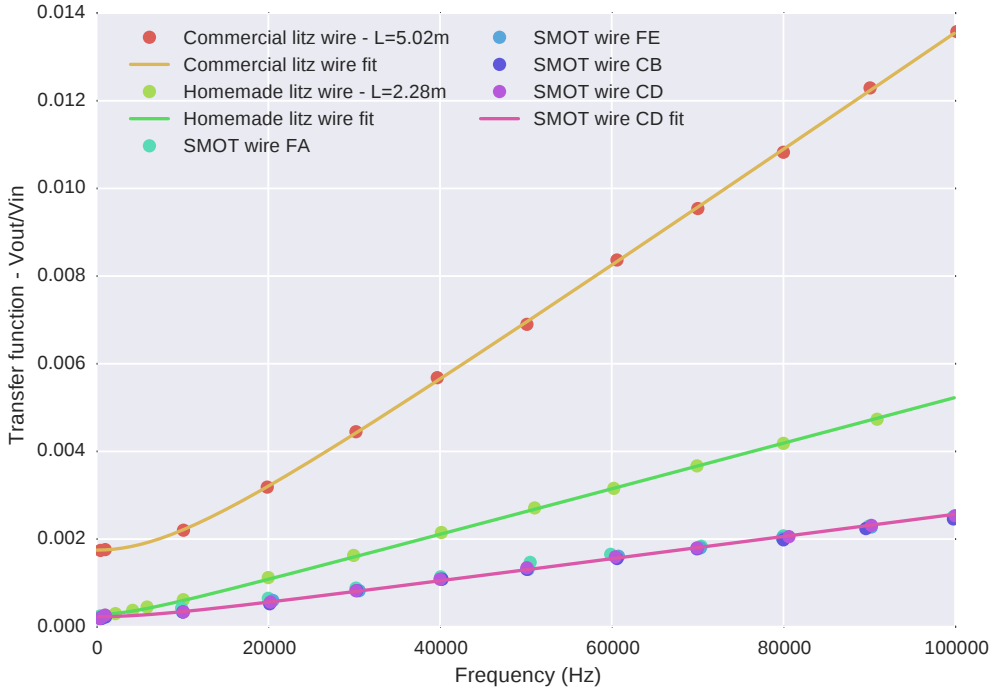

Figure 6.18: Comparison of the inductance of commercial and home made litz wire via measurement of the transfer function of a voltage divider. Measurements of the SMOT wires are shown for reference, which were probed directly at the terminals of the vacuum chamber.

Modelling each litz wire as an inductor in series with a resistor yields a transfer function of:

$$\frac{V_{out}}{V_{in}} = \frac{\sqrt{\left[R_L\left(R_L+R\right)+\left(\omega L\right)^2\right]^2+\left[\omega L R\right]^2}}{\left(R_L+R\right)^2+\left(\omega L\right)^2} \tag{6.20}$$

where R is the resistance of the $51\,\Omega$ resistor, R_L is the DC resistance of the litz wire and L is the inductance of the litz wire. Figure 6.18 shows the data and fits to the two types of litz wire in addition to fits of the wires internal to the SMOT shown for reference. The fits to the data showed that the home-made litz wire had a inductance per unit length of $0.19\,\mu\mathrm{H\,m^{-1}}$ compared to the commercial wire's $0.22\,\mu\mathrm{H\,m^{-1}}$, while all of the SMOT's wires had inductances around $0.21\,\mu\mathrm{H}$. In conclusion, the home-made woven litz wire has been shown to have better performance than that of the commercial design. It remains to be seen if the improvement was worth the effort of its construction, however the home-made litz was weaved at a time when the commercial product was not yet available. Interestingly it has been suggested that standard stranded wire without

individually enamelled strands can be used as a low cost alternative to litz wire, however this method was not adopted here[124].

6.3 MOT Loading Rate and Atom Number

The first parameters of the SMOT that are to be characterized here are the loading rate, the atom lifetime and atom number. All of these values are to be taken with respect to the SMOT switching frequency, and can all be derived from measurements of the atom cloud fluorescence as the trap is turned on.

Given a scattering rate Γ_s, atom number N and photon energy $\hbar\omega$ a cloud of atoms trapped within a MOT will fluoresce a power given by:

$$P = N\Gamma_s\hbar\omega \tag{6.21}$$

where the scattering rate is given by equation 3.1. This power will be uniformly radiated over a solid angle of 4π, so if a lens of diameter D is positioned at a distance f away from the atom cloud then it will be able to capture a proportion of its fluorescence corresponding to a cone of half-angle $\theta_F = \tan^{-1}(\frac{D}{2f})$. By integrating the infinitesimal element of solid angle we can find the proportion of light emitted into this cone:

$$\int_0^{2\pi}\int_0^{\theta_F}\frac{1}{4\pi}\sin\theta\,\mathrm{d}\theta\mathrm{d}\phi = \sin^2\left[\frac{1}{2}\tan^{-1}\left(\frac{D}{2f}\right)\right] \tag{6.22}$$

This shows the obvious result that the closer an imaging lens is to the radiation source and the larger the lens is, the greater the proportion of the MOT's power will be able to be captured. If the lens focuses this proportion of the MOT's fluorescing power, P_{PD}, onto a photodetector with a wavelength dependent responsivity $R(\lambda)$ and transimpedance gain G, it will output a voltage V:

$$V = P_{PD}R(\lambda)G\eta \tag{6.23}$$

where the η term describes the efficiency of the optical system. A MOT has a loading rate R and an atom lifetime of τ, which leads to the simple differential equation that describes the number of atoms in the MOT[125]:

$$\frac{\mathrm{d}N(t)}{\mathrm{d}t} = R - \frac{N(t)}{\tau} \tag{6.24}$$

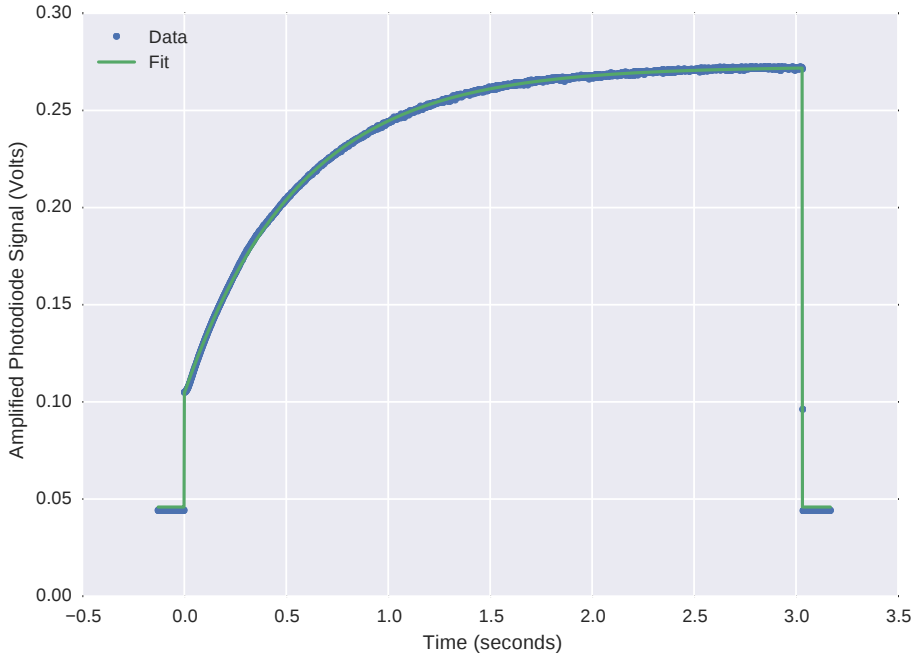

Figure 6.19: Loading curve of the SMOT at a switching frequency of 20kHz. The fit to the data shows a rise-time of approximately 0.56s. If the conversion from photodiode voltage to the MOT's emitted optical power is known then the loading rate of the MOT can be calculated.

Solving this equation yields the result:

$$N(t) = N_0(1 - e^{-t/\tau}) \tag{6.25}$$

where $N_0 = R\tau$ corresponds to the maximum atom number that the trap holds when the system has reached equilibrium. Given the information we have the steady state atom number can be derived:

$$N_0 = \frac{V_0}{\eta R(\lambda) G} \frac{1}{\Gamma_s \hbar\omega} \frac{1}{\sin^2\left[\frac{1}{2}\tan^{-1}(\frac{D}{2f})\right]} \tag{6.26}$$

where V_0 is the maximum voltage rise measured by the photodiode, which occurs when the atom number is maximised. The atom number is proportional to the rise of the photodiode voltage, so the trap lifetime τ can be found simply by determining the time constant of the voltage rise as the trap fills.

Figure 6.19 shows an example of a SMOT loading curve taken at a switching frequency of 20 kHz. The atom fluorescence was measured by positioning a column of collection optics underneath the vacuum chamber that focused the emitted light

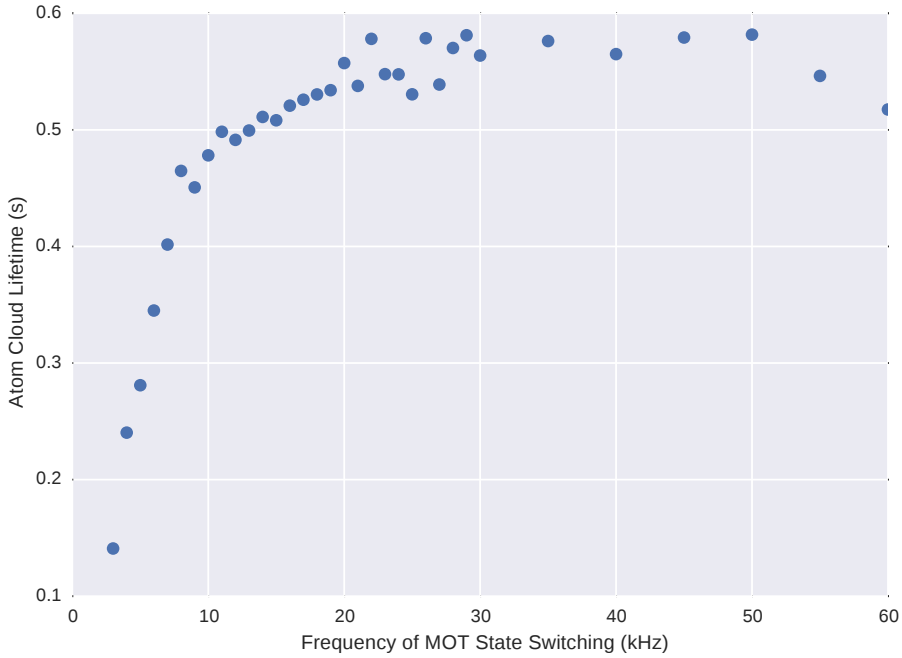

Figure 6.20: Frequency dependence of the atom cloud lifetime in the SMOT. The data points of this figure were generated from fits to MOT loading curves such as that shown in figure 6.19.

upon a Thorlabs PDA36A-EC photodetector. The optical column had an optical efficiency of $\eta \sim 63\,\%$ and the detector had an responsivity of $R(\lambda) \sim 0.48\,\mathrm{A\,W^{-1}}$ and a gain of $1.5 \times 10^6\,\mathrm{V\,A^{-1}}$. In an earlier version of the experiment control of the loading was determined by attenuating the sine wave signal to the audio amplifier that generates the switching magnetic fields, but more recently the loading was determined by externally controlling the switching AOMs to completely shutter off all light into the chamber. The voltage output from the photodetector can be modelled with the following function:

$$V(t) = V_{bg} + \left[V_{lbg} + V_0(1.0 - e^{(t_0-t)/\tau})\right] H(t-t_0)H(t_1-t) \tag{6.27}$$

where $H(t)$ is the Heaviside step function, t_0 is the time when the laser beams are turned on and the MOT begins loading, t_1 is the time when the beams are turned off, V_{bg} is the background voltage caused by ambient light on the photodiode when the lasers are shuttered and V_{lbg} is the background voltage that is due to the scatter of the laser beams. This function has been fit to the data in figure 6.19 to find the atom lifetime at a switching frequency of 20 kHz, whilst figure 6.20 shows the result of 34 similar fits to determine the trap lifetime with respect to

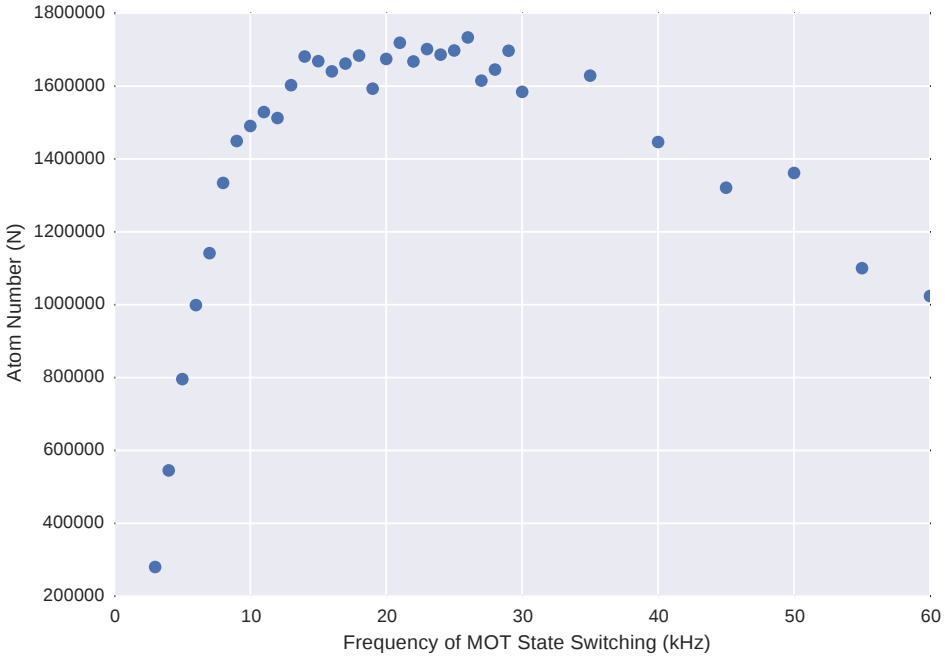

Figure 6.21: Frequency dependence of the atom number in the SMOT. The data points of this figure were generated from fits to MOT loading curves such as the one shown in figure 6.19.

switching frequency. The fits to these plots have also been used in combination with equation 6.26 to determine the frequency dependence of the SMOT atom number (figure 6.21), and the loading rate (figure 6.22).

The data indicates that the SMOT performs optimally at frequencies between 15 kHz to 30 kHz where the atom number peaks around 1.7×10^6. Looking at figures 6.20 and 6.22 it seems that both the loading rate and atom lifetime contribute to the rapid increase in atom number below 15 kHz, whilst the drop off in atom number above 30 kHz is purely due to a reduced loading rate.

Figure 6.23 shows a comparison between the atom numbers of microfabricated pyramidal MOTs, grating MOTs and switching MOTs at varying trap volumes. In the ranges tested, and as mentioned in section 3.6, the microfabricated pyramidal MOTs exhibit $N \propto L^6$ scaling while the grating MOTs exhibit $N \propto L^{3.6}$ scaling. The scaling relationship of the SMOT seems to be $N \propto L^{4.5}$, however this is only based upon two data points which were taken with wildly different parameters, and so this number should only be regarded as a first estimate. The data point of the SMOT with the lower trap volume was taken from measurements using the Behringer audio amplifier, whilst the other data point corresponds to the loading rate measurements that have already been presented in this section, which were

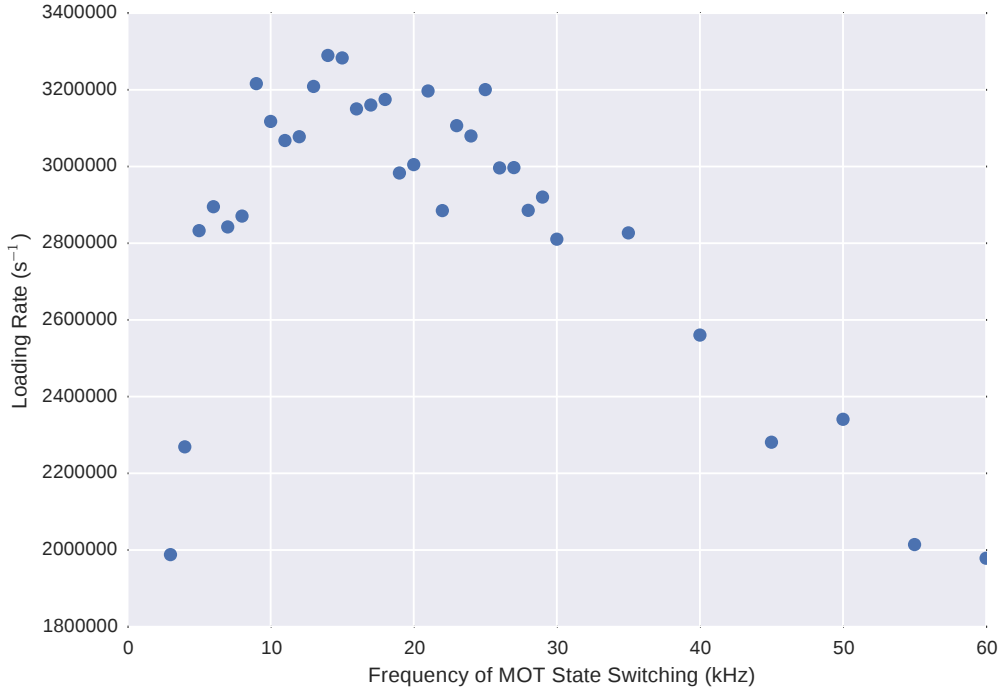

Figure 6.22: Frequency dependence of the loading rate in the SMOT. The data points of this figure were generated from fits to MOT loading curves such as that shown in figure 6.19.

all collected with the new bespoke current driver. Due to the much higher field gradients offered by the new amplifier, it would seem reasonable to expect that if the data point corresponding to the smaller trap volume were to be retaken it would produce a greater atom number, and this should give a better fit to the scaling law for large traps. Regardless of the scope for possible improvements, the atom numbers shown here are still fairly respectable given the trap volumes, and indicate that the SMOT performs somewhere between the two alternative geometries. It is not particularly surprising that the atom number of the SMOT should be lower than the grating MOT, because for rapidly switching beams the atoms only experience a slowing force in each axis for half the time they are in the trapping region, and so have an effective stopping distance that is half of a DC MOT with otherwise similar parameters. In creating figure 6.23, the trap volume due to a beam of width w was estimated as a regular square pyramid with sides of length w and height $w/2$ situated above a cuboid with dimensions $w \times w \times w(\sqrt{2}-1)$. The trap volumes were thus given by $V = \frac{w^3}{2}(\sqrt{2}-2/3)$.

All of the data in this section, except for the data point of figure 6.23 with an atom number of $\sim 8.0 \times 10^4$, was taken with a peak current of 20 A through the SMOT's

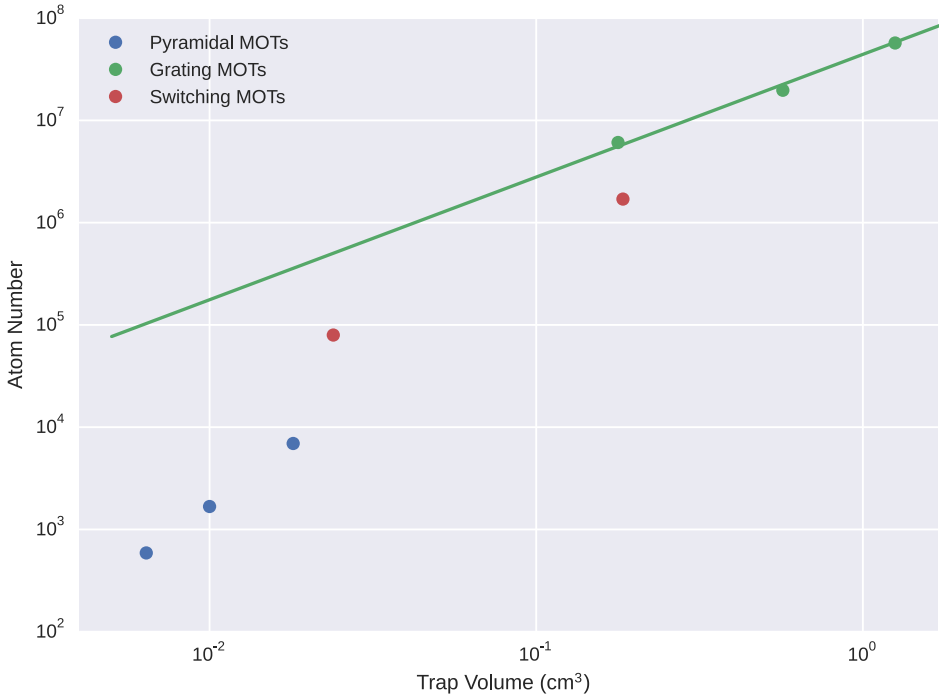

Figure 6.23: Atom number dependence on trap volume for microfabricated pyramidal MOTs[78], grating MOTs[86] and switching MOTs. The scaling law for the SMOT is $N \propto L^{4.5}$, but given the traps had wildly different detunings, beam intensities and magnetic field gradients the relationship should only be regarded as an initial estimate.

wires corresponding to a magnetic field gradient of $6.8\,\mathrm{G\,cm^{-1}}$. The cooling laser had a detuning of $\delta = -2\pi{\cdot}10.5\,\mathrm{MHz}$, with the two pairs of beams having average (post shuttered) powers of 1.9 mW and 2.1 mW, both with a $1/e^2$ radius of 4.0 mm. The pressure reading on the ion pump was 2.1×10^{-9} mbar, which given the peak atom lifetime of figure 6.20 indicates a pressure conversion of $(1.2 \times 10^{-9}\,\mathrm{mbar\,s})/\tau$ rather than the $(2 \times 10^{-8}\,\mathrm{mbar\,s})/\tau$ measured by Arpornthip *et al.*[40]. The discrepancy can be accounted for by considering that the atom source was located in the main SMOT chamber whilst the ion pump was attached to the chamber via a right angled port on a cross shaped vacuum pipe. The finite vacuum conductance of the path from the chamber to the pump means that the pressure in the SMOT chamber would have been higher than the measured value, and thus this would have led to an underestimate of the conversion factor between atom lifetime and chamber pressure. The data point from figure 6.23 with an atom number of $\sim 8.0 \times 10^4$ was taken with the Behringer audio amplifier driving a peak current of 4.9 A through the SMOT's wires, corresponding to a magnetic field gradient of $1.7\,\mathrm{G\,cm^{-1}}$. The cooling laser had a detuning of $\delta = -2\pi{\cdot}5.5\,\mathrm{MHz}$, and each beam

had an average (post shuttered) power of 2 mW and a $1/e^2$ radius of 2.0 mm. The pressure reading on the ion pump was 1.7×10^{-9} mbar.

6.4 Temperature measurements

There are a number of methods that can be used to measure the temperature of atoms in a magneto optical trap. These include 'Release and Recapture', 'Time of Flight' and Raman velocimetry[76, 126]. Whilst release and recapture can be implemented relatively easily, the author did not have a great deal of confidence in the accuracy of the technique because the temperature calculation requires knowledge of the volume of the capture region within the MOT, which is ill defined. Raman velocimetry is an interesting way of directly probing an atom cloud's velocity distribution through the use of velocity sensitive Raman pulses, however the equipment was not available here to perform that type of measurement. The two methods that were employed here to measure the SMOT's temperatures are both considered time of flight measurements, and these techniques work by probing the spatial distribution of cooled atoms that are released from the trap after they are allowed to expand for a number of different 'flight' times.

6.4.1 Light Sheet

The first method attempted to calculate the MOT temperature was through the use of a 'light sheet'. This technique entails focusing a resonant beam of light to a wide, but thin sheet that lies underneath the trapping region.

Upon extinguishing the cooling beams the atoms are allowed to escape the trap, so they fall due to gravity and pass through the sheet. As the atom cloud descends it expands in all directions, giving rise to a time dependent width that is determined by its temperature. This spread of atomic positions can be probed by measuring the time dependence of either the absorption or the fluorescence of the slice of atoms that intersects the light sheet, and numerical fits to this data can then determine the achieved temperature.

The SMOT's mirror was located very close to a viewport underneath the vacuum chamber to allow for the trapping beams to enter the chamber at 45° to the window's surface. As a result of this constraint there was no direct line of sight through the side of the vacuum chamber under the trapping region and so as seen

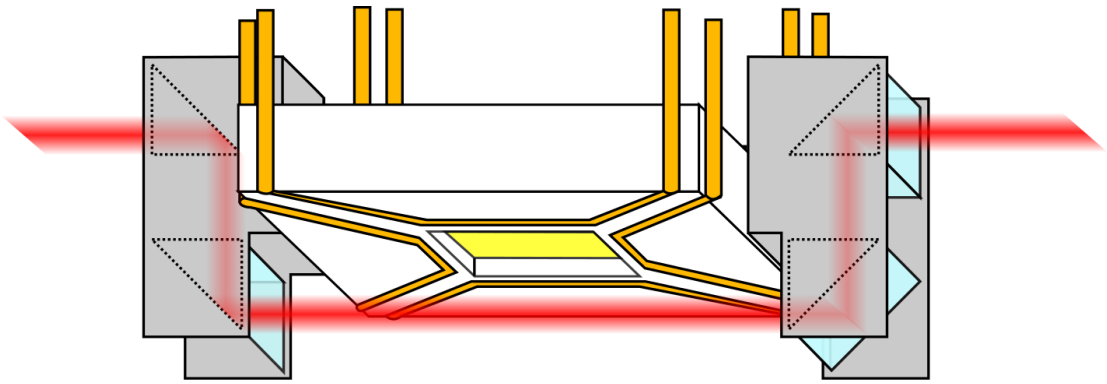

Figure 6.24: Diagram of the beam path of the light sheet used to determine atom cloud temperature in the SMOT.

in figure 4.2 and as illustrated in figure 6.24 a pair of periscopes were required to redirect the light sheet underneath the trap. To create the light sheet, a small portion of the cooling beam was removed from the laser setup before it reached the optical shutters (see figure 6.3). This cooling light was then passed through a telescope built from a pair of cylindrical lenses to reduce the beam's vertical size, and was then passed through the vacuum chamber via the periscopes. This light was then retro reflected to produce a counter propagating light sheet approximately 10 mm below the trapping region of the MOT.

After an atom cloud within the trap becomes fully loaded the cooling beams are turned off by attenuating the driving signal to the switching AOMs, which is achieved through the use of the control pins of the Minicircuits Z80-DR230-S+ RF switch shown in figure 6.25. In the absence of the trapping beams the atoms are released from the trap and allowed to fall through the light sheet. The absorption of the retro-reflected light sheet was then observed with a photodiode while a column of optics underneath the chamber focused the scattered light from the light sheet onto a second photodiode (see figure 6.26).

Whilst extremely high sensitivity to low atom numbers have been reported with this technique, with some groups being able to measure the mere hundreds of atoms expanding upwards after being released from confinement[127], no signal was ever detected to come from the light sheet, even with the use of a lock-in amplifier to increase sensitivity. Due to the complete absence of any signal it was questioned whether the atoms were being thrown to the side of the light sheet upon being released from the trap. However from the subsequent time of flight imaging it became clear that the atom cloud dropped vertically as expected.

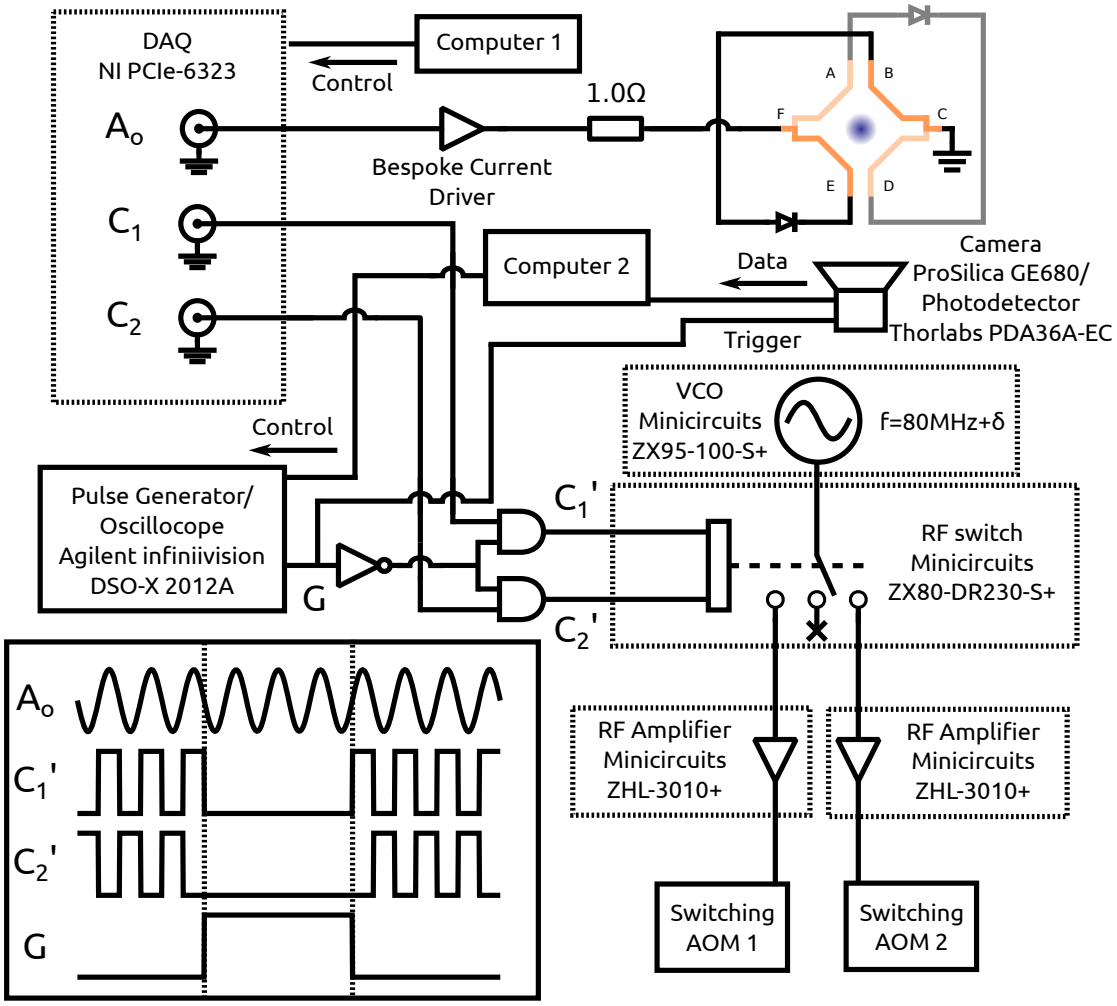

Figure 6.25: Electronics set-up to perform the SMOT switching and pulsing for loading rate and temperature measurements. Computer 1 is used to configure a data acquisition card, which is used to generate three signals at the SMOT switching frequency. One of the signals is a sine wave and is fed to an audio amplifier to perform the current switching. The remaining signals are two square waves which are π out of phase with each other and these are sent to an RF switch to control which switching AOM receives the driving signal from a VCO. The driving signal to both switching AOMs can be turned off by the use of a gate voltage output from a pulse generator, and this same pulse can be used to trigger the shutter of a fast camera which images the cold atom cloud. Computer 2 is used to control the output of the pulse generator and to download images from the fast camera. A photodetector can be positioned in place of the camera in order to collect fluorescence for loading rate data, and this can be measured by an oscilloscope, which also serves as the pulse generator.

To understand why there was no signal detected we first consider the background pressure within the vacuum chamber, which we assume to be $P_{BG} = 1.0 \times 10^{-9}$ mbar at a temperature of $T_{BG} = 300$ K. The ideal gas law can be used to determine the number density of atoms within the background vapour:

$$\frac{N}{V} = \frac{P_{BG}}{k_B T_{BG}} \sim 2.4 \times 10^7 \,\text{atoms}\,\text{cm}^{-3} \tag{6.28}$$

where k_B is the Boltzmann constant. The light-sheet method was only attempted while the magnetic fields were generated with the Behringer audio amplifier. This configuration produced a maximum of $N \sim 8.0 \times 10^4$ atoms at a switching frequency of 20 kHz, and as shown in the following subsection this corresponded to a cloud of Gaussian width $\sigma = 280$ µm with a temperature of ~ 260 µK. The density of the cloud can be estimated by taking the volume of the atom cloud as a sphere with radius equal to the Gaussian width, and this leads to an initial density of 8.7×10^8 atoms cm^{-3}. The Gaussian width, $\sigma_c(t)$, of the atom cloud after a time of flight of length t can be modelled by the function[86]:

$$\sigma_c(t)^2 = \sigma_{c0}^2 + \frac{k_B T}{M} t^2 \tag{6.29}$$

where σ_{c0} is the size of the atom cloud before expansion, T is its temperature and M is the mass of a single atom of ^{85}Rb. If this atom cloud were to be released from the trap then it would ballistically expand as it falls the $d = 10$ mm separation between the trapping region and the light sheet. The centre of mass of the atom cloud would take $t = \sqrt{2d/g} \sim 45$ ms to reach the light sheet as it accelerates due to gravity, by which time it will have expanded to a Gaussian width of 720 mm. This expanded cloud would have a corresponding density of 5.1×10^4 atoms cm^{-3}, significantly lower than that of the background vapour. If the minimum detectable signal from the light sheet's fluorescence is given at the point where the atomic density of the expanded MOT equals to the background vapour, then this would explain the lack of any perceived signal. The situation is even worse when attempting to resolve a signal in the light sheet's absorption, because the path length of the beam in the chamber (~ 200 mm) is over an order of magnitude longer than the path length of the beam through the expanded cloud.

6.4.2 Time of Flight Imaging

Due to the difficultly in detecting a signal with the light sheet technique it was decided that it should be abandoned and in its place, time of flight imaging was

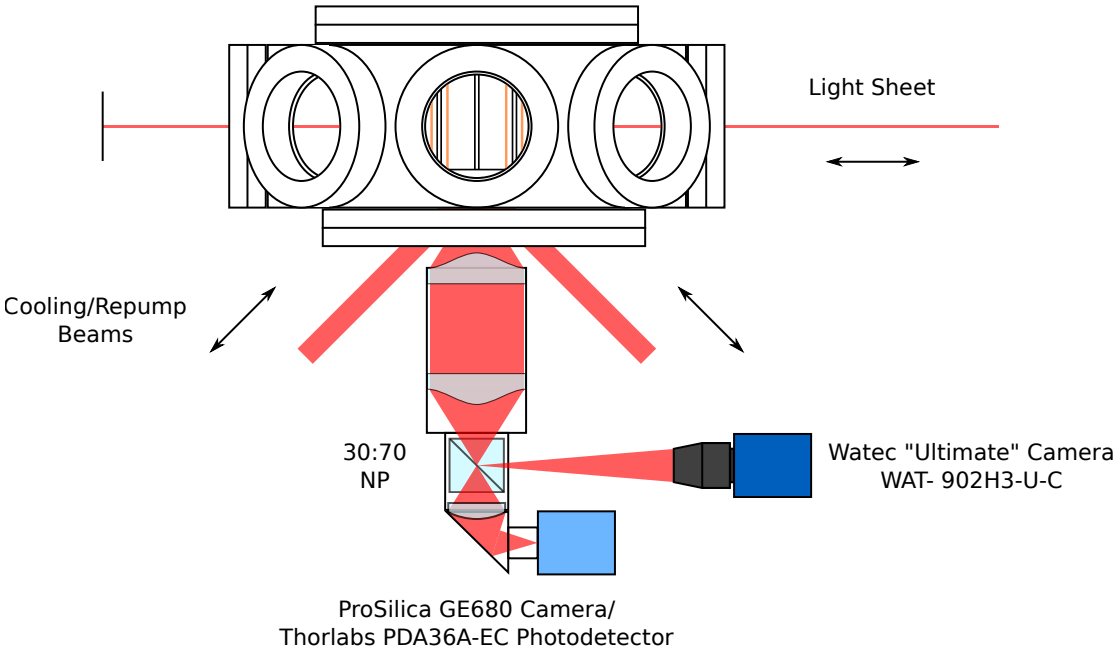

Figure 6.26: Illustration of the imaging optics positioned underneath the vacuum chamber used to observe the atom clouds trapped in the SMOT. A ProSilica GE680 is used to take time of flight images of the clouds as they ballistically expand, and it is replaced with a Thorlabs PDA36A-EC Photodetector to perform the loading rate measurements. A Watec 'Ultimate' camera is also shown, which is used for general imaging during alignment.

adopted. As with the light sheet method, this scheme involves turning off the cooling beams to allow the atom cloud to expand, but differs in that after a certain expansion time the beams are switched back on to stimulate atom fluorescence. This scattered light from the expanded atom cloud is captured with a fast TTL triggered camera (ProSilica GE680) to determine its size, and if a series of images are taken for different length expansion times then the cloud's velocity distribution, and thus temperature, can be inferred.

The set-up of the experiment is illustrated in figure 6.25 and 6.26. The flight times of the atom expansion events were determined by the width of a pulse emitted by the waveform generator of an Agilent Infiniivision DSO-X 2012A oscilloscope. The pulse had a repetition rate of 1Hz, and widths varying from 0.5 ms to 5.0 ms in 0.5 ms increments. The pulse signal was connected to a custom CMOS logic circuit which routes the switching signals from a National Instrument PCIe-6323 data acquisition card to a Minicircuits Z80-DR230-S+ RF switch unless the output of the waveform generator is logic high, i.e. for the duration of the pulse. This has the effect of blanking the cooling beams during the length of the pulse, allowing the atoms to drop and expand. The pulse width was remotely programmed using

VISA commands sent from a computer within the laboratory, which also controlled the data collection from the camera. The pulse signal was also wired to the trigger input of the camera, so that an image would be taken of the cloud on the falling edge of the pulse, when the beams were switched back on. The image parameters were solely controlled through the exposure and gain settings of the camera, and the lasers were left on after each image was taken so that the atoms could be recollected by the trap in preparation for the next image.

The camera had an exposure time of 1.9 ms to 2.5 ms, and at the beginning of each frequency setting the camera's gain was adjusted appropriately until the largest signal was detected without it becoming saturated. The sizes of the expanded clouds were estimated via 2D Gaussian fits and to aid this fitting algorithm, software background subtraction was employed to remove the vast majority of the laser scatter from the mirror and wires. Figure 6.27 shows an example of nine background subtracted images of atom clouds formed in the SMOT which have been allowed to expand for flight times of up to 4.0 ms. As with the light-sheet technique, the Gaussian width $\sigma_c(t)$ of the atom cloud after a time of flight of length t can be modelled by equation 6.29. Figure 6.28 shows an example of a fit of this function to the Gaussian widths of atom clouds expanded from the SMOT while operating at a frequency of 19 kHz. The fit indicates that the SMOT was producing clouds at 229.4(58) µK.

In reality the cloud's spatial distribution is not truly Gaussian. In particular, interference fringes caused by slightly misaligned beams change the MOT's shape, and in addition, instability in beam optics causes these fringes to shift position, moving the cloud around. For each pulse width setting of each temperature measurement 100 images were taken of the atom cloud. This was both an attempt to reduce error in the temperature measurements caused by instabilities in the set-up, and also to give a more accurate figure of the error. In total 1100 images are taken to produce a single temperature measurement.

Figure 6.29 shows the switching frequency dependence of the temperature of atom clouds captured within the SMOT. The figure was produced from 37400 photographs like those shown in figure 6.27 and took approximately 24 hours to collect. Because of the long time required to collect the data, the frequency measurements were taken in a random order in an attempt to remove fictitious trends caused by long term drifts in the laser set-up.

All of the data presented in this section, with the exception of the fourth set of figure 6.30, was taken using the Behringer audio amplifier, and collected with the

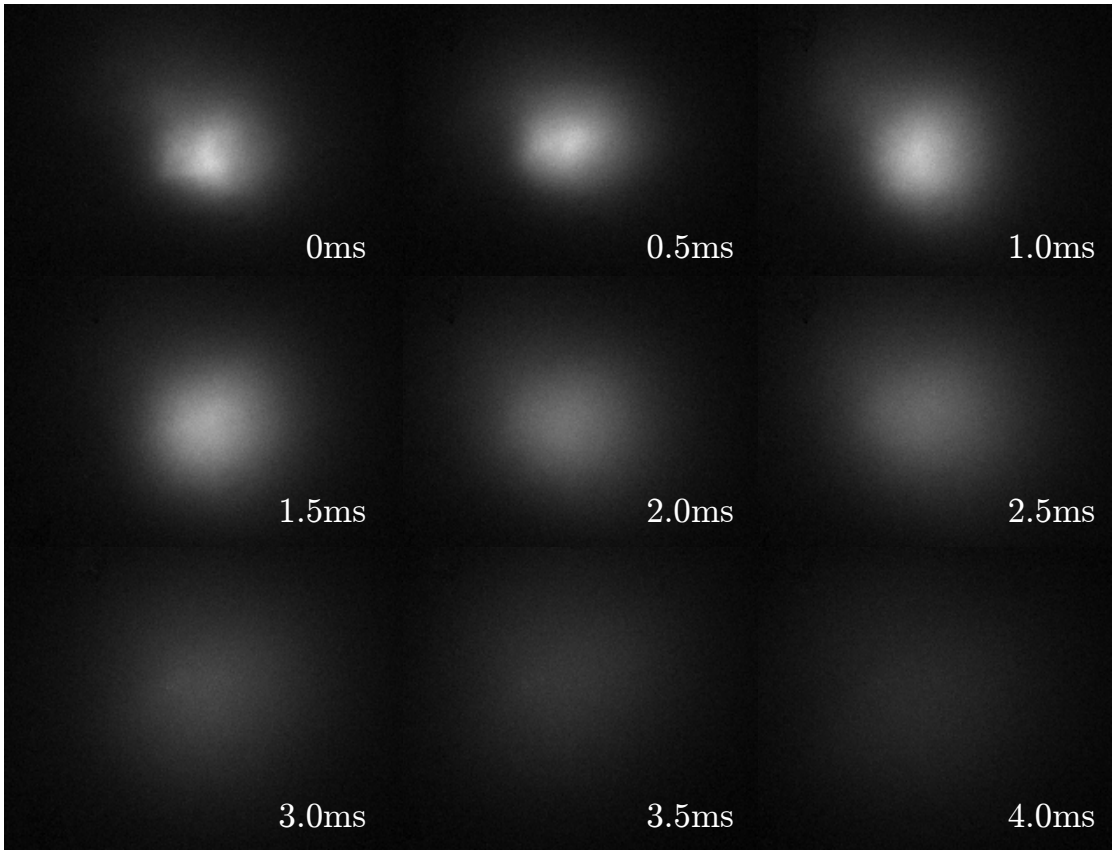

Figure 6.27: Photographs of the atom cloud after various expansion times used to determine the cloud temperature. 1100 photographs such as these were used to create figure 6.28, and 37400 images were required in total to produce figure 6.29. Here the SMOT was operating at a switching frequency of 13 kHz and software based background subtraction was used to improve the clarity of the images and produce better 2D Gaussian fits. In principle a series of 1D Gaussians could be fit to this data to determine the differing temperatures in the two dimensions, however as the camera was imaging the atom clouds from underneath the chamber we would expect from symmetry that the temperatures should be the same in each axis. Fitting one dimensional Gaussians would be more useful if the atom clouds were imaged horizontally, perpendicular to the axis along which they fall, as it is in this case that the symmetry of the trapping is broken.

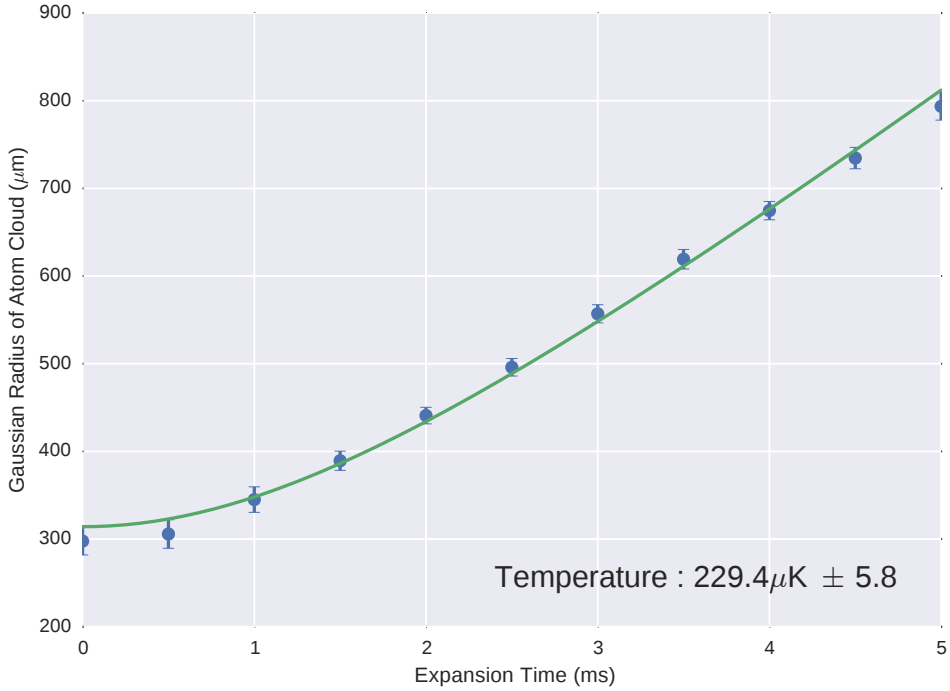

Figure 6.28: Temperature fit for an atom cloud produced in the SMOT at a switching frequency of 13kHz. This fit, along with 34 others was used to create figure 6.29.

same experimental parameters as those listed in section 6.3: The SMOT wires had a peak current of 4.9 A, corresponding to a magnetic field gradient of $1.7\,\mathrm{G\,cm^{-1}}$. The cooling laser had a detuning of $\delta = -2\pi{\cdot}5.5\,\mathrm{MHz}$ and each of the switched cooling beams had an average (post shuttered) power of 2 mW and $1/e^2$ radius of 2.0 mm. Looking at figure 6.29 there is no obvious trend in atom temperatures with respect to SMOT switching frequency. The measured temperatures become lower as the switching frequency increases, but the spread in the data is so wide that it cannot be said with any confidence this correlation is anything other than due to experimental drift. The new data set of figure 6.30 was taken with a peak current of 20 A through the SMOT's wires corresponding to a magnetic field gradient of $6.8\,\mathrm{G\,cm^{-1}}$. The cooling laser had a detuning of $\delta = -2\pi{\cdot}10.5\,\mathrm{MHz}$, with the two pairs of beams having average (post shuttered) powers of 1.7 mW and 1.5 mW, both with a $1/e^2$ radius of 4.0 mm. The pressure reading on the ion pump was 2.1×10^{-9} mbar.

Figure 6.30 shows a compilation of all of the temperature data for the SMOT. The plot shows preliminary results taken using the new bespoke current driver detailed in section 6.2.3, but the remaining data was taken whilst using the Behringer

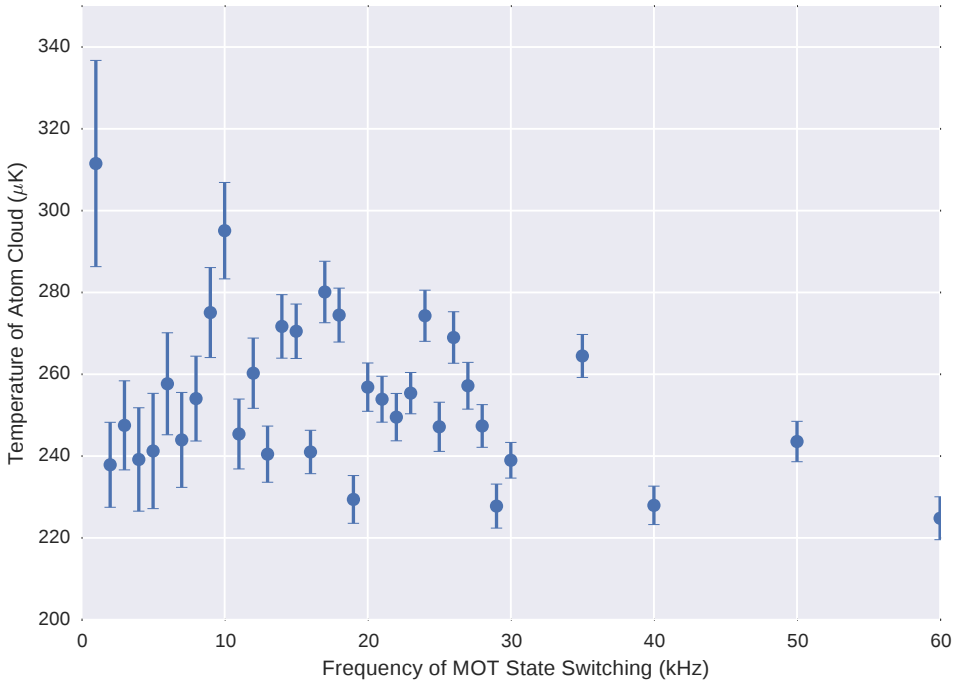

Figure 6.29: Frequency dependence of the atom cloud temperature in the SMOT. The data points were taken in a randomized order to prevent slow drifts in the set-up, for example detuning drifts or power fluctuations, from giving a false trend apparent in the results. In total, 37400 photographs were required to produce this plot.

audio amplifier. Surprisingly the newer data set shows temperatures that are much greater (>500 µK) than those found using the lower field strengths of the audio amplifier (mostly 200 µK to 300 µK). The poorer temperature performance that was found whilst using higher magnetic field gradients could be explained by considering that bias fields were required to bring the magnetic field zero of the trap further into the capture volume of the SMOT. These bias fields were necessary because the beams were already being shadowed by the SMOT's wires, and so any further enlargement of them would not make the capture volume any bigger. Although the trapping point can be moved with an appropriate choice of bias field, the sine wave nature of the switching currents acts with the bias fields to continuously move the zero point throughout the duration of the switching period. It is currently suspected that the oscillating zero point is effectively heating the atoms as they attempt to follow its location. This problem could be overcome by moving the mirror closer to the SMOT's wires and by removing any bias fields which are not serving to null the the Earth's magnetic field. If the bias fields are removed then as the current through the SMOT's wires increases the trapping

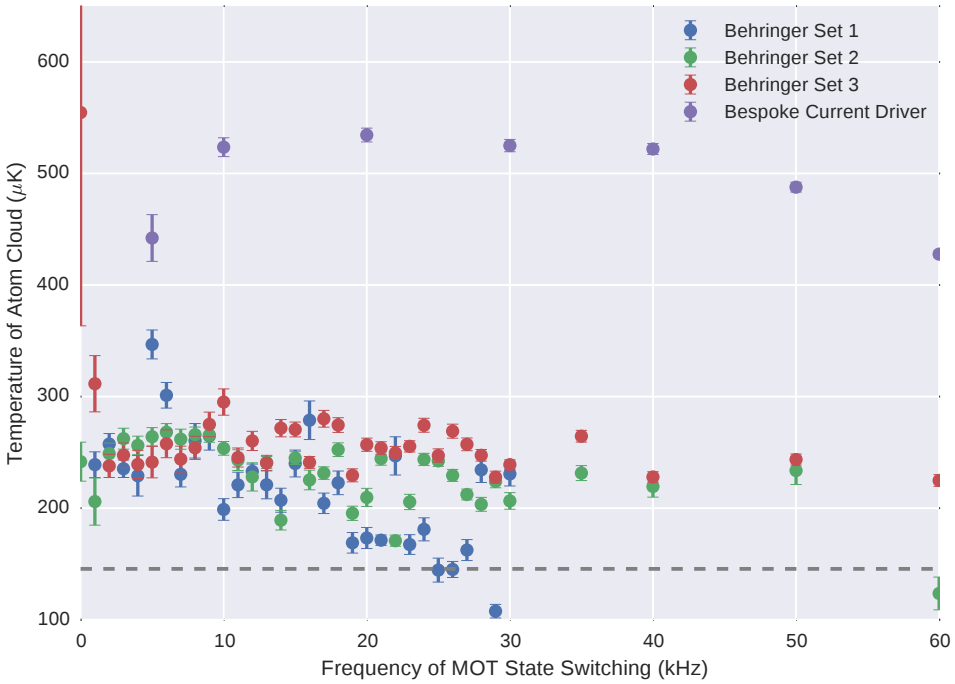

Figure 6.30: Frequency dependence of the atom cloud temperature in the SMOT measured within four separate data sets, each taken over a month apart. The data points of each set were taken in a random order, but it should be noted that the earliest set only had 10 Gaussian 2D fits per expansion time measurement, as opposed to the 100 fits that were later adopted for the subsequent sets. The dashed line marks the Doppler temperature, of which four data points were measured below.

position would remain constant and the heating effect should be eliminated. If square wave switching were still being used then there would be no shifting of the trapping point throughout the switching period, and so the presence of bias fields would not be so detrimental. Even with square wave switching, these bias fields should be avoided because they also prevent efficient sub-Doppler cooling. A sub-Doppler cooling stage is often initiated after collecting a large number of atoms by turning off the magnetic field while increasing the laser's detuning and reducing the intensity of the cooling beams. It is expected that the presence of a bias field would act to prevent efficient cooling, so to obtain the lowest temperatures the bias fields would have to be switched as well. No attempt at performing a sub-Doppler cooling stage has been performed here yet, as it is thought that the mirror's position should be moved first, however the shift in the laser's detuning should be fairly painless to implement by adjusting the centre frequencies of the 'switching' AOMs.

Chapter 7

Conclusion

Since their introduction 15 years ago interest has not waned in so called atom chips, microfabricated structures that allow for the cooling and manipulation of atoms close to surfaces. These devices have long been promised for use in applications ranging from sensors, clocks and even quantum computers, however they will never be able to gain widespread adoption unless their vacuum chambers and other bulky ancillary equipment that is needed to sustain them can be miniaturized. Work by many groups has taken the route of scaling down existing techniques, for example machining smaller versions of what otherwise are standard vacuum chambers. We instead wish to microfabricate these devices, borrowing techniques from the semiconductor industry to create integrated atom chips. The first generation of integrated atom chips will each have, in their simplest form, an etched cavity in a substrate in which a vacuum is maintained through the seal of a glass capping wafer. This design of integrated atom chip presents a level of optical access which is highly restricted and incompatible with many of the existing geometries of magneto optical traps.

This thesis has described the design and construction of a new magneto optical trap that is suitable for use in integrated atom chips and other vacuum systems in which optical access is limited to a single window. Like the AC MOT of M. Harvey and A.J. Murray[95], this new trap design relies on the switching of optical and magnetic fields and can operate at frequencies at least within the region of 1 kHz to 60 kHz. The design does not need patterned surfaces in order to generate the necessary beam geometry, requiring only the use of a single, standard mirror. Early temperature measurements have indicated that the trap may be capable of sub-Doppler cooling, at least at low magnetic field strengths, however additional

data needs to be collected to verify that this is not a result of experimental error. The frequency dependence of the loading rate of the SMOT has also been probed, and the data indicates that the optimum atom number lies between a switching frequency of 15 kHz to 30 kHz, where the maximum value recorded was approximately 1.7×10^6 atoms for a capture volume of $0.18\,\mathrm{cm}^3$. Even though this is an early measurement taken with the higher fields afforded by a new current amplifier, this atom number still compares fairly favourably with other geometries, performing somewhere between the microfabricated pyramidal MOT and the Grating MOT (figure 6.23).

Whilst only two different beam sizes have been tried with the SMOT, the corresponding data has been used to provide an estimate of its scaling law between trap size and atom number of $N \propto L^{4.5}$. As expected, the corresponding trap volumes were too large to exhibit the rapid scaling of $N \propto L^6$ that is found with small traps, but equally the SMOT does not quite reach the scaling regime of $N \propto L^{3.6}$ that large MOTs follow. The two data points, however, were taken with wildly different trap parameters, the trap with the smaller beams having the much lower magnetic field gradient generated by the older current driver, and so it would not be surprising that if the old data were to be reproduced that the scaling law of large MOTs would be observed.

The results for the frequency dependence of cloud temperature were not so conclusive given the large amount of scatter in the results, but there does seem to be a weak relationship whereby the temperatures reduce slightly at higher frequencies. These results certainly need to be replicated before they are accepted as being representative of the trap's true behaviour, but given the apparent weak relationship it would seem sensible to choose an operating frequency to maximize the atom number, and then decrease the temperature of the collected atoms in a subsequent sub-Doppler cooling stage.

Over the course of this project the prototype SMOT design has been conceived, simulated and then constructed. Starting from an empty laboratory, testing of this new MOT geometry required the assembly of an ultra high vacuum system from scratch, numerous pieces of electronic equipment to be designed and built and a whole table of optics aligned. Many pieces of software were written to simulate experiments, control laboratory equipment and to collect and analyse results.

Along the way, several laser stabilization techniques were employed to varying degrees of success before the set-up eventually was finalized to use the highly effective technique of modulation transfer spectroscopy. This was implemented

with an acousto-optic modulator rather than the ordinary approach of employing an electro-optic modulator and produced very sharp error signals with which to lock the cooling laser. The secondary repumping laser was then referenced to the cooling light with an offset phase lock servo, producing a laser system which was significantly more stable than those which came before it.

A variety of optical and magnetic switching methods have been evaluated in order to test the SMOT including square wave current pulses that were generated by the switching of field effect transistors and half-wave rectification of sinusoidal waveforms output by a high power audio amplifier. More recently a new current driver has been designed and built in order to test the SMOT at greater magnetic field gradients than before, of which the previous methods of magnetic field generation were incapable of sustaining. Early results with this new current driver have shown significant improvements in the atom number of the SMOT, and have done so without suffering any of the overheating issues that plagued older switching methods. The temperature of the atom clouds captured with this bespoke driver are hotter than those that were collected when the Behringer audio amplifier was used to generate the magnetic fields. It is currently suspected though that this heating is due to the oscillating magnetic field conspiring with the bias fields, which act to move the trapping point throughout the switching cycle. The SMOT would certainly benefit from an optical molasses stage to cool the large number of trapped atoms below the Doppler temperature, but to do so the SMOT's mirror should be moved closer to its wires in order to remove the need for any bias fields and to reduce the shadowing of the beams.

It remains to be seen if the trap geometry described here will become adopted elsewhere, especially in light of the impressive results demonstrated by the microfabricated grating MOT. In addition to being an easy to fabricate design, the SMOT still does have scope for applications in which the microfabricated surface of a grating could interfere with probing beams, or under circumstances when the magnetic fields need to be rapidly switched off. Regardless of the fate of the SMOT, the miniaturization of atom physics clearly has a bright future.

Appendix A

Fundamental Constants

2014 CODATA recommended values.

Speed of Light in Vacuum	c	$2.997\,924\,58 \times 10^{8}\,\mathrm{m\,s^{-1}}$ (exact)
Magnetic Constant	μ_0	$4\pi \times 10^{-7}\,\mathrm{N\,A^{-2}}$ (exact)
Electric Constant	ϵ_0	$(\mu_0 c^2)^{-1}$ (exact) $= 8.854\,187\,817 \times 10^{-12}\,\mathrm{F\,m^{-1}}$
Planck's Constant	h $\hbar$	$6.626\,070\,040(81) \times 10^{-34}\,\mathrm{J\,s}$ $1.054\,571\,800(13) \times 10^{-34}\,\mathrm{J\,s}$
Elementary Charge	e	$1.602\,176\,620\,8(98) \times 10^{-19}\,\mathrm{C}$
Bohr Magneton	μ_B	$927.400\,999\,4(57) \times 10^{-26}\,\mathrm{J\,T^{-1}}$
Atomic Mass Constant	m_u	$1\,\mathrm{u}$ $1.660\,539\,040(20) \times 10^{-27}\,\mathrm{kg}$
Electron Mass	m_e	$9.109\,383\,56(11) \times 10^{-31}\,\mathrm{kg}$
Bohr Radius	a_0	$0.529\,177\,210\,67(12) \times 10^{-10}\,\mathrm{m}$
Boltzmann Constant	k_B	$1.380\,648\,52(79) \times 10^{-23}\,\mathrm{J\,K^{-1}}$
Avogadro Constant	k_B	$6.022\,140\,857(74) \times 10^{23}\,\mathrm{mol^{-1}}$
Molar Gas Constant	R	$8.314\,459\,8(48)\,\mathrm{J\,mol^{-1}\,K^{-1}}$

Appendix B

The Zeeman Effect in Quantum Mechanics

In the absence of a magnetic field the zeroth order Hamiltonian corresponding to the central field, the residual electrostatic interaction and the spin orbit interaction of an atom is given by H_0. The eigenstates of this Hamiltonian have two complete sets of commuting observables $\mathbf{J}^2, J_z, \mathbf{I}^2, I_z$, which is $(2J+1)(2I+1)$ fold degenerate and $\mathbf{J}^2, \mathbf{I}^2, \mathbf{F}^2, F_z$ where $\mathbf{F} = \mathbf{I} + \mathbf{J}$, which is $2F+1$ fold degenerate.

Under consideration of the hyperfine interaction we construct a new total Hamiltonian $H = H_0 + H_{HFS}$, where the additional interaction is given by[128]:

$$\begin{aligned} H_{HFS} =& A_{HFS}\mathbf{I}\cdot\mathbf{J} + B_{HFS}\frac{3(\mathbf{I}\cdot\mathbf{J})^2 + \frac{3}{2}(\mathbf{I}\cdot\mathbf{J}) - I(I+1)J(J+1)}{2I(2I-1)J(2J-1)} \\ &+ C_{HFS}\frac{10(\mathbf{I}\cdot\mathbf{J})^3 + 20(\mathbf{I}\cdot\mathbf{J})^2 + 2(\mathbf{I}\cdot\mathbf{J})[I(I+1)+J(J+1)+3]}{I(I-1)(2I-1)J(J-1)(2J-1)} \\ &+ C_{HFS}\frac{-3I(I+1)J(J+1) - 5I(I+1)J(J+1)}{I(I-1)(2I-1)J(J-1)(2J-1)} \end{aligned} \tag{B.1}$$

where A_{HFS} is the magnetic dipole constant, B_{HFS} is the electric quadrupole constant and C_{HFS} is the magnetic octupole constant. As this interaction is much weaker than that given by the spin orbit interaction we can use perturbation theory to find the corresponding first order energy level shift. To calculate this shift without resorting to degenerate perturbation theory we must choose a set of observables which commute both with the unperturbed, but also the perturbing Hamiltonian so the solution does not diverge. Neither J_z, nor I_z commute with H_{HFS} so we cannot use J, m_J, I, m_I as our set of quantum numbers, however all

of the operators in the set $\mathbf{J}^2, \mathbf{I}^2, \mathbf{F}^2, F_z$ commute, so J, I, F, m_F is the appropriate choice. Thus the energy shift is given by:

$$\begin{aligned}
\Delta E_{HFS} =& \langle J, I, F, m_F | H_{HFS} | J, I, F, m_F \rangle \\
\Delta E_{HFS} =& \frac{1}{2} A_{HFS} K + B_{HFS} \frac{\frac{3}{2}K(K+1) - 2I(I+1)J(J+1)}{4I(2I-1)J(2J-1)} \\
&+ C_{HFS} \frac{5K^2(K/4+1) + K[I(I+1) + J(J+1) + 3]}{I(I-1)(2I-1)J(J-1)(2J-1)} \\
&+ C_{HFS} \frac{-3I(I+1)J(J+1) - 5I(I+1)J(J+1)}{I(I-1)(2I-1)J(J-1)(2J-1)}
\end{aligned} \tag{B.2}$$

where the $\mathbf{I} \cdot \mathbf{J}$ terms have been replaced with $\mathbf{I} \cdot \mathbf{J} = \frac{1}{2}(\mathbf{F}^2 - \mathbf{I}^2 - \mathbf{J}^2)$ and then the expectation value calculated to give $\frac{1}{2}K = \langle J, I, F, m_F | \mathbf{I} \cdot \mathbf{J} | J, I, F, m_F \rangle = \frac{1}{2}(F(F+1) - I(I+1) - J(J+1))$. This expression has been used to produce figure B.1, which shows the hyperfine splitting of rubidium 85.

Now we consider the interaction H_B with an external magnetic field $\mathbf{B}$:

$$H_B = \frac{\mu_B}{\hbar}(g_J \mathbf{J} + g_I \mathbf{I}) \cdot \mathbf{B} \tag{B.3}$$

where g_J and g_I are the total electron and nuclear Landé g factors. Giving us a total Hamiltonian of $H = H_0 + H_{HFS} + H_B$. If the magnetic field is weak enough so that this interaction is small compared with the hyperfine splitting then we can again use perturbation theory to determine the first order energy shift. m_J and m_I are not good quantum numbers, and so we must use the projection theorem to continue working in our J, I, F, m_F basis.

$$\begin{aligned}
H_B &= \frac{\mu_B}{\hbar}\left(g_J \frac{\langle \mathbf{J} \cdot \mathbf{F} \rangle}{F(F+1)} + g_I \frac{\langle \mathbf{I} \cdot \mathbf{F} \rangle}{F(F+1)} \right) \mathbf{F} \cdot \mathbf{B} \\
&= \frac{\mu_B}{\hbar}\left(g_J \frac{F(F+1) + J(J+1) - I(I+1)}{2F(F+1)} \right. \\
&\qquad \left. + g_I \frac{F(F+1) + I(I+1) - J(J+1)}{2F(F+1)} \right) \mathbf{F} \cdot \mathbf{B} \\
H_B &= \frac{\mu_B}{\hbar} g_F \mathbf{F} \cdot \mathbf{B}
\end{aligned} \tag{B.4}$$

Giving a first order energy splitting of:

$$\Delta E_B = \mu_B g_F m_F B_z \tag{B.5}$$

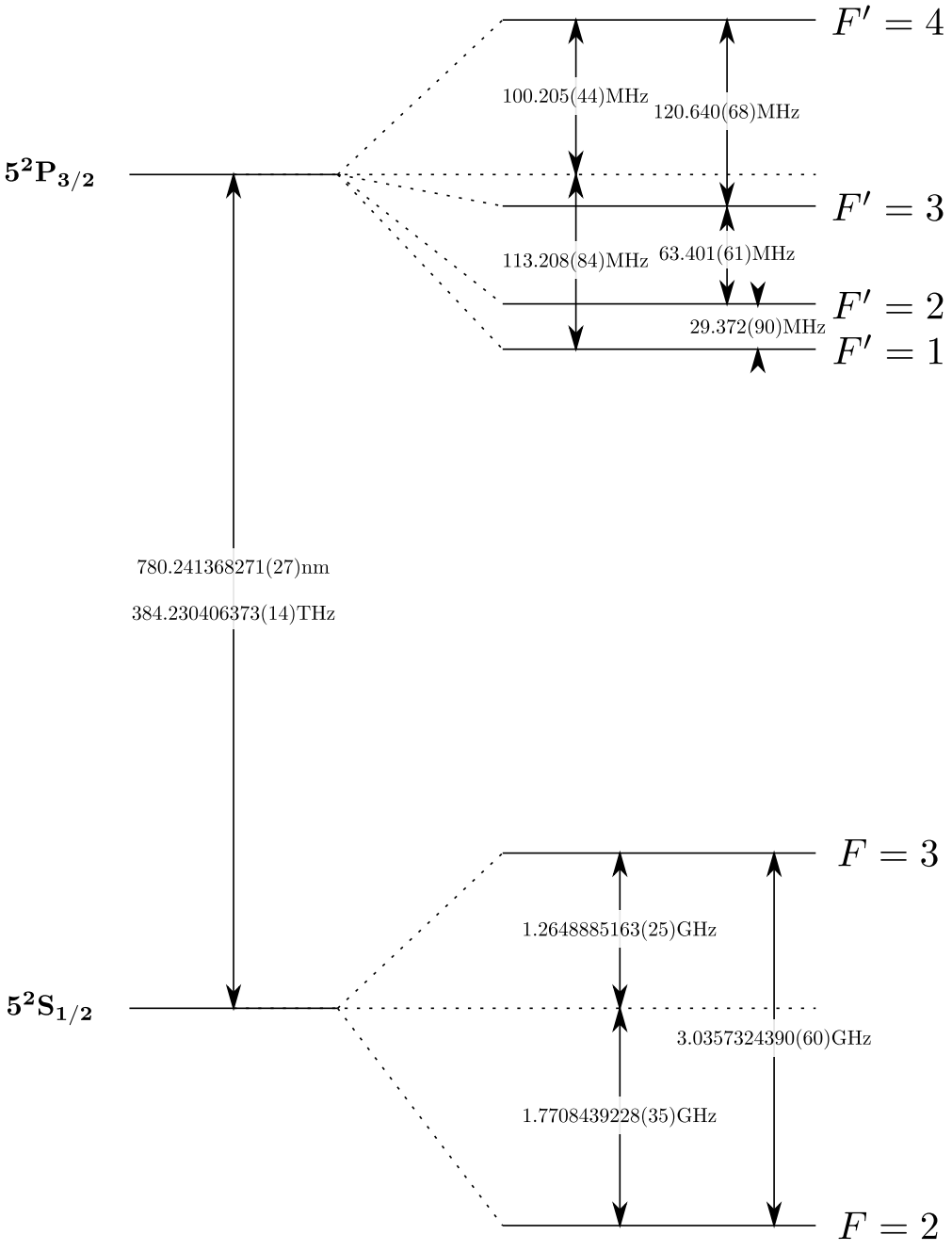

Figure B.1: Hyperfine structure which gives rise to the D_2 transitions of ^{85}Rb. Adapted from work by D.Steck[128].

If, however, the magnetic interaction is much stronger than the hyperfine interaction then it cannot be treated as a perturbation to the hyperfine structure. Instead we must first perturb H_0 with the magnetic interaction and treat the hyperfine interaction as a smaller perturbation afterwards. In performing these perturbations we must choose the basis with the set of operators $\mathbf{J}^2, J_z, \mathbf{I}^2, I_z$ because $\mathbf{I}$ and $\mathbf{J}$ precess independently around $\mathbf{B}$, and thus F is no longer a good quantum number. Applying both of these perturbations leads us to the Paschen-Back effect, where the first order energy shift is given by:

$$\begin{aligned}\Delta E_{PB} =& A_{HFS} m_I m_J + B_{HFS} \frac{(3m_I^2 - I(I+1))(3m_J^2 - J(J+1))}{4I(2I-1)J(2J-1)} \\ &+ \mu_B (g_I m_I + g_J m_J) B_z \end{aligned} \tag{B.6}$$

In the regime of intermediate field strength neither of these approximations is valid and we have to numerically solve the whole Hamiltonian, $H = H_0 + H_{HFS} + H_B$.

We already know that F is not a good quantum number at high fields, and equally m_J and m_I aren't good quantum numbers at low fields. At all field strengths, however, $F_z = J_z + I_z$ commutes with the Hamiltonian so we can always choose to use the basis corresponding to the quantum numbers $J, I, m_J + m_I$. Associated with each pair of quantum numbers J and I are $2(J+I)+1$ different possible values of $m_J + m_I$, where $-(J+I) \leq m_J + m_I \leq J + I$.

If we define the angular momentum raising and lowering operators:

$$\begin{aligned} I_\pm &= I_x \pm i I_y \\ J_\pm &= J_x \pm i J_y \end{aligned} \tag{B.7}$$

that have the property of increasing or decreasing angular momentum:

$$\begin{aligned} J_\pm |J, m_J\rangle &= \hbar \sqrt{J(J+1) - m_J(m_J \pm 1)} |J, m_J \pm 1\rangle \\ I_\pm |I, m_I\rangle &= \hbar \sqrt{I(I+1) - m_I(m_I \pm 1)} |I, m_I \pm 1\rangle \end{aligned} \tag{B.8}$$

then we can rewrite the operator $\mathbf{I} \cdot \mathbf{J}$ as:

$$\mathbf{I} \cdot \mathbf{J} = I_x J_x + I_y J_y + I_z J_z = I_z J_z + \frac{1}{2} \left[I_+ J_- + I_- J_+ \right] \tag{B.9}$$

This shows that the $\mathbf{I} \cdot \mathbf{J}$ terms in the hyperfine Hamiltonian act to transfer quanta of the z component of angular momentum between I and J, but the total angular

momentum in the direction of z, $(m_J + m_I)$ remains constant as expected. Substituting this into our total Hamiltonian and ignoring the C_{HFS} term (of which a non zero value is not currently known accurately enough to be considered[128]), we find:

$$\begin{aligned} H = H_0 &+ A_{HFS}(I_z J_z + \frac{1}{2}\left[I_+ J_- + I_- J_+\right]) \\ &+ B_{HFS}\frac{3(I_z^2 J_z^2 + \frac{1}{2} I_z J_z \left[I_+ J_- + I_- J_+\right] + \frac{1}{2}\left[I_+ J_- + I_- J_+\right] I_z J_z)}{2I(2I-1)J(2J-1)} \\ &+ B_{HFS}\frac{\frac{3}{4}\left[I_+ J_- I_+ J_- + I_+ J_- I_- J_+ + I_- J_+ I_+ J_- + I_- J_+ I_- J_+\right]}{2I(2I-1)J(2J-1)} \\ &+ B_{HFS}\frac{\frac{3}{2}(I_z J_z + \frac{1}{2}\left[I_+ J_- + I_- J_+\right]) - I(I+1)J(J+1)}{2I(2I-1)J(2J-1)} \\ &+ \frac{\mu_B}{\hbar}(g_I I_z + g_J J_z)B_z \end{aligned} \tag{B.10}$$

So to find the energy shift due to these interactions we have to diagonalize the matrix with on-diagonal elements:

$$\begin{aligned} \langle J, I, m_J + m_I | H - H_0 | J, I, m_J + m_I \rangle = A_{HFS} m_I m_J \\ + B_{HFS}\frac{3m_I^2 m_J^2 + \frac{3}{2} m_I m_J - I(I+1)J(J+1)}{2I(2I-1)J(2J-1)} \\ + B_{HFS}\frac{\frac{3}{4}\left[i_+ j_- i_- j_+ + i_- j_+ i_+ j_-\right]}{2I(2I-1)J(2J-1)} \\ + \mu_B(g_I m_I + g_J m_J)B_z \end{aligned} \tag{B.11}$$

where $i_\pm j_\mp i_\mp j_\pm = (I(I+1) - m_I(m_I \mp 1))(J(J+1) - m_J(m_J \pm 1))$. The off-diagonal elements are given by:

$$\begin{aligned} \langle J, I, m_J - 1, m_I + 1 | H - H_0 | J, I, m_J, m_I \rangle = A_{HFS}\frac{1}{2} I_+ J_- \\ + B_{HFS}\frac{\frac{3}{2} i_+ j_- [m_i m_J + (m_I + 1)(m_J - 1)]}{2I(2I-1)J(2J-1)} \\ + B_{HFS}\frac{\frac{3}{4} i_+ j_-}{2I(2I-1)J(2J-1)} \end{aligned} \tag{B.12}$$

and

$$\langle J, I, m_J - 2, m_I + 2 | H - H_0 | J, I, m_J, m_I \rangle = B_{HFS}\frac{\frac{3}{4}(i_+ j_-)^2}{2I(2I-1)J(2J-1)} \tag{B.13}$$

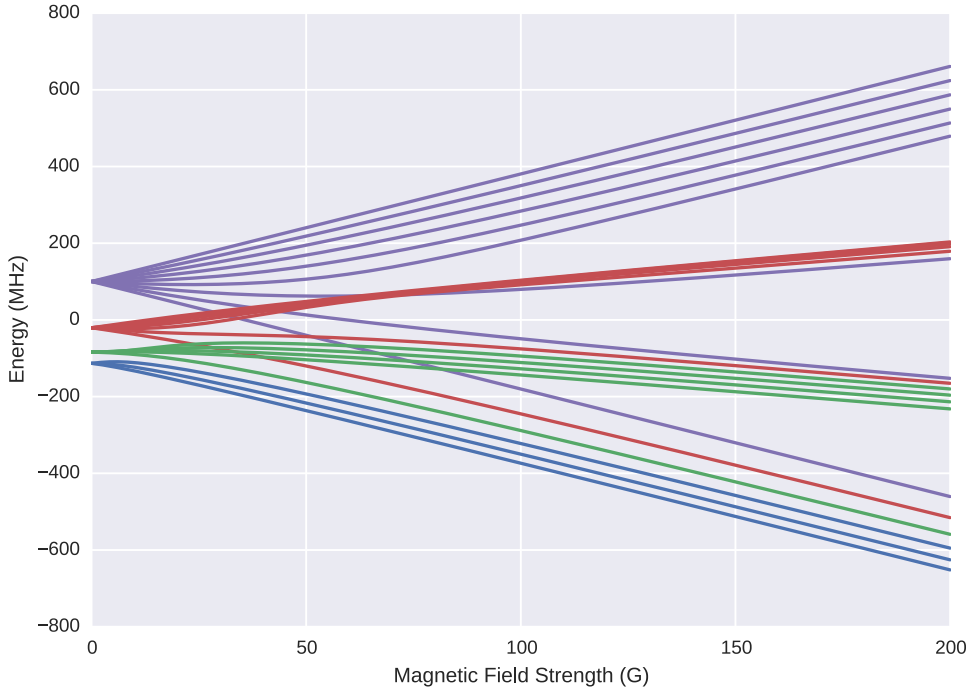

Figure B.2: Zeeman splitting of the $5^2P_{3/2}$ levels of ^{85}Rb. In calculating this figure, H_0 was removed from the Hamiltonian to illustrate the level splitting relative to the energy of the spin-orbit interaction.

where $i_{\pm}j_{\mp} = \sqrt{I(I+1) - m_I(m_I \pm 1)}\sqrt{J(J+1) - m_J(m_J \mp 1)}$.

Figure B.2 shows the energy level splitting of the $5^2P_{3/2}$ levels of ^{85}Rb in the presence of an external magnetic field. The energy level structure was computed by diagonalizing the Hamiltonian with the above matrix elements and the values given are relative to the energy found by computing the Hamiltonian up to the spin-orbit interaction. It can be seen from the diagram that states with the same value of $m_F = m_J + m_I$ repel each other to give band-bending. Two of the states have unique values of $m_F = \pm 4$ so these levels still remain linear in this regime calculated.

Appendix C

Selected Permeation Data

One of the earliest studies of the permeation of impurities through silicon was performed by A.Van Wieringen and N.Warmoltz in a paper that is sometimes referred to in the literature by the acronym 'vWW'[129]. Van Wieringen and Warmoltz experimentally analysed the diffusion of hydrogen and helium through silicon, and presented the first estimates of the corresponding solubility and diffusivity parameters. Their paper experimentally considered the situation described in section 2.2.2.1, namely the permeation of gases through a material that is initially completely degassed. The authors observed that the ratio of the non-steady state permeation rate to the steady state permeation rate is independent of the solubility of material, allowing for the determination of the diffusion coefficient.

There were a sufficient number of data points of the diffusion coefficient for hydrogen in the vWW data to be able to produce reasonable fits of the energy and the pre-exponential factor for diffusion ($D_0 = 9.4 \times 10^{-3}\,\mathrm{cm^2\,s^{-1}}$ and $E_D = 11\,\mathrm{kcal\,mol^{-1}}$). In the case of helium in silicon, however, only four values were calculated at a total of two temperatures which meant that a reliable fit to the data could not be produced. Instead of estimating these diffusion parameters from the best fit the authors performed a subsequent experiment where measuring the permeation rate immediately after changing the temperature of the sample could be used to infer both the diffusion and solution energies. The fact that the resulting parameters do not match particularly well with subsequent experimental data raises doubts about the validity of this direct extraction. Concerns have also been expressed about extrapolating their results too readily[130, 131], given that they were taken within a narrow temperature range ($967\,^{\circ}\mathrm{C}<T<1207\,^{\circ}\mathrm{C}$), however looking at all of the literature of helium in silicon (figure C.1) there does not seem to be a significant deviation from an Arrhenius relationship. It should be noted

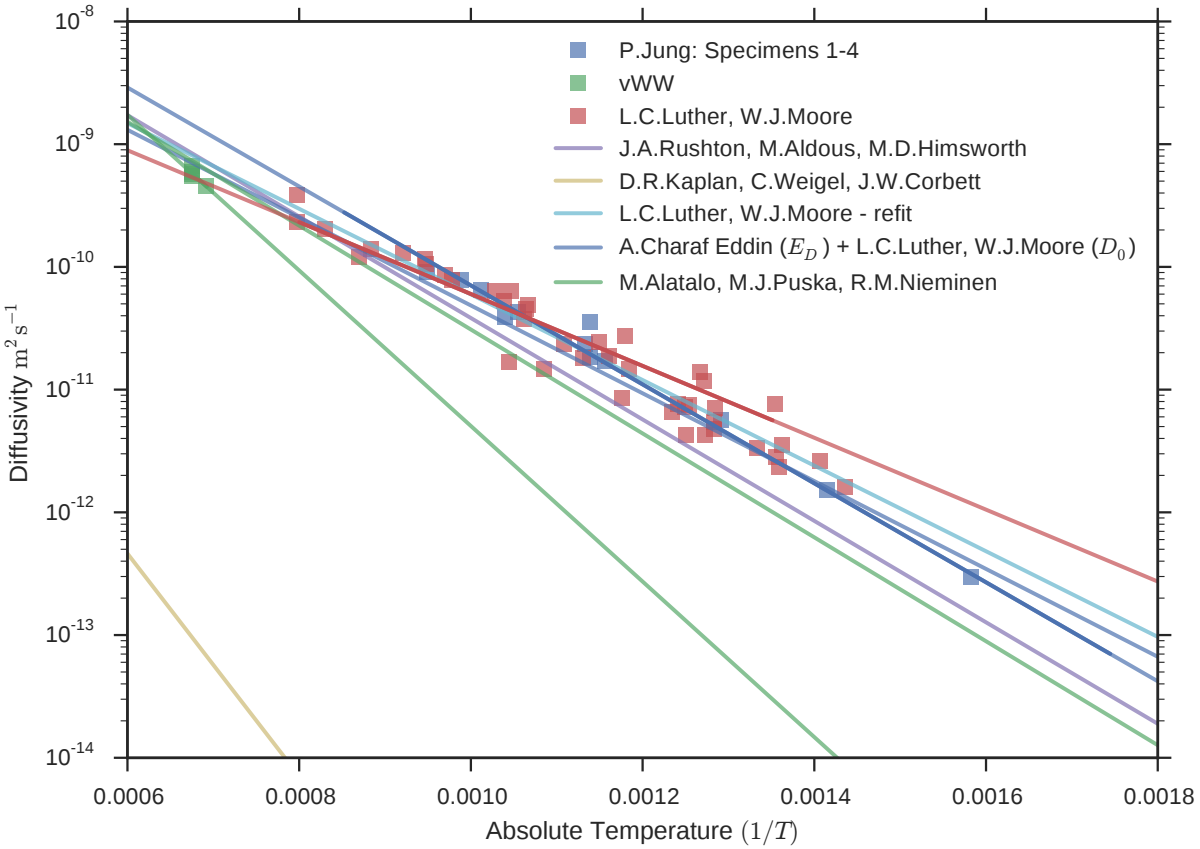

Figure C.1: Diffusivity of helium in silicon. Dark lines represent fits stated in the respective papers in their stated range while lighter coloured lines show both extrapolations outside this range and diffusivities drawn from purely theoretical diffusion parameters. Note that the data extracted from L.C. Luther and W.J. Moore may be somewhat questionable due to the source having a pseudo-logarithmic scale. Data extracted from[1, 129–134]

that vWW could not detect any permeation of neon, argon or nitrogen through the silicon samples they tested.

L.C.Luther and W.J.Moore quoted diffusion parameters of $D_0 = 5.1 \times 10^{-4}\,\mathrm{cm^2\,s^{-1}}$ and $E_D = 13.4(18)\,\mathrm{kcal\,mol^{-1}}$ in the temperature region $740\,\mathrm{K}<T<1250\,\mathrm{K}$ for helium in silicon[132]. Looking at the data in their paper shows an incorrectly drawn logarithmic plot, and so in analysis of this paper it was assumed that the tick marks labelling each order of magnitude were correct. Extracting the data from the graph and replotting it along with a diffusion line using their best fit diffusion parameters yields a line that, although passing through the vWW data, does not fit well with either their data points, or those of P. Jung[131]. Figure C.1 also shows a new fit to the extracted L.C.Luther and W.J.Moore data ($D_0 =$

$1.84 \times 10^{-7}\,\mathrm{m^2\,s^{-1}}$, $E_D = 0.69\,\mathrm{eV}$) which does correspond fairly well to all of the available data in the literature.

The most recent, and final, experimental data of helium in silicon was published by P.Jung in 1994, who calculated diffusion parameters of $D_0 = 7.6 \times 10^{-7}\,\mathrm{m^2\,s^{-1}}$ and $E_D = 0.80\,\mathrm{eV}$ in the temperature range of $300\,^{\circ}\mathrm{C}<T<900\,^{\circ}\mathrm{C}$. The post-implantation data of P. Jung was not considered here which shows significantly lower diffusivites that are likely as a result of helium-helium interactions induced by the high helium concentrations[131].

Theoretical studies of helium in silicon show that it diffuses as an interstitial, moving between the empty regions that lie between the atoms of even a perfect silicon crystal. This diffusion process was found to be significantly more energetically favourable than diffusion through silicon vacancies, the latter only becoming favoured for krypton and higher mass noble gas atoms (but of course at a much higher diffusion energy)[133]. There are two interstitial sites in silicon where impurities can remain trapped. These locations are known as the tetrahedral and hexagonal interstitials, and can be crudely pictured as the most spacious locations in the crystal lattice in which impurities are able to fit. Calculations using Density Functional Theory (DFT) have determined the energies of these sites for various impurities[133–135]. Impurities diffuse through silicon via these interstitial sites, and so the energy for diffusion is given by the difference in the energy between these two locations.

S.Fabian *et al.* performed a beautiful experiment where silicon samples were implanted with hydrogen by a $^1H_2^+$ beam from a Penning source[136]. The authors were able to measure the concentration of ^{1}H inside their samples as a function of depth through the use of Nuclear Reaction Analysis (NRA). In this particular example the samples were bombarded by $^{15}N^{2+}$ ions which could be focused to a spot size of 3 mm, giving rise to a depth resolution of 1 nm. The nitrogen ions provide a measure of the concentration of the hydrogen in the sample due to the $^1\mathrm{H}(^{15}\mathrm{N}, \alpha\gamma)^{12}\mathrm{C}$ nuclear reaction, which reacts the ^{15}N with the ^{1}H in the sample to produce ^{12}C and a helium nucleus, whilst emitting a 4.4 MeV gamma ray that is detected. The process has a sharp resonance at a ^{15}N energy of 6.40 MeV, and so ions have to penetrate a certain depth to lose enough energy to become resonant[155]. If the rate at which this energy loss is known then the energy of bombardment can be tuned to probe the hydrogen concentration of the sample at a specific depth, the concentration being then measured by the intensity of the gamma rays that are emitted from the reaction.

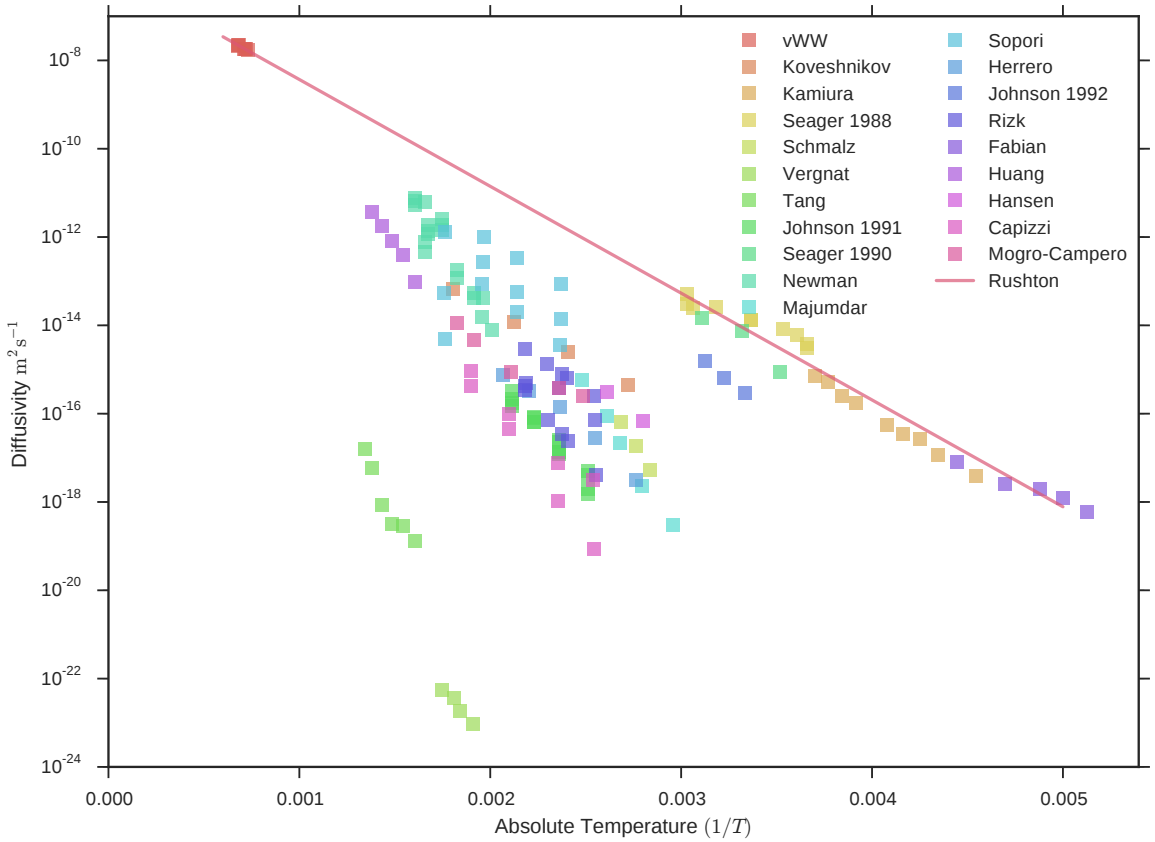

Figure C.2: Diffusivity of hydrogen in silicon. The large cluster of data below the line of Rushton *et al.* is explained in the work of S. Fabian *et al.*[136] who determined that the often underestimated diffusivity of hydrogen in silicon is due to trapping caused by implantation above energies of 1 keV. Data extracted from[1, 129, 136–154]

It was discovered that the diffusion rate through the silicon was largely dependent on the energy of implantation. Above 150 eV ^{1}H implantation energy, Frenkel pair defects occur in the silicon crystal. These vacancies act to trap the hydrogen itself, hence reducing the measured diffusion rate, whilst nearly all of the hydrogen becomes trapped at energies above 1 keV. This indicates that many previous studies may have underestimated the diffusivity as a result of this trapping, and explains the large spread of data in figures C.2 and C.3. Hydrogen concentration also greatly influences trapping, above 10^{20} H/cm^3 of which 100 percent is rendered immobile.

There is not a great deal of information regarding the solubility of helium and hydrogen in silicon across the literature. One of the first papers was once again by A.Van Wieringen and N.Warmoltz, who quoted values of $S_0 = 6.5 \times 10^{14}$ molec cm^{-3}

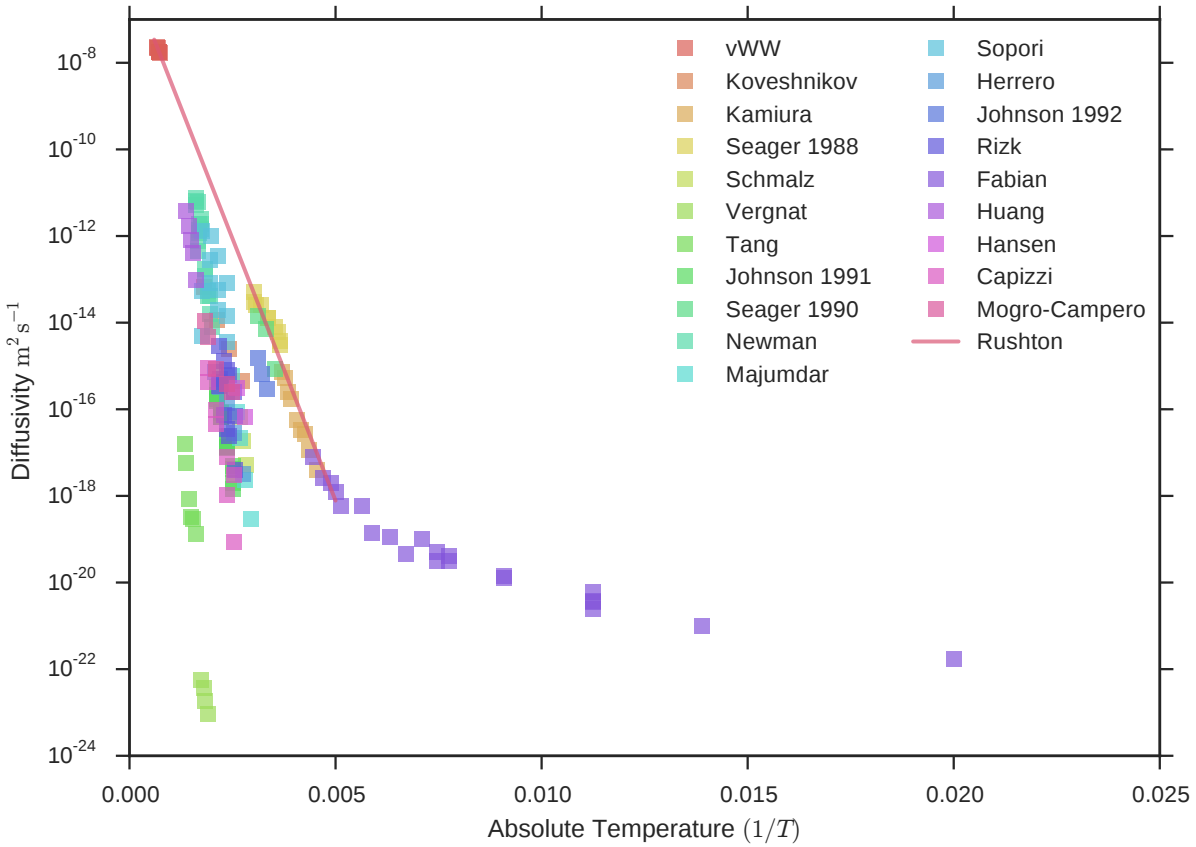

Figure C.3: Diffusivity of hydrogen in silicon. The large cluster of data below the line of Rushton *et al.* is explained in the work of S. Fabian *et al.*[136] who determined that the often underestimated diffusivity of hydrogen in silicon is due to trapping caused by implantation above energies of 1 keV. The data of Fabian also shows the significant deviation from the Arrhenius realtionship that occurs at low temperatures, the cause of which was deemed to be due to quantum tunnelling. Data extracted from[1, 129, 136–154]

and $E_S = 11\,\mathrm{kcal\,mol^{-1}}$ for helium and values of $S_0 = 2.4 \times 10^{21}\,\mathrm{molec\,cm^{-3}}$ and $E_S = 43\,\mathrm{kcal\,mol^{-1}}$ for hydrogen. As mentioned earlier, in the case of helium the solution energy was determined by a secondary experiment that monitored the silicon permeability after a rapid temperature change, and the resulting fit does not model their data particularly well, and so the results once again seem suspect.

	Silicon	Aluminosilicate	Pyrex	Stainless steel
Helium				
D_0 ($cm^2\,s^{-1}$)	5.2×10^{-3}	3.7×10^{-4}	4.6×10^{-4}	Impermeable
E_D (eV)	0.82	0.52	0.28	-
S_0 (cm^3(STP)/cm^3)	2.8×10^{-4}	0.0016	0.0056	-
E_S (eV)	0.77	-	-	-
K ($cm^2\,s^{-1}$) @ 20°C	3.2×10^{-34}	6.8×10^{-16}	3.5×10^{-11}	-
K ($cm^2\,s^{-1}$) @ 500°C	4.8×10^{-17}	2.4×10^{-10}	3.4×10^{-8}	-
Hydrogen				
D_0 ($cm^2\,s^{-1}$)	9.7×10^{-3}	$2.08\times10^{-7}K^{-1}$	1.4×10^{-5}	1.2×10^{-2}
E_D (eV)	0.48	0.67	0.24	0.56
S_0 (cm^3(STP)/cm^3)	90.4	0.038	0.038	0.3
E_S (eV)	1.86	0.12	0.12	0.11
K ($cm^2\,s^{-1}$) @ 20°C	5.7×10^{-40}	6.1×10^{-23}	3.4×10^{-16}	1.0×10^{-14}
K ($cm^2\,s^{-1}$) @ 500°C	1.2×10^{-15}	4.3×10^{-14}	2.4×10^{-12}	1.4×10^{-7}

Table C.1: Solubilities and diffusivities for helium and hydrogen in various materials. Data from[1]

Appendix D

Model of Modulation Transfer Spectroscopy

If a sufficiently weak probe beam of angular frequency ω_L passes through a vapour cell then its absorption may be characterized by the Beer-Lambert relation:

$$\frac{dI(\omega_L)}{dz} = -N\sigma(\omega_L)I_0 \tag{D.1}$$

where N is the number density of the atoms in the vapour cell, I_0 is the intensity of the probe beam as it enters the cell and $\sigma(\omega_L)$ is the frequency dependent cross section for a transition in a two level atom $|g\rangle \rightarrow |e\rangle$, with an energy level separation of ω_0. This cross section is given by:

$$\sigma(\omega_L) = \frac{\hbar\omega_0}{c}(B_{eg}n_e - B_{ge}n_g)L(\omega_L)dv \tag{D.2}$$

where the B terms are the Einstein B coefficients, the n terms are the fractional populations of the states and $L(\omega_L)$ is a Lorentzian which describes the atomic absorption line shape.

Here we attempt to model the modulation transfer process by first calculating the time dependence of the levels' populations due to the modulated pump beam. From the preceding equation we see that the time dependence of the levels' populations results in a time dependence of the probe beam's absorption by the vapour and thus the signal measured by the photodiode.

Ignoring the probe beam, the Hamiltonian of the system is given by:

$$H = H_A + V = \hbar\omega_0|e\rangle\langle e| + V \tag{D.3}$$

where $H_A = \hbar\omega_0|e\rangle\langle e|$ is the Hamiltonian of the two level atom and V corresponds to its interaction with the pump laser. As shown in section 5.3, the pump beam can be described by an electric field composed of a carrier oscillating at angular frequency ω_L with side bands of opposite sign to each other and relative magnitude A to the carrier, separated in frequency space by ω_m:

$$\begin{aligned} E_{pump} &= E_0\left[\sin(\omega_L t) + A\sin((\omega_L+\omega_m t)t) - A\sin((\omega_L-\omega_m)t)\right] \\ &= \frac{E_0}{2i}\Big[\left(e^{i\omega_L t} - e^{-i\omega_L t}\right) + A\left(e^{i(\omega_L+\omega_m)t} - e^{-i(\omega_L+\omega_m)t}\right) \\ &\qquad - A\left(e^{i(\omega_L-\omega_m)t} - e^{-i(\omega_L-\omega_m)t}\right)\Big] \end{aligned} \tag{D.4}$$

where for simplicity we have set $\omega_{AOM_0} = 0$, equivalent to changing the reference frame of the problem. In this expression the electric dipole approximation has been made, where the spatial variation of the electric field is assumed to be negligible across the atom because its size is much smaller than the wavelength of the light.

The electric dipole interaction is given by:

$$\begin{aligned} V(t) &= -dE_{pump}(t) = -d_{eg}(|e\rangle\langle g| + |g\rangle\langle e|)E_{pump}(t) \\ &= -\frac{d_{eg}E_0}{2i}(|e\rangle\langle g| + |g\rangle\langle e|)\Big[\left(e^{i\omega_L t} - e^{-i\omega_L t}\right) \\ &\quad + A\left(e^{i(\omega_L+\omega_m)t} - e^{-i(\omega_L+\omega_m)t}\right) - A\left(e^{i(\omega_L-\omega_m)t} - e^{-i(\omega_L-\omega_m)t}\right)\Big] \end{aligned} \tag{D.5}$$

So the total Hamiltonian in matrix form is:

$$H = \begin{bmatrix} \hbar\omega_0 & \langle e|V|g\rangle \\ \langle g|V|e\rangle & 0 \end{bmatrix} \tag{D.6}$$

In order to calculate the time dependence of the state populations we use the density matrix formulation to model an ensemble of atoms in the vapour cell.

The ensemble averaged density operator, and thus matrix, for the N atoms in the vapour cell is given by:

$$\rho = \frac{1}{N}\sum_i^N \sum_{m,n} c_m^{*i} c_n^i |n\rangle\langle m| = \begin{bmatrix} \rho_{ee} & \rho_{eg} \\ \rho_{ge} & \rho_{gg} \end{bmatrix} \tag{D.7}$$

where c_n^i is the expansion coefficient for the ith atom to be measured in the state $|n\rangle$. Initially the ensemble is assumed to be in a pure state, with all the atoms in the ground level, so $\rho(t=0) = |g\rangle\langle g|$; $\rho_{gg} = 1, \rho_{ee} = \rho_{eg} = \rho_{ge} = 0$.

The time evolution of the density operator is given by the Liouville equation:

$$\frac{d\rho}{dt} = \frac{1}{i\hbar}[H, \rho] \tag{D.8}$$

As with all operators, the density operator in the interaction picture is related to that in the Schrödinger picture by the transformation:

$$\rho_{IR} = e^{iH_0 t/\hbar}\rho_{SR}e^{-iH_0 t/\hbar} \tag{D.9}$$

and so its time evolution is given by:

$$\begin{aligned}
\frac{d\rho_{IR}}{dt} &= \frac{i}{\hbar}H_0 e^{iH_0 t/\hbar}\rho_{SR}e^{-iH_0 t/\hbar} - \frac{i}{\hbar}e^{iH_0 t/\hbar}\rho_{SR}H_0 e^{-iH_0 t/\hbar} + e^{iH_0 t/\hbar}\left(\frac{d\rho_{SR}}{dt}\right)e^{-iH_0 t/\hbar} \\
&= \frac{i}{\hbar}[H_0, \rho_{IR}] + e^{iH_0 t/\hbar}\left(\frac{d\rho_{SR}}{dt}\right)e^{-iH_0 t/\hbar} \\
&= \frac{i}{\hbar}[H_0, \rho_{IR}] - \frac{i}{\hbar}e^{iH_0 t/\hbar}[H, \rho_{SR}]e^{-iH_0 t/\hbar} \\
&= \frac{i}{\hbar}[\rho_{IR}, V_{IR}]
\end{aligned} \tag{D.10}$$

where $V_{IR} = e^{iH_0 t/\hbar}V_{SR}e^{-iH_0 t/\hbar}$ is the electric dipole interaction in the interaction picture with the following matrix elements:

$$\begin{aligned}
\langle e|V_{IR}(t)|g\rangle &= -\frac{d_{eg}E_0}{2i}e^{i\omega_0 t}\left[\left(e^{i\omega_L t} - e^{-i\omega_L t}\right)\right. \\
&\quad \left. + A\left(e^{i(\omega_L+\omega_m)t} - e^{-i(\omega_L+\omega_m)t}\right) - A\left(e^{i(\omega_L-\omega_m)t} - e^{-i(\omega_L-\omega_m)t}\right)\right] \\
&= -\frac{d_{eg}E_0}{2i}\left[\left(e^{i(\omega_0+\omega_L)t} - e^{i\Delta t}\right)\right. \\
&\quad \left. + A\left(e^{i(\omega_0+\omega_L+\omega_m)t} - e^{i(\Delta-\omega_m)t}\right) - A\left(e^{i(\omega_0+\omega_L-\omega_m)t} - e^{i(\Delta+\omega_m)t}\right)\right]
\end{aligned} \tag{D.11}$$

$$\begin{aligned}\langle g|V_{IR}(t)|e\rangle = -\frac{d_{eg}E_0}{2i}\Big[&\left(e^{i\omega_L t} - e^{-i\omega_L t}\right) \\ &+A\left(e^{i(\omega_L+\omega_m)t} - e^{-i(\omega_L+\omega_m)t}\right) - A\left(e^{i(\omega_L-\omega_m)t} - e^{-i(\omega_L-\omega_m)t}\right)\Big] e^{-i\omega_0 t} \\ = -\frac{d_{eg}E_0}{2i}\Big[&\left(e^{-i\Delta t} - e^{-i(\omega_0+\omega_L)t}\right) \\ &+A\left(e^{-i(\Delta-\omega_m)t} - e^{-i(\omega_0+\omega_L+\omega_m)t}\right) - A\left(e^{-i(\Delta+\omega_m)t} - e^{-i(\omega_0+\omega_L-\omega_m)t}\right)\Big]\end{aligned} \tag{D.12}$$

$$\langle e|V_{IR}(t)|e\rangle = \langle g|V_{IR}(t)|g\rangle = 0 \tag{D.13}$$

where $\Delta = \omega_0 - \omega_L$ is the detuning of the laser from the resonant frequency of the transition. As $\Delta, \omega_m \ll \omega_0, \omega_L$ the fast oscillating terms $\pm(\omega_0 + \omega_L), \pm(\omega_0 + \omega_L \pm \omega_m)$ can be neglected, leaving the simplified expressions:

$$\begin{aligned}\langle e|V_{IR}(t)|g\rangle &\approx -\frac{d_{eg}E_0}{2i}\left[-e^{i\Delta t} - Ae^{i(\Delta-\omega_m)t} + Ae^{i(\Delta+\omega_m)t}\right] \\ &\approx \frac{\Omega\hbar}{2i}e^{i\Delta t}\left[1 - 2Ai\sin(\omega_m t)\right]\end{aligned} \tag{D.14}$$

$$\begin{aligned}\langle g|V_{IR}(t)|e\rangle &\approx -\frac{d_{eg}E_0}{2i}\left[e^{-i\Delta t} + Ae^{-i(\Delta-\omega_m)t} - Ae^{-i(\Delta+\omega_m)t}\right] \\ &\approx -\frac{\Omega\hbar}{2i}e^{-i\Delta t}\left[1 + 2Ai\sin(\omega_m t)\right]\end{aligned} \tag{D.15}$$

where Ω is the Rabi frequency given by:

$$\Omega = \frac{d_{eg}E_0}{\hbar} \tag{D.16}$$

This is known as the Rotating Wave Approximation (RWA), and is justified because the removed terms correspond to transitions moving the atom from the ground to the excited state while emitting a photon, and the atom moving from the excited to ground state while absorbing a photon[77].

If the carrier is on resonance and the side bands are absent (setting $A = 0$), the probability of the atom being observed in the excited state oscillates at the Rabi frequency. If, however, the carrier is detuned from the transition then these oscillations occur at the generalized Rabi frequency given by $\Omega' = \sqrt{\Omega^2 + \Delta^2}$.

In order to add relaxation from spontaneous emission into the model, the Linblad operator is added to the Liouville equation in the interaction picture:

$$\frac{d\rho_{IR}}{dt} = \frac{i}{\hbar}[\rho_{IR}, V_{IR}] + L(\rho_{IR}) \tag{D.17}$$

where the Linblad operator is given by:

$$L(\rho_{IR}) = \sum_n C_n \rho C_n^\dagger - \frac{1}{2}\sum_n \left(C_n^\dagger C_n \rho + \rho C_n^\dagger C_n \right) \tag{D.18}$$

and the C_n operators describe the various decay modes in the system. In the model of a two level atom there is only one decay mode; the excited state relaxes to the ground state at a rate determined by the natural linewidth:

$$C_e = \sqrt{\Gamma}|g\rangle\langle e| \tag{D.19}$$

$$L(\rho_{IR}) = \sum_n C_n \rho C_n^\dagger - \frac{1}{2}\sum_n \left(C_n^\dagger C_n \rho + \rho C_n^\dagger C_n \right) \tag{D.20}$$

$$L(\rho_{IR}) = \begin{bmatrix} -\Gamma\rho_{ee} & -\frac{1}{2}\Gamma\rho_{eg} \\ -\frac{1}{2}\Gamma\rho_{ge} & \Gamma\rho_{ee} \end{bmatrix} \tag{D.21}$$

As expected, and as shown in figure D.1, setting the relative side band strength, A, to zero removes the side bands from the model and the time evolution of the density matrix simply yields damped Bloch oscillations. As the strength of this factor increases the oscillations become increasingly distorted, although regardless of the modulation strength the excitation probability eventually settles around the same steady state value that is found without including the side bands into the model. It is interesting to note that the modulated beam of strength $A = 4.0$ experiences significantly less damping than the unmodulated beam, and that after the first oscillation the ensemble of atoms is almost completely brought back into their ground states.

The traces shown in figure D.1 are all calculated with zero detuning, and thus the carrier is on resonance. Fourier transforms of these traces show that, after the initial Bloch oscillations become damped, the signal is composed of frequency components at multiples of, but not at, the modulation frequency. As shown in figure D.2, as the carrier is brought away from resonance the residual oscillations become more complex due to the presence of a component which emerges at the

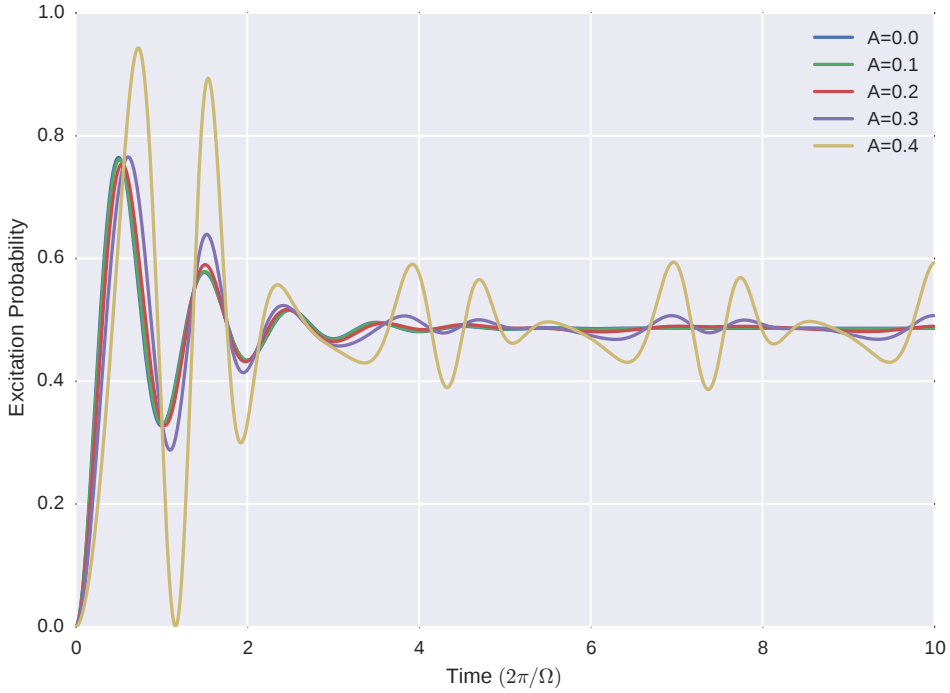

Figure D.1: Damped Bloch oscillations of an ensemble of two level atoms with varying strengths of beam modulation, A. For each trace the carrier is on resonance $\Delta = 0$, $\Omega \approx 4.2\Gamma$ and $\omega_m \approx 0.69\Gamma$.

modulation frequency. Figure D.3 shows that as the carrier is swept across resonance the strength of this component varies to give the zero crossing expected from an error signal.

The preceding discussion has only dealt with the case of a two level atom, which is a fairly good model of the closed transitions of the two isotopes of rubidium. In general though the atoms can collapse from their excited state to a number of levels which are invisible to the pumping laser and thus this optical pumping removes these atoms from the system. As shown in equation D.2 the absorption cross section of the vapour is related to the difference in the populations of the ground and excited states coupled by the probe laser. In the case of transitions which are open these populations are depleted, reducing the absorption cross section to zero and preventing the modulation from being transferred to the probe beam. For the closed transitions, however, the atoms are not pumped into dark states so they always remain coupled by the pump laser and so the modulation is transferred to the pump beam.

Because we are dealing with an ensemble rather than a single atom, for the derived model to make sense the electric field oscillating at the modulation frequency must

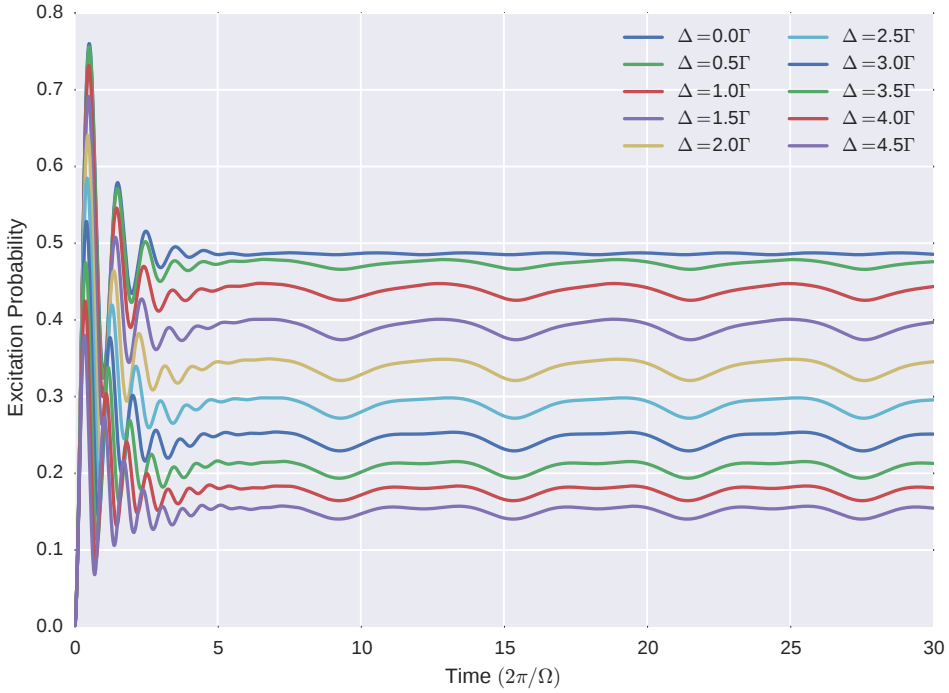

Figure D.2: Bloch oscillations of and ensemble of two level atoms at various levels of detuning of the carrier from resonance. Each trace is taken with $A = 0.11$

be approximately constant along the cell to prevent dephasing. This is similar to the dipole approximation that was made earlier, however now we are concerned with the envelope moving at ω_m rather than the carrier at ω_L.

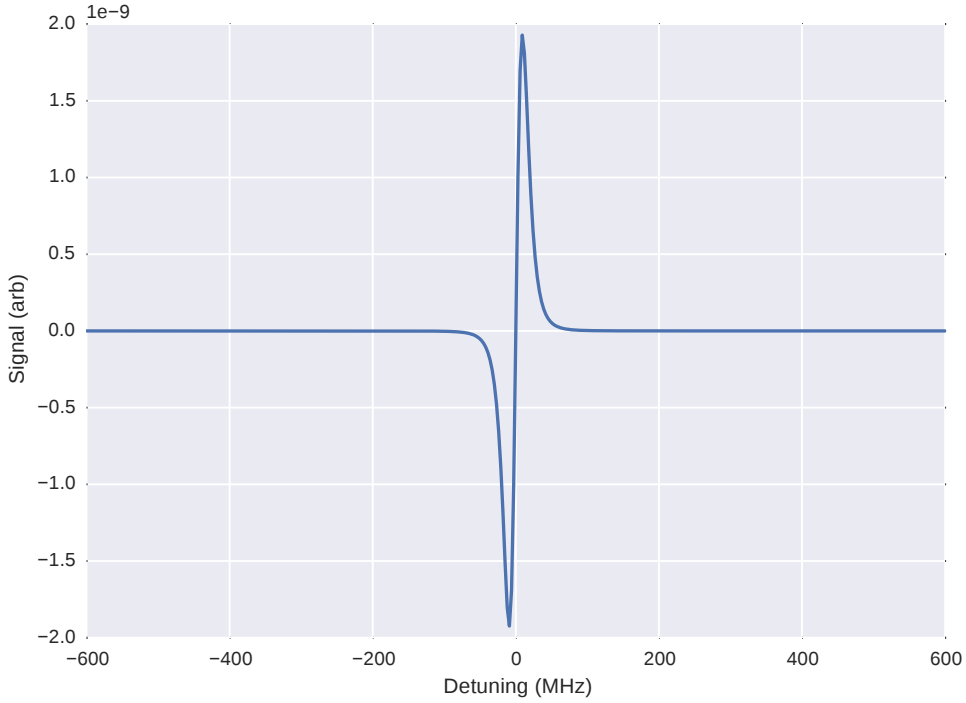

Figure D.3: Strength of the modulation of the excitation probability at frequency ω_m with respect to detuning of the carrier from resonance. The trace has a zero crossing at a detuning of $\Delta = 0$, that expected for an error signal. The parameters used in creating this plot were: $A = 0.11$, $\Gamma = 2\pi{\cdot}6.07\,\mathrm{MHz}$, $\omega_m = 2\pi{\cdot}4.26\,\mathrm{MHz}$ and $\Omega = 2\pi{\cdot}25.6\,\mathrm{MHz}$

Appendix E

Microcontroller Based Laser Locking

Prior to the arrival of an updated design of Matthew Himsworth's analogue Proportional Integral Differential (PID) laser locking circuit the author was set the task of designing an interim Proportional Integral (PI) controller based upon the popular prototyping platform known as the 'Arduino'. The goal of this was to rapidly produce a circuit that, through piezo feedback, would provide frequency stabilization of Southampton's external cavity diode lasers and that later could conceivably be extended to bring additional software features such as lock detection. The development platform chosen was the 'ChipKit Max32' made by Digilent, a device designed to be broadly compatible with the 'Arduino Mega 2560'. The Max32 is based upon the PIC32MX795F512 microcontroller from Microchip running with a clock speed of 80 MHz, as opposed to the ATmega2560 from Atmel found in the Arduino Mega 2560 which has a clock speed of 16 MHz. This particular platform was chosen because it was the fastest of its type at the time, however the differing architectures meant that the low-level programming required to achieve the fastest bandwidth was not compatible with both devices. The microcontroller in the Max32 is also only able to read up to 3.3 V analogue signals, again breaking compatibility with the Arduino, which is capable of measuring up to 5 V.

The Max32 provides numerous digital input/output pins in addition to 16 10-bit resolution analogue inputs and 5 further pins that can drive 8-bit Pulse Width Modulated (PWM) analogue outputs. To achieve a greater bandwidth it was decided that a plug-in 'Locking Shield' would be designed that would utilize a DAC8562 12-bit parallel Digital to Analogue Converter (DAC) to rapidly drive

the piezo with a high resolution over a narrow voltage range, and that this would be used in combination with a MCP4821 12-bit serial DAC to give a slower, coarse adjustment over a much greater voltage range. Other op-amps were required on the board to sum these output signals and to provide level shifting to interface the external bipolar signals with the microcontroller, which is only capable of reading and driving positive waveforms. The bipolar nature of the external signals meant that a separate power supply had to be connected to the shield to provide $\pm 18\,\mathrm{V}$ rails which were filtered and subsequently regulated to $\pm 15\,\mathrm{V}$ and $+5\,\mathrm{V}$ rails. To improve signal fidelity the externally provided analogue rails were isolated from the digital rails, and their grounds were also separated except at a single point.

To achieve the greatest possible bandwidth and to reduce glitches caused by out of sync pin writes, communication with the parallel DAC was performed by setting the value of an output port register to drive all of the lines of the bus simultaneously. This restricted the parallel DAC to be wired to Port B of the microcontroller as it was the only one where all of the first 12-pins were both available and positioned sequentially on the Chipkit's headers. A rotary encoder was included in the design to allow for many turn control of the offset voltage output by the serial DAC. Two trimmers were used to set the P and I coefficients, and these were attached to two analogue pins of the microcontroller to be read during the PID loop function. Reading these analogue values would cause a slight reduction of the circuit's bandwidth, so once appropriate settings were found any calls to these analogue reads were removed from the loop. Two further potentiometers are used to set the centre voltage of the piezo sweep and to adjust the voltage range of the parallel DAC. The centre voltage of the piezo sweep, a secondary offset to that determined by the serial DAC, can be coarsely or finely adjusted and this state is toggled by a momentary switch.

The full schematic of the PID shield can be seen in figure E.2, while a code listing used to program the microcontroller is given at the end of this chapter. Figure E.1 shows a histogram of the error signal produced by Zeeman modulation as the microcontroller maintains its lock to a crossover resonance of rubidium 87. The full width at half maximum of the histogram gives an estimate of the narrowed linewidth of the stabilized laser of around 1.3 MHz. It has been observed, however, that this method of linewidth measurement is fraught with systematic errors, because the variation of the error signal does not necessarily correspond to laser frequency fluctuations. A more appropriate approach would be to infer the linewidth from the beat note obtained between two independently locked lasers[98], from a self-heterodyne measurement via the use of an optical fibre delay line, or

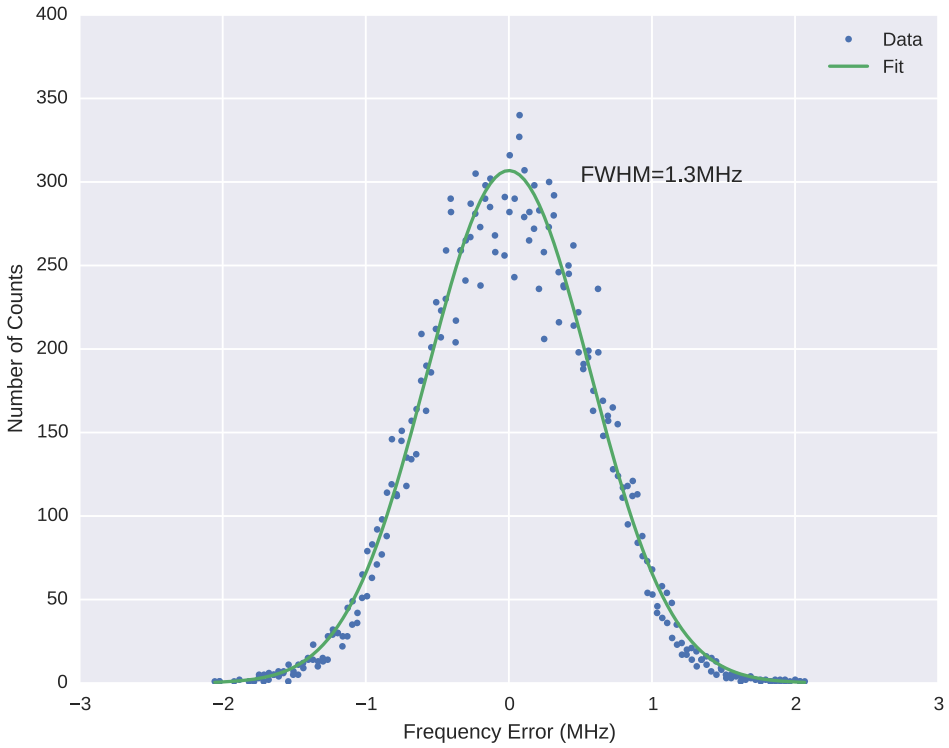

Figure E.1: Histogram of the error signal produced by Zeeman modulation as an external cavity diode laser is locked by the 'Locking Shield' to a crossover resonance of rubidium 87. An estimate of the laser's linewidth is given from the histogram, however this technique is known to produce systematic errors[98].

from the histogram of the laser's spectroscopic signal (as opposed to the error signal) as it is locked to the side of an atomic transition.

Whilst the usability of this implementation of a digital laser lock was somewhat lacking, it certainly proved adequate to perform the stabilization that it was designed for, namely the ability to lock to the cooling transitions of rubidium. This scheme was soon replaced by one using a more traditional and user friendly analogue PID circuit, earlier designs of which were able to achieve a narrower linewidth of $570 \pm 140\,\mathrm{kHz}$[111]. The digital lock, however, worked well as a proof of principle, can be built quickly with easily available parts and could possibly be further extended to include additional features such as lock detection.

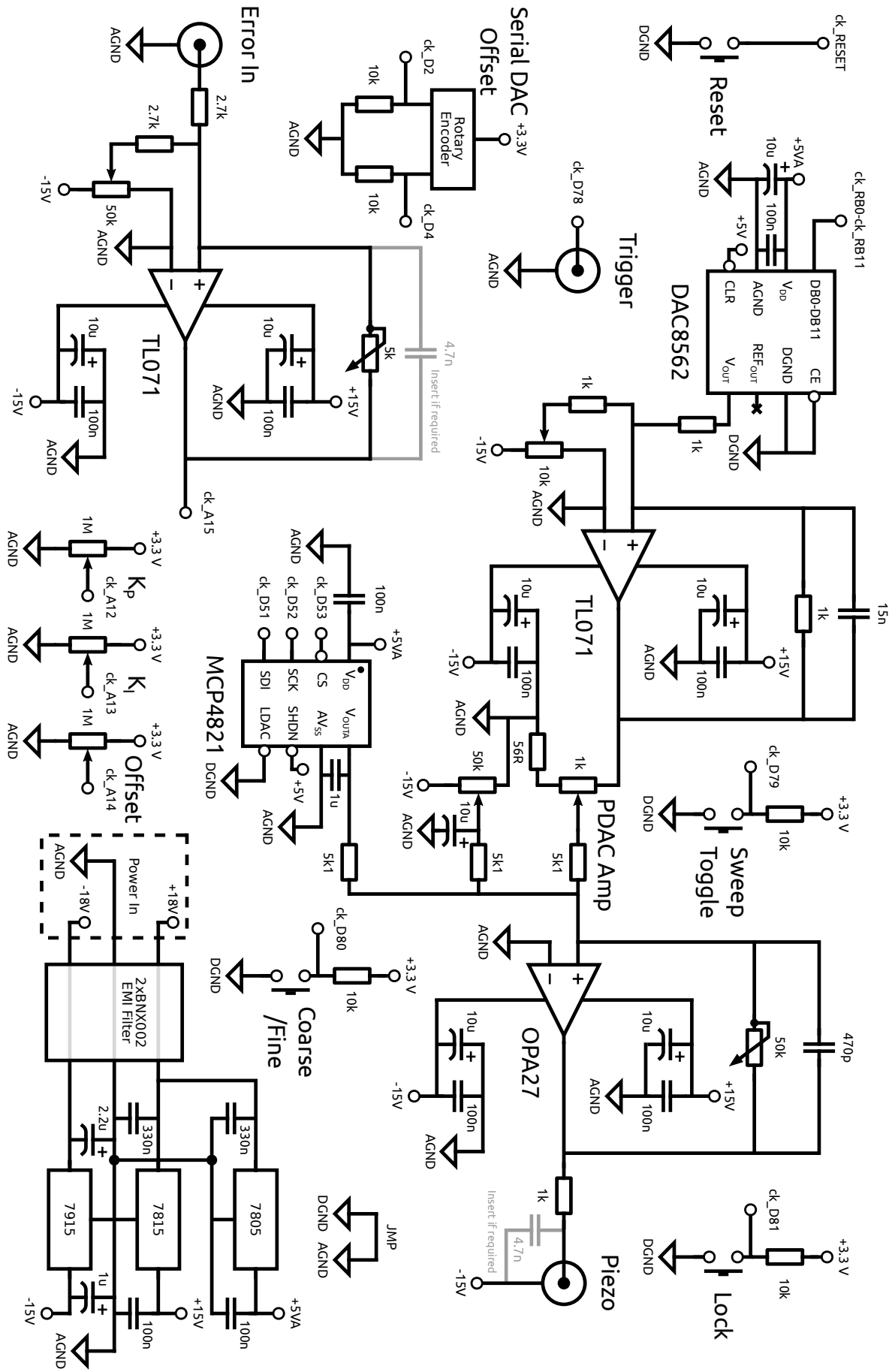

Figure E.2: Schematic for PID board for connection to a Digilent Chipkit Max32 microcontroller.

E.1 Source Code

```
#include <DSPI.h>
#include <SoftSPI.h>

#define TIMESTEP 24
#define PGAIN 1.0
#define IGAIN 0.5*TIMESTEP
#define ZEROPOINT 2048
#define MAX_VAL 4095
#define FREQUENCY 5
#define MAXCHANGE 1000

static boolean rotating=false;
DSPI0 SPI;
uint16_t serVol;

void rotEncoder(){ // Callback function upon detecting movement of
    rotary encoder
  rotating=true;
}

int i;
int dir;
int offset;
int triwave;
float I;
int coarse;
int fine;

int lock;

float Kp;
float Ki;

unsigned long lstprss;
unsigned long lstanlg;
unsigned long lsttime;

unsigned long prevtime;

void pidloop();


void setup() {
  pinMode(2,INPUT); // input 1 for rotary encoder
```

```
44    pinMode(4,INPUT); // input 2 for rotary encoder
45    attachInterrupt(1, rotEncoder, RISING);
46
47    serVol=2047;
48
49    SPI.setMode(DSPI_MODE1);
50    SPI.setSpeed(20000000);
51    SPI.begin();
52
53    TRISGSET = 1;    // Set pin 0 of RG as input (ck_D79 = piezo
       sweep toggle button)
54    TRISGCLR = 2;    // Set pin 1 of RG as output (ck_D78 = Trigger)
55    TRISASET = 192; // Set pins 6 and 7 of RA as inputs (ck_D80=
       coarse/fine toggle button, ck_D81=lock button)
56    TRISB = 0xF000; // Set pins 0 to 11 of RB as outputs and the
       remaining as inputs (Parallel DAC)
57    ODCB  = 0;       // Set Parallel DAC output pins to push-pull
       mode
58
59    i=0;
60    dir=0;
61    I=0;
62    offset=0;
63    triwave=1;
64    lstprss = millis();
65    lstanlg = millis();
66    prevtime = micros();
67
68    fine=0;
69    lock=0;
70  }
71
72  void dighandle(){ // NOTE: No account for overflow (will occur in
       approximately 50 days).
73    if(!(PORTA & (1 << 7)) ) { // if lock button pressed
74      lock=1;
75    }
76    if(!(PORTA & (1 << 6)) && (lstprss + 1000 < millis())) { // if
       coarse/fine toggle button pressed
77      coarse = offset;
78      fine ^= 1;
79
80      lstprss = millis();
81    }
82    if(!(PORTG & 1) && (lstprss + 1000 < millis())) { // if piezo
       sweep toggle pressed
```

```
83      triwave ^= 1;
84      lstprss = millis();
85    }
86
87    if(fine==0 && (lstanlg + 100 < millis())){
88      offset=(int)(analogRead(14)*(MAX_VAL/1023.0))-ZEROPOINT;
89      lstanlg = millis();
90    }
91    else if(fine==1 && (lstanlg + 100 < millis())){
92      offset=(int)(coarse + (analogRead(14)/1023.0)*(MAX_VAL/50.0))
       -(int)(ZEROPOINT/50.0);
93      lstanlg = millis();
94    }
95
96  }
97
98  void sweep(){
99    unsigned long deltat = micros()-prevtime;
100   float ifl =-offset + (1.0/1000000.0)*deltat*FREQUENCY*2.0*4095;
        // Find the change in output since beginning of the current
       loop
101
102   if(ifl+offset<=MAX_VAL) {
103     i=ifl;
104     LATB = i+offset;
105
106     if (i==ZEROPOINT){
107       LATGSET = (1 << 1);
108       if(lock==1){
109         pidloop();  //Lock only if piezo is currently at lock
       point
110       }
111     }
112
113   }
114   else if(ifl+offset>=2*MAX_VAL) {
115     i=-offset;
116     LATB = i+offset;
117     prevtime = micros();
118
119   }
120   else {
121     i=(2*MAX_VAL)-(ifl+2*offset);
122     LATB = i+offset;
123     if(i+2*offset==ZEROPOINT){
124       LATGCLR = (1 << 1);
```

```
125     }
126   }
127 }
128
129 void offsetsweep(){
130   unsigned long deltat = micros()-prevtime;
131   float ifl =-offset + (1.0/1000000.0)*deltat*FREQUENCY*2.0*4095;
        // Find the change in output since beginning of the current
       loop
132
133   if(ifl+offset<=MAX_VAL) {
134     i=ifl;
135     if (i==ZEROPOINT){
136       LATGSET = (1 << 1);
137     }
138   }
139   else if(ifl+offset>=2*MAX_VAL) {
140     i=-offset;
141     prevtime = micros();
142   }
143   else {
144     i=(2*MAX_VAL)-(ifl+2*offset);
145     if(i+2*offset==ZEROPOINT){
146       LATGCLR = (1 << 1);
147     }
148   }
149
150   if(lock==1){
151     pidloop();
152   }
153 }
154
155 void setcoeff(){ // Read PI coeffients from trimmer pots attached
       to ck_A12 and ck_A13
156   Kp=analogRead(12)*0.87; // scale Kp and Ki down from read values
       .
157   Ki=analogRead(13)*0.87;
158
159 }
160
161 void pidloop(){
162
163   setcoeff();
164   detachInterrupt(1);
165   noInterrupts();
166
```

```
167   unsigned long thistime;
168   float deltatime;
169   int response=ZEROPOINT+offset;
170   int startvoltage=response;
171
172   lsttime=micros();
173   lstanlg=lsttime;
174
175   while(1){
176     int errorsig = analogRead(15)-512;  // Read error signal, zero
      should correspond to half the range
177     thistime=micros();
178
179     deltatime=(float)(thistime-lsttime);
180     I+=errorsig*deltatime*0.0001;
181     int Iout=I*Ki*0.001;
182     lsttime=thistime;
183     int P=errorsig*Kp*0.0001;
184     int change= P + Iout;
185     LATB = response + change;
186
187
188     if(thistime>lstanlg+400){
189       setcoeff();
190       lstanlg=thistime;
191     }
192
193   }
194 }
195
196 void rotcheck(){
197   while(rotating){
198     delay(2);
199     if(digitalRead(4)==digitalRead(2)){ // Turning CCW
200       if(serVol<10){
201         serVol=0;
202       } else {
203         serVol-=10;
204       }
205     }
206     else { // Turning CW
207       serVol+=10;
208       if(serVol>4095){
209         serVol=4095;
210       }
211     }
```

```
212
213     int spiMask;
214     uint16_t spiData;
215
216     spiMask=0x1000; // Sets DACA output, output Gain=2, SHDN bit,
217     spiData=spiMask|(serVol & 0x0FFF);
218     uint16_t temp;
219     temp = (spiData<<8) | (spiData>>8);
220     SPI.setSelect(LOW);
221     SPI.transfer((uint16_t)2, (uint8_t*)&temp);
222     SPI.setSelect(HIGH);
223
224     rotating=false;
225   }
226 }
227
228 void triloop(){
229   while(triwave == 1 || i!=ZEROPOINT){  // Prevents putting stress
        on the piezo
230
231     sweep();
232     dighandle();
233     rotcheck();
234   }
235 }
236
237 void offsetloop(){
238   while(triwave == 0 || i!=ZEROPOINT){  // Prevents putting stress
        on the piezo
239     offsetsweep();
240
241     LATB = ZEROPOINT + offset;
242     dighandle();
243     rotcheck();
244   }
245 }
246
247 void loop() {
248   if(triwave==1)
249     triloop();
250   else
251     offsetloop();
252 }
```

References

[1] J. A. Rushton, M. Aldous, and M. D. Himsworth. Contributed review: The feasibility of a fully miniaturized magneto-optical trap for portable ultracold quantum technology. *Rev. Sci. Instrum.*, 85(12):121501, 2014. doi:10.1063/1.4904066. URL http://scitation.aip.org/content/aip/journal/rsi/85/12/10.1063/1.4904066.

[2] A. Ashkin. Atomic-beam deflection by resonance-radiation pressure. *Phys. Rev. Lett.*, 25:1321–1324, 1970. doi:10.1103/PhysRevLett.25.1321. URL http://link.aps.org/doi/10.1103/PhysRevLett.25.1321.

[3] T.W. Hänsch and A.L. Schawlow. Cooling of gases by laser radiation. *Opt. Commun.*, 13(1):68–69, 1975. ISSN 0030-4018. doi:10.1016/0030-4018(75)90159-5. URL http://www.sciencedirect.com/science/article/pii/0030401875901595.

[4] V. G. Minogin. Theory of a radiative atomic trap. *Sov. J. Quantum Electron.*, 12(3):299, 1982. doi:10.1070/QE1982v012n03ABEH012095. URL http://stacks.iop.org/0049-1748/12/i=3/a=A09.

[5] V. G. Minogin and J. Javanainen. A tetrahedral light pressure trap for atoms. *Opt. Commun.*, 43(2):119–122, 1982. ISSN 0030-4018. doi:10.1016/0030-4018(82)90104-3. URL http://www.sciencedirect.com/science/article/pii/0030401882901043.

[6] A. Ashkin and J. P. Gordon. Stability of radiation-pressure particle traps: an optical Earnshaw theorem. *Opt. Lett.*, 8(10):511–513, 1983. doi:10.1364/OL.8.000511. URL http://ol.osa.org/abstract.cfm?URI=ol-8-10-511.

[7] S. Chu, L. Hollberg, J. E. Bjorkholm, A. Cable, and A. Ashkin. Three-dimensional viscous confinement and cooling of atoms by resonance radiation

pressure. *Phys. Rev. Lett.*, 55:48–51, 1985. doi:10.1103/PhysRevLett.55.48. URL http://link.aps.org/doi/10.1103/PhysRevLett.55.48.

[8] A. Ashkin. Stable radiation-pressure particle traps using alternating light beams. *Opt. Lett.*, 9(10):454–456, 1984. doi:10.1364/OL.9.000454. URL http://ol.osa.org/abstract.cfm?URI=ol-9-10-454.

[9] D. E. Pritchard, E. L. Raab, V. Bagnato, C. E. Wieman, and R. N. Watts. Light traps using spontaneous forces. *Phys. Rev. Lett.*, 57:310–313, 1986. doi:10.1103/PhysRevLett.57.310. URL http://link.aps.org/doi/10.1103/PhysRevLett.57.310.

[10] P. Bouyer, P. Lemonde, M. Ben Dahan, A. Michaud, C. Salomon, and J. Dalibard. An atom trap relying on optical pumping. *Europhys. Lett.*, 27(8):569, 1994. doi:10.1209/0295-5075/27/8/003. URL http://stacks.iop.org/0295-5075/27/i=8/a=003.

[11] E. L. Raab, M. Prentiss, A. Cable, S. Chu, and D. E. Pritchard. Trapping of neutral sodium atoms with radiation pressure. *Phys. Rev. Lett.*, 59:2631–2634, 1987. doi:10.1103/PhysRevLett.59.2631. URL http://link.aps.org/doi/10.1103/PhysRevLett.59.2631.

[12] A. L. Migdall, J. V. Prodan, W. D. Phillips, T. H. Bergeman, and H. J. Metcalf. First observation of magnetically trapped neutral atoms. *Phys. Rev. Lett.*, 54:2596–2599, 1985. doi:10.1103/PhysRevLett.54.2596. URL http://link.aps.org/doi/10.1103/PhysRevLett.54.2596.

[13] M. H. Anderson, J. R. Ensher, M. R. Matthews, C. E. Wieman, and E. A. Cornell. Observation of Bose-Einstein condensation in a dilute atomic vapor. *Science*, 269(5221):198–201, 1995. doi:10.1126/science.269.5221.198. URL http://www.sciencemag.org/content/269/5221/198.abstract.

[14] C. S. Adams, M. Sigel, and J. Mlynek. Atom optics. *Physics Reports*, 240(3):143–210, 1994. ISSN 0370-1573. doi:10.1016/0370-1573(94)90066-3. URL http://www.sciencedirect.com/science/article/pii/0370157394900663.

[15] S. M. Dickerson, J. M. Hogan, A. Sugarbaker, D. M. S. Johnson, and M. A. Kasevich. Multiaxis inertial sensing with long-time point source atom interferometry. *Phys. Rev. Lett.*, 111:083001, 2013. doi:10.1103/PhysRevLett.111.083001. URL http://link.aps.org/doi/10.1103/PhysRevLett.111.083001.

[16] S. Gupta, K. Dieckmann, Z. Hadzibabic, and D. E. Pritchard. Contrast interferometry using Bose-Einstein condensates to measure h/m and α. *Phys. Rev. Lett.*, 89:140401, 2002. doi:10.1103/PhysRevLett.89.140401. URL http://link.aps.org/doi/10.1103/PhysRevLett.89.140401.

[17] N. Gaaloul, H. Ahlers, T. A. Schulze, Y. Singh, S. T. Seidel, W. Herr, W. Ertmer, and E. Rasel. Quantum tests of the equivalence principle with atom interferometry. *Acta Astronautica*, 67(9-10):1059–1062, 2010. ISSN 0094-5765. doi:10.1016/j.actaastro.2010.06.043. URL http://www.sciencedirect.com/science/article/pii/S0094576510002341.

[18] J. B. Fixler, G. T. Foster, J. M. McGuirk, and M. A. Kasevich. Atom interferometer measurement of the newtonian constant of gravity. *Science*, 315(5808):74–77, 2007. doi:10.1126/science.1135459. URL http://www.sciencemag.org/content/315/5808/74.abstract.

[19] R. Folman, P. Krüger, D. Cassettari, B. Hessmo, T. Maier, and J. Schmiedmayer. Controlling cold atoms using nanofabricated surfaces: Atom chips. *Phys. Rev. Lett.*, 84:4749–4752, 2000. doi:10.1103/PhysRevLett.84.4749. URL http://link.aps.org/doi/10.1103/PhysRevLett.84.4749.

[20] T. Schumm, S. Hofferberth, L. M. Andersson, S. Wildermuth, S. Groth, I. Bar-Joseph, J. Schmiedmayer, and P. Krüger. Matter-wave interferometry in a double well on an atom chip. *Nature Physics*, 1(1):57–62, 2005. ISSN 1745-2473. doi:10.1038/nphys125. URL http://dx.doi.org/10.1038/nphys125.

[21] S. Wildermuth, S. Hofferberth, I. Lesanovsky, S. Groth, P. Krüger, J. Schmiedmayer, and I. Bar-Joseph. Sensing electric and magnetic fields with Bose-Einstein condensates. *Appl. Phys. Lett.*, 88(26):264103, 2006. doi:10.1063/1.2216932. URL http://scitation.aip.org/content/aip/journal/apl/88/26/10.1063/1.2216932.

[22] P. Treutlein, P. Hommelhoff, T. Steinmetz, T. W. Hänsch, and J. Reichel. Coherence in microchip traps. *Phys. Rev. Lett.*, 92:203005, 2004. doi:10.1103/PhysRevLett.92.203005. URL http://link.aps.org/doi/10.1103/PhysRevLett.92.203005.

[23] W. Hänsel, J. Reichel, P. Hommelhoff, and T. W. Hänsch. Magnetic conveyor belt for transporting and merging trapped atom clouds. *Phys. Rev. Lett.*, 86:

608–611, 2001. doi:10.1103/PhysRevLett.86.608. URL http://link.aps.org/doi/10.1103/PhysRevLett.86.608.

[24] M. A. Cirone, A. Negretti, T. Calarco, P. Krüger, and J. Schmiedmayer. A simple quantum gate with atom chips. *The European Physical Journal D - Atomic, Molecular, Optical and Plasma Physics*, 35(1):165–171, 2005. ISSN 1434-6060. doi:10.1140/epjd/e2005-00175-8. URL http://dx.doi.org/10.1140/epjd/e2005-00175-8.

[25] L. Liew, S. Knappe, J. Moreland, H. Robinson, L. Hollberg, and J. Kitching. Microfabricated alkali atom vapor cells. *Appl. Phys. Lett.*, 84(14):2694–2696, 2004. doi:10.1063/1.1691490. URL http://scitation.aip.org/content/aip/journal/apl/84/14/10.1063/1.1691490.

[26] S. Knappe, V. Shah, P. D. D. Schwindt, L. Hollberg, J. Kitching, L. Liew, and J. Moreland. A microfabricated atomic clock. *Appl. Phys. Lett.*, 85(9):1460–1462, 2004. doi:10.1063/1.1787942. URL http://scitation.aip.org/content/aip/journal/apl/85/9/10.1063/1.1787942.

[27] J. Kitching, N. Vukicevic, L. Hollberg, S. Knappe, C. Affolderbach, and R. Wynands. Microwave frequency reference based on VCSEL-driven dark-line resonances in Cs vapor. In *Frequency Control Symposium and Exhibition, 2000. Proceedings of the 2000 IEEE/EIA International*, pages 687–693, 2000. doi:10.1109/FREQ.2000.887438. URL http://ieeexplore.ieee.org/xpl/articleDetails.jsp?arnumber=887438.

[28] J. Kitching, L. Hollberg, S. Knappe, and R. Wynands. Compact atomic clock based on coherent population trapping. *Electronics Letters*, 37(24):1449–1451, 2001. ISSN 0013-5194. doi:10.1049/el:20010959. URL http://ieeexplore.ieee.org/xpl/articleDetails.jsp?arnumber=970386.

[29] E. A. Salim, J. DeNatale, D. M. Farkas, K. M. Hudek, S. E. McBride, J. Michalchuk, R. Mihailovich, and D. Z. Anderson. Compact, microchip-based systems for practical applications of ultracold atoms. *Quantum Information Processing*, 10(6):975–994, 2011. ISSN 1570-0755. doi:10.1007/s11128-011-0300-8. URL http://dx.doi.org/10.1007/s11128-011-0300-8.

[30] B. R. Chalamala, R. H. Reuss, and K. A. Dean. Real-time measurement of pressure inside field-emission displays. *Appl. Phys. Lett.*, 79(16):2648–2650,

2001. doi:10.1063/1.1412280. URL http://scitation.aip.org/content/aip/journal/apl/79/16/10.1063/1.1412280.

[31] A. Grecka-Drzazga. Miniature and MEMS-type vacuum sensors and pumps. *Vacuum*, 83(12):1419–1426, 2009. ISSN 0042-207X. doi:10.1016/j.vacuum.2009.05.003. URL http://www.sciencedirect.com/science/article/pii/S0042207X09002711.

[32] C. C. Peng and C. Tsai. Built in ion pump for field emission display, 1996. URL http://www.google.co.uk/patents/US5578900. US Patent 5,578,900.

[33] I. Garcia. *Advances in the design and operation of atom chips*. PhD thesis, Imperial College London, 2008.

[34] S. Du, M. Squires, Y. Imai, L. Czaia, R. Saravanan, V. Bright, J. Reichel, T. Hänsch, and D. Anderson. Atom-chip Bose-Einstein condensation in a portable vacuum cell. *Phys. Rev. A*, 70:053606, 2004. doi:10.1103/PhysRevA.70.053606. URL http://link.aps.org/doi/10.1103/PhysRevA.70.053606.

[35] A. Schram. La désorption sous vide. *Le Vide*, 103:55–68, 1963.

[36] N. Yoshimura. *Vacuum Technology: Practice for Scientific Instruments*. SpringerLink: Springer e-Books. Springer Berlin Heidelberg, 2007. ISBN 9783540744337. URL http://books.google.co.uk/books?id=6rsc8IK-ymsC.

[37] S. McNamara and Y. B. Gianchandani. On-chip vacuum generated by a micromachined Knudsen pump. *Journal of Microelectromechanical Systems*, 14(4):741–746, 2005. ISSN 1057-7157. doi:10.1109/JMEMS.2005.850718. URL http://ieeexplore.ieee.org/xpl/articleDetails.jsp?arnumber=1492425.

[38] V. Lindroos, M. Tilli, A. Lehto, and T. Motooka. *Handbook of silicon based MEMS materials and technologies*. Elsevier, 2009. URL http://www.sciencedirect.com/science/book/9780815515944.

[39] W. B. Choi, B. K. Ju, Y. H. Lee, S. J. Jeong, N. Y. Lee, M. Y. Sung, and M. H. Oh. Glass to glass bonding for vacuum packaging of field emission display in an ultra high vacuum chamber using silicon thin film.

J. Electrochem. Soc., 146(1):400–404, 1999. doi:10.1149/1.1391621. URL http://dx.doi.org/10.1149/1.1391621.

[40] T. Arpornthip, C. Sackett, and K. Hughes. Vacuum-pressure measurement using a magneto-optical trap. *Phys. Rev. A*, 85:033420, 2012. doi:10.1103/PhysRevA.85.033420. URL http://link.aps.org/doi/10.1103/PhysRevA.85.033420.

[41] F. J. Norton. Permeation of gases through solids. *J. Appl. Phys.*, 28(1): 34–39, 1957. doi:10.1063/1.1722570. URL http://scitation.aip.org/content/aip/journal/jap/28/1/10.1063/1.1722570.

[42] M. Li and H. F. Dylla. Model for the outgassing of water from metal surfaces. *J. Vac. Sci. Technol. A*, 11(4):1702–1707, 1993. doi:10.1116/1.578482. URL http://scitation.aip.org/content/avs/journal/jvsta/11/4/10.1116/1.578482.

[43] B. C. Moore. Recombination limited outgassing of stainless steel. *J. Vac. Sci. Technol. A*, 13(3):545–548, 1995. ISSN 0734-2101. doi:10.1116/1.579782. URL http://scitation.aip.org/content/avs/journal/jvsta/13/3/10.1116/1.579782.

[44] H. Mehrer. *Diffusion in Solids: Fundamentals, Methods, Materials, Diffusion-Controlled Processes*. Springer Series in Solid-State Sciences. Springer, 2007. ISBN 9783540714880. URL http://books.google.co.uk/books?id=IUZVffQLFKQC.

[45] H. S. Carslaw and J. C. Jaeger. *Conduction of Heat in Solids*. Oxford science publications. Clarendon Press, 1986. ISBN 9780198533689. URL http://books.google.co.uk/books?id=KxS1LDD6GbQC.

[46] W. A. Rogers, R. S. Buritz, and D. Alpert. Diffusion coefficient, solubility, and permeability for helium in glass. *J. Appl. Phys.*, 25(7):868–875, 1954. doi:10.1063/1.1721760. URL http://scitation.aip.org/content/aip/journal/jap/25/7/10.1063/1.1721760.

[47] V. O. Altemose. Helium diffusion through glass. *J. Appl. Phys.*, 32(7): 1309–1316, 1961. doi:10.1063/1.1736226. URL http://scitation.aip.org/content/aip/journal/jap/32/7/10.1063/1.1736226.

[48] J. Covino and J. M. Bennett. Laser-gyro materials studies. Technical report, DTIC Document, 1986. URL http://www.dtic.mil/dtic/tr/fulltext/u2/a169595.pdf.

[49] M. Ozima and F. A. Podosek. *Noble Gas Geochemistry*. Cambridge University Press, 2002. ISBN 9780521803663. URL https://books.google.co.uk/books?id=TMIAfSIe428C.

[50] J. C. G. Walker. *Evolution of the atmosphere*. Macmillan, 1977. URL https://books.google.co.uk/books?id=nFJRAAAAMAAJ.

[51] D. L. Hartmann. Chapter 1 tables: Composition of the atmosphere. www.atmos.washington.edu/~dennis/321/Chapter_01_Tables.pdf, 2014. Accessed: 24-03-2015.

[52] G. Wallis and D. I. Pomerantz. Field assisted glass-metal sealing. *J. Appl. Phys.*, 40(10):3946–3949, 1969. doi:10.1063/1.1657121. URL http://scitation.aip.org/content/aip/journal/jap/40/10/10.1063/1.1657121.

[53] J. F. Shackelford, P. L. Studt, and R. M. Fulrath. Solubility of gases in glass. II. He, Ne, and H2 in fused silica. *J. Appl. Phys.*, 43(4):1619–1626, 1972. doi:10.1063/1.1661371. URL http://scitation.aip.org/content/aip/journal/jap/43/4/10.1063/1.1661371.

[54] F. J. Norton. Helium diffusion through glass. *Journal of the American Ceramic Society*, 36(3):90–96, 1953. ISSN 1551-2916. doi:10.1111/j.1151-2916.1953.tb12843.x. URL http://dx.doi.org/10.1111/j.1151-2916.1953.tb12843.x.

[55] K. Jousten. Thermal outgassing. (OPEN-2000-274), 1999. URL https://cds.cern.ch/record/455558.

[56] P. A. Redhead. Thermal desorption of gases. *Vacuum*, 12(4):203–211, 1962. doi:10.1016/0042-207X(62)90978-8. URL http://www.sciencedirect.com/science/article/pii/0042207X62909788.

[57] V. Baglin. Cold/sticky systems. 2007. URL http://cds.cern.ch/record/1047076.

[58] P. Chiggiato and P. Costa Pinto. Ti-Zr-V non-evaporable getter films: From development to large scale production for the large hadron

collider. *Thin Solid Films*, 515(2):382 – 388, 2006. ISSN 0040-6090. doi:10.1016/j.tsf.2005.12.218. URL http://www.sciencedirect.com/science/article/pii/S0040609005025496.

[59] H. Chang, C. Huang, S. Liu, S. Lin, M. Liao, S. Chiu, and C. Chen. High hermetic performance of glass frit for MEMS package. In *5th International Microsystems Packaging Assembly and Circuits Technology Conference (IMPACT)*, pages 1–3, 2010. doi:10.1109/IMPACT.2010.5699539. URL http://ieeexplore.ieee.org/xpl/articleDetails.jsp?arnumber=5699539.

[60] D. Sparks, J. Trevino, S. Massoud-Ansari, and N. Najafi. An all-glass chip-scale MEMS package with variable cavity pressure. *J. Micromech. Microeng.*, 16(11):2488, 2006. doi:10.1088/0960-1317/16/11/033. URL http://stacks.iop.org/0960-1317/16/i=11/a=033.

[61] N. Lorenz, S. Millar, M. Desmulliez, and D. P. Hand. Hermetic glass frit packaging in air and vacuum with localized laser joining. *J. Micromech. Microeng.*, 21(4):045039, 2011. doi:10.1088/0960-1317/21/4/045039. URL http://stacks.iop.org/0960-1317/21/i=4/a=045039.

[62] N. Lorenz. *Laser-based packaging of micro-devices*. PhD thesis, Heriot-Watt University, 2011.

[63] R. F. Wolffenbuttel. Low-temperature intermediate Au-Si wafer bonding; eutectic or silicide bond. *Sensors and Actuators A: Physical*, 62(1-3):680–686, 1997. ISSN 0924-4247. doi:10.1016/S0924-4247(97)01550-1. URL http://www.sciencedirect.com/science/article/pii/S0924424797015501. Proceedings of Eurosensors X.

[64] S. Caplet, N. Sillon, M Delaye, and P Berruyer. Vacuum wafer-level packaging for MEMS applications. In *Micromachining and Microfabrication Process Technology VIII*, volume 4979, pages 271–278, 2003. doi:10.1117/12.478249. URL http://dx.doi.org/10.1117/12.478249.

[65] U. Gösele, H. Stenzel, T. Martini, J. Steinkirchner, D. Conrad, and K. Scheerschmidt. Self propagating room temperature silicon wafer bonding in ultrahigh vacuum. *Appl. Phys. Lett.*, 67(24):3614–3616, 1995. doi:10.1063/1.115335. URL http://scitation.aip.org/content/aip/journal/apl/67/24/10.1063/1.115335.

[66] L. Mele, F. Santagata, G. Pandraud, B. Morana, F. D. Tichelaar, J. F. Creemer, and P. M. Sarro. Wafer-level assembly and sealing of a MEMS

nanoreactor for in situ microscopy. *J. Micromech. Microeng.*, 20(8):085040, 2010. doi:10.1088/0960-1317/20/8/085040. URL http://stacks.iop.org/0960-1317/20/i=8/a=085040.

[67] S. Radhakrishnan and A. Lal. Alkali metal-wax micropackets for chip-scale atomic clocks. In *Digest of Technical Papers. TRANSDUCERS '05. The 13th International Conference on Solid-State Sensors, Actuators and Microsystems*, volume 1, pages 23–26 Vol. 1, 2005. doi:10.1109/SENSOR.2005.1496349. URL http://ieeexplore.ieee.org/xpl/articleDetails.jsp?arnumber=1496349.

[68] P. F. Griffin, K. J. Weatherill, and C. S. Adams. Fast switching of alkali atom dispensers using laser-induced heating. *Rev. Sci. Instrum.*, 76(9):093102, 2005. doi:10.1063/1.2038167. URL http://scitation.aip.org/content/aip/journal/rsi/76/9/10.1063/1.2038167.

[69] H. J. Metcalf and P. Van Der Straten. *Laser Cooling and Trapping*. Graduate Texts in Contemporary Physics. Springer, 1999. ISBN 9780387987477. URL http://books.google.co.uk/books?id=KTO1QgAACAAJ.

[70] T. W. Hodapp, C. Gerz, C. Furtlehner, C. I. Westbrook, W. D. Phillips, and J. Dalibard. Three-dimensional spatial diffusion in optical molasses. *Appl. Phys. B*, 60(2-3):135–143, 1995. ISSN 0946-2171. doi:10.1007/BF01135855. URL http://dx.doi.org/10.1007/BF01135855.

[71] C. J. Foot. *Atomic physics*. Oxford master series in physics. Oxford University Press, 2005. ISBN 9780198506966. URL http://books.google.co.uk/books?id=kXYpAQAAMAAJ.

[72] H. A. Lorentz. *The Theory of Electrons and Its Applications to the Phenomena of Light and Radiant Heat*. Leipzig: B.G. Teubner; New York: G.E. Stechert, 1916. URL https://archive.org/details/electronstheory00lorerich.

[73] G. K. Woodgate. *Elementary Atomic Structure*. Oxford science publications. Clarendon Press, 1980. ISBN 9780198511564. URL http://books.google.co.uk/books?id=akoxmQEACAAJ.

[74] D. Budker, D. F. Kimball, and D. P. DeMille. *Atomic physics: an exploration through problems and solutions*. Atomic Physics: An Exploration Through Problems and Solutions. Oxford University Press,

2008. ISBN 9780199532414. URL http://books.google.co.uk/books?id=OAI2AQAAIAAJ.

[75] V. Devanathan. *Angular Momentum Techniques in Quantum Mechanics*. Fundamental Theories of Physics. Springer, 1999. ISBN 9780792358664. URL http://books.google.co.uk/books?id=VeiursWZeoUC.

[76] P. D. Lett, R. N. Watts, C. I. Westbrook, W. D. Phillips, P. L. Gould, and H. J. Metcalf. Observation of atoms laser cooled below the doppler limit. *Phys. Rev. Lett.*, 61:169–172, 1988. doi:10.1103/PhysRevLett.61.169. URL http://link.aps.org/doi/10.1103/PhysRevLett.61.169.

[77] C. Cohen-Tannoudji and D. Guéry-Odelin. *Advances in Atomic Physics: An Overview*. World Scientific, 2011. ISBN 9789812774972. URL http://books.google.co.uk/books?id=md_cNwAACAAJ.

[78] S. Pollock, J. P. Cotter, A. Laliotis, F. Ramirez-Martinez, and E. A. Hinds. Characteristics of integrated magneto-optical traps for atom chips. *New J. Phys.*, 13(4):043029, 2011. doi:10.1088/1367-2630/13/4/043029. URL http://stacks.iop.org/1367-2630/13/i=4/a=043029.

[79] K. Lindquist, M. Stephens, and C. Wieman. Experimental and theoretical study of the vapor-cell zeeman optical trap. *Phys. Rev. A*, 46:4082–4090, 1992. doi:10.1103/PhysRevA.46.4082. URL http://link.aps.org/doi/10.1103/PhysRevA.46.4082.

[80] K. E. Gibble, S. Kasapi, and S. Chu. Improved magneto-optic trapping in a vapor cell. *Opt. Lett.*, 17(7):526–528, 1992. doi:10.1364/OL.17.000526. URL http://ol.osa.org/abstract.cfm?URI=ol-17-7-526.

[81] G. W. Hoth, E. A. Donley, and J. Kitching. Atom number in magneto-optic traps with millimeter scale laser beams. *Opt. Lett.*, 38(5):661–663, 2013. doi:10.1364/OL.38.000661. URL http://ol.osa.org/abstract.cfm?URI=ol-38-5-661.

[82] J. Reichel, W. Hänsel, and T. W. Hänsch. Atomic micromanipulation with magnetic surface traps. *Phys. Rev. Lett.*, 83:3398–3401, 1999. doi:10.1103/PhysRevLett.83.3398. URL http://link.aps.org/doi/10.1103/PhysRevLett.83.3398.

[83] K. I. Lee, J. A. Kim, H. R. Noh, and W. Jhe. Single-beam atom trap in a pyramidal and conical hollow mirror. *Opt. Lett.*, 21(15):1177–1179, 1996.

doi:10.1364/OL.21.001177. URL http://ol.osa.org/abstract.cfm?URI=ol-21-15-1177.

[84] M. Vangeleyn, P. F. Griffin, E. Riis, and A. S. Arnold. Single-laser, one beam, tetrahedral magneto-optical trap. *Opt. Express*, 17(16):13601–13608, 2009. doi:10.1364/OE.17.013601. URL http://www.opticsexpress.org/abstract.cfm?URI=oe-17-16-13601.

[85] M. Vangeleyn, P. F. Griffin, E. Riis, and A. S. Arnold. Laser cooling with a single laser beam and a planar diffractor. *Opt. Lett.*, 35(20):3453–3455, 2010. doi:10.1364/OL.35.003453. URL http://ol.osa.org/abstract.cfm?URI=ol-35-20-3453.

[86] C. C. Nshii, M. Vangeleyn, J. P. Cotter, P. F. Griffin, E. A. Hinds, C. N. Ironside, P. See, A. G. Sinclair, E. Riis, and A. S. Arnold. A surface-patterned chip as a strong source of ultracold atoms for quantum technologies. *Nature Nanotechnology*, 8(5):321–324, 2013. ISSN 1748-3387. doi:10.1038/nnano.2013.47. URL http://dx.doi.org/10.1038/nnano.2013.47. Letter.

[87] J. Reichel. Microchip traps and Bose-Einstein condensation. *Appl. Phys. B*, 74(6):469–487, 2002. ISSN 0946-2171. doi:10.1007/s003400200861. URL http://dx.doi.org/10.1007/s003400200861.

[88] J. J. Arlt, O. Maragò, S. Webster, S. Hopkins, and C. J. Foot. A pyramidal magneto-optical trap as a source of slow atoms. *Opt. Commun.*, 157(1-6):303–309, 1998. ISSN 0030-4018. doi:10.1016/S0030-4018(98)00499-4. URL http://www.sciencedirect.com/science/article/pii/S0030401898004994.

[89] M. Trupke, F. Ramirez-Martinez, E. A. Curtis, J. P. Ashmore, S. Eriksson, E. A. Hinds, Z. Moktadir, C. Gollasch, M. Kraft, G. Vijaya Prakash, and J. J. Baumberg. Pyramidal micromirrors for microsystems and atom chips. *Appl. Phys. Lett.*, 88(7):071116, 2006. doi:10.1063/1.2172412. URL http://scitation.aip.org/content/aip/journal/apl/88/7/10.1063/1.2172412.

[90] G. N. Lewis, Z. Moktadir, C. Gollasch, M. Kraft, S. Pollock, F. Ramirez-Martinez, J. P. Ashmore, A. Laliotis, M. Trupke, and E. A. Hinds. Fabrication of magnetooptical atom traps on a chip. *Journal of Microelectromechanical Systems*, 18(2):347–353, 2009. ISSN 1057-7157.

doi:10.1109/JMEMS.2008.2007200. URL http://ieeexplore.ieee.org/xpl/articleDetails.jsp?arnumber=4797887.

[91] S. Pollock, J. P. Cotter, A. Laliotis, and E. A. Hinds. Integrated magneto-optical traps on a chip using silicon pyramid structures. *Opt. Express*, 17(16):14109–14114, 2009. doi:10.1364/OE.17.014109. URL http://www.opticsexpress.org/abstract.cfm?URI=oe-17-16-14109.

[92] S. Pollock. *Integration of Magneto Optical Traps in Atom Chips*. PhD thesis, Imperial College London, 2010.

[93] F. Ramirez. *Integration of Optical Components and Magnetic Field Sources in Atom Chips*. PhD thesis, Imperial College London, 2008.

[94] M. Vangeleyn. *Atom trapping in non-trivial geometries for micro-fabrication applications*. PhD thesis, University of Strathclyde, 2011.

[95] M. Harvey and A. J. Murray. Cold atom trap with zero residual magnetic field: The ac magneto-optical trap. *Phys. Rev. Lett.*, 101:173201, 2008. doi:10.1103/PhysRevLett.101.173201. URL http://link.aps.org/doi/10.1103/PhysRevLett.101.173201.

[96] Y. T. Chough and W. Jhe. A computational analysis of an axiconic magneto-optical trap. *J. Phys. Soc. Jpn.*, 69(5):1366–1373, 2000. doi:10.1143/JPSJ.69.1366. URL http://dx.doi.org/10.1143/JPSJ.69.1366.

[97] J. W. Jun and H. S. Lee. Kinetic theory of magneto-optical traps with finite-linewidth lasers. *Phys. Rev. A*, 62:063407, 2000. doi:10.1103/PhysRevA.62.063407. URL http://link.aps.org/doi/10.1103/PhysRevA.62.063407.

[98] C. E. Wieman and L. Hollberg. Using diode lasers for atomic physics. *Rev. Sci. Instrum.*, 62(1):1–20, 1991. doi:10.1063/1.1142305. URL http://scitation.aip.org/content/aip/journal/rsi/62/1/10.1063/1.1142305.

[99] A. S. Arnold, J. S. Wilson, and M. G. Boshier. A simple extended-cavity diode laser. *Rev. Sci. Instrum.*, 69(3):1236–1239, 1998. doi:10.1063/1.1148756. URL http://scitation.aip.org/content/aip/journal/rsi/69/3/10.1063/1.1148756.

[100] L. D. Turner, K. P. Weber, C. J. Hawthorn, and R. E. Scholten. Frequency noise characterisation of narrow linewidth diode lasers. *Opt. Commun.*, 201 (4-6):391–397, 2002. ISSN 0030-4018. doi:10.1016/S0030-4018(01)01689-3. URL http://www.sciencedirect.com/science/article/pii/S0030401801016893.

[101] T. P. Dinneen, C. D. Wallace, and P. L. Gould. Narrow linewidth, highly stable, tunable diode laser system. *Opt. Commun.*, 92(4-6):277–282, 1992. ISSN 0030-4018. doi:10.1016/0030-4018(92)90636-6. URL http://www.sciencedirect.com/science/article/pii/0030401892906366.

[102] V. Negnevitsky and L. D. Turner. Wideband laser locking to an atomic reference with modulation transfer spectroscopy. *Opt. Express*, 21(3):3103–3113, 2013. doi:10.1364/OE.21.003103. URL http://www.opticsexpress.org/abstract.cfm?URI=oe-21-3-3103.

[103] J. H. Shirley. Modulation transfer processes in optical heterodyne saturation spectroscopy. *Opt. Lett.*, 7(11):537–539, 1982. doi:10.1364/OL.7.000537. URL http://ol.osa.org/abstract.cfm?URI=ol-7-11-537.

[104] E. A. Donley, T. P. Heavner, F. Levi, M. O. Tataw, and S. R. Jefferts. Double-pass acousto-optic modulator system. *Rev. Sci. Instrum.*, 76(6): 063112, 2005. doi:10.1063/1.1930095. URL http://scitation.aip.org/content/aip/journal/rsi/76/6/10.1063/1.1930095.

[105] C. C. Davis. *Lasers and Electro-optics: Fundamentals and Engineering*. Cambridge University Press, 2014. ISBN 9781107728974. URL https://books.google.co.uk/books?id=5NMNAwAAQBAJ.

[106] V. Negnevitsky. FPGA-based laser stabilisation using modulation transfer spectroscopy. Bachelor's thesis, Monash University, 2010.

[107] E. Jaatinen and D. J. Hopper. Compensating for frequency shifts in modulation transfer spectroscopy caused by residual amplitude modulation. *Optics and Lasers in Engineering*, 46(1):69–74, 2008. ISSN 0143-8166. doi:10.1016/j.optlaseng.2007.06.011. URL http://www.sciencedirect.com/science/article/pii/S0143816607001224.

[108] J. Ringot, Y. Lecoq, J. C. Garreau, and P. Szriftgiser. Generation of phase-coherent laser beams for Raman spectroscopy and cooling by direct current modulation of a diode laser. *Eur. Phys. J. D*, 7(3):285–288,

1999. doi:10.1007/s100530050571. URL http://dx.doi.org/10.1007/s100530050571.

[109] A. Waxman, M. Givon, G. Aviv, D. Groswasser, and R. Folman. Modulation enhancement of a laser diode in an external cavity. *Appl. Phys. B*, 95(2): 301–305, 2009. ISSN 0946-2171. doi:10.1007/s00340-008-3356-0. URL http://dx.doi.org/10.1007/s00340-008-3356-0.

[110] Thorlabs Inc. Fabry-perot tutorial. https://www.thorlabs.com/tutorials.cfm?tabID=e9d2d96f-1efd-4ef0-bb17-fa2ca60f8a8d. Accessed: 29-06-2015.

[111] M. D. Himsworth. *Coherent Manipulation of Ultracold Rubidium*. PhD thesis, University of Southampton, 2009.

[112] C. J. Myatt, N. R. Newbury, and C. E. Wieman. Simplified atom trap by using direct microwave modulation of a diode laser. *Opt. Lett.*, 18 (8):649–651, 1993. doi:10.1364/OL.18.000649. URL http://ol.osa.org/abstract.cfm?URI=ol-18-8-649.

[113] P. Feng and T. Walker. Inexpensive diode laser microwave modulation for atom trapping. *Am. J. Phys.*, 63(10):905–908, 1995. doi:10.1119/1.18031. URL http://scitation.aip.org/content/aapt/journal/ajp/63/10/10.1119/1.18031.

[114] J. Appel, A. MacRae, and A. I. Lvovsky. A versatile digital GHz phase lock for external cavity diode lasers. *Meas. Sci. Technol.*, 20(5):055302, 2009. doi:10.1088/0957-0233/20/5/055302. URL http://stacks.iop.org/0957-0233/20/i=5/a=055302.

[115] J. Liu. *Photonic Devices*. Cambridge University Press, 2005. ISBN 9781139441148. URL http://books.google.co.uk/books?id=E7Au7ifAFXkC.

[116] W. J. Schwenger and J. M. Higbie. High-speed acousto-optic shutter with no optical frequency shift. *Rev. Sci. Instrum.*, 83(8):083110, 2012. doi:10.1063/1.4746292. URL http://scitation.aip.org/content/aip/journal/rsi/83/8/10.1063/1.4746292.

[117] R. Elliott. Power amplifier design guidelines. http://sound.westhost.com/amp_design.htm, 2006. Accessed: 10-03-2015.

[118] R. Elliott. Power amplifier efficiency explained. http://sound.westhost.com/efficiency.htm, 2000. Accessed: 10-03-2015.

[119] R. Elliott. Insanity can be yours :-), 1,500W/4 ohms power amplifier. http://sound.westhost.com/project117.htm, 2006. Accessed: 11-03-2015.

[120] J. Firestone. Build a simple, soft-action muting switch. http://goo.gl/4JCK0x, 2004. Accessed: 2-07-2015.

[121] D. J. Griffiths. *Introduction to Electrodynamics*. Always learning. Pearson, 2013. ISBN 9780321856562. URL https://books.google.co.uk/books?id=6KSSAgAAQBAJ.

[122] C. R. Sullivan and R. Y. Zhang. Simplified design method for litz wire. In *Twenty-Ninth Annual IEEE Applied Power Electronics Conference and Exposition (APEC)*, pages 2667–2674, 2014. doi:10.1109/APEC.2014.6803681. URL http://ieeexplore.ieee.org/xpl/articleDetails.jsp?arnumber=6803681.

[123] C. R. Sullivan. Optimal choice for number of strands in a litz-wire transformer winding. *IEEE Transactions on Power Electronics*, 14(2):283–291, 1999. ISSN 0885-8993. doi:10.1109/63.750181. URL http://ieeexplore.ieee.org/xpl/articleDetails.jsp?arnumber=750181.

[124] X. Tang and C. R. Sullivan. Stranded wire with uninsulated strands as a low-cost alternative to litz wire. In *IEEE 34th Annual Power Electronics Specialist Conference (PESC)*, volume 1, pages 289–295 vol.1, 2003. doi:10.1109/PESC.2003.1218308. URL http://ieeexplore.ieee.org/xpl/articleDetails.jsp?arnumber=1218308.

[125] C. Monroe, W. Swann, H. Robinson, and C. Wieman. Very cold trapped atoms in a vapor cell. *Phys. Rev. Lett.*, 65:1571–1574, 1990. doi:10.1103/PhysRevLett.65.1571. URL http://link.aps.org/doi/10.1103/PhysRevLett.65.1571.

[126] A. Dunning. *Coherent atomic manipulation and cooling using composite optical pulse sequences*. PhD thesis, University of Southampton, 2014.

[127] A. K. Mohapatra and C. S. Unnikrishnan. High sensitivity probe absorption technique for time-of-flight measurements on cold atoms. *Pramana*, 66(6):1027–1035, 2006. ISSN 0304-4289. doi:10.1007/BF02708456. URL http://dx.doi.org/10.1007/BF02708456.

[128] D. A. Steck. Rubidium 85 D line data, revision 2.1.6, 2013. URL http://steck.us/alkalidata.

[129] A. Van Wieringen and N. Warmoltz. On the permeation of hydrogen and helium in single crystal silicon and germanium at elevated temperatures. *Physica*, 22(6-12):849–865, 1956. ISSN 0031-8914. doi:10.1016/S0031-8914(56)90039-8. URL http://www.sciencedirect.com/science/article/pii/S0031891456900398.

[130] D. R. Kaplan, C. Weigel, and J. W. Corbett. Calculations on the properties of helium in silicon. *Physica Status Solidi (b)*, 94(2):359–366, 1979. ISSN 1521-3951. doi:10.1002/pssb.2220940204. URL http://dx.doi.org/10.1002/pssb.2220940204.

[131] P. Jung. Diffusion of implanted helium in Si and SiO_2. *Nuclear Instruments and Methods in Physics Research Section B: Beam Interactions with Materials and Atoms*, 91(1-4):362–365, 1994. ISSN 0168-583X. doi:10.1016/0168-583X(94)96249-9. URL http://www.sciencedirect.com/science/article/pii/0168583X94962499.

[132] L. C. Luther and W. J. Moore. Diffusion of helium in silicon, germanium, and diamond. *J. Chem. Phys.*, 41(4):1018–1026, 1964. doi:10.1063/1.1726000. URL http://scitation.aip.org/content/aip/journal/jcp/41/4/10.1063/1.1726000.

[133] A. Charaf Eddin, G. Lucas, M. F. Beaufort, and L. Pizzagalli. DFT calculation of the stability and mobility of noble gas atoms in silicon. *Computational Materials Science*, 44(4):1030–1033, 2009. ISSN 0927-0256. doi:10.1016/j.commatsci.2008.07.014. URL http://www.sciencedirect.com/science/article/pii/S0927025608003510.

[134] M. Alatalo, M. J. Puska, and R. M. Nieminen. First-principles study of He in Si. *Phys. Rev. B*, 46:12806–12809, 1992. doi:10.1103/PhysRevB.46.12806. URL http://link.aps.org/doi/10.1103/PhysRevB.46.12806.

[135] S. K. Estreicher, J. Weber, A. Derecskei-Kovacs, and D. S. Marynick. Noble-gas-related defects in Si and the origin of the 1018 meV photoluminescence line. *Phys. Rev. B*, 55:5037–5044, 1997. doi:10.1103/PhysRevB.55.5037. URL http://link.aps.org/doi/10.1103/PhysRevB.55.5037.

[136] S. Fabian, S. Kalbitzer, Ch. Klatt, M. Behar, and Ch. Langpape. ^{1}H tunneling transport in crystalline Si of different doping. *Phys. Rev. B*, 58:

16144–16153, 1998. doi:10.1103/PhysRevB.58.16144. URL http://link.aps.org/doi/10.1103/PhysRevB.58.16144.

[137] S. V. Koveshnikov, S. V. Nosenko, and E. B. Yakimov. The peculiarities of deep level defect passivation in Si by atomic hydrogen. *Physica Status Solidi (a)*, 120(2):391–395, 1990. ISSN 1521-396X. doi:10.1002/pssa.2211200211. URL http://dx.doi.org/10.1002/pssa.2211200211.

[138] Y. Kamiura, M. Yoneta, and F. Hashimoto. Hydrogen diffusivities below room temperature in silicon evaluated from the photoinduced dissociation of hydrogen-carbon complexes. *Appl. Phys. Lett.*, 59(24):3165–3167, 1991. doi:10.1063/1.105772. URL http://scitation.aip.org/content/aip/journal/apl/59/24/10.1063/1.105772.

[139] C. H. Seager and R. A. Anderson. Real-time observations of hydrogen drift and diffusion in silicon. *Appl. Phys. Lett.*, 53(13):1181–1183, 1988. doi:10.1063/1.100015. URL http://scitation.aip.org/content/aip/journal/apl/53/13/10.1063/1.100015.

[140] K. Schmalz and K. Tittelbach-Helmrich. On the hydrogen diffusion in silicon at about 100°C. *Physica Status Solidi (a)*, 113(1):K9–K13, 1989. ISSN 1521-396X. doi:10.1002/pssa.2211130130. URL http://dx.doi.org/10.1002/pssa.2211130130.

[141] M. Vergnat, S. Houssaini, C. Dufour, A. Bruson, G. Marchal, Ph Mangin, R. Erwin, J. J. Rhyne, and C. Vettier. Determination of short-range motion of hydrogen in amorphous silicon multilayers by low-angle neutron scattering. *Europhys. Lett.*, 14(5):457, 1991. doi:10.1209/0295-5075/14/5/012. URL http://stacks.iop.org/0295-5075/14/i=5/a=012.

[142] X.-M. Tang, J. Weber, Y. Baer, and F. Finger. Annealing-temperature influence on the dispersive diffusion of hydrogen in undoped *a*-Si:H. *Phys. Rev. B*, 42:7277–7279, 1990. doi:10.1103/PhysRevB.42.7277. URL http://link.aps.org/doi/10.1103/PhysRevB.42.7277.

[143] N. M. Johnson and C. Herring. Migration of the H_2^* complex and its relation to H^- in *n*-type silicon. *Phys. Rev. B*, 43:14297–14300, 1991. doi:10.1103/PhysRevB.43.14297. URL http://link.aps.org/doi/10.1103/PhysRevB.43.14297.

[144] C. H. Seager, R. A. Anderson, and D. K. Brice. *Insitu* measurements of hydrogen motion and bonding in silicon. *J. Appl. Phys.*, 68(7):3268–3284,

1990. doi:10.1063/1.346378. URL http://scitation.aip.org/content/aip/journal/jap/68/7/10.1063/1.346378.

[145] R. C. Newman, J. H. Tucker, A. R. Brown, and S. A. McQuaid. Hydrogen diffusion and the catalysis of enhanced oxygen diffusion in silicon at temperatures below 500°C. *J. Appl. Phys.*, 70(6):3061–3070, 1991. doi:10.1063/1.349338. URL http://scitation.aip.org/content/aip/journal/jap/70/6/10.1063/1.349338.

[146] A. Majumdar, S. Balasubramanian, V. Venkataraman, and N. Balasubramanian. Reactivation kinetics of boron acceptors in hydrogenated silicon during zero bias anneal. *J. Appl. Phys.*, 82(1):192–195, 1997. doi:10.1063/1.365797. URL http://scitation.aip.org/content/aip/journal/jap/82/1/10.1063/1.365797.

[147] B. L. Sopori, K. Jones, and X. J. Deng. Observation of enhanced hydrogen diffusion in solar cell silicon. *Appl. Phys. Lett.*, 61(21):2560–2562, 1992. doi:10.1063/1.108126. URL http://scitation.aip.org/content/aip/journal/apl/61/21/10.1063/1.108126.

[148] C. P. Herrero, M. Stutzmann, A. Breitschwerdt, and P. V. Santos. Trap-limited hydrogen diffusion in doped silicon. *Phys. Rev. B*, 41:1054–1058, 1990. doi:10.1103/PhysRevB.41.1054. URL http://link.aps.org/doi/10.1103/PhysRevB.41.1054.

[149] N. M. Johnson and C. Herring. Diffusion of negatively charged hydrogen in silicon. *Phys. Rev. B*, 46:15554–15557, 1992. doi:10.1103/PhysRevB.46.15554. URL http://link.aps.org/doi/10.1103/PhysRevB.46.15554.

[150] R. Rizk, P. de Mierry, D. Ballutaud, M. Aucouturier, and D. Mathiot. Hydrogen diffusion and passivation processes in p- and n-type crystalline silicon. *Phys. Rev. B*, 44:6141–6151, 1991. doi:10.1103/PhysRevB.44.6141. URL http://link.aps.org/doi/10.1103/PhysRevB.44.6141.

[151] Y. L. Huang, Y. Ma, R. Job, and A. G. Ulyashin. Hydrogen diffusion at moderate temperatures in p-type Czochralski silicon. *J. Appl. Phys.*, 96 (12):7080–7086, 2004. doi:10.1063/1.1812379. URL http://scitation.aip.org/content/aip/journal/jap/96/12/10.1063/1.1812379.

[152] W. L. Hansen, S. J. Pearton, and E. E. Haller. Bulk acceptor compensation produced in p-type silicon at near-ambient temperatures by a H_2O plasma.

Appl. Phys. Lett., 44(6):606–608, 1984. doi:10.1063/1.94849. URL http://scitation.aip.org/content/aip/journal/apl/44/6/10.1063/1.94849.

[153] M. Capizzi and A. Mittiga. Hydrogen in Si: Diffusion and shallow impurity deactivation. *Physica B+C*, 146(1-2):19–29, 1987. ISSN 0378-4363. doi:10.1016/0378-4363(87)90048-9. URL http://www.sciencedirect.com/science/article/pii/0378436387900489.

[154] A. Mogro-Campero, R. P. Love, and R. Schubert. Drastic changes in the electrical resistance of gold-doped silicon produced by a hydrogen plasma. *J. Electrochem. Soc.*, 132(8):2006–2009, 1985. doi:10.1149/1.2114270. URL http://jes.ecsdl.org/content/132/8/2006.abstract.

[155] M. D. McCluskey and E. E. Haller. *Dopants and Defects in Semiconductors*. CRC Press, 2012. ISBN 9781439831533. URL https://books.google.co.uk/books?id=fV3RBQAAQBAJ.

The Feasibility of a Fully Miniaturized Magneto-Optical Trap for Portable Ultracold Quantum Technology

J.A. Rushton, M. Aldous and M.D. Himsworth*
School of Physics & Astronomy, University of Southampton, Southampton, SO17 1BJ, UK
(Dated: July 22, 2015)

Experiments using laser cooled atoms and ions show real promise for practical applications in quantum-enhanced metrology, timing, navigation, and sensing as well as exotic roles in quantum computing, networking and simulation. The heart of many of these experiments has been translated to microfabricated platforms known as atom chips whose construction readily lend themselves to integration with larger systems and future mass production. To truly make the jump from laboratory demonstrations to practical, rugged devices, the complex surrounding infrastructure (including vacuum systems, optics, and lasers) also needs to be miniaturized and integrated. In this paper we explore the feasibility of applying this approach to the Magneto-Optical Trap; incorporating the vacuum system, atom source and optical geometry into a permanently sealed micro-litre system capable of maintaining 10^{-10} mbar for more than 1000 days of operation with passive pumping alone. We demonstrate such an engineering challenge is achievable using recent advances in semiconductor microfabrication techniques and materials.

I. ULTRACOLD QUANTUM TECHNOLOGY

Since the first demonstrations of atoms and ions at sub-millikelvin temperatures in the mid-1980s, the field of atomic physics has been revolutionized by laser cooling and trapping as it provides researchers with a method to probe some of the purest, most sensitive, and controllable quantum systems available. This field is still highly productive and recently has put significant emphasis on the practical applications of this technology beyond the laboratory [1, 2]. It was evident very early on that ultracold matter would be an indispensable tool in precise timing applications and a recent demonstration [3] has shown extremely low instabilities at the 10^{-18} level. The wavelike nature of atoms as they are cooled to lower temperatures can be used to form atomic interferometers that outperform their optical counterparts in measurements of accelerated reference frames [4–7], which are important for inertial guidance systems, but can also provide sensitive measurements of mass, charge and magnetic fields [8–11]. Greater sensitivity beyond the classical limit is possible via squeezed states [12], interacting particles [13, 14] and entangled states [15–17], which are also fundamental attributes for quantum computing [18, 19], and long distance quantum networking [20]. Ultracold matter has been used in the emerging field of quantum simulation [21] and is an indispensable tool in determining fundamental constants [22], testing general relativity [23] and defining measurement standards [24]. Many researchers and industries believe such tools will be a major part of the 'second quantum revolution' in which the more 'exotic' properties of quantum physics are applied for practical applications [25, 26].

The field of ultracold matter has reached maturity in both experimental methods and theoretical understanding allowing experiments to begin leaving the laboratory [27–29]. These systems are bespoke, rarely take up a volume less than a cubic metre, and require a team of experts to operate. The many applications that will benefit most from ultracold quantum technology are likely to compromise sensitivity for far smaller and more rugged devices, which can be mass-produced and do not require the user to understand the internal operation in detail. Commercial pressure will always push toward reduced size, weight and power. One can already see the opportunities made possible with the move to microfabricated atom and ion traps [30–33], but these firmly remain 'chip-in-a-lab' *components* rather than 'lab-in-a-chip' *systems*.

The miniaturization we envisage is analogous to that demonstrated by the recent development of commercially available [34] chip-scale atomic clocks (CSACs), which have shrunk a traditionally bulky optical spectroscopic system down to one smaller than a grain of rice [35]. Some work has begun on miniaturizing the entire ultracold atom system, most noteably the backpack-sized iSense gravimeter [36], but to achieve the CSAC level of sophistication, size and robustness in ultracold technology will require at least another decade of development.

The trapping and cooling of hot vapour-phase atoms or ions below millikelvin temperatures is the first stage in all ultracold experiments, therefore the miniaturization of this system known as the Magneto-Optical Trap [37] (MOT) would be a significant step forward towards our goal. Several academic and commercial research groups have begun looking at the various ways the MOT can be miniaturized using machined glass chambers [38], conical retro-reflectors [39, 40], and etched multi-section silicon and glass substrates [41]. Most of these demonstrations are small-scale versions of standard MOTs, with only the last device beginning to redesign the system from a microfabricated and integrated approach.

In this study we explore the feasibility of miniaturizing and integrating the ultra-high vacuum system, atom source and MOT optics into a centimetre-scale device. This will be achieved by using recent advances in ma-

* m.d.himsworth@soton.ac.uk

terials and techniques adapted from the semiconductor and MEMS industries used in wafer-level mass production. We will refer to the device as a 'MicroMOT' because the internal volume is sub-millilitre compared to the typically litre-sized standard MOTs. The initial target operational lifetime is set at 1000 days, as this would be at the lower end of a typical commercial service life whilst still presenting a significant challenge. We also aim to maintain an internal vacuum of 10^{-10} mbar under normal atmospheric external conditions, and do so with only passive pumping elements and thus no power. Our objective is to focus on this as an engineering challenge from which a mass-producible technology can be developed, thus avoiding bespoke systems which may only be suitable for proof-of-concept purposes.

In Sections II and III we describe a typical Magneto-Optical Trap system, its construction, and how it can be miniaturized including the lasers and optical systems. In Section IV we discuss the source of vapour phase atoms and how to control them. In Section V we explore solutions to provide pumping, prevent permeation, limit leaks, and overcome outgassing. In Section VI we bring the above technologies together to design a prototype Micro-MOT. In Section VII we discuss the assumptions made in the study and highlight areas for further research.

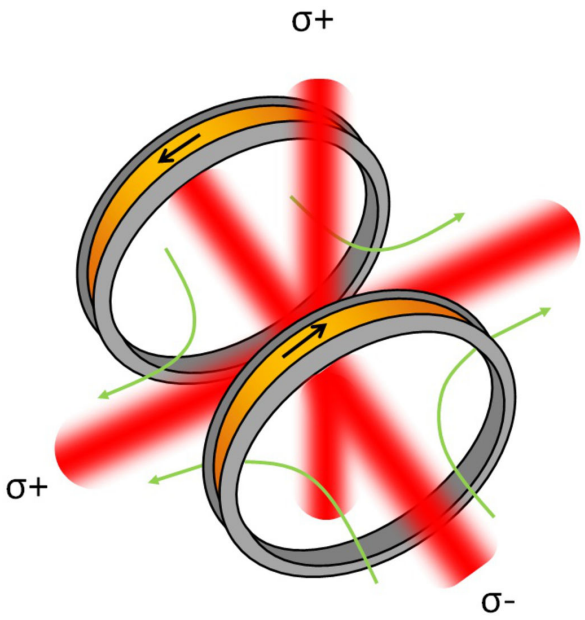

FIG. 1. The standard MOT geometry. The laser polarizations are indicated in text and the magnetic field direction in green arrows.

II. THE MAGNETO OPTICAL TRAP SYSTEM

Nearly all cold atom experiments begin with a Magneto Optical Trap of which a typical design comprises an Ultra-High Vacuum (UHV, $<10^{-9}$ mbar) chamber with internal volumes of around a litre with numerous optical ports, atom sources, gauges and pumps attached. UHV is obtained by thorough cleaning of the polished glass and metal (typically stainless steel) components. The entire system is assembled and evacuated using roughing and turbomolecular pumps down to around 10^{-7} mbar. It is then baked in the vicinity of 200°C for several days whilst being evacuated by ion and sublimation pumps and, once cooled, will obtain vacua in the region of 10^{-10} mbar. Obtaining vacua much beyond this, in the extreme high vacuum (XHV) regime, can be very difficult and may require getters, cryogenic pumps, deeper cleaning regimes and alternative chamber materials.

Once UHV is obtained, the MOT is formed of several stabilized and finely-tuned laser beams that are retro-reflected along each Cartesian axis intersecting at the zero of a quadrupole magnetic field (see Figure 1). Vapour-phase atoms are released into the chamber, cooled, trapped, and finally manipulated for their intended task. Typically 10^7 atoms are trapped in a dense cloud with diameters usually below 1 mm and, for many experiments (excluding ultra-sensitive long freefall experiments), the atoms rarely move more than a few millimetres away from this point. The past decade has seen the emergence of atom chips which allows for manipulation of atoms microns away from surfaces using high magnetic field gradients, created by microfabricated wires [42].

This raises the question to why such a large vacuum system is required? The answer is that without resorting to bespoke designs the pumps and gauges one can purchase for UHV systems are very large, and regardless, using current approaches the system is still difficult to reduce below the size of a shoebox. Typically these are far too bulky, expensive, and labour intensive to mass-produce and so an alternative architecture and manufacturing approach is required, starting with the MOT geometry.

For an integrated device the 'standard' geometry presented above is impractical due to the need for many optical ports, complex alignment, large volumes, numerous fragile optical elements and the difficulty in bringing the atoms close to an atom chip surface. Several alternative geometries have been proposed including the mirror-MOT [43], pyramid-MOT [44, 45], and tetrahedral MOT [46]. The latter two are attractive as they need only a single incident beam, whose phase stability aids in sub-Doppler cooling mechanisms, and both are suitable for microfabrication. Miniaturized pyramid MOTs, however, suffer from low atom capture rates due to the small volume in which the beams overlap [47, 48], significant backscatter making the atoms difficult to detect [49], and the geometry making transfer of the atoms to magnetic surface traps non-trivial. A recently demonstrated planar version of the tetrahedral-MOT using a two dimensional grating as a reflector (which we refer to as the 'G-MOT', see Figure 2) can capture a large number of atoms, has

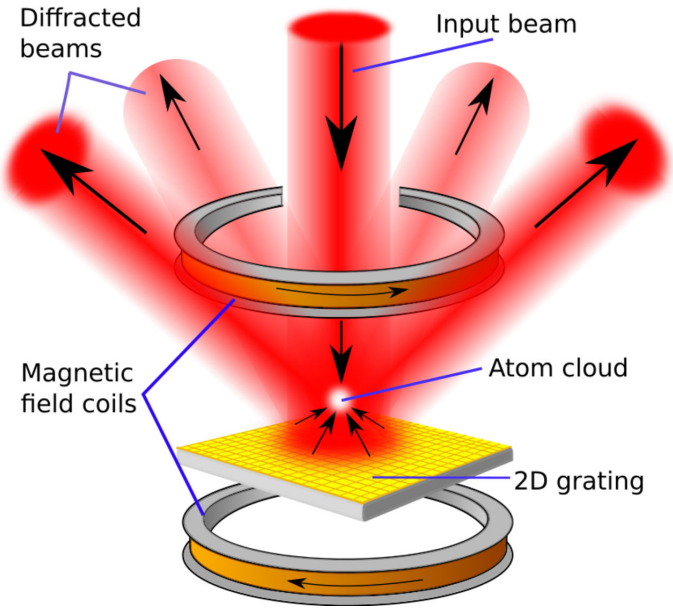

FIG. 2. A grating MOT geometry.

TABLE I. Comparison of the properties of various microfabricated MOT geometries (M=Mirror, P=Pyramid, T=Tetrahedral, G=Grating, S=Standard.) compatible with atom chips. Therefore we consider only the small scale pyramid MOTs here, but larger reflectors follow $V^{1.2}$ scaling and are suitable for compact space-borne cold atom systems [54].

MOT	M	P	T	G	S
Number of beams	4	1	1	1	6
Optical ports	3	1	1	1	6
Volume scaling [a]	$V^{1.2}$	V^2	$V^{1.2}$	$V^{1.2}$	$V^{1.2}$
Scatter	low	high	low	medium	none
Bandwidth[b]	all	all	all	100nm	all
Fabricatability	simple[c]	difficult	difficult	medium[d]	N/A

[a] Larger exponents lead to lower numbers at smaller volumes. We include scaling laws for beams diameters greater than 1mm.
[b] Limited by surface coatings and windows.
[c] For the MicroMOT design in Section VI, wide parallel beams are not trivial [55].
[d] This can be made simple with 'nanoimprint' techniques.

lower backscatter [50], and can be easily integrated with atom chip structures [51]. Some disadvantages include the effect of the grating on the wavefronts and polarizations of the manipulation beams [52], and added difficulty in situations which require several widely-spaced wavelengths (greater than 100nm [53]). Nevertheless, the G-MOT appears to be the most suitable geometry for microfabricated devices. A comparison of the most suitable MOT geometries is given in Table I.

A MOT should trap sufficient atoms to obtain adequate sensitivities for intended application which will ultimately be limited by the quantum projection noise. Typical numbers of atoms range from 10^4 for clock standards [56] to 10^8 atoms for the initial cooling stage into degeneracy. Of course, there exists other parameters which define the performance of cold atom systems, such as coherence time, shot noise, quantum state fidelity, etc. but these factors are somewhat unrelated to the MOT itself where one can only affect the atom number, density, capture rate and temperature. The temperature is typically in the region of tens to hundreds of microkelvin, no matter the MOT geometry if sub-Doppler cooling mechanisms exist, whereas atom number and density are inter-related and are significantly affected by MOT geometry and dimensions. The capture rate depends more on the atom source/loading mechanism and background gas pressure than the MOT geometry and will be discussed in Section IV.

For most cold atom experiments, the practical number of trapped atoms is on the order of $N_t = 10^6$. The G-MOT characteristics show that the beam overlap volume, V_t (cm^3), follows the scaling law of $N_t = 4 \times 10^7 V_t^{1.2}$, resulting in a minimum practical volume of $0.045\,\mathrm{cm}^3$. This is equal to a 0.65 cm diameter, uniformly illuminated, beam [57] forming a pyramidal volume. To ensure the correct number of atoms and to take into account the effects of non-uniformly shaped beams, a pragmatic beam diameter would be 1 cm. Experiments requiring degenerate gases may require up to 10^8 atoms to ensure a stable phase density for condensation and also improve detection. This would warrant a beam diameter over double that described above.

We assume that the device would incorporate an atom chip structure so that the atoms are trapped and manipulated with magnetic fields close to the surface, therefore the dimensions of the device have little impact on the measurement. Studies have shown that laser cooling close to surfaces begins to show losses as the atom-surface separation decreases below 1 mm [49, 58]. Thus, assuming a typical MOT cloud with a diameter less than 1 mm, a lower limit on the vertical dimension would be 3 mm. We aim to explore this issue in another study, but point out here that for a 1 cm diameter GMOT beam, $\sim 94\%$ of the overlap volume is contained within the first 3 mm from the grating surface.

In other matterwave experiments which manipulate the atoms during free fall, the interaction time may be limited to several milliseconds in a 3 mm thick chamber. For example, if we assume our trapped species is rubidium which has been cooled to the Doppler limit of $146\,\mu$K (r.m.s. speed of $20\,\mathrm{cm\,s^{-1}}$), and the atoms have 1 mm to travel before losses occur, then the maximum interaction time is 5 ms neglecting gravity. This makes the system applicable to recent work on high repetition rate cold atom intertial sensors [59]. Sub-Doppler cooling can increase the interaction time by a factor of 3 to 4, approaching the limit imposed by gravitational acceleration to the surface, which may be acceptable in many situations. Alternatively, optical lattices can increase the interaction time of matterwave interferometers without drastically increasing the dimensions of the system [60]. These guided matter waves are a promising technique

which could aid miniaturization and improve sensitivity.

III. LASERS AND OPTICS

In this study we will mainly concentrate on the UHV system as this has had very little development in terms of miniaturization and integration. However, the MOT also requires laser systems, optics, optical modulators, spectrometers, and control electronics which could become the limiting factor to the smallest scale cold atom technology can achieve. A single laser systems can be used to provide optical power to a number of MOTs which might be necessary in multi-axis inertial sensing, or spatial resolved gravity gradiometry; therefore one could accept a larger scale of laser system, but the optics used to couple and expand the beam into the MOTs would need to be significantly reduced in size and made far more robust with the possibility of mass-production. Diode lasers, by their very nature are extremely small and it is the surrounding optics that controls and couples the light to external systems that determines the size of the 'laser system'. Miniaturization can also improve the properties of these lasers by reducing the effects of thermal expansion and vibration of the external components.

Feasible approaches to miniaturize the optics of the laser system - as well as switching, modulating and routing the beams beyond the laser - include optical MEMS, planar optics, precision placed micro-optics, and optical waveguides (including fibers). Exploring each of these fields compehensively is beyond the scope of this report but we shall highlight a few technologies directly suitable for miniaturized MOTs. For this the crucial components to miniaturize and integrate are the laser diodes, wavelength control elements, optical isolators, routing, and beam expansion.

Micro-optical systems for cold atom applications have been pioneered by the Ferdinand-Braun Institut which have integrated diode lasers, Bragg reflectors, isolators, modulators, spectrometers, optical amplifiers and fiber couplers, all on a thermally-stable ceramic substrate no bigger than a credit card [61, 62]. They have developed lasers both for the MOT and high power systems [63] for exciting Raman transitions used in the iSense project [36].

The smallest scale devices, and most applicable to mass-production, are planar-waveguide coupled lasers, which are commercially available at the telecoms wavelengths, and show remarkably narrow linewidths and mode-hop free operations along with reasonable powers [64–66]. For cooling rubidium at 780nm there is a direct frequency doubling route from 1560nm for these lasers and is currently being developed for compact and robust space-based atom interferometers [67]. Waveguide coupled lasers can take advantage of the various chip-based control mechanisms such as phase-modulators [68], coupler/splitters, switches and isolators [69]. There will need to be some development to improve the efficiency of these systems at short wavelengths where the effect of refractive index inhomogeneities will have a greater impact compared to existing telecoms wavelengths. More development is also required in the areas of chip-based non-reciprocal optical isolators and high-attenuation, high-speed, switches for the demanding constraints imposed by decoherence-free atomic interactions. Integrating several optical elements onto a single substrate will be a sizeable challenge so optical fibre connected elements will likely dominate.

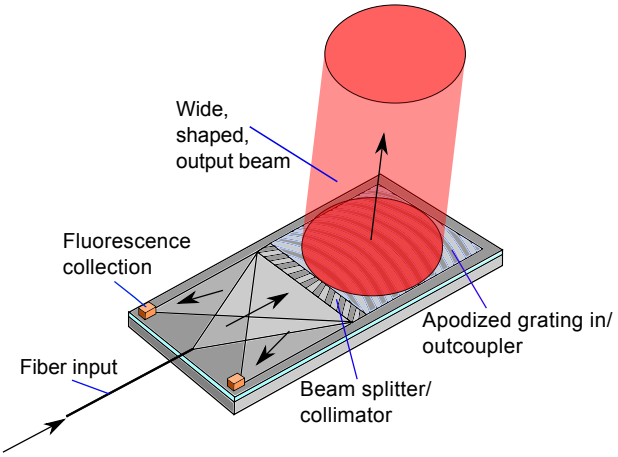

FIG. 3. An integrated confocal microscope adapted from [70]. Such technology can be used to produce large diameter shaped beams from planar waveguides and also provide fluoresence detection.

As discussed in the previous section, MOTs require quite large beam diameters which result in large optical systems to expand and collimate beams. We see that a promising route towards miniaturising this is with grating-based waveguide outcouplers. Coupling free-space laser beams into a waveguide is typically achieved with prisms placed on top of the waveguide to enable a reduced wavevector difference between the guided and free-space modes. This can be shrunk into grating couplers which allow one to improve efficiency by altering the dimensions of the grating. Concordantly, this process can be used in reverse to out-couple beams and even focus and shape the beam profile. One directly-applicable example is the work on integrated confocal microscopes [70], as shown in figure 3, that also provide a means to measure the reflected light intensity, or in our case the fluorescence of the atoms. Due to the diffractive nature of the light coupling the beam profile can be designed with top-hat shapes with flat phase wavefronts – very important properties in efficient atom interferometry using Raman transitions. These grating out-couplers have recently been developed to address individual trapped ions [71]. Planar optics offer alternative methods to expand beams in compact systems using total internal reflection and patterned surfaces within waveguides [72].

For applications which require laser beams access along several axes integrated prisms and reflectors within the

vacuum chamber are being developed along with integrated windows in silicon substrates [41] and Fresnel lenses [73–75]. Fibre coupling into and out of vacuum would be beneficial for strong coupling to atoms and interconnectable cold-atom systems. Waveguides are, yet again, a viable route for this [76] and possibly recent advances in tapered nano-fibers [77] which can have several alternative applications [78]. The recent development of light-field imaging allows one to perform 3D imaging via computer deconvolution along a single optical axis, thus greatly simplifying the optical system where multiple viewpoints are required [79].

The lasers must be stabilised to a specific closed-cycle resonance of the atoms which are to be trapped. Many techniques are available to produce useful spectroscopic signals and the advances in chip scale atomic clocks [80], hollow waveguides [81], and sub-wavelength fibres [82] and cells [83] provide techniques for coupling beams into atomic vapours. Therefore one can see that miniaturization of the above systems has several clear development route.

IV. ATOM SOURCE AND CONTROL

The atomic species to be cooled and trapped can be sourced either from a hot vapour, or captured from an atomic beam. The latter is usually produced from a hot Knudsen oven, and requires additional cooling to obtain a suitable capture efficiency in the MOT, usually via a Zeeman slower [84] or chirped cooling [85]. Our chip based system will be far too small for such slowers as they require tens of centimetres for adequate deceleration, although they can be made smaller using bichromatic force techniques [86]. Loading from a background vapour is a common method which results in reasonably fast loading rates, but requires a vapour pressure greater than UHV, resulting in increased collisions and decoherence during subsequent manipulation [87]. Therefore the vapour pressure must be controllable on short times scales, ideally within a second. A common method to achieve this uses a MOT cooled in two dimensions (2D-MOT) in one chamber separated from a 3D-MOT in another via a narrow conductance channel [88]. The 2D-MOT chamber may be kept at a high vapour pressure so that it may load many atoms into a low velocity beam directed into the higher vacuum 3D-MOT chamber. This technique has been used in miniaturized BEC systems [41]. Such multichamber systems are likely to be necessary for obtaining BECs which require a higher level of vacuum, however in this study we aim solely to produce a cold non-degenerate cloud of atoms, concentrating on loading a single MOT from a room temperature vapour, and to control it on short timescales. In situations where long coherent times are not required, such as in high data rate interferometers, one can tolerate higher vapour pressures and even recapture the cold atom cloud [59].

Each laser cooled species has different chemical properties which bring different challenges. In this study we look at rubidium as it is ubiquitous across the whole scope of cold atom experiments, and poses the challenge of a vapour pressure which is too high at room temperature for efficient trapping. Species with lower vapour pressure, such as strontium, could be easier to use as they do not endanger the vacuum, but the high temperatures needed to obtain a suitable background pressure results in less efficient trap loading, and so may require the additional cooling mechanisms discussed above. Rubidium melts at 39°C and at room temperature has a (^{87}Rb) vapour pressure of 3×10^{-7} mbar [89]. This results in significant collisional rates with trapped atoms and also excessive fluorescence, making the detection of the cold atoms very difficult. Moreover, the very small volume of the MicroMOT will quickly result in vapour saturation with no pumping mechanisms. A sufficient vapour pressure to load a rubidium MOT is $\sim 10^{-8}$ mbar, but one must reduce this by an order of magnitude for any decoherence-sensitive measurements. Therefore, one must have a method to carefully regulate the flow of rubidium into the MOT chamber.

The past decade's development of CSACs has provided a range of methods to introduce alkali atoms into microfabricated devices. These sources include pure metal [90, 91], alkali compounds [90], wax pellets [92], alkali azides [93], and alkali-enriched glass [94]. Most are not suitable for UHV or result in poorly controlled, or limited lifetime, sources. Pure rubidium is not suitable unless it is sealed away during fabrication as its high pressure vapour will ruin vacuum at the elevated temperatures required for baking and bonding. Commercial alkali dispensers, such as *SAES Getters Alkali Metal Dispensers* (AMDs) and *Alvatec Alvasources* are alkali compounds which are stable up to temperatures of 300-600°C. AMDs are chromates combined with a Zr-Al getter material held in a nichrome dispenser [95]. Heating of the AMDs results in a reduction reaction releasing pure rubidium and some additional gases which are gettered away. *Alvasources* are alkalis alloyed with 'poor' metals, such as bismuth, which form stable compounds with higher sublimation temperatures than their constituent elements. They also result in far less residual gas than AMDs [96], albeit at a higher cost. Both of these sources can be controlled with Joule heating, but they can also be activated with a focused laser [97, 98], removing the need for electrical feedthroughs and reducing the heat transfer to the chip [99].

Rubidium vapour will reach saturation very quickly within micro-litre volumes, especially as the previously mentioned sources may be difficult to control accurately, so a system to pump away the vapour must be incorporated. Glass and metals are effective pumps for alkali atoms: surface studies have found binding energies around 3 eV and extremely high pumping rates [87] of

$10^3\,\mathrm{l\,s^{-1}cm^{-2}}$. Studies looking at vapour cell coatings [100] have highlighted a significant 'curing time' after filling, during which the vapour pressure stabilizes due to strong chemisorption [101]. After the surface is saturated the adsorption energy drops to $\sim 0.5\,\mathrm{eV}$ and is thus only weakly physisorbed. If we assume the MicroMOT produces a 10 second pulse of rubidium every minute, with a peak pressure of 10^{-8}mbar, which is pumped away at $1\,\mathrm{l\,s^{-1}}$, one would require a total of 10^{19} atoms (about 1 mg) to last for our 1000 day target. A typical monolayer is around $5 \times 10^{14}\,\mathrm{cm^{-2}}$, so one cannot rely on surface pumping alone if it cannot be degassed regularly [102]. We note that the limited surface area can be increased with materials such as aerogel, porous silicon, zeolites, and anodic alumina.

An obvious and effective method to control the vapour is by simply reducing the temperature of the MicroMOT. To get to 10^{-10} mbar one must cool rubidium to $-30°$C. This can be accomplished by cooling the entire chip or with an integrated 'cold finger', such as a micro-peltier device [103]. This latter method will avoid rubidium condensation on critical features such as the windows or reflectors, and also avoid water accumulating on external surfaces. The pumping of alkali metals by getter films has been reported to be negligible [104, 105], but little data is available [106], so may not be useful in its regulation. Many atom chips require gold films for reflective surfaces and conductors and it is known in the field that these may degrade over time when exposed to a hot rubidium source. The phase diagram [107] between gold and rubidium shows a stable alloy forms around 500°C. Therefore one can use a heated gold surface to pump away excess rubidium [108]. Another method could utilize the rubidium/bismuth alloying effect mentioned earlier as a thermally controlled pump, but one must be wary of the low melting point of this metal (271°C) during fabrication. Both alloying methods work for all alkali metals but, as shown in Table II, these occur at different temperatures. A common getter for caesium in frequency standards is polycrystalline graphite [109]. There exists extensive theoretical work due to the recent interest in graphene electronics [110], but limited data on the adsorption and intercalation of alkalis with graphite (with the exception of potassium [111]), however the heavier alkalis display similar charateristics and therefore this type of getter could be applicable.

A common method to quickly control the vapour pressure whilst remaining at room temperature is Light Induced Atomic Desorption (LIAD) [112]. This technique involves the illumination of metal or glass surfaces with non-resonant ultraviolet light (UV) in order to increase the desorption rate of physisorbed alkali atoms. The exact mechanism by which this occurs is still under debate [113–115]. Once the UV light is extinguished the desorption rate reduces so that atoms can return to the surfaces. This reloading of the atom sources means that the total number of atoms in the device can be reduced through recycling. Studies have shown an order of magnitude improvement of MOT loading rates with this technique [116, 117], and it has been used to make BECs, which are very sensitive to background gas collisions, in a single chamber [118]. In chip-scale systems the surface area is far too small for effective use of LIAD [119] but, as mentioned earlier, one can introduce high surface area materials [120, 121] providing they can be degassed sufficiently prior to encapsulation.

TABLE II. Gold and bismuth alkali alloys with 1:1 compositions for use as alkali pumping mechanisms. Many of the phase diagrams exhibit several phases with additional alloys forming above and below these temperatures and the reader should refer to the original sources. The approximate values are due to indistinct alloying temperatures.

Alkali metal (M)	Au-M alloy °C	Bi-M alloy °C
Li[122, 123]	∼660	∼400
Na [124, 125]	372	444
K [126, 127]	532	355
Rb[107, 128]	498	376
Cs [129, 130]	585	390

For any pumping mechanism the production of rubidium from the source should be well controlled to ensure consistent loading of the MOT and to prevent permanent vapour saturation. If the source reactively produces hot vapour at unpredictable rates, due to material or heating inhomogeneities, then additional mechanisms are needed to control the flow. Separating two chambers of different pressures is a common challenge in UHV systems, as discussed earlier in 2D/3D MOT loading, and can be achieved by carefully limiting the gas conductance between them with a narrow channel. A channel 1 mm long with a cross-section of $100 \times 100\,\mu$m, can maintain UHV in the MicroMOT chamber at room temperature [131] whilst the source chamber is at saturation pressure, as long as there is a pumping rate greater than $0.1\,\mathrm{l\,s^{-1}}$ in the laser cooling chamber. Locally heating the source chamber by 100°C will sufficiently increase the vapour pressure for loading the MOT. The narrow aperture also leads to a 'beaming effect' which may aid the loading of the trap.

V. UHV IN A CHIP

Table III highlights the various challenges in terms of leak, permeation, and outgassing rates that must be tackled to realize sealed passive UHV chips, and compares them to those required by typical UHV systems. Reaching many of these values, especially those for noble gases, may seem unachievable, however we have identified methods to do so by careful choice of materials, fabrication processes and also structural features.

Vacuum encapsulation of microfabricated devices is a large and mature industry and nearly all MEMS devices require some level of hermetic sealing. The range of

TABLE III. General characteristics of standard UHV MOT systems, and those for the MicroMOT

	Standard	MicroMOT
Internal volume (l)	>1	$<10^{-3}$
Lifetime (days)	indefinite	1000 (target)
Pump rate ($\mathrm{l\,s^{-1}}$)	>20	<1
Leak rate ($\mathrm{mbar\,l\,s^{-1}}$)	$<10^{-11}$	$<10^{-19}$(Ar) $<10^{-14}$(N_2)
Outgassing rate ($\mathrm{mbar\,l\,s^{-1}cm^{-2}}$)	$<10^{-11}$	$<10^{-21}$(He) $<10^{-16}$(H_2)
Permeation rate[a] ($\mathrm{cm^2s^{-1}}$)	$<10^{-7}$	$<10^{-17}$

[a] For helium using Equations 2 and 5.

vacuum levels required ranges from 10^2 mbar in MEMS accelerometers to 10^{-4} mbar in microbolometers [132]. Very low vacua are also needed in field emission devices and the lowest recorded encapsulated pressure the authors have found in the literature, 10^{-8} mbar [133], was achieved using this technology. Maintaining UHV is also important to photomultiplier tubes and we highlight the work of Erjavec [134] who have performed a similar study to this one. Lower pressures in encapsulated microdevices have probably been achieved, but the means to measure them do not exist as most gauges with capability down to UHV have far greater internal volumes than the devices themselves. We are fortunate that the device we are aiming to produce, by its very nature, is capable of measuring such low pressures. It is commonly known in the atom trapping field that the loading rate, γ (Hz), of an atom cloud is linearly related to the background pressure, with an approximate scaling of $2 \times 10^{-8}\gamma$ mbar s, and Arpornthip et al [87] performed a systematic study of this gauging technique. It was found to vary little with systematic variations, such as cooling beam power and detuning, and had a sensitivity range from 10^{-7} to below 10^{-9} mbar, limited by collisions between cold atoms within the trapped cloud. This sensitivity range is slightly above the range of our target pressure but will provide an adequate indication of the internal environment. An improved sensitivity down to 10^{-12} mbar may be possible if the background rubidium vapour can be quickly reduced after loading [135] using the techniques discussed in the previous section.

Two methods are commonly used to encapsulate low pressures inside chips [132]: wafer to wafer bonding under vacuum, or sealing of an evacuation tube after bonding (as shown in Figure 4). The latter is simpler to construct as the various chip layers do not need to be manipulated and bonded under UHV. This method has been used in the NIST atom chip system in which the evacuation tube is constantly pumped by a miniature ion pump. However, efficient evacuation to UHV through a small aperture is difficult and the sealing process is non-trivial on a wafer-level scale in terms of complexity, uniformity and time. We shall see that wafer-to-wafer bonding under vacuum, whilst complicated to implement, allows one to

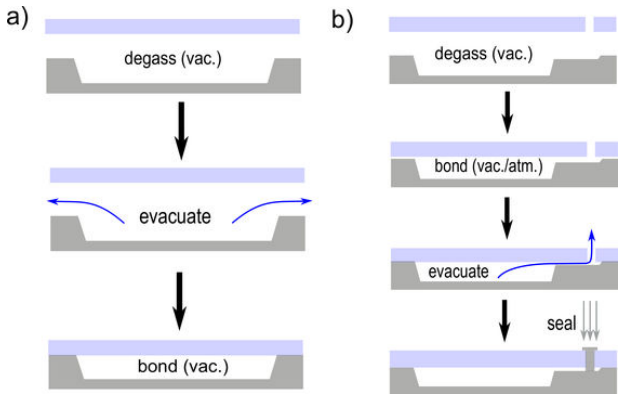

FIG. 4. Techniques to encapsulate a vacuum by evacuation before (a) and after (b) bonding.

thoroughly degas and evacuate chips and also allows the introduction of a novel structural scheme to drastically reduce leak rates discussed in Section V C.

The choice of materials from which the micro-MOT can be constructed is dependent on the sealing method and the typical process environments. Suitable materials for UHV have negligible vapour pressures, low outgassing and permeability rates, and are mechanically strong and machinable. Therefore metals such as stainless steel, aluminium, titanium and copper are predominant. The MicroMOT would require optical access for the cooling beams and fluorescence detection and so the chip must include an optically transparent section using a glass or glass-ceramic. Unfortunately there is a mismatch in the coefficients of thermal expansion (CTE) between glass and metal components which limit their baking, bonding, and operating temperatures. The exceptions are low expansion alloys such as Kovar and Invar, the former being specifically developed for glass-metal seals. Any remaining CTE mismatch can typically be alleviated with specially shaped sealing edges [136]. Nevertheless, we find that the majority of metals [137] do not have the extremely low outgassing rates [138, 139] highlighted in Table III, and their glass-metal seals [136] may not be adequately hermetic [140], or are impractical to implement into the microfabrication process (i.e. very high temperatures for extended periods). Alternative bonding methods are discussed in Section V C.

The MicroMOTs are likely to incorporate atom chips which commonly use silicon as a substrate due to its high thermal conductivity and the vast array of available semiconductor processing techniques [31]. Coincidentally silicon, as we shall see in the following sections, is a very suitable UHV material: it has extremely low permeation and outgassing rates at room temperature, it has several CTE-matched optical materials available, it is produced with a high purity (to the 9N level), and can withstand high temperatures necessary for baking and bonding [141]. The disadvantage of this material is its brittle-

ness [142], so only small structures can be fabricated using specialized techniques which is acceptable in our application, but not for large scale vacuum systems. Several well studied processes exist to clean silicon wafers and the lowest leak rates we have found for sealing technologies have been found for silicon-glass bonding (Section V C). It is also interesting to note that polysilicon coatings are commercially available to reduce the outgassing rates of stainless steel chambers [143]. Another advantage is that silicon is completely non-magnetic, which is important for manipulating atoms, and is a poor electrical conductor which reduces the deleterious effect of eddy currents during fast magnetic field switching [144] - a common issue with MOTs. Hence, in the following section we assume the chips are predominantly constructed from silicon and glass, with additional metal films for reflectors and getters.

A. Pumping

One cannot maintain a high vacuum without any form of pumping because no seal is perfect, all materials outgas to some extent, and no material is impermeable to all gases. However, by reducing the above effects as much as possible one can sustain vacuum with minimal pumping, especially in small volumes. A series of pumps are typically required to obtain UHV conditions, with roughing pumps achieving millibar pressures, turbo-molecular pumps down to to 10^{-8} mbar, and ion and sublimation pumps to finally reach 10^{-10} mbar and below. Once this is achieved the chamber is permanently sealed leaving only the latter two pumps to remove outgassing and permeated species. The roughing and turbo-molecular pumps no longer have any role in maintaining the vacuum and are usually removed. Operating an unsealed system is possible but should be avoided due to unnecessary power consumption and limitations on the ultimate vacuum due to 'backstreaming' and compression ratios of the pumps. If the commercial interest in cold atom technology required mass-production, the development and integration of sub-UHV pumps would be uneconomical due to their limited operating range. A more economical, and simpler, route would be to obtain UHV in a larger encapsulation chamber where several devices can be sealed leaving the need for only on-chip UHV maintenance pumps. In situations where the chip is regularly opened to atmosphere there exist several technologies, instigated in part by the DARPA 'Chip-Scale Vacuum Micro Pumps' program which aimed at obtaining 10^{-6} mbar with coin-sized pumps. This has resulted in impressively miniature displacement [145, 146], Knudsen [147], turbo-molecular [148] and ion pumps [149–151]. Laser and Santiago [152] and Górecka-Drzazga [153] presented reviews of micropump developments previous to the DARPA programme. We shall see in Section V D that it is possible to construct chambers with extremely low outgassing materials such that minimal pumping is required. Ion pumps and getter pumps are good candidates for this role with the latter being more attractive due to their passive nature. Ion pumps are necessary in situations where ungettered species such as noble gases exist in the system. We aim to circumvent this issue by using impermeable windows and throughly degassed components.

Passive pumping elements take the form of getters which are metals, or alloys, that chemisorb typical gases found in high vacuum, namely O_2, CO, N_2, and H_2. Getters generally come in two varieties [154]: Evaporable getters are metals which are heated until their increased vapour pressure causes them to deposit on surrounding surfaces. This traps residual gases under the deposited layers, but the new surface also acts as a pump to impinging gases through chemisorption. Non-Evaporable Getters (NEGs) also chemisorb gases onto their surface, but in addition they absorb the reacted surface material into the getter bulk during heating (known as activation). Both types keep pumping gases at room temperature, albeit at a reduced rate, providing their surfaces are not saturated. NEGs activate at temperatures ranging around 200-800°C, depending on their composition, whereas evaporable getters need to be heated to well above 700°C. Therefore the choice of NEGs for our MicroMOT is obvious, and is further validated by its adoption in the MEMs vacuum encapsulation industry, however we shall also discuss recent advances in Group I/II evaporable (or reactive) getters.

Non-evaporable getters are made of Group IV/V metals and alloys, such as Ti, Zr, V, Hf etc, and may also include metals such as Al and Fe. These are elements with high oxygen solubility, high diffusivity, and high enthalpy of adsorption for many gases found in vacuum [155]. When exposed to air, the surface of the NEG quickly passivates forming oxides, nitrides and carbides in an 2-3 nm layer [156]. Heating the NEG in vacuum, known as activation, causes these compounds to diffuse into the bulk leaving a fresh metallic surface pump. Typical oxygen solubilities for NEG compounds are on the order of 10%, so a 1 μm thin film can undergo $\sim$100 reactivation cycles after air exposure, however the pumping efficiency begins to reduce after a few cycles [157]. This corresponds to an approximate total capacity of 10^{12} molecules per cubic centimetre. Recent *in-situ* studies of NEG activation with individual gases at temperatures above activation indicate far higher capacities of the order of 10^5 monolayers of carbon monoxide [158] due to the increasingly uniform oxygen concentration in the film with temperature. Hydrogen diffuses readily in the bulk, and so the capacity is approximately two orders of magnitude higher than surface pumped species at room temperature. Embrittlement of the film at very high hydrogen concentrations (above 1%) can result in delamination and so should be avoided [159]. When NEGs are deposited as thin films they also act as outgassing barriers [160], thus turning gas sources into pumps and greatly reducing the ultimate pressure. Noble gases and some hydrocarbons,

such as methane, are not pumped by NEGs at room temperature. Therefore the MicroMOT will need to be sealed at UHV to ensure the majority of gases, especially the nobles, are evacuated prior to encapsulation.

The bonding techniques discussed in Section V C require temperatures up to 400°C, which will lead to increased outgassing (see Section V D) and a reduction of the NEG lifetime due to saturation. Moreover, reactivation of the getter to rejuvenate its pumping rate during the sealed devices' lifetime will lead to increased outgassing, permeation and possibly leakage. Therefore it is prudent to use an NEG alloy with a very low activation temperature, and high pumping rate and capacity. The beam lines of particle accelerators require XHV environments, and their very large volume presents an issue for efficient and uniform pumping. Several decades of research at CERN have been devoted to finding NEGs both which activate during the chamber baking procedure (~ 250°C) and can also coat all internal surfaces [161]. Their findings have shown that sputtered Ti-Zr-V alloys of nearly equal ratios can be activated at 180°C, and using these coatings, together with ion pumps, they have demonstrated the lowest room temperature vacuum of 10^{-14} mbar [162]. The pumping rate of NEG films depends on their surface area and so the CERN team have also looked into the effects of substrate and deposition parameters to increase pumping rates and capacities [163]. Additional attractive properties of Ti-Zr-V NEG films are their high adhesion, thermal and vibration stability, resilience to standard wafer cleaning processes, and commercial availability [164]. Table IV shows the typical pumping rates and capacities of Ti-Zr-V NEG thin films whose values will be used in the following sections. Not all gases are pumped equally and some lead to reduced pumping speed of the NEG at high surface coverage (for example, CO reduces the pumping rate and capacity of H_2 and N_2) which are shown in Table IV. This effect must be accounted for when calculating the lifetime of getter pumped devices. The unintentional incorporation of noble gases in sputtered films can result in outgassing which may endanger the vacuum [165, 166] and this will be discussed in Section V D. As a result, alternative methods, such as vacuum arc deposition [156] or e-beam evaporation [167], should be considered.

Most gases only chemisorb on the NEG surface and show negligible pumping after a monolayer is formed. Hydrogen is the exception as it diffuses throughout the entire bulk of the getter and so only the thickness of the film defines the capacity. There exists a thermal equilibrium between the absorption and desorption of hydrogen from the NEG. This is dependent on the hydrogen concentration [168] and thus can be used to predict the residual pressure in our devices. This value, known as the disassociation pressure, follows Sieverts' law and has been measured for Ti-Zr-V films [157]. It was found to be given by:

$$\log_{10}(P_{H_2}) = 2\log_{10}(x_H) + 14.324 - \frac{8468}{T} \qquad (1)$$

Where P_{H_2} is in millibar, x_H is the fraction of hydrogen in the film and T is the temperature in kelvin. We can see that for a very saturated film ($x_H = 0.01$) the pressure is negligible at room temperature (10^{-19} mbar) and only endangers the vacuum at temperatures above 150°C, at which point helium permeation through the glass wafer becomes equally problematic, as we shall see in Section V B.

Earlier we dismissed evaporable getters on the basis of high operating temperatures and vapour phase gases. There is a new type of evaporable, or more specifically reactive, getter [169] being investigated which uses Group I/II atoms, specifically lithium, as the pumping medium [170–173]. Early studies of alkali metal dispensers showed that they improve the pumping rate of the system [105], and barium is the original and highly effective getter material widely used in cathode ray tubes. Reactive getters will react and bind strongly to the common residual gases found at UHV and therefore our devices may experience an improvement of the vacuum during operation. Experiments have shown that the pumping rate for carbon monoxide by lithium getter films is similar to Ti-Zr-V NEGs but with a capacity over 10^4 times greater. This would be very advantageous to remove outgassed species during bonding which could otherwise saturate Ti-Zr-V films. Most of the work on these reactive getters has focused on lithium due to its low vapour pressure and ability to form stable compounds with a number of gases. We suspect rubidium will provide some gettering, but not to the extent of lithium due to the former's high vapour pressure. For example, the disassociation pressure [170] of LiH at 300 K is 10^{-21} mbar whereas that of RbH is 10^{-7} mbar, only marginally less than rubidium vapour pressure [89, 174]. It is expected, however, that pumping of oxygen and carbon monoxide will be more effective. With its greater capacity and ability to pump additional gases such as methane, which NEGs cannot, a lithium getter could replace, or complement, the NEG in the MicroMOT if the necessary vacuum cannot be pumped by NEGs alone [175].

TABLE IV. Typical pumping rates, sticking factors and capacities of Ti-Zr-V NEGs at room temperature for a 1 μm film. The values in parentheses indicate the pumping rate after carbon monoxide saturation [157]. The capacities can be increased by nearly an order of magnitude by heating the substrate during deposition to increase surface area.

Gas	Sticking factor	Pumping rate ($ls^{-1}cm^{-2}$)	Capacity (cm^{-2})
H_2	8×10^{-3}	0.35 (0.1)	$> 10^{16}$
N_2	1.5×10^{-2}	0.17 (0.1)	1.5×10^{14}
CO	0.7	8	10^{15}

In the following sections we assume:

- An internal volume of $0.5\,\mathrm{cm}^3$.
- A surface area of $5\,\mathrm{cm}^2$.
- An NEG area of $1\,\mathrm{cm}^2$ with a thickness of $1\,\mu\mathrm{m}$.

B. Permeation

No material is absolutely impermeable to all gases, and so it is inevitable that they will diffuse through the walls of any chamber and finally desorb into the vacuum. We shall address the issue of permeation before that of outgassing and leaks as this is seen by many as the limiting factor in achieving UHV in small, sealed, well-degassed volumes. Permeation is complex and requires several processes to become a vacuum risk: 1) The gas molecules in the external environment impinge on the outer surface of the chamber wall and physisorbed, 2) they disassociate if the surface enthalpy is greater than their bonds, 3) they are absorbed under the surface layer and diffuse through the bulk along the concentration gradient (Fick's law), 4) the gas atoms must then overcome any surface energy barriers, and 5) desorb from the surface directly or recombine with other ions to desorb as a molecule. These processes strongly depend on the type of permeating gas and the chamber wall material. For example, noble gases will permeate glasses, but not most metals due to the latter's more crystalline structure and weak surface interaction. As noble gases are not pumped by NEGs their permeation is of greatest importance and we shall devote the majority of this section to them, however we will also discuss the effect of hydrogen as this is the second fastest permeating gas (see Table VI).

Surface effects, which will be discussed in Section V D, tend to reduce the permeation rate so the simple process of bulk diffusion can be considered the limiting factor of permeation. The amount of gas flowing diffusively across a membrane of area A and thickness d between two regions of pressure P_{ext} and P_{int} is

$$\frac{dQ}{dt} = \frac{KA(P_{ext} - P_{int})}{d} \tag{2}$$

where $K = DS$ is the permeation rate ($\mathrm{cm}^2\,\mathrm{s}^{-1}$), D is the diffusion constant ($\mathrm{cm}^2\,\mathrm{s}^{-1}$) and S is the solubility (cm^3 (STP)/cm^3). Both D and S typically follow an Arrhenius-type temperature dependence and the former is quoted in the literature as

$$D(T) = D_0 \exp\left(\frac{-E_D}{k_B T}\right) \tag{3}$$

where E_D is the diffusion energy, k_B is the Boltzmann constant and T is the temperature. The variation of S can be much more complicated [176], however over a limited range of temperatures the Arrhenius form is adequate, and for most materials S does not change appreciably compared to D with temperature. Values of diffusion, solubility and permeability of the materials highlighted in this study can be found compared to the common vacuum materials, stainless steel and Pyrex, in Table V. Equation 2 assumes the gas is already fully dissolved in the membrane, which is not the case in thoroughly degassed materials. Therefore there is a period of time before the gas will 'break through' to the evacuated volume, and in materials with very low diffusion rates this can be extremely long [177]. The pressure increase of a cavity of volume V at a time t due to a gas permeating through a degassed membrane is [178]:

$$P_c = \frac{ADSP_{ext}}{Vd}\left[t - \frac{d^2}{6D} - \frac{2d^2}{\pi^2 D}\sum_{m=1}^{\infty}\frac{(-1)^m e^{\frac{-m^2\pi^2 Dt}{d^2}}}{m^2}\right] \tag{4}$$

Since the micro-MOT chambers will require at least one optically transparent viewport the permeation of helium through glass will be a significant issue. The amorphous network structure of glass forming oxides provide channels for helium to diffuse. Not all glasses are alike however, and the addition of 'modifier' molecules can act to plug the holes in the network, resulting in very low permeation rates [179]. We aim to seal glass to silicon and therefore must match CTEs to reduce stresses and therefore increase yield. Pyrex is the most common glass bonded to silicon due to their comparable CTEs and its sodium content required for anodic bonding [181] (see Section V C). This borosilicate glass is so highly permeable to helium that we should expect to lose UHV several days after bonding (see Figure 5). Much work was carried out in the 1960s and 1970s on the permeation

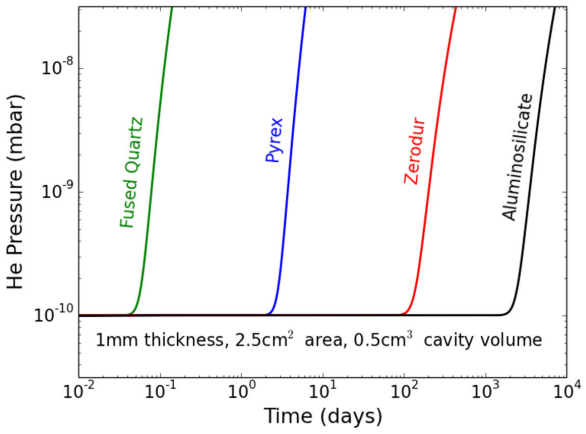

FIG. 5. The permeation rate of various 1 mm optical wafers exposed to atmospheric helium after initial evacuation to 10^{-10} mbar after complete degassing. We have calculated the values using Equation 4 and used the data for *Corning* 1720 to define the properties of AS glass [179, 180].

rates of gases through glass, and the results showed that Alumino-Silicate (AS) glass, those with approximately 20% Al_2O_3 or more composition, had permeation rates five orders of magnitude lower than Pyrex [179, 182]. Figure 5 shows a comparison of the permeation rates of helium through AS glass, Pyrex, fused silica, and *Schott* Zerodur glass-ceramic, calculated using Equation 4. This latter material is commonly used in UHV systems requiring low permeation and its very low CTE makes it well suited for bonding. We can also see that *Corning* 1720 series AS glass is more than capable of maintaining vacuum for our target time. Its CTE is well matched with silicon to which is can be anodically bonded, albeit at much higher temperatures than Pyrex due to the low alkali content [183–185].

Other AS glasses are commercially available, but too numerous to list here, and we mention that load-borate and soda-lime glasses also have low permeability. Silicon carbide [186] has a very low permeability [187], can be bonded to silicon [188], and has been used for atom chips due to its transparency and high thermal conductivity [189]. Sapphire and glass-ceramics such as Spinel [190] are likely to have extremely low permeation rates, but yet again are not well CTE matched. Hard crystalline optical coatings may also reduce permeation. Graphene, amongst its many other attractive properties, has shown a permeability rate equal to bulk Pyrex, yet requiring only a single monolayer [191]. Unfortunately uniform coatings over large areas are as yet unavailable, but graphene-oxide may be a suitable alternative [192].

Norton [199] measured the permeation of other gases through fused silica, as shown in Table VI, and we can see that, in general, larger molecules have lower permeation rates but can depend on surface interactions and solubilities (compare H_2 and Ne). Hydrogen diffuses through glass as a molecule [176, 197] and so, as shown in Table V, it will have a far lower permeation rate than helium. Coupled with an order of magnitude lower atmospheric partial pressure compared to helium, and the ability to pump the gas with NEGs, hydrogen permeation can be neglected. Very little data is available on the hydrogen permeability through AS glass and so we have used a scaling law by Souers et al [195], the glass composition from Altemose [179], and the Pyrex solubility to calculate the diffusivity constants in Table V.

TABLE VI. Permeation of different gases [204, 205] through fused silica [199].

Gas	Relative permeation rate at 700°C	Van der Waals radius, nm
He	1	0.133
H_2	0.1	0.15
Ne	0.02	0.141
Ar	$<10^{-7}$	0.176

We now address the second material in our system: silicon. Measurements of helium permeation through silicon extrapolated from high temperatures show that, like metals, silicon is practically impermeable to all noble gases. Using measured values for solubility [193, 206] and typical atmospheric helium content, we should not expect to find a single atom within a cubic centimetre of silicon. We note that recent studies [207, 208] looking at the hermeticity of glass frit encapsulation and other bonding methods have indicated that helium permeation through silicon at room temperature may be more significant than expected. However, more work is required to confirm this against the large bulk of research into helium bubble formation in silicon which agrees with the original low permeation result [209]. Hydrogen, on the other hand, is known to permeate silicon albeit predominantly in atomic form at room temperature. This matter will be discussed in great detail in Section V D as the permeation rate is related to outgassing. The results in Table V show that the permeation rate of hydrogen through silicon at room temperature is negligible.

C. Leaking

No seal is perfect as the bonding of materials will inevitably lead to a route for gases to travel, via microchannels and defects, or merely a local variation in the permeation rate. Standard UHV systems predominantly use Conflat type seals which employ knife-edges to bite into OHFC copper gaskets and join metal components together, and 'housekeeper' type seals for glass-to-metal interfaces. Commercial vacuum products quote leak rates less than 10^{-11}mbar l s^{-1} (STP), usually limited by the resolution of the leak detector [210]. These types of seals are not suitable for wafer-level fabrication of vacuum encapsulated micro-electronics and so several new methods have been developed using chemically formed seals, or simply relying on the attraction between perfectly flat surfaces [211]. The small volume and long lifetime of many microelectronic chips may preclude the use of internal pumping mechanisms, meaning that the seals must have extremely low leakage, more so than those demanded by standard vacuum systems.

$$Q_L = \frac{V\Delta P}{\Delta t} \tag{5}$$

Using Equation 5 we can calculate the highest permissible leak rate for a gas at atmospheric pressure leaking into our specified volume of $V = 0.5\,\mathrm{cm}^3$, such that the pressure does not rise by 50% ($\Delta P = 0.5 \times 10^{-10}$ mbar) over $\Delta t = 1000$ days, to be 3×10^{-22} mbar l s^{-1}. This rate seems unachievable, but we must consider that some gases are pumped away by the NEGs and so may permit a higher leak rate, and many gases have low atmospheric partial pressures. For example the partial pressure of helium in the atmosphere is 5×10^{-3} mbar and so one can permit a leak rate [212] of 1.5×10^{-17} mbar l s^{-1}.

TABLE V. Bulk diffusivities and solubilities (at STP) of helium and hydrogen in silicon, Pyrex (*Corning* 7740), aluminosilicate (*Corning* 1720), and stainless steel. We have also tabulated the permeation rates at 20°C and 500°C to compare values more easily.

	Silicon [193, 194]	Aluminosilicate [179, 195, 196]	Pyrex [176, 179, 195–198]	Stainless steel [199, 200]
Helium[a]				
D_0 ($cm^2 s^{-1}$)	5.2×10^{-3}	3.7×10^{-4}	4.6×10^{-4}	Impermeable [199, 203]
E_D (eV)	-0.82	-0.52	-0.28	-
S_0 (cm^3 (STP) cm^{-3})	2.8×10^{-4}	0.0016	0.005	-
E_S (eV)	-0.77	-	-	-
K ($cm^2 s^{-1}$) @ 20°C	3.2×10^{-34}	6.8×10^{-16}	3.5×10^{-11}	-
@ 500°C	4.8×10^{-17}	2.4×10^{-10}	3.4×10^{-8}	-
Hydrogen[b] [c]				
D_0 ($cm^2 s^{-1}$)	9.7×10^{-3}	2.08×10^{-7} K^{-1}	1.4×10^{-5}	1.2×10^{-2}
E_D (eV)	-0.48	-0.67	-0.24	-0.56
S_0 (cm^3 (STP) cm^{-3})	90.4	0.038	0.038	0.3
E_S (eV)	-1.86	-0.12	-0.12	-0.11
K ($cm^2 s^{-1}$) @ 20°C	5.7×10^{-40}	6.1×10^{-23}	3.4×10^{-16}	1.0×10^{-14}
@ 500°C	1.2×10^{-15}	4.3×10^{-14}	2.4×10^{-12}	1.4×10^{-7}

[a] We are unable to find helium solubility in silicon data other than van Wieringen et al [193] which is somewhat unreliable due to the limited measurement range. In the tabulated values we have used that data with the theoretical energy of solution [194] to calculate the prefactor. The diffusivity values are also theoretical but agree with experimental results [193, 201, 202].

[b] We have assumed the same solubility for AS glass as for Pyrex due to the small variation found between glasses and the minimal temperature variation[197, 198].

[c] Like helium, the commonly quoted values measured by van Wieringen et al [193] are extrapolated from a narrow high temperature range and can be assumed to indicate the highest diffusion rate (see Section V D).

Reactive gas leakage is limited by the pump rate and capacity of the NEG films. In light of this we may model the lifetime of the device due to NEG saturation using the following formula:

$$\frac{dP_c}{dt} = \frac{1}{V}\left(Q_L - L_P P_c (1-\theta)^k\right) \tag{6}$$

Where P_c is the internal pressure (mbar), Q_L is the leak rate (mbar l s^{-1}), L_P is the pumping rate of the getter (l s^{-1}), θ is the fractional surface coverage, and k is the order of desorption. The effect of surface coverage on pumping depends on the gas/surface chemistry, temperature, and surface geometry (flat, granular, etc.). This topic is too extensive to detail here but can be found in most surface science graduate texts [213]. We find that the Langmuir adsorption isotherm, $(1-\theta)^k$, models the majority of data on NEG pumping rates [157] adequately for our purposes due to the low surface coverage. The pressure inside the cavity will drop to base value:

$$P_{base} = \frac{Q_L}{L_p} \tag{7}$$

As noted earlier, the effect of saturation by some gases (for example carbon monoxide) reduces the pumping speed of other gases [157] which we do not take into account dynamically in the model, but assume the lowest pumping speed as the 'worst case scenario'.

There is a sharp drop in pumping speed at saturation allowing us to simplify the lifetime calculation. By assuming that the pumping rate is constant until the NEG has reached its capacity of C_G (moles), at which point it ubruptly drops to zero ($\theta = 1$), and substituting the ideal gas formula into Equation 6, we find an approximate value for the maximum permissible leak rate:

$$Q_L(max) = \frac{C_G R T}{\tau_L} \tag{8}$$

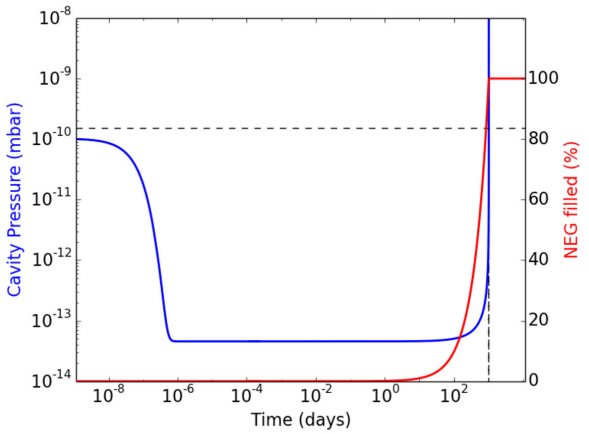

FIG. 6. The internal pressure (blue) and NEG coverage (red) with an atmospheric leak of nitrogen at a rate 6.5×10^{-15} mbar l s^{-1} (air) calculated using Equation 6. The horizontal dashed line indicates the target pressure and the vertical line the result of Equation 8. The cavity is initially at 10^{-10} mbar.

where R is the ideal gas constant, T (K) is the temperature and τ_L (sec) is the lifetime. If we assume a pumping speed for nitrogen, the most abundant atmospheric gas, of $0.1\,\mathrm{l\,s^{-1}}$, a capacity of 10^{14} molecules, with a lifetime of 1000 days: the maximum permissible leak rate is $5{\times}10^{-15}\,\mathrm{mbar\,l\,s^{-1}}$ with $P_{base} = 5{\times}10^{-14}\,\mathrm{mbar}$. Note that Equation 8 is independent of both the pumping rate and background pressure because it assumes them to be at equilibrium, therefore one must use this equation alongside Equation 7 to ensure the correct base pressure. Figure 6 compares the numerical solution of Equation 6 with the approximate value from Equation 8 and we find perfect agreement. We note that the capacity is that for a single monolayer and so the lifetime can simply be extended through reactivation cycles. Hydrogen diffuses into the bulk and so reactivation does not increase the getter lifetime, but the NEG capacity for hydrogen can be two to three orders of magnitude greater (see Table IV), so is not as much of a concern.

In Section V we discussed the methods to encapsulate microfabricated vacuum devices and here we shall explore the details of suitable bonding methods and their quality. We foresee the need for at least two bonding processes: one to bond the 'atom chip' to the structure wafer (silicon to silicon, or gold to silicon), and another to bond the glass capping wafer to the structure layer (glass to silicon). As many bonding technologies exist we will only consider those which are well established, have demonstrated leak rates below $10^{-14}\,\mathrm{mbar\,l\,s^{-1}}$ (air), and do not require temperatures above 400°C so as to reduce outgassing, stress, and protect chip components. We have not included indium bonding (or alloys thereof) as indium melts below the activation temperature of NEGs and therefore requires specialized surface geometries and processes [134] to reduce outgassing and ensure good seals. Also, indium bonding can require several additional films to improve surface wetting, and the leak rate may not sufficiently low [214].

Glass Frit

Glass frit bonding is a well established technique which involves the deposition of a low melting point glass compound between two materials. The glass is heated first to outgas the organic binder compounds, and is then raised to the glass transition temperature which melts and seals the two surfaces upon cooling. The vacuum hermeticity of this technique has been explored extensively by Sparks et al [215], but no absolute leaks rates have been quoted. We believe glass frit bonding to have a leak rate below $10^{-15}\,\mathrm{mbar\,l\,s^{-1}}$ by considering the lifetime, internal volume, and pressure inferred by the integrated resonator's Q-factor [216]. However, the pressure measured ($\sim 10^{-3}\,\mathrm{mbar}$) is at the limit of the gauging technique and one does not know the residual pressure immediately after bonding. Possible issues may include insufficient degassing of the organic binder materials, limitations on pre-baking temperatures, incompatible CTEs (although they can be engineered to match the application) and the need for additional materials. Of the four bonding methods presented here, glass frit has the least sensitivity to surface quality and can be used to seal electrical feedthroughs.

Eutectic Bonding

A eutectic alloy is one where the melting point of the constituent materials is lowered on contact. For example gold and silicon individually have melting points above 1000°C, but when they are pressed together they will melt at 363°C at their interface [217, 218]. Subsequent cooling will form an alloy with high hermeticity and a strong bond. Other suitable eutectic alloys exist, such as gold and tin [219], but we highlight the gold-silicon system as many atoms chips employ gold as a reflector and conductor. This bond has demonstrated the lowest leak rate that we have found [132], below $10^{-15}\,\mathrm{mbar\,l\,s^{-1}}$. Possible disadvantages include the need for multilayer films to prevent interlayer diffusion [218], the requirement of inert gas storage before bonding to prevent the native oxide growth on silicon, and the temperature restrictions post bonding, as further heating remelts the alloy and degrades the bond [220].

Anodic Bonding

Anodic bonding occurs between an oxide forming metal (or semiconductor) and an alkali containing glass, by heating the two materials together (300-500°C) with the simultaneous application of a high voltage (100-1000 V) across the interface[181, 183]. The mobility of the alakli ions (typically sodium or lithium) in the glass is increased with temperature and they are pulled away from the interface by the electric potential. The residual non-bridging oxygen atoms at the interface then bond with the silicon. The high electric potential gradient has the additional effect of pulling the two surfaces into intimate contact which overcomes surface inhomogeneities. The two materials (usually silicon and borosilicate glass) must have very flat surfaces, below 10 nm, and be CTE matched to avoid stress fractures during cooling. Hermeticity measurements show that the leak rate is below $10^{-14}\,\mathrm{mbar\,l\,s^{-1}}$, with few residual gases other than oxygen, which is produced during bonding at the inner seam. This residual gas source can be significant, especially in small evacuated volumes, and so getter films are mandatory (see Section V D). The leak rate measurements [221, 222] included the effect of the bonding area around the cavity and found no variation, from which we infer that the seal is absolutely hermetic and possibly limited only by permeation.

Direct Bonding

Direct bonding is the result of the attractive Van der Walls forces between atomically flat surfaces. Semiconductor and glass wafers are routinely produced with the required flatness and this technique requires no additional materials, does not release gases (unlike anodic and frit bonding), and is hermetic [222] (Leak rates below 10^{-14} mbar l s^{-1}). Unfortunately, for the silicon-silicon direct bond, very high post-annealing temperatures (up to 1000°C) are required to ensure a high bonding yield and to reduce voids. This latter effect is due to gases desorbing between the surfaces which becomes trapped. Bonding in vacuum produces fewer voids, due to a thorough degassing before sealing, to the point that strong bonds form at room temperature without the need for post annealing [223]. The extremely flat surfaces are difficult to retain during processing and even sub-micron particles will result in debonding. CTE-matched glass-silicon direct bonding occurs with lower annealing temperatures [224], and the glass can absorb gases released between the interface.

To summarize the bonding techniques, there are several methods to obtain reliable leak rates lower than 10^{-14} mbar l s^{-1} and even below 10^{-15} mbar l s^{-1} which are required to maintain UHV. Anodic and direct bonds may even be absolutely hermetic, limited by permeation, but their absolute leak rates were beyond the sensitivity of their measurements. Eutectic bonding has shown the lowest measured leak rates and is a reliable and low outgassing method. Glass frit may also have equally low leak rates, but the residual gas pressure released during bonding is unknown.

The atmosphere contains several noble gases [132] including argon (9.3 mbar), neon (1.8×10^{-2} mbar), and helium (5×10^{-3} mbar), where the values in parentheses are the atmospheric partial pressures. Their leak rates are proportional to $(T/M)^{0.5}$, where T is the temperature in kelvin and M is their mass, hence helium leaks at the fastest rate and is often used in hermeticity tests [225] known as 'Helium Bombing'. If we assume a leak rate which is proportional to the pressure differential across the bond, the effect of argon, due to its relatively high atmospheric partial pressure will be most significant. The maximum permissible leak rate for argon is 1×10^{-19} mbar l s^{-1}. The significance of this gas has been mentioned in the literature [226], but is generally ignored as helium permeation through glass is considered to be a more pressing issue. If we compare the lowest measured leak rate for the bonding methods of 10^{-15} mbar l s^{-1} (air) we find all the noble gases endanger UHV, however helium and neon leakage need only be reduced by factor of 15 and 25, respectively, which may be possible with thicker bonding seams or external barrier coatings, whereas argon must be reduced by nearly 10^4.

There is, however, a very simple scheme to reduce the leak rate by several orders of magnitude: Simply by placing the vacuum chamber inside another. This can be achieved practically by introducing a buffer cavity, or moat, within the seam such that the slow leakage into the moat results in an even slower leakage into the main vacuum cavity [227]. This can be modeled by the following formulae and solved numerically:

$$\frac{dP_b}{dt} = \frac{1}{V_b}\left(C_{ab}(P_a - P_b) - C_{bc}(P_b - P_c)\right) \tag{9}$$

$$\frac{dP_c}{dt} = \frac{C_{bc}(P_b - P_c)}{V_c} \tag{10}$$

where P_i is the pressure, V_i is the volume, and C_{ij} is the conductance between i, and j, in which the subscripts $i, j = a, b, c$ refer to the air, buffer, and cavity, respectively. We have independently modelled this effect and found stark, but advantageous, differences from the original study by Gan et al [227]. We suspect that an error was made in tabulating their results, which also clarifies their unexplained lifetime increase for 100 mbar cavities. If we assume a main cavity volume of 0.5 cm^3 and a moat volume of 0.05 cm^3 we can reduce the leakage rate by factor of 2×10^5 as shown in Figure 7. This allows us to use bonds with leak rates in the range of 10^{-14} mbar l s^{-1} (air) which is technically feasible with all the bonding techniques considered earlier, and also reduces the NEG limitations on reactive gases. The moat does not have to be bonded at UHV as the model shows very little variation below an initial moat pressure of 10^{-6} mbar.

D. Outgassing

Outgassing is the release of gas from a material's surface and bulk. We distinguish this from permeation in that the latter assumes a completely degassed material, whereas outgassing is the result of gases that are difficult to remove from the bulk. These have entered either from diffusion during storage, processing, or from the production of the material itself. Cleanliness is of utmost importance in achieving UHV and we assume all components have been through standard wafer cleaning processes, such as an RCA and ozone plasma. This latter technique has also been shown to improve bond strengths and reduce temperatures direct and anodic bonding [228, 229]. We shall not go into further detail regarding cleaning here and direct the interested reader to the references [230–233]. We do highlight that detergents were found to remove vanadium from the NEG films and so should be avoided [234].

Outgassing is the largest source of gas in well-sealed UHV systems and so usually defines the lowest base pressure for a specific pumping rate L_p according to Equation 7. Hydrogen is the dominant gas at UHV, for

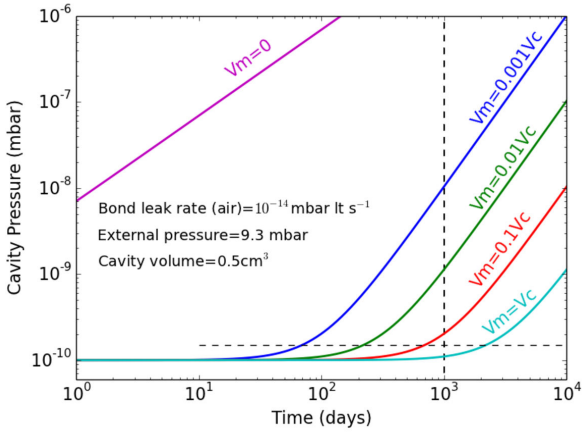

FIG. 7. Numerical solution of Equations 9 for various ratios of moat/cavity volume. We assume argon is leaking from the atmosphere, and the quoted leak rate is for each bond seam (air-to-moat and moat-to-cavity) adjusted to atmospheric pressure to compare with literature values. The horizontal dotted line represents a 50% rise in pressure from an initial value of 10^{-10} Pa, and the vertical line indicates 1000 days. In this simulation $V_m = 0.25\,V_c$ would meet the target property with an overall leak rate of $6{\times}10^{-21}$ mbar $\mathrm{m^3 s^{-1}}$ (air).

which the NEGs have a pumping rate on the order of $0.1\,\mathrm{l\,s^{-1}cm^{-2}}$, and so to achieve 10^{-10} mbar one must ensure the outgassing rate is below 10^{-11} mbar $\mathrm{l\,s^{-1}cm^{-2}}$. This is greater than NEG capacity-limited outgassing rate calculated using Equation 8 and so the base pressure will not be limited by the pumping rate [235].

There is no standard model for predicting the outgassing properties of all materials as many different mechanisms are involved [236, 237] but can be essentially split into two sources: surface and bulk. We assume that the surfaces are clean in that common contaminates such as organics have been thoroughly removed leaving only atmospheric and some processing species, namely water, hydrogen, carbon monoxide, and noble gases. We can calculate the surface desorption rate using:

$$\frac{dN}{dt} = \frac{N\theta^k}{\tau_s} \exp\left(\frac{-E_S}{k_B T}\right) \tag{11}$$

where N is the surface density (molecules $\mathrm{cm^{-2}}$), θ is the fractional surface coverage, k is the desorption order, τ_s is the sojourn time (typically 10^{-13} s), and E_S is the desorption energy [238]. Outgassing from the surface usually occurs at the fastest rate as physisorbed, or weakly chemisorbed gases, have low desorption energies. Strongly bound molecules ($E_S >$ 1.1 eV) can in general be ignored as they do not appreciably desorb from surfaces at room temperature, whereas weakly bound species ($E_S <$ 0.7 eV) can be pumped away quickly. Molecules in the middle of this range are difficult to pump out in a practical time and so high temperature baking is required [239]. We shall refer to this as the 'Outgassing Energy Range (OER)'.

Outgassing of reactive species from the bulk is more complex than simple diffusion. Gases, such as hydrogen, diffuse ionically and can form bonds with the bulk material or impurities in a process known as trapping. Ions may also recombine within the solid and become trapped in lattice defects, and any ion reaching the surface needs to recombine in order to desorb. At low surface coverage this latter, second order, step can be the limiting rate. Many of the transport processes are activated and so only occur at elevated temperatures. This can result in unreliable predictions when extrapolating high temperature data down to room temperature. The effects are further complicated by surface oxides or nitrides which, in general, act to reduce outgassing rates by providing a barrier layer [240–242]. Noble gases, on the other hand, only travel diffusively through the bulk and easily desorb from surfaces at all temperatures due to their weak interaction. All of the effects outlined above act to reduce the outgassing rate compared to a simple diffusion model and therefore one can assume bulk diffusion as the most significant factor and use the rate calculated by Lewin [239] for a 'slab' geometry:

$$\frac{Q_{OG}}{A} = \frac{8x_0 D}{d} \sum_{m=0}^{\infty} \exp\left[-Dt\left(\frac{\pi(2m+1)}{d}\right)^2\right] \tag{12}$$

Where D is diffusion rate, A is the surface area, d is the thickness and x_0 is the initial concentration of the gas in the bulk. For a non-disassociative gas $x_0 = SP$, where S is the solubility and P is the partial pressure of the gas. For a disassociative gas the concentration is proportional to $P^{0.5}$ instead, and the solubility units are adjusted accordingly. By using values for diffusion found experimentally, effects such as trapping are automatically included into the model. As highlighted by Chuntonov et al [169] the increase of outgassing during the high temperature bonding process can cause the NEG film to become saturated and limit the lowest obtainable vacuum and lifetime of the device. To calculate actual lifetime including the effect of bonding we can consider the reduction of getter capacity by the number of molecules released during bonding, and using Equation 8 to find:

$$\tau_L = \frac{T}{Q}\left(C_G R - \frac{\tau_B}{T_B} \sum_{gases} Q_B\right) \tag{13}$$

where T is room (or operating) temperature, T_B is the bonding temperature, τ_B is the bonding time (seconds), Q is the outgassing rate at T, and Q_B is the outgassing rate at T_B. We have assumed the temperatures are changed instantaneously and the bonding period is short enough not to affect the operating outgassing rate. The same formula can be used to predict the increased

outgassing due to reactivation of the NEG during the MicroMOT lifetime. The effect of the bonding can be neglected if:

$$\eta = \frac{\tau_B Q_B}{R C_G T_B} << 1 \tag{14}$$

Assuming an NEG with a hydrogen capacity of 10^{-7} moles ($x_H = 0.01$), a bonding time of $\tau_B = 3600$s at a temperature of $T_B = 400°$C, and we wish to keep $\eta = 0.1$, the bonding outgassing rate must be $Q_B < 10^{-7}\,\mathrm{mbar\,l\,s^{-1}cm^{-2}}$. If this is the result of bulk diffusion which scales as

$$Q = \frac{D(T)}{D(T_B)} Q_B = Q_B \exp\left(\frac{-E_D(T - T_B)}{k_B T_B T}\right) \tag{15}$$

and we use a diffusion energy in the middle of the OER of $E_D = 0.9\,$eV, then one must reduce room temperature hydrogen outgassing rate to $Q_B < 10^{-16}\,\mathrm{mbar\,l\,s^{-1}cm^{-2}}$. Equation 15 also applies for surface desorption (for which $E_D = E_S$). Gases such as carbon monoxide, for which the NEG has only a single monolayer capacity, require outgassing rates over a hundred times lower compared to hydrogen without continuous reactivation. These are extremely low outgassing rates and are the main hurdle in obtaining very low vacua in microelectronic devices. In the following subsection we explore the outgassing rates of the main gases found at UHV - H_2, CO, as well as noble gases - from the materials considered for the MicroMOT and we have tabulated measured and theoretical values for outgassing rates in Table VII.

Hydrogen

Hydrogen can be a major issue in semiconductor devices and so extensive work has been carried out to understand its interaction with silicon [262–266]. The most common and earliest citation in the literature is to the work done by van Wieringen and Warmoltz [193] (which we shall refer to vWW). Their diffusivity and solubility data was taken at very high temperatures (967-1207°C) and these values are shown in Table V. Extrapolation down to room temperature is fraught with possible errors as hydrogen readily dissociates upon diffusing into the bulk, interacting with the silicon lattice and impurities in various forms. Figure 8 shows the results of subsequent diffusion studies and one can see the large variation in measurements in the literature. Advances in understanding have shown that hydrogen migration through bulk silicon predominantly occurs in atomic form at room temperature with an activation barrier of $\sim 0.5\,$eV, but can recombine into a dimer which is then trapped by a barrier of $0.8 - 1.2\,$eV. Exact values are difficult to predict and depend on various doping and impurity levels, growth methods, defects and lattice orientations, and even quantum effects [267]. The vWW diffusivity results are consistently higher than every subsequent measurement and can be taken as the upper limit in our analysis [268].

Whichever diffusivity one uses, the vWW solubility results extrapolate to 10^{-10} molecules per cubic centimetre at room temperature under 1 bar of H_2 and so there should be no hydrogen whatsoever within the bulk. Other measurements have found agreement with a very low value , with the highest at only a few hundred hydrogen atoms per cubic centimetre at room temperature [206, 269, 270]. Using any one of these solubilities does not alter the permeation values in Table V by a more than a factor of two or three.

Standard semiconductor processing, such as mechanical polishing, HF etching, plasma treatments etc, can result in far higher levels of hydrogen close to the surface [262]. Several studies have found values as high as 10^{18} molecules per cubic centimetre and drops significantly after a depth of one micron[271]. This concentration will lead to outgassing rates of $10^{-7}\,\mathrm{mbar\,l\,s^{-1}cm^{-2}}$, using Equation 12 and the vWW diffusivity scaling law, but can be completely degassed to below $10^{-30}\,\mathrm{mbar\,l\,s^{-1}cm^{-2}}$ within an hour under vacuum as shown in Figure 9, limited by surface recombination. Moreover, surface oxides and nitrides act as efficient permeation barriers [240–242]. Hydrogen bound on the silicon surface has very high desorption energy [272, 273] (above 1.8 eV) such that the desorption rate from one monolayer coverage would be below $10^{-22}\,\mathrm{mbar\,l\,s^{-1}cm^{-2}}$ using Equation 11. Thermal desorption studies [273] show that most hydrogen complexes can be desorbed from silicon by annealing at 600°C.

Hickmott [274] studied the interaction between hydrogen and glass and found that the hot filament of the ionization gauge had a detrimental effect on determining the residual gas content at UHV. He noted that hydrogen was desorbed at the two distinct activation energies of 0.29 eV and 1.08 eV. The former is so low that it will desorb completely at room temperature under vacuum, whereas the latter requires baking above 400°C. Spectroscopic studies by Hickmott showed that after a high temperature bake the main residual gases were water and carbon monoxide. Todd [275] measured the residual water composition in a variety of glasses and found negligible outgassing ($\sim 10^{-23}\,\mathrm{mbar\,l\,s^{-1}cm^{-2}}$) in AS glass after high temperature baking. This low outgassing rate is due to the strong Si-H and Si-OH bonds. Using the values from Table V and Equation 12 to calculate the lowest hydrogen outgassing rate from AS glass, as shown in Table VII, we find remarkable agreement between the theoretical value of just over $10^{-17}\,\mathrm{mbar\,l\,s^{-1}cm^{-2}}$ and experimental result [276, 277] of just below [278] $10^{-16}\,\mathrm{mbar\,l\,s^{-1}cm^{-2}}$.

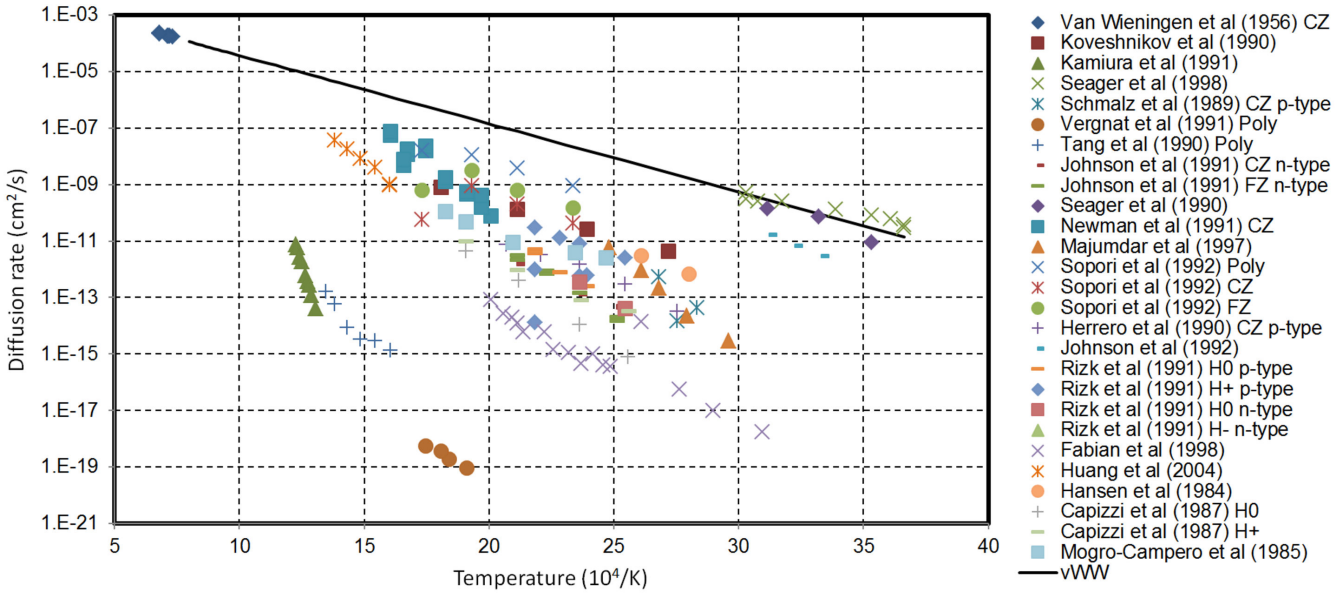

FIG. 8. The large scatter in data for diffusion of hydrogen through silicon [193, 243–261]. We have only plotted data for hydrogen diffusion (no isotopes) and have indicated the type of silicon where known. The solid black line is the commonly quoted vWW diffusion rate.

Noble gases

Noble gases cannot be removed once the MicroMOTs are sealed and so must be *completely* degassed from all components before bonding. As discussed in Section V B negligible levels of noble gases, specifically helium, should be found in silicon unless additional data corroborates a recent study [207]. Noble gases in glasses are expected to reach concentrations of 10 ppb when exposed to atmosphere, which will outgas from the bulk diffusively. Figure 10 shows the results of degassing AS glass using Equation 12, and we see that a thin slab can be completely degassed easily. This would scale proportionally to the area when wafer level degassing is required.

The last materials in our chips are metals such as gold for the atom chip and those for the NEG. Noble gases do not permeate most metals and so one should be able to ignore these materials, however the method of their deposition is important: Sputtered thin films have been found to incorporate large quantities of argon, as this process gas is used to remove the metal atoms from the sputter target. The argon is then buried in the growing thin film and permeates to the surface along dislocations and pores, as well as via self-diffusion. Where possible films should be deposited by vacuum arc deposition [156] or e-beam evaporation which do not require additional gases. In situations where sputtering is unavoidable several modifications can be made to reduce contamination by this gas source including [165, 166]: increasing the sputter gas pressure [279] , increasing the substrate temperature, reducing the deposition rate, post annealing, and finally changing to a heavier gas. Using this last modification by replacing argon with krypton has been shown to reduce the gas incorporation by a factor of 10^3 or even lower, but moving to xenon shows little improvement [166]. Measurements of Ti-Zr-V NEG films have detected krypton outgassing rates [280] at the sensitivity limit of the detector - down to 10^{-19} mbar l s^{-1}cm^{-2} after several activations - which is still too high for our device, but this could be further reduced with higher temperature anneals.

Carbon monoxide

Carbon monoxide is the second most significant gas at UHV. Due to its relatively large size (compared to helium or hydrogen) diffusion through the bulk will be negligible and so carbon monoxide is largely a surface outgassing species [281]. Studies looking at the residual gases in glass have shown that the carbon monoxide concentrations vary widely [282] and it is difficult to obtain repeatable results. In addition, this also depends on glass type, processing history, and the effects of ionization cathodes. We do not know the desorption energy for carbon monoxide on glass, but due to the latter's low reactivity we expect carbon monoxide to only be physisorbed and so quickly degassed. Similar conclusions have been noted in photodesorption measurements [283]. One study looking at the effect of breaking glass substrates in vacuum found that the carbon monoxide level remained constant, but carbon dioxide quickly decreased [284]. This was attributed to the reaction with residual hydrogen forming methane, which was seen to increase.

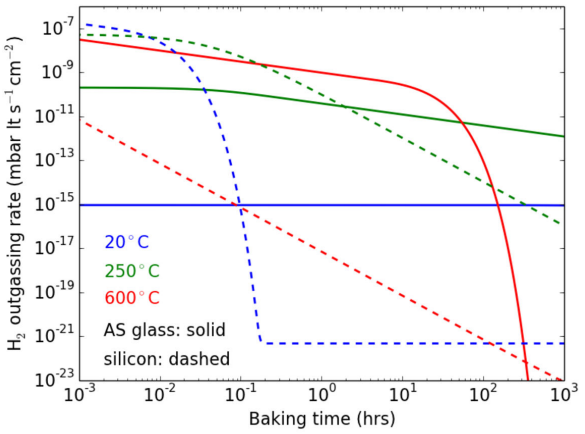

FIG. 9. The theoretical outgassing rate of hydrogen for 1 mm thick silicon (dashed line) and AS glass (solid line) for three baking temperatures. We have assumed AS glass is diffusion limited and calculated the rate using Equation 12 and values from Table V after exposure to 1 bar hydrogen (i.e. immersion into water). We have calculated the rate for silicon using a summation of diffusion (Equation 12) from the bulk as well as considering the higher concentration at the surface (see text), and also recombination-limited surface desorption using Equation 11 ($k = 2$) with values from Gupta et al [273]. The room temperature silicon outgassing shows an initially high rate due to diffusion of the high concentration near the surface and is eventually limited by surface desorption of the dihydride surface species (as are the higher temperature bakes).

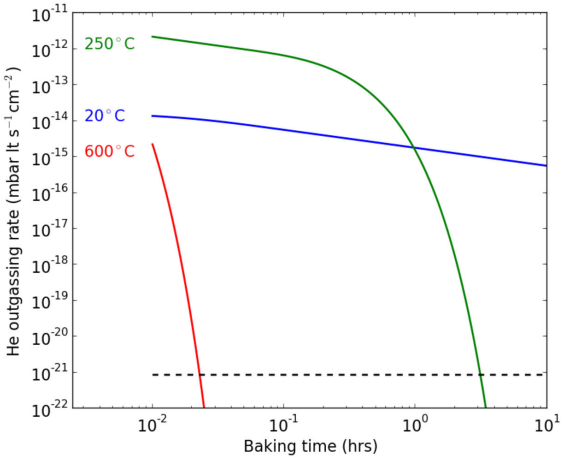

FIG. 10. The He outgassing rate from 1 mm thick aluminosilicate glass slab at various temperatures after storage in atmosphere (5 ppm He content), calculated with Equation 12. The black dashed line indicates the target outgassing rate.

A careful study [285] avoiding the effects of gauges measured carbon monoxide outgassing rates from stainless steel less than 6×10^{-17} mbar l s^{-1}cm^{-2}, three orders of magnitude less than hydrogen.

Thermal desorption studies of carbon monoxide released from silicon surfaces are few, but show that the thermal desorption energy is below 0.5 eV [286] and so should be degassed easily. Photodesorption and plasma cleaning have also been shown to efficiently remove carbon and oxygen contamination from silicon surfaces.

Other gases

Methane is commonly found in UHV environments is not pumped by Ti-Zr-V getters at room temperature. It is thought to be produced from reactions on the high temperature electrodes of ionization gauges, so should not be an issue in our gauge-less MicroMOTs. It may also be formed from reactions between carbon monoxide and hydrogen during their diffusion on NEG or glass surfaces [284], as mentioned before. A desorption rate of 10^{-14} mbar lt s^{-1}cm^{-2} of methane was measured by Setina et al [287] from Ti-Zr-V-Fe getter strips which would be a serious vacuum risk in the MicroMOTs, however one would expect the methane production rate to be related to the partial pressures of H_2 and CO which was not seen in other studies [288] below 10^{-8} mbar. Therefore, methane should be completely evacuated before the MicroMOT is sealed, otherwise one must use reactive getters, or briefly elevate the NEG temperature to achieve some pumping. Other organic species have been found in encapsulated MEMs-type devices which are likely due to insufficent cleaning or residual gases prior to sealing [132, 289].

Should anodic bonding be used to seal the chips, oxygen will be released along the inner bonding edges where the voltage is high and no silicon exists to bond with the non-bridging oxygen atoms [181, 221, 290]. Predicting the amount of oxygen released is unreliable due to the lack of data and the effects of bonding parameters, chip dimensions, and increased outgassing at raised temperatures. However, by analyzing the few studies on this subject [221, 290, 291] we estimate 10^{13} to 10^{14} molecules per millimetre inner bonding circumference. For our MicroMOT design this can lead to a monolayer coverage of oxygen on the NEGs and result in saturation. It should be noted that oxygen penetrates the NEG surface resulting in a capacity of about five monolayers [157]. Therefore it is important to maintain the chip at high temperatures after bonding to absorb the oxidized NEG layers into the bulk. Once rubidium is released into the chip it will quickly oxidize with any remaining oxygen forming Rb_2O, which also reacts exothermically with water and hydrogen forming stable hydroxides and hydrides which do not contaminate vacuum.

E. Vacuum discussion

We have identified all the main sources of residual gases which could threaten our sealed UHV environment. We

TABLE VII. Lowest and typical room temperature outgassing rates for 2mm thick materials. The theoretical values (Th.) have been estimated using Equation 12 and Figure 9 with a 10 hr 250°C vacuum bake for 'typical outgassing' and an additional 1 hr 600°C vacuum bake for 'lowest outgassing'.

Outgassing rate ($\mathrm{mbar\,l\,s^{-1}cm^{-2}}$)	Lowest	Typical
Silicon[a]	10^{-30} (Th.)	10^{-24} (Th.)
Aluminosilicate	10^{-17}	10^{-16} (Th.[b])
Pyrex	10^{-14}	10^{-10}
Stainless steel	10^{-15}[c]	10^{-12}

[a] Theoretical values taken from Figure 9.
[b] Using values from Table V
[c] Thinner materials have lower outgassing rates and Nemanič et al [298] have demonstrated 10^{-17} with 150 μm foil.

have seen that helium permeation through glass can be reduced to a negligible level with the use of aluminosilicates and could further be improved with optical coatings such as graphene [191]. Leaking through bonds must be several orders of magnitude lower than has been measured, but can be sufficiently improved by incorporating a 'moat' within the bonding seam. We also note that leakage can be further reduced by coating the inner edges of bonding seams with NEG films and by applying a barrier coating on the outer edges of the device. Several bonding techniques are available and we highlight eutectic and direct bonding as the most suitable methods due to their low outgassing and high hermeticity, with anodic bonding as a suitable and simpler alternative if the oxygen released during bonding can be pumped away. Lowering the temperatures of these bonding techniques should be investigated as they can reduce the outgassing limitations by two or three orders of magnitude [219, 223, 224, 228, 292–297].

The greatest hurdle we are left with is to reduce outgassing. This can be tackled in two ways: 1) improve the pumping rate and capacity of the getter films, and 2) reduce the outgassing rate by extensive degassing procedures and careful choice of materials.

It has been shown that the pumping rate of NEGs is difficult to improve even with reactive lithium getters, however the latter retains a constant pumping rate irrespective of its history. NEGs are more straightforward to deposit, can be used to coat surfaces to reduce outgassing and are stable in air. Reactive getters need to be deposited under vacuum and could result in unwanted coating on components in the chamber. However, they have far higher capacities and can pump gases such as methane, which NEGs cannot. Therefore we see a combination of NEGs and reactive getters as a good compromise with the former activated during bonding and the latter activated after bonding.

For the second method to tackle outgassing we have seen in Table VII that at room temperature the materials we have chosen for the device are more than adequate once degassed to achieve the room temperature (hydrogen) outgassing rate of $10^{-12}\,\mathrm{mbar\,l\,s^{-1}cm^{-2}}$ (Equation 8). When we consider the outgassing with a bonding process at around 400°C during which outgassing can increase by eight orders of magnitude and put stricter room temperature rates of less than $10^{-16}\,\mathrm{mbar\,l\,s^{-1}cm^{-2}}$ (Equation 14) for bulk gettered gases such as hydrogen, $10^{-18}\,\mathrm{mbar\,l\,s^{-1}cm^{-2}}$ for surface gettered gases such as carbon monoxide, and less than $10^{-21}\,\mathrm{mbar\,l\,s^{-1}cm^{-2}}$ for non-gettered noble gases. We can see in Table VII that silicon outgassing is likely to be negligible compared to AS glass whose rate matches our target. When calculating this latter value we assumed a diffusion energy of 0.9 eV. We can now be confident that AS glass will be the major source of hydrogen so if we use a more realistic value of 0.79 eV (Table V) we lower our target to $10^{-15}\,\mathrm{mbar\,l\,s^{-1}cm^{-2}}$, which is certainly achievable. Carbon monoxide outgassing is difficult to predict but we expect it to be far lower than hydrogen, as found in stainless steel [285]. We have seen that noble gases may be sufficiently removed from the chamber material with realistic baking parameters and by using the separated wafer fabrication method shown in Figure 4, one can ensure the optimum baking regime for each material.

VI. PROTOTYPE MICROMOT

We are now at the stage where a prototype MicroMOT can be designed to provide realistic values from which we can estimate the vacuum performance and lifetime. We are currently in the process of fabricating these devices based on the following design which we will characterize and present detailed processes at a later date. We have consciously avoided designing the MicroMOT around a single application or manipulation technique, e.g. free-falling atom interferometers, or BECs on atom chips. This is because the MicroMOT will likely need to be adapted for the specific task, so we have chosen a simple generic design to demonstrate what is possible.

As discussed in Section II we assume a G-MOT type geometry using a 10 mm diameter grating structure and a cavity volume of $15\times15\times3\,\mathrm{mm}^3$ to avoid light scattering off sidewalls. Around 90% of the beam overlap volume is within 2.5 mm of the grating surface, and so this is a reasonable choice of height and is also feasible to fabricate from silicon using deep reactive ion etching, wet etching, machining, or powder blasting [299]. The chip is formed of four chambers: a large science chamber for cooling and manipulating the atoms, an atom source chamber in which to hold the alkali dispensers, an alkali getter/LIAD/peltier chamber, and a reactive getter chamber. The source chamber is connected to the science chamber by a very thin channel to restrict the vapour flow. The top 2 mm thick capping wafer is anti-reflection coated and is anodically or direct bonded to the silicon 'cavity wafer'. The thickness of the glass layer is determined by several factors including the permeation rates, bondability, structural integrity and price. This

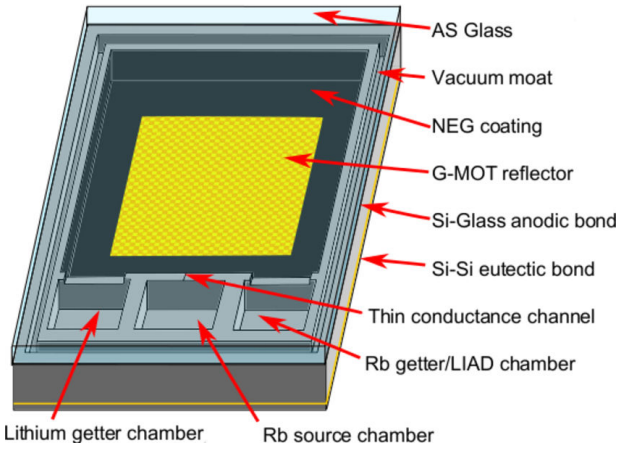

FIG. 11. Prototype design of a miniaturized magneto-optical trap incorporating all the elements discussed in the text. Dimensions are $20\times24\times5\,\mathrm{mm}^3$.

wafer incorporates a moat within the bonding region on both sides to reduce argon leakage. The reflector layer is coated by a thin alumina layer to prevent alkali corrosion of the gold and is eutectically bonded to the cavity wafer. Future designs will include atom chip wires and electrical feedthroughs forming this chamber wall. We have not shown the quadrupole magnetic field coils as these are trivial to implement and may simply be bonded, or deposited, onto the top and bottom external surfaces, or could be approximated with a double loop on single surface [300].

Following extensive cleaning and baking procedures, the glass and silicon wafers are first bonded in vacuum so that the oxygen released during anodic bonding can be removed without saturating the NEG. An NEG thin film is sputtered on the internal sidewalls and onto some of the bottom layer (with the reflector masked off) to provide the largest NEG area and reduce outgassing. The remaining reflector layer is then eutectically bonded under UHV after high temperature baking to desorb hydrogen, carbon monoxide and noble gases.

Table VIII provides a detailed summary of dimensions and an estimation on the vacuum properties of the device using values calculated in this study. We can see that the lifetime of the device is determined by the argon leakage, but is nearly an order of magnitude greater than our target. The extremely low outgassing rate of AS glass results in negligible outgassing after bonding such that the base pressure is in the XHV regime for an essentially unlimited lifetime. Practically, the lifetime and base pressure will be determined by the atom source and the residual noble gas partial pressure in the bonding chamber which we typically achieve levels below 10^{-11} mbar.

VII. DISCUSSION AND CONCLUSIONS

We have shown that it is feasible to maintain UHV, and even XHV, environments for extended periods inside sealed chips using materials and methods borrowed from the semiconductor industry. However, it is necessary to highlight the assumptions we have made if these type of devices are to become a realistic technology. A great emphasis has been made on degassing the materials at temperatures up to 600°C to ensure a sufficiently low outgassing rate once sealed. For the bulk materials discussed this is certainly possible, but more sophisticated devices are likely to have additional components, such as micro-Peltier coolers, detectors, field emission tips (for active pumping or ionization), or even light sources (such as UV LEDs for LIAD), which can be sensitive to extreme temperatures. Moreover, thin films, such as gold on silicon, can diffuse at moderate temperatures if additional barrier layers are not used [218]. In these situations one must use lower temperature degassing, such as UV desorption or plasma cleaning, and also develop lower temperature bonding methods [219, 223, 224, 228, 292–297].

The very low leak rates we have predicted are possible by a combination of hermetic bonding and additional moat cavities. We have assumed that the materials to be joined are reliably homogeneous and intact (e.g. perfect crystallinity in the case of silicon) but in reality fabrication processes may lead to defects which can result in additional leakage routes such as microcracks, crystal plane dislocations, surface defects, or thin oxide films. Surface barrier films, NEG coatings and stress-relief annealing can reduce these effects but these possible sources of leakage are still worth bearing in mind.

We have used the large amount of data on hydrogen diffusion in silicon to predict that it has a very low outgassing rate. We find that this rate is consistently low whichever values we use from the literature, especially after a high temperature bake for several hours, and so we are confident in the estimate. However, as mentioned in Section V D, there is no absolutely reliable method to predict the outgassing rate from real materials and the simple diffusion-limited model is only useful to an order of magnitude at best, especially when considering the migration of reactive species such as hydrogen. This can be seen with studies looking at the outgassing of stainless steel, where the diffusion limited model produces reasonable estimate for low temperature bakes (below 300°C), but generally fails to predict the effect of very high temperatures. This is usually attributed to the effect of surface oxides which are more stable during low temperature baking and act as diffusion barriers [301]. Therefore we expect silicon to have a very low outgassing rate but probably higher than the value stated in Table VII. Experimental studies focusing specifically on outgassing are required. We have used measured values for AS glass outgassing, but glasses are notorious for producing variable results [302] so it is necessary to perform additional outgassing studies on the specific glass one uses to ensure

TABLE VIII. Expected vacuum properties of the prototype MicroMOT in atmosphere at 20°C.

Internal volume (cm^3)	0.65	including subchambers	
Surface area (cm^2)	7.8	2.6 glass	
NEG[a] area (cm^2)	3.3	all sides and some of the reflector surface	
Glass thickness (cm)	0.2		
Moat volume (cm^3)	0.03	1×0.5 mm trench within each bonding seam	
Bonder base pressure (mbar)	10^{-9}	equal H_2 and CO, negligible noble gases	
Bonding parameters	1 hr at 400°C	typical eutectic bond	
Gas source ($mbar\,l\,s^{-1}$)	Surface pumped (CO)	Bulk pumped (H_2)	Noble gas
Permeation[b]	-	1.3×10^{-23}	7.3×10^{-23}
Leakage[c]	1.9×10^{-23}	3.8×10^{-24}	2.3×10^{-22}
Outgassing[d]	4.5×10^{-17}	2.6×10^{-16}	$< 10^{-24}$
Base pressure[e] (mbar)	10^{-18}	10^{-15}	-
Lifetime (days to reach 1.5×10^{-10} mbar)	10^6	10^9	3200

[a] Surface capacity of 5×10^{14} molecules cm^{-2} and bulk capacity of 7.5×10^{16} molecules cm^{-2} (1 μm film with $x_H = 0.01$).
[b] The permeation rates are calculated using the breakthrough time from Equation 4 substituted into Equation 5.
[c] Bond leak rate (air) of 10^{-15} $mbar\,l\,s^{-1}$ for 2 bonding seams (top wafer and bottom wafer). We have assumed the carbon monoxide leak is from atmospheric carbon dioxide.
[d] As the carbon monoxide outgassing rate is unknown we have assumed a value which is ten times less than hydrogen as discussed in the text as a worst case scenario.
[e] The base noble gas pressure will be equal to the residual level in the bonding chamber.

suitability. For the sake of bevity we have limited our discussions to silicon and glasses but there are likely to be many other suitable materials, most noteably ceramics.

In conclusion, the aim of this study was to prove that Magneto-Optical Traps can be miniaturised and integrated into devices capable of leaving the laboratory. We have shown that recent advances in microfabrication techniques and materials can lead to sealed chambers with microlitre volumes that maintain UHV for at least 1000 days using only passive pumping elements. The MOT geometry can be miniaturized to use a single laser beam, patterned reflectors, planar optics, and atom source. Controlled by a number of methods including LIAD, integrated cold fingers, conductance channels and several pumping mechanisms. The main issues to maintain sealed UHV environments are the need for extremely low leakage bonds, low outgassing materials, and also negligible noble gas outgassing from chamber walls and sputtered films. We hope that this work motivates the development of ultracold quantum technology which has a vast number of practical applications and promises to be a fruitful technology in a number of fields.

ACKNOWLEDGMENTS

We would like to acknowledge Tim Freegarde, David Smith, James Gates, Peter Smith, Erling Riis, Aidan Arnold, Joe Cotter, Wolfgang Reinert, and Kai Bongs, for their helpful and insightful advice and ideas in the development of this study. This work was supported by the Royal Academy of Engineering, pdfRC, the Royal Society, and DSTL.

[1] B. Barrett, P.-A. Gominet, E. Cantin, L. Antoni-Micollier, A. Bertoldi, B. Battelier, P. Bouyer, J. Lautier, and A. Landragin, arXiv preprint arXiv:1311.7033 (2013).
[2] J. Kitching, S. Knappe, and E. A. Donley, Sensors Journal, IEEE **11**, 1749 (2011).
[3] N. Hinkley, J. A. Sherman, N. B. Phillips, M. Schioppo, N. D. Lemke, K. Beloy, M. Pizzocaro, C. W. Oates, and A. D. Ludlow, Science **341**, 1215 (2013).
[4] S. M. Dickerson, J. M. Hogan, A. Sugarbaker, D. Johnson, and M. A. Kasevich, arXiv preprint arXiv:1305.1700 (2013).
[5] B. Canuel, F. Leduc, D. Holleville, A. Gauguet, J. Fils, A. Virdis, A. Clairon, N. Dimarcq, C. J. Bordé, A. Landragin, *et al.*, Physical review letters **97**, 010402 (2006).
[6] C. J. Bordé, Metrologia **39**, 435 (2002).
[7] F. Yver-Leduc, P. Cheinet, J. Fils, A. Clairon, N. Dimarcq, D. Holleville, P. Bouyer, and A. Landragin, Journal of Optics B: Quantum and Semiclassical Optics **5**, S136 (2003).
[8] M. Edwards, Nature Physics **9**, 68 (2013).
[9] D. Budker and M. Romalis, Nature Physics **3**, 227 (2007).
[10] N. Behbood, F. Martin Ciurana, G. Colangelo, M. Napolitano, M. W. Mitchell, and R. J. Sewell, Applied Physics Letters **102**, 173504 (2013).
[11] S. Wildermuth, S. Hofferberth, I. Lesanovsky, S. Groth, P. Kruger, J. Schmiedmayer, and I. Bar-Joseph, Applied physics letters **88**, 264103 (2006).
[12] D. Oblak, P. G. Petrov, C. L. G. Alzar, W. Tittel, A. K.

Vershovski, J. K. Mikkelsen, J. L. Sørensen, and E. S. Polzik, Physical Review A **71**, 043807 (2005).
[13] M. Napolitano, M. Koschorreck, B. Dubost, N. Behbood, R. Sewell, and M. W. Mitchell, Nature **471**, 486 (2011).
[14] S. Boixo, A. Datta, M. J. Davis, S. T. Flammia, A. Shaji, and C. M. Caves, Physical review letters **101**, 040403 (2008).
[15] L. Pezzé and A. Smerzi, Physical review letters **102**, 100401 (2009).
[16] J. Appel, P. J. Windpassinger, D. Oblak, U. B. Hoff, N. Kjærgaard, and E. S. Polzik, Proceedings of the National Academy of Sciences **106**, 10960 (2009).
[17] R. Sewell, M. Koschorreck, M. Napolitano, B. Dubost, N. Behbood, and M. Mitchell, Physical review letters **109**, 253605 (2012).
[18] C. Monroe, Nature **416**, 238 (2002).
[19] A. Kozhekin, K. Mølmer, and E. Polzik, Physical Review A **62**, 033809 (2000).
[20] L.-M. Duan, M. Lukin, J. I. Cirac, and P. Zoller, Nature **414**, 413 (2001).
[21] S. Diehl, A. Micheli, A. Kantian, B. Kraus, H. Büchler, and P. Zoller, Nature Physics **4**, 878 (2008).
[22] H. Marion, F. P. Dos Santos, M. Abgrall, S. Zhang, Y. Sortais, S. Bize, I. Maksimovic, D. Calonico, J. Grünert, C. Mandache, *et al.*, Physical review letters **90**, 150801 (2003).
[23] S. Dimopoulos, P. W. Graham, J. M. Hogan, and M. A. Kasevich, Physical review letters **98**, 111102 (2007).
[24] C. J. Bordé, Philosophical Transactions of the Royal Society A: Mathematical, Physical and Engineering Sciences **363**, 2177 (2005).
[25] J. P. Dowling and G. J. Milburn, Philosophical Transactions of the Royal Society of London. Series A: Mathematical, Physical and Engineering Sciences **361**, 1655 (2003).
[26] J. Pritchard and S. Till, "UK Quantum Technology Landscape 2014,".
[27] T. Könemann, W. Brinkmann, E. Göklü, C. Lämmerzahl, H. Dittus, T. Van Zoest, E. Rasel, W. Ertmer, W. Lewoczko-Adamczyk, M. Schiemangk, *et al.*, Applied Physics B **89**, 431 (2007).
[28] R. Geiger, V. Ménoret, G. Stern, N. Zahzam, P. Cheinet, B. Battelier, A. Villing, F. Moron, M. Lours, Y. Bidel, *et al.*, Nature communications **2**, 474 (2011).
[29] T. Van Zoest, T. Müller, T. Wendrich, M. Gilowski, E. Rasel, W. Ertmer, T. Könemann, C. Lämmerzahl, H. Dittus, A. Vogel, *et al.*, International Journal of Modern Physics D **16**, 2421 (2007).
[30] S. Groth, P. Kruger, S. Wildermuth, R. Folman, T. Fernholz, J. Schmiedmayer, D. Mahalu, and I. Bar-Joseph, Applied Physics Letters **85**, 2980 (2004).
[31] J. Reichel and V. Vuletic, *Atom Chips* (John Wiley & Sons, 2010).
[32] D. Stick, W. Hensinger, S. Olmschenk, M. Madsen, K. Schwab, and C. Monroe, Nature Physics **2**, 36 (2005).
[33] M. Brownnutt, G. Wilpers, P. Gill, R. Thompson, and A. Sinclair, New Journal of Physics **8**, 232 (2006).
[34] Symmetricom SA.45 chip scale atomic clock.
[35] S. Knappe, V. Gerginov, P. Schwindt, V. Shah, H. Robinson, L. Hollberg, and J. Kitching, Optics Letters **30**, 2351 (2005).
[36] M. de Angelis, M. Angonin, Q. Beaufils, C. Becker, A. Bertoldi, K. Bongs, T. Bourdel, P. Bouyer, V. Boyer, S. Dörscher, *et al.*, Procedia Computer Science **7**, 334 (2011).
[37] S. Chu, Reviews of Modern Physics **70**, 685 (1998).
[38] K. Salit, J. Sebby-Strabley, K. Nelson, and J. Kriz, in *Frequency Control Symposium (FCS), 2012 IEEE International* (IEEE, 2012) pp. 1–4.
[39] B. Xu, X. Chen, J. Wang, and M. Zhan, Optics Communications **281**, 5819 (2008).
[40] V. Shah, M. Mescher, R. Stoner, V. Vuletic, and R. Lutwak, arXiv preprint arXiv:1111.5890 (2011).
[41] E. A. Salim, J. DeNatale, D. M. Farkas, K. M. Hudek, S. E. McBride, J. Michalchuk, R. Mihailovich, and D. Z. Anderson, Quantum Information Processing **10**, 975 (2011).
[42] R. Folman, P. Krüger, D. Cassettari, B. Hessmo, T. Maier, and J. Schmiedmayer, Physical Review Letters **84**, 4749 (2000).
[43] S. Wildermuth, P. Krüger, C. Becker, M. Brajdic, S. Haupt, A. Kasper, R. Folman, and J. Schmiedmayer, Physical Review A **69**, 030901 (2004).
[44] K. Lee, J. Kim, H. Noh, and W. Jhe, Optics letters **21**, 1177 (1996).
[45] J. Arlt, O. Marago, S. Webster, S. Hopkins, and C. Foot, Optics communications **157**, 303 (1998).
[46] M. Vangeleyn, P. F. Griffin, E. Riis, and A. S. Arnold, Optics express **17**, 13601 (2009).
[47] M. Trupke, F. Ramirez-Martinez, E. Curtis, J. Ashmore, S. Eriksson, E. Hinds, Z. Moktadir, C. Gollasch, M. Kraft, G. Vijaya Prakash, *et al.*, Applied physics letters **88**, 071116 (2006).
[48] S. Pollock, J. Cotter, A. Laliotis, and E. Hinds, Optics Express **17**, 14109 (2009).
[49] S. Pollock, J. Cotter, A. Laliotis, F. Ramirez-Martinez, and E. Hinds, New Journal of Physics **13**, 043029 (2011).
[50] This can be mitigated with background free imaging [303].
[51] C. Nshii, M. Vangeleyn, J. Cotter, P. Griffin, E. Hinds, C. Ironside, P. See, A. Sinclair, E. Riis, and A. Arnold, Nature nanotechnology (2013).
[52] J. Lee, J. Grover, L. Orozco, and S. Rolston, JOSA B **30**, 2869 (2013).
[53] E. Riis, J. McGilligan, and A. Arnold, in *ICAP 2014 Proceedings* (2014) pp. Tues–058.
[54] Q. Bodart, S. Merlet, N. Malossi, F. P. Dos Santos, P. Bouyer, and A. Landragin, Applied Physics Letters **96**, 134101 (2010).
[55] M. A. Perez, U. Nguyen, S. Knappe, E. A. Donley, J. Kitching, and A. M. Shkel, Sensors and Actuators A: Physical **154**, 295 (2009).
[56] G. W. Hoth, E. A. Donley, and J. Kitching, Optics Letters **38**, 661 (2013).
[57] Several studies have shown the scaling laws for various beam overlap volumes, however we highlight that none have considered the effect of unsymmetrical volumes for which reducing one dimension could be beneficial in wafer-level microfabrication by reducing chamber size whilst maintaining a large capture volume.
[58] L. Huet, M. Ammar, E. Morvan, N. Sarazin, J.-P. Pocholle, J. Reichel, C. Guerlin, and S. Schwartz, in *International Quantum Electronics Conference* (Optical Society of America, 2011) p. I1188.
[59] A. V. Rakholia, H. J. McGuinness, and G. W. Bieder-

mann, arXiv preprint arXiv:1407.3847 (2014).
[60] T. Kovachy, J. M. Hogan, D. M. Johnson, and M. A. Kasevich, Physical Review A **82**, 013638 (2010).
[61] A. Sahm, C. Fiebig, S. Spiesberger, M. Schiemangk, E. Luvsandamdin, K. Paschke, G. Erbert, and G. Trankle, in *Electronic Components and Technology Conference (ECTC), 2012 IEEE 62nd* (IEEE, 2012) pp. 1852–1857.
[62] C. Grzeschik, M. Schiemangk, K. Lampmann, M. Krutzik, and A. Peters, in *CLEO: Science and Innovations* (Optical Society of America, 2013) pp. CM1N–6.
[63] S. Spießberger, M. Schiemangk, A. Sahm, A. Wicht, H. Wenzel, A. Peters, G. Erbert, and G. Tränkle, Optics express **19**, 7077 (2011).
[64] K. Numata, M. Alalusi, L. Stolpner, G. Margaritis, J. Camp, and M. Krainak, Optics letters **39**, 2101 (2014).
[65] S. Lynch, F. Chen, J. Gates, C. Holmes, S. Staines, S. James, J. Hodgkinson, P. Smith, and R. Tatam, in *SPIE OPTO* (International Society for Optics and Photonics, 2014) pp. 900209–900209.
[66] K. Numata, J. Camp, M. A. Krainak, and L. Stolpner, Optics express **18**, 22781 (2010).
[67] T. Lévèque, L. Antoni-Micollier, B. Faure, and J. Berthon, Applied Physics B , 1 (2013).
[68] G. T. Reed, G. Mashanovich, F. Gardes, and D. Thomson, Nature photonics **4**, 518 (2010).
[69] Y. Shoji and T. Mizumoto, Science and Technology of Advanced Materials **15**, 014602 (2014).
[70] S. Sheard, T. Suhara, and H. Nishihara, Lightwave Technology, Journal of **11**, 1400 (1993).
[71] K. Mehta, A. Eltony, I. Chuang, and R. Ram, in *ICAP 2014 Proceedings* (2014) pp. Tues–077.
[72] R. Shechter, Y. Amitai, and A. A. Friesem, Applied optics **41**, 1236 (2002).
[73] O. Alloschery, R. Mathevet, J. Weiner, and H. Lezec, Optics express **14**, 12568 (2006).
[74] E. W. Streed, B. G. Norton, A. Jechow, T. J. Weinhold, and D. Kielpinski, Physical review letters **106**, 010502 (2011).
[75] J. T. Merrill, C. Volin, D. Landgren, J. M. Amini, K. Wright, S. C. Doret, C. Pai, H. Hayden, T. Killian, D. Faircloth, *et al.*, New Journal of Physics **13**, 103005 (2011).
[76] M. Trupke, J. Goldwin, B. Darquié, G. Dutier, S. Eriksson, J. Ashmore, and E. Hinds, Physical review letters **99**, 063601 (2007).
[77] E. Vetsch, D. Reitz, G. Sagué, R. Schmidt, S. Dawkins, and A. Rauschenbeutel, Physical review letters **104**, 203603 (2010).
[78] G. Brambilla, F. Xu, P. Horak, Y. Jung, F. Koizumi, N. P. Sessions, E. Koukharenko, X. Feng, G. S. Murugan, J. S. Wilkinson, *et al.*, Advances in Optics and Photonics **1**, 107 (2009).
[79] K. Sakmann and M. Kasevich, Opt. Lett. **39**, 5317 (2014).
[80] S. A. Knappe, H. G. Robinson, and L. Hollberg, Optics express **15**, 6293 (2007).
[81] W. Yang, D. B. Conkey, B. Wu, D. Yin, A. R. Hawkins, and H. Schmidt, Nature Photonics **1**, 331 (2007).
[82] S. Spillane, G. Pati, K. Salit, M. Hall, P. Kumar, R. Beausoleil, and M. Shahriar, Physical review letters **100**, 233602 (2008).
[83] A. Sargsyan, D. Sarkisyan, A. Papoyan, Y. Pashayan-Leroy, P. Moroshkin, A. Weis, A. Khanbekyan, E. Mariotti, and L. Moi, Laser Physics **18**, 749 (2008).
[84] W. D. Phillips and H. Metcalf, Physical Review Letters **48**, 596 (1982).
[85] W. D. Phillips, J. V. Prodan, and H. J. Metcalf, JOSA B **2**, 1751 (1985).
[86] T. Liebisch, E. Blanshan, E. Donley, and J. Kitching, Physical Review A **85**, 013407 (2012).
[87] T. Arpornthip, C. Sackett, and K. Hughes, Physical Review A **85**, 033420 (2012).
[88] P. Berthoud, A. Joyet, G. Dudle, N. Sagna, and P. Thomann, EPL (Europhysics Letters) **41**, 141 (1998).
[89] D. A. Steck, "Rubidium 87 D line data," (2001).
[90] L.-A. Liew, S. Knappe, J. Moreland, H. Robinson, L. Hollberg, and J. Kitching, Applied Physics Letters **84**, 2694 (2004).
[91] F. Vecchio, V. Venkatraman, H. Shea, T. Maeder, and P. Ryser, Procedia Engineering **5**, 367 (2010).
[92] S. Radhakrishnan and A. Lal, in *Solid-State Sensors, Actuators and Microsystems, 2005. Digest of Technical Papers. TRANSDUCERS'05. The 13th International Conference on*, Vol. 1 (IEEE, 2005) pp. 23–26.
[93] L.-A. Liew, J. Moreland, and V. Gerginov, Applied physics letters **90**, 114106 (2007).
[94] F. Gong, Y.-Y. Jau, K. Jensen, and W. Happer, Review of scientific instruments **77**, 076101 (2006).
[95] S. Bartalini, I. Herrera, L. Consolino, L. Pappalardo, N. Marino, G. D'Arrigo, and F. Cataliotti, The European Physical Journal D-Atomic, Molecular, Optical and Plasma Physics **36**, 101 (2005).
[96] Www.alvatec.com.
[97] P. Griffin, K. Weatherill, and C. Adams, Review of scientific instruments **76**, 093102 (2005).
[98] A. Douahi, L. Nieradko, J. Beugnot, J. Dziuban, H. Maillote, S. Guerandel, M. Moraja, C. Gorecki, and V. Giordano, Electronics Letters **43**, 33 (2007).
[99] Integrating high power focused beams into a chip scale system would not be trivial and the beam must be moved once sections of the dispenser are depleted. An alternative heating method could include induction heating.
[100] M. Stephens, R. Rhodes, and C. Wieman, Journal of applied physics **76**, 3479 (1994).
[101] In that study they found that Pyrex took an order of magnitude longer to cure than sapphire. The glass used in this study is likely to have properties in between these materials.
[102] The effect of hard optical coatings on the glass, such as MgF_2 to reduce reflections or ITO for heating, may also reduce the effectiveness of glass as a pump.
[103] H. Bottner, in *Thermoelectrics, 2002. Proceedings ICT'02. Twenty-First International Conference on* (IEEE, 2002) pp. 511–518.
[104] D. R. Scherer, D. B. Fenner, and J. M. Hensley, Journal of Vacuum Science & Technology A: Vacuum, Surfaces, and Films **30**, 061602 (2012).
[105] P. della Porta, C. Emili, and J. Hellier, in *IEEE Conference on tube techniques* (IEEE, 1968).
[106] Scherer et a l[104] state that NEGs do not pump rubidium at all, whereas della Porta et al [105] state that alkali atoms do not affect the pumping speed for other gases. We suspect there is some pumping due to the high reactivity of alkali atoms with metals and with most ad-

sorbed gases.
[107] A. Pelton, Bulletin of Alloy Phase Diagrams **7**, 139 (1986).
[108] M. B. Squires, *High repetition rate Bose-Einstein condensate production in a compact, transportable vacuum system*, Ph.D. thesis, University of Colorado (2008).
[109] N. Bhaskar and C. Kahla, Ultrasonics, Ferroelectrics and Frequency Control, IEEE Transactions on **37**, 355 (1990).
[110] P. V. Medeiros, F. de Brito Mota, A. J. Mascarenhas, and C. M. de Castilho, Nanotechnology **21**, 115701 (2010).
[111] M. Caragiu and S. Finberg, Journal of Physics: Condensed Matter **17**, R995 (2005).
[112] L. Torralbo-Campo, G. D. Bruce, G. Smirne, and D. Cassettari, arXiv preprint arXiv:1312.6442 (2013).
[113] A. Hatakeyama, M. Wilde, and K. Fukutani, arXiv preprint cond-mat/0512451 (2005).
[114] K. Rębilas and M. J. Kasprowicz, Physical Review A **79**, 042903 (2009).
[115] S. Villalba, H. Failache, and A. Lezama, Physical Review A **82**, 56902 (2010).
[116] S. Atutov, R. Calabrese, V. Guidi, B. Mai, A. Rudavets, E. Scansani, L. Tomassetti, V. Biancalana, A. Burchianti, C. Marinelli, *et al.*, Physical Review A **67**, 053401 (2003).
[117] B. Anderson and M. Kasevich, Physical Review A **63**, 023404 (2001).
[118] D. Xiong, F. Wang, X. Li, T.-F. Lam, and D. Wang, arXiv preprint arXiv:1303.0333 (2013).
[119] S. Du, M. B. Squires, Y. Imai, L. Czaia, R. Saravanan, V. Bright, J. Reichel, T. Hänsch, and D. Z. Anderson, Physical Review A **70**, 053606 (2004).
[120] A. Burchianti, C. Marinelli, A. Bogi, J. Brewer, K. Rubahn, H.-G. Rubahn, F. Della Valle, E. Mariotti, V. Biancalana, S. Veronesi, *et al.*, EPL (Europhysics Letters) **67**, 983 (2004).
[121] S. Villalba, H. Failache, and A. Lezama, Physical Review A **81**, 032901 (2010).
[122] A. Pelton, Journal of Phase Equilibria **7**, 228 (1986).
[123] J. Sangster and A. Pelton, Journal of phase equilibria **12**, 447 (1991).
[124] A. Pelton, Bulletin of Alloy Phase Diagrams **7**, 136 (1986).
[125] J. Sangster and A. Pelton, Journal of phase equilibria **12**, 451 (1991).
[126] A. Pelton, Journal of Phase Equilibria **7**, 23 (1986).
[127] A. Petric and A. Pelton, Journal of phase equilibria **12**, 29 (1991).
[128] A. Pelton and A. Petric, Journal of phase equilibria **14**, 368 (1993).
[129] A. Pelton, Bulletin of Alloy Phase Diagrams **7**, 19 (1986).
[130] J. Sangster and A. Pelton, Journal of phase equilibria **12**, 443 (1991).
[131] J. F. O'Hanlon, *A user's guide to vacuum technology* (John Wiley & Sons, 2005).
[132] V. Lindroos, M. Tilli, A. Lehto, and T. Motooka, *Handbook of silicon based MEMS materials and technologies* (Elsevier, 2009).
[133] W. Choi, B. Ju, Y. Lee, S. Jeong, N. Lee, M. Sung, and M. Oh, Journal of The Electrochemical Society **146**, 400 (1999).
[134] B. Erjavec, Vacuum **64**, 15 (2001).
[135] P. Willems and K. Libbrecht, Physical Review A **51**, 1403 (1995).
[136] A. Roth, *Vacuum sealing techniques* (Springer, 1994).
[137] The lowest outgassing rates for metals are tabulated by Redhead [277] with high temperature annealed stainless steel and OFHC copper displaying outgassing rates between 10^{-15} and $10^{-16}\,\mathrm{mbar\,l\,s^{-1}cm^{-2}}$.
[138] W. Perkins, Journal of Vacuum Science and Technology **10**, 543 (1973).
[139] S.-w. Zhang, Z.-j. Zhang, C.-h. XU, and L. Wang, Journal of Northeastern University (Natural Science) **8**, 027 (2008).
[140] To be more precise, the authors cannot find absolute leak rate of these seals in the literature and commercial glass-metal, or glass-ceramic, seals only state leak rates 'below $10^{-10}\,\mathrm{mbar\,l\,s^{-1}}$'. However, our discussions with commercial vacuum tube manufacturers indicate that the leak rate for metal-ceramic seals could be as low as $10^{-18}\,\mathrm{mbar\,l\,s^{-1}}$ or lower.
[141] H.-C. Chuang and C.-S. Huang, Review of Scientific Instruments **85**, 053107 (2014).
[142] K. E. Petersen, Proceedings of the IEEE **70**, 420 (1982).
[143] Http://www.silcotek.com/silcod-technologies/SilcoGuard-high-purity-coating/.
[144] C. Dedman, K. Baldwin, and M. Colla, Review of Scientific Instruments **72**, 4055 (2001).
[145] A. Besharatian, K. Kumar, R. L. Peterson, L. P. Bernal, and K. Najafi, in *Micro Electro Mechanical Systems (MEMS), 2012 IEEE 25th International Conference on* (IEEE, 2012) pp. 1001–1004.
[146] H. Zhou, H. Li, V. Sharma, and M. Schmidt, in *Micro Electro Mechanical Systems (MEMS), 2011 IEEE 24th International Conference on* (IEEE, 2011) pp. 1095–1098.
[147] S. An, N. K. Gupta, and Y. B. Gianchandani, (2014).
[148] W. Yang, "Radially staged microscale turbomolecular pump," (2007), uS Patent App. 11/859,682.
[149] V. Jayanty, *Miniaturized electron-impact-ionization pumps using double-gated isolated vertically aligned carbon nanotube arrays*, Ph.D. thesis, Massachusetts Institute of Technology (2012).
[150] S. R. Green, R. Malhotra, and Y. B. Gianchandani, Microelectromechanical Systems, Journal of **22**, 309 (2013).
[151] D. Jang *et al.*, *Carbon nanotube-based field ionization vacuum*, Ph.D. thesis, Massachusetts Institute of Technology (2012).
[152] D. Laser and J. Santiago, Journal of micromechanics and microengineering **14**, R35 (2004).
[153] A. Górecka-Drzazga, Vacuum **83**, 1419 (2009).
[154] For a more detailed up to date sub-division of getter types see Chuntonov et al [169].
[155] C. Benvenuti, J. Cazeneuve, P. Chiggiato, F. Cicoira, A. Escudeiro Santana, V. Johanek, V. Ruzinov, and J. Fraxedas, Vacuum **53**, 219 (1999).
[156] R. Sharma, N. Mithal, K. Bhushan, D. Srivastava, H. Prabhakara, S. Gadkari, J. Yakhmi, V. Sahni, *et al.*, in *Journal of Physics: Conference Series*, Vol. 114 (IOP Publishing, 2008) p. 012050.
[157] P. Chiggiato and P. Costa Pinto, Thin Solid Films **515**, 382 (2006).
[158] M. Bender, H. Kollmus, M. Bellachioma, and W. Assmann, Nuclear Instruments and Methods in Physics Research Section B: Beam Interactions with Materials and

Atoms **268**, 1986 (2010).
[159] K. Jousten, *Handbook of vacuum technology* (John Wiley & Sons, 2008).
[160] C. Benvenuti, P. Chiggiato, F. Cicoira, and V. Ruzinov, Vacuum **50**, 57 (1998).
[161] A. Prodromides, C. Scheuerlein, and M. Taborelli, Vacuum **60**, 35 (2001).
[162] C. Benvenuti, A. Escudeiro Santana, and V. Ruzinov, Vacuum **60**, 279 (2001).
[163] A. Prodromides and F. Lévy, *Non-Evaporable Getter Thin Film Coatings for Vacuum Applications*, Tech. Rep. (CERN, 2002).
[164] *SAES getters* and *Nanogetters*.
[165] S. Amorosi, M. Anderle, C. Benvenuti, S. Calatroni, J. Carver, P. Chiggiato, H. Neupert, and W. Vollenberg, Vacuum **60**, 89 (2001).
[166] B. Window, Journal of Vacuum Science & Technology A: Vacuum, Surfaces, and Films **11**, 1522 (1993).
[167] V. Chidambaram, X. Ling, and C. Bangtao, Journal of electronic materials **42**, 485 (2013).
[168] C. Liu, L. Shi, S. Xu, Z. Zhou, S. Luo, and X. Long, Vacuum **75**, 71 (2004).
[169] K. A Chuntonov and S. P Yatsenko, Recent Patents on Materials Science **6**, 29 (2013).
[170] K. Chuntonov and J. Setina, Journal of Alloys and Compounds **455**, 489 (2008).
[171] K. Chuntonov, A. Ivanov, and D. Permikin, Journal of Alloys and Compounds **456**, 187 (2008).
[172] K. Chuntonov, J. Setina, A. Ivanov, and D. Permikin, Journal of Alloys and Compounds **460**, 357 (2008).
[173] K. Chuntonov, A. Ivanov, and D. Permikin, Journal of Alloys and Compounds **471**, 211 (2009).
[174] J. Sangster and A. Pelton, Journal of phase equilibria **15**, 87 (1994).
[175] One could consider using lithium as the trapped species instead.
[176] J. F. Shackelford, P. L. Studt, and R. M. Fulrath, Journal of Applied Physics **43**, 1619 (1972).
[177] A common value quoted in the literature is the 'characteristic time' $t_c = \frac{d^2}{6D}$, this is time it takes to produce a constant flow, not for the gas to initially break through and so overestimates the time it take for the permeating gas to effect the vacuum.
[178] W. Rogers, R. Buritz, and D. Alpert, Journal of Applied Physics **25**, 868 (1954).
[179] V. Altemose, Journal of Applied Physics **32**, 1309 (1961).
[180] J. Covino and J. M. Bennett, *Laser-Gyro Materials Studies*, Tech. Rep. (DTIC Document, 1986).
[181] K. Knowles and A. Van Helvoort, International materials reviews **51**, 273 (2006).
[182] J. Shelby and R. J. Eagan, Journal of the American Ceramic Society **59**, 420 (1976).
[183] G. Wallis and D. I. Pomerantz, Journal of Applied Physics **40**, 3946 (1969).
[184] P. Baine, L. Quinn, B. Lee, S. Mitchell, B. Armstrong, and H. Gamble, Thin solid films **296**, 141 (1997).
[185] L. Spangler and K. Wise, in *Solid-State Sensor and Actuator Workshop, 1988. Technical Digest., IEEE* (IEEE, 1988) pp. 140–143.
[186] P. M. Sarro, Sensors and Actuators A: Physical **82**, 210 (2000).
[187] P. Jung, Journal of nuclear materials **191**, 377 (1992).
[188] C. Tudryn, S. Schweizer, R. Hopkins, L. Hobbs, and A. J. Garratt-Reed, Journal of the Electrochemical Society **152**, E131 (2005).
[189] A. Shevchenko, M. Heiliö, T. Lindvall, A. Jaakkola, I. Tittonen, M. Kaivola, and T. Pfau, Physical Review A **73**, 051401 (2006).
[190] P. Trocellier, S. Agarwal, and S. Miro, Journal of Nuclear Materials **445**, 128 (2014).
[191] J. S. Bunch, S. S. Verbridge, J. S. Alden, A. M. van der Zande, J. M. Parpia, H. G. Craighead, and P. L. McEuen, Nano letters **8**, 2458 (2008).
[192] R. Nair, H. Wu, P. Jayaram, I. Grigorieva, and A. Geim, Science **335**, 442 (2012).
[193] A. Van Wieringen and N. Warmoltz, Physica **22**, 849 (1956).
[194] M. Alatalo, M. Puska, and R. Nieminen, Physical Review B **46**, 12806 (1992).
[195] P. Souers, I. Moen, R. Lindahl, and R. Tsugawa, Journal of the American Ceramic Society **61**, 42 (1978).
[196] S. Steward, *Review of hydrogen isotope permeability through materials*, Tech. Rep. (Lawrence Livermore National Lab., CA (USA), 1983).
[197] N. Kurita, N. Fukatsu, H. Otsuka, and T. Ohashi, Solid state ionics **146**, 101 (2002).
[198] H. Laska, R. Doremus, and P. Jorgensen, The Journal of Chemical Physics **50**, 135 (1969).
[199] F. J. Norton, Journal of Applied Physics **28**, 34 (1957).
[200] P. Marin, M. Dialinas, G. Lissillour, A. Marraud, and A. Reboux, Vacuum **49**, 309 (1998).
[201] P. Jung, Nuclear Instruments and Methods in Physics Research Section B: Beam Interactions with Materials and Atoms **91**, 362 (1994).
[202] C. Griffioen, J. Evans, P. D. Jong, and A. V. Veen, Nuclear Instruments and Methods in Physics Research Section B: Beam Interactions with Materials and Atoms **27**, 417 (1987).
[203] C.-A. Chen, Y. Sun, Z. Huang, C. Liu, and S. Wu, Physica Scripta **2003**, 97 (2003).
[204] M. Mantina, A. C. Chamberlin, R. Valero, C. J. Cramer, and D. G. Truhlar, The Journal of Physical Chemistry A **113**, 5806 (2009).
[205] S. Batsanov, Inorganic materials **37**, 871 (2001).
[206] M. Binns, S. McQuaid, R. Newman, and E. Lightowlers, Semiconductor science and technology **8**, 1908 (1993).
[207] D. Sparks, Journal of Micromechanics and Microengineering **23**, 015016 (2013).
[208] D. Sparks, J. Mitchell, and S. Lee, Journal of Sensor Technology **3**, 101 (2013).
[209] G. F. Cerofolini, F. Corni, S. Frabboni, C. Nobili, G. Ottaviani, and R. Tonini, Materials Science and Engineering: R: Reports **27**, 1 (2000).
[210] Ultra low helium leak detectors using the accumulation method and NEG pumps have measured leak rates [304] as low as $10^{-15}\mathrm{mbar\,l\,s^{-1}}$.
[211] S. H. Christiansen, R. Singh, and U. Gosele, Proceedings of the IEEE **94**, 2060 (2006).
[212] The relative conductance, or leak rate, of non-interacting gases, is proportional to the square root of their masses. Hence helium will leak 2.6 times faster than nitrogen. For the following calculation we has assumed the average molecular mass of is 29.
[213] G. Attard and C. Barnes, *Surfaces* (Oxford University Press Oxford, UK, 1998).

[214] R. Straessle, M. Pellaton, C. Affolderbach, Y. Pétremand, D. Briand, G. Mileti, and N. de Rooij, Journal of Applied Physics **113**, 064501 (2013).
[215] D. Sparks, S. Massoud-Ansari, and N. Najafi, in *Micromachining and Microfabrication* (International Society for Optics and Photonics, 2004) pp. 70–78.
[216] D. Sparks, J. Trevino, S. Massoud-Ansari, and N. Najafi, Journal of Micromechanics and Microengineering **16**, 2488 (2006).
[217] R. Wolffenbuttel and K. Wise, Sensors and Actuators A: Physical **43**, 223 (1994).
[218] S. Lani, A. Bosseboeuf, B. Belier, C. Clerc, C. Gousset, and J. Aubert, Microsystem technologies **12**, 1021 (2006).
[219] C. C. Lee, C. Y. Wang, and G. Matijasevic, Components, Hybrids, and Manufacturing Technology, IEEE Transactions on **16**, 311 (1993).
[220] This is not the case for Au-Sn eutectic as the formation of the alloy increases the eutectic point.
[221] S. Mack, H. Baumann, U. Gösele, H. Werner, and R. Schlögl, Journal of the Electrochemical Society **144**, 1106 (1997).
[222] S. Mack, H. Baumann, and U. Gosele, in *Micro Electro Mechanical Systems, 1997. MEMS'97, Proceedings, IEEE., Tenth Annual International Workshop on* (IEEE, 1997) pp. 488–493.
[223] U. Gosele, H. Stenzel, T. Martini, J. Steinkirchner, D. Conrad, and K. Scheerschmidt, Applied physics letters **67**, 3614 (1995).
[224] T.-K. Chuang, A. Usenko, and J. Cites, ECS Transactions **33**, 501 (2010).
[225] S. Millar and M. Desmulliez, Sensor Review **29**, 339 (2009).
[226] W. Reinert, D. Kahler, and G. Longoni, in *Electronic Packaging Technology Conference, 2005. EPTC 2005. Proceedings of 7th*, Vol. 1 (IEEE, 2005) pp. 6–pp.
[227] Z. Gan, D. Huang, X. Wang, D. Lin, and S. Liu, Sensors and Actuators A: Physical **149**, 159 (2009).
[228] S.-W. Choi, W.-B. Choi, Y.-H. Lee, B.-K. Ju, M.-Y. Sung, and B.-H. Kim, Journal of The Electrochemical Society **149**, G8 (2002).
[229] O. Zucker, W. Langheinrich, M. Kulozik, and H. Goebel, Sensors and Actuators A: Physical **36**, 227 (1993).
[230] W. Kern, Journal of the Electrochemical Society **137**, 1887 (1990).
[231] W. Kern *et al.*, *Handbook of semiconductor wafer cleaning technology*, Vol. 623 (Noyes Park Ridge, NJ, 1993).
[232] J. R. Vig, Journal of Vacuum Science & Technology A: Vacuum, Surfaces, and Films **3**, 1027 (1985).
[233] S. Franssila, *Introduction to microfabrication* (Wiley. com, 2010).
[234] M. Taborelli, *Cleaning and surface properties*, Tech. Rep. (CERN, 2006).
[235] We assume a hydrogen capacity of 10^{-7} mols ($x_H = 0.01$) which results in $Q_{OG} \sim 10^{-12}\,\mathrm{mbar\,l\,s^{-1}cm^{-2}}$.
[236] R. Elsey, Vacuum **25**, 299 (1975).
[237] R. Elsey, Vacuum **25**, 347 (1975).
[238] Typically $k = 1$ for high surface coverage, but increases to 2 when desorption is recombination limited at low coverage.
[239] G. S. Lewin, *Fundamentals of Vacuum Science and Technology* (McGraw-Hill, USA, 1965).
[240] W. Perkins and D. Begeal, The Journal of Chemical Physics **54**, 1683 (1971).
[241] V. Nemanič, P. J. McGuiness, N. Daneu, B. Zajec, Z. Siketić, and W. Waldhauser, Journal of alloys and compounds **539**, 184 (2012).
[242] N. Nickel, W. Jackson, I. Wu, C. Tsai, and A. Chiang, Physical Review B **52**, 7791 (1995).
[243] S. Koveshnikov, S. Nosenko, and E. Yakimov, physica status solidi (a) **120**, 391 (1990).
[244] Y. Kamiura, M. Yoneta, and F. Hashimoto, Applied physics letters **59**, 3165 (1991).
[245] C. Seager and R. Anderson, Applied physics letters **53**, 1181 (1988).
[246] K. Schmalz and K. Tittelbach-Helmrich, physica status solidi (a) **113**, K9 (1989).
[247] M. Vergnat, S. Houssaini, C. Dufour, A. Bruson, G. Marchal, P. Mangin, R. Erwin, J. Rhyne, and C. Vettier, EPL (Europhysics Letters) **14**, 457 (1991).
[248] X.-M. Tang, J. Weber, Y. Baer, and F. Finger, Physical Review B **42**, 7277 (1990).
[249] N. Johnson, C. Nebel, P. Santos, W. Jackson, R. Street, K. Stevens, and J. Walker, Applied physics letters **59**, 1443 (1991).
[250] C. Seager, R. Anderson, and D. Brice, Journal of applied physics **68**, 3268 (1990).
[251] R. Newman, J. Tucker, A. Brown, and S. McQuaid, Journal of applied physics **70**, 3061 (1991).
[252] A. Majumdar, S. Balasubramanian, V. Venkataraman, and N. Balasubramanian, Journal of applied physics **82**, 192 (1997).
[253] B. Sopori, X. Deng, J. Benner, A. Rohatgi, P. Sana, S. Estreicher, Y. Park, and M. Roberson, Solar Energy Materials and Solar Cells **41**, 159 (1996).
[254] C. Herrero, M. Stutzmann, A. Breitschwerdt, and P. Santos, Physical Review B **41**, 1054 (1990).
[255] N. Johnson and C. Herring, Physical Review B **46**, 15554 (1992).
[256] R. Rizk, P. De Mierry, D. Ballutaud, M. Aucouturier, and D. Mathiot, Physical review B **44**, 6141 (1991).
[257] S. Fabian, S. Kalbitzer, C. Klatt, M. Behar, and C. Langpape, Physical Review B **58**, 16144 (1998).
[258] Y. Huang, Y. Ma, R. Job, and A. Ulyashin, Journal of applied physics **96**, 7080 (2004).
[259] W. Hansen, S. Pearton, and E. Haller, Applied Physics Letters **44**, 606 (1984).
[260] M. Capizzi and A. Mittiga, Applied physics letters **50**, 918 (1987).
[261] A. Mogro-Campero, R. Love, and R. Schubert, Journal of The Electrochemical Society **132**, 2006 (1985).
[262] S. J. Pearton, J. W. Corbett, and T. Shi, Applied Physics A **43**, 153 (1987).
[263] J. Chevallier and M. Aucouturier, Annual Review of Materials Science **18**, 219 (1988).
[264] E. E. Haller, Semiconductor Science and Technology **6**, 73 (1991).
[265] S. Myers, H. Birnbaum, J. Corbett, G. DeLeo, S. Estreicher, E. Haller, P. Jena, N. Johnson, R. Kirchheim, and S. Pearton, Reviews of Modern Physics **64**, 559 (1992).
[266] C. G. Van de Walle and J. Neugebauer, Annu. Rev. Mater. Res. **36**, 179 (2006).
[267] T. Miyake, T. Ogitsu, and S. Tsuneyuki, Physical review letters **81**, 1873 (1998).
[268] B. Sopori, Y. Zhang, and N. Ravindra, Journal of electronic materials **30**, 1616 (2001).
[269] T. Ichimiya and A. Furuichi, The International Journal

of Applied Radiation and Isotopes **19**, 573 (1968).
[270] S. McQuaid, R. Newman, J. Tucker, E. Lightowlers, R. A. Kubiak, and M. Goulding, Applied physics letters **58**, 2933 (1991).
[271] Even higher surface concentrations can be produced with high energy ion bombardment, but we regard this as a non-standard process.
[272] M. Dürr and U. Höfer, Surface science reports **61**, 465 (2006).
[273] P. Gupta, V. Colvin, and S. George, Physical Review B **37**, 8234 (1988).
[274] T. Hickmott, Journal of Applied Physics **31**, 128 (1960).
[275] B. J. Todd, Journal of Applied Physics **26**, 1238 (1955).
[276] J. Hobson, Journal of Vacuum Science and Technology **1**, 1 (1964).
[277] P. Redhead, Vacuum **53**, 137 (1999).
[278] Hobson [276] measured a 'leak rate' (which we assume to be outgassing) of $1.8\times10^{-14}\,\mathrm{Torr\,l\,s^{-1}}$ (equiv. nitrogen) but gave no value for the glass surface area other than it being similar to Redhead et al's apparatus [282] who used a 500 ml bulb. Assuming the surface area of $300\,\mathrm{cm}^2$ we calculate an outgassing rate of $8\times10^{-17}\,\mathrm{mbar\,l\,s^{-1}cm^{-2}}$.
[279] This appears counter-intuitive, but the greater pressure results in more collisions and thermalization with the surrounding gas atoms which reduces the velocity and, therefore, the probability of being buried in the growing film.
[280] G.-Y. Hsiung, C. Cheng, C. Yang, C. Chan, and J. Chen, in *AIP Conference Proceedings* (2009).
[281] W. Palosz, Journal of crystal growth **267**, 475 (2004).
[282] P. Redhead, E. Kornelsen, and J. Hobson, Canadian Journal of Physics **40**, 1814 (1962).
[283] W. Lange, Journal of Vacuum Science and Technology **2**, 74 (1965).
[284] R. Baptist and F. Levy, Vacuum **43**, 213 (1992).
[285] J. Bennett, S. Hughes, R. Elsey, and T. Parry, Vacuum **73**, 149 (2004).
[286] D. Hu, W. Ho, X. Chen, S. Wang, and W. A. Goddard III, Physical review letters **78**, 1178 (1997).
[287] J. Setina, S. Avdiaj, and B. Erjavec, Vacuum **92**, 20 (2013).
[288] J. Kamiya, V. Baglin, G. Bregliozzi, and J. M. Jimenez, Vacuum **85**, 1178 (2011).
[289] M. Hasegawa, R. K. Chutani, R. Boudot, L. Mauri, C. Gorecki, X. Liu, and N. Passilly, Journal of Micromechanics and Microengineering **23**, 055022 (2013).
[290] H. Henmi, S. Shoji, Y. Shoji, K. Yoshimi, and M. Esashi, Sensors and Actuators A: Physical **43**, 243 (1994).
[291] T. Rogers, Journal of Micromechanics and Microengineering **2**, 164 (1992).
[292] S. Shoji, H. Kikuchi, and H. Torigoe, Sensors and Actuators A: Physical **64**, 95 (1998).
[293] J. Wei, H. Xie, M. Nai, C. Wong, and L. Lee, Journal of Micromechanics and Microengineering **13**, 217 (2003).
[294] A. Gerlach, D. Maas, D. Seidel, H. Bartuch, S. Schundau, and K. Kaschlik, Microsystem technologies **5**, 144 (1999).
[295] U. Mescheder, M. Alavi, K. Hiltmann, C. Lietzau, C. Nachtigall, and H. Sandmaier, Sensors and Actuators A: Physical **97**, 422 (2002).
[296] H. Takagi, R. Maeda, T. R. Chung, and T. Suga, Sensors and Actuators A: Physical **70**, 164 (1998).
[297] V. Dragoi, G. Mittendorfer, C. Thanner, and P. Lindner, Microsystem Technologies **14**, 509 (2008).
[298] V. Nemanič and J. Šetina, Vacuum **49**, 233 (1998).
[299] H. Wensink, J. Berenschot, H. V. Jansen, and M. C. Elwenspoek, in *Micro Electro Mechanical Systems, 2000. MEMS 2000. The Thirteenth Annual International Conference on* (IEEE, 2000) pp. 769–774.
[300] B. Jian and W. A. van Wijngaarden, JOSA B **30**, 238 (2013).
[301] Y. Ishikawa and T. Yoshimura, Journal of Vacuum Science & Technology A: Vacuum, Surfaces, and Films **13**, 1847 (1995).
[302] N. Robinson, *The Physical Principles of Ultra-high Vacuum: Systems and Equipment*, High vacuum series (Chapman and Hall, 1968).
[303] H. Ohadi, M. Himsworth, A. Xuereb, and T. Freegarde, Optics express **17**, 23003 (2009).
[304] L. E. Bergquist and Y. T. Sasaki, Journal of Vacuum Science & Technology A: Vacuum, Surfaces, and Films **10**, 2650 (1992).